Dissertation zur Erlangung des Doktorgrades

der Fakultät für Chemie und Pharmazie

der Ludwig-Maximilians-Universität München

Templated Macro/Mesoporous

Titania and Carbon Nanostructures

Benjamin Mandlmeier

aus

Starnberg, Deutschland

2013

Erklärung

Diese Dissertation wurde im Sinne von § 7 der Promotionsordnung vom 28. November 2011 von Herrn Professor Dr. Thomas Bein von der Fakultät für Chemie und Pharmazie vertreten.

Eidesstattliche Versicherung

Diese Dissertation wurde eigenständig und ohne unerlaubte Hilfe erarbeitet.

München, den 11.02.2013

....

(Unterschrift des Autors, B. Mandlmeier)

Dissertation eingereicht am 28.02.2013

1. Gutachter: Prof. Dr. Thomas Bein

2. Gutachterin: Prof. Dr. Christina Scheu

Mündliche Prüfung am 26.03.2013

Danksagung

Als erstes bedanke ich mich bei meinem Doktorvater Professor Thomas Bein für die stete Unterstützung und die ausgezeichnete Betreuung meiner Forschungsvorhaben und für die grandiosen Wandertage, die zu einem freundlichen und freien Arbeitsklima beigetragen haben. Selbstverständlich geht auch ein recht herzlicher Dank an Frau Professorin Christina Scheu für ihr Gutachten.

Angefangen im AK hat es einmal bei meinem F-Praktikum und ich lernte während der Promotion die Welt der Nanomaterialien so richtig kennen und konnte mich immer auf die jetzige Gruppe und auf meine ehemaligen Kollegen verlassen. Dank weitreichender kreativer Ideen hatte ich genug Gelegenheiten interessante Techniken zu erlernen und spannende Projekte zu erkunden. Darum ermöglichte es mir Thomas Bein weiterhin ausgiebig die Ergebnisse auf diversen DZTs, Winterschools, Workshops und Konferenzen in Valencia (HOPV) und San Francisco (MRS Meeting) zu präsentieren und die lokalen Köstlichkeiten zu studieren.

Dina, vielen lieben Dank für die ganze Unterstützung und die Ermutigungen! Echt bärig, mir fehlen einfach die Worte, wie du bestimmt schon einmal bemerkt haben solltest.

Im AK Bein habe ich neben den unzähligen Geräten, besonders unser REM in der sehr warmen Dunkelkammer zu schätzen gelernt, danke Markus und Steffen für die erstklassige hervorragende Ausbildung und v.a. für die noch besseren TEM Aufnahmen.

Ich danke auch meinen weitreichenden Nachbarschaften, die immer für einen kleinen oder großen Spaß zu haben und nicht nachtragend waren, wenn sie und ich mal wieder eine nötige Frischluftkur bekommen haben. Den Mitgliedern der Subgroups möchte ich ganz herzlich für

die wöchentlichen Diskussionen danken, die manchmal etwas ausschweifend, jedoch aber stets weiterführend, interessant und grundsätzlich immer wichtig waren. Aber ohne euch, v.a. Johann und Jörg, wäre es manchmal nicht so rund gegangen, super! An diesem Punkt möchte ich mich bei Norma und Hans dankbar äußern, denn wir wären sonst auch bei den vielen sportlichen und gesellschaftlichen Unternehmungen, die z.T. ohne Schnäppchen nicht realisierbar sind, verloren und durstig geblieben.

Großen Dank möchte ich selbstverständlich auch an meine Masterstudenten Carminna Ottone, Erika Mühlbauer und Enrico Greul für ihre tollen Arbeiten richten. Hierbei möchte ich natürlich auch nicht meine hilfreichen Praktikanten und Bachelorstudenten Alexander Hofer, Jonathan Baily, Alexander Dippold, Areenan In-Iam, Michael Hörmansdorfer, Bianca Wattenberg, Marie Asano, Diana Car, Marta Wolfshorndl, Martina Täglich und Burǧa Kayaalp vergessen. Ich wünsche euch weiterhin viel Erfolg!

Meinen weiteren Kooperationspartnern Guang He und Prof. Linda Nazar (Univ. of Waterloo), Valentina Cauda (Centre for Space Human Robotics) und Hynek Němec (Academy of Sciences of the Czech Republic) bin ich für ihre fantastische Zusammenarbeit zu tiefstem Dank verpflichtet. Somit möchte ich auch dem „Enzo" Armenitsch für die Betreuung an der Beamline danken. Vielen Dank an Prof. Laurie Peter und Renate für die gastfreundlichen und lehrreichen Wochen im malerischen Bath, das jederzeit eine Reise wert ist.

Für finanzielle Unterstützung danke ich dem NIM Graduierten-Programm (DFG Excellenzcluster), besonders aber Dr. Peter Sonntag und Silke Mayerl-Kink, die mir eine Serie von hilfreichen Kursen und eine spannende Förderung von hochbegabten Schülern ermöglichten. In diesem Zusammenhang bedanke ich mich auch gerne beim DAAD und der GDCh für die großzügigen Reisestipendien. Susanne und Marilena vom CeNS Team danke ich besonders für die wunderbaren und perfekt organisierten Workshops.

Regina und Tina, euch zwei Lieben habe ich nicht vergessen und Ihr bekommt ein ganz herzliches dickes Lob von mir für alle eure Mühen und Taten, denn ohne Euch geht es einfach nicht.

Zu guter Letzt geht mein größter Dank an meine Frau, Eltern und Schwestern und alle anderen Familienmitglieder (inkl. Maira), die mich so super und liebevoll unterstützten und immer für mich da waren. Besonders danke ich auch den Omas für die unübertroffene Nervennahrung. Alle zusammen für den nötigen Ausgleich im Urlaub, beim Sport und Spielen. Merci!

„Leider lässt sich eine wahrhafte Dankbarkeit mit Worten nicht ausdrücken.“

J.W. von Goethe

List of Abbreviations

3D	Three dimensional
3DOM	Three dimensional ordered macroporous
AAM	Anodic aluminum membrane
AAO	Anodic aluminum oxide
ALD	Atomic layer deposition
AM	Air mass
AU	Auger electrons
BET	Brunauer-Emmett-Teller
bmc	Bimodal mesoporous carbon
BSE	Back scattered electrons
CB	Conduction band
CCD	Charge-coupled device
CCT	Colloidal crystal templating
cmc	Critical micelle concentration
cnf	Carbon nanofibers
conc.	Concentrated
CVD	Chemical vapor deposition
DFT	Density functional theory
DHT	Delayed humidity treatment
DLS	Dynamic light scattering
DSC	Dye-sensitized solar cell
EB	Binding energy
E_g	Band gap energy
EISA	Evaporation-induced self assembly
EQE	External quantum efficiency
EtOH	Ethanol
eV	Electron volt
fcc	Face-centered cubic
FESEM	Field emission scanning electron microscopy
FF	Fill factor

FFT	Fast Fourier transform
FTO	Fluorine doped tin oxide
FWHM	Full width at half maximum
GISAXS	Grazing-incidence small-angle scattering
HAADF	High angle annular dark field
hcp	Hexagonal closed-packed
HOMO	Highest occupied molecular orbital
HR	High resolution
HRTEM	High resolution transmission electron microscopy
IPCE	Incident photon-to-current conversion efficiency
I_{SC}	Short circuit current
ITO	Tin-doped indium oxide
I-V	Current-voltage
KLE	Poly(ethylene-co-butylene)-b-poly(ethylene oxide)
KPG	Kerngezogenes Präzisions-Glasgerät
LHE	Light harvesting efficiency
LIB	Lithium-ion battery
LUMO	Lowest unoccupied molecular orbital
MMA	Methyl methacrylate
NHE	Normal hydrogen electrode
N719	Ruthenuim based dye; $[C_{58}H_{86}N_8O_8RuS_2]^{2-}[N(n\text{-}Bu)_4]^{2+}$
nmc	Nanosized mesoporous carbon
NPs	Nanoparticles
PMMA	Poly (methyl methacrylate)
PS	Polystyrene
PVD	Physical vapor deposition
QDs	Quantum dots
QSDFT	Quenched solid state DFT
rcf	Relative centrifugal force
rpm	Revolutions per minute
SAED	Selected area electron diffraction
SAXS	Small angle X-ray scattering
SDS	Sodium dodecylsulfate

SE	Secondary electrons
SEM	Scanning electron microscopy
STEM	Scanning transmission electron microscopy
SLB	Supported lipid bilayer
TCO	Transparent conducting oxide
TEM	Transmission electron microscopy
TEOS	Tetraethyl orthosilicate
TEOT	Tetraethyl orthotitanate
Tert-BuOH	Tert-butanol
TGA	Thermo-gravimetric analysis
THF	Tetrahydrofuran
UV/Vis	Ultraviolet/visible
V_{OC}	Open circuit potential
XRD	X-ray diffraction

Abstract

Due to their unique properties, nanomaterials are becoming increasingly important in our life. Nanostructuring introduces additional functional properties to existing materials that can greatly enhance their performance in various applications, and can open a way towards novel devices and techniques. The ability to control the formation of the nanomaterials on all levels, from morphology to composition, is one of the key challenges in the development of the efficient functional nanosystems.

This thesis deals with the development of approaches enabling fabrication in a controlled way of various porous titania and carbon morphologies for energy conversion and energy storage applications. We focus on the possibility to tune and to control several nanomorphology parameters such as: (i) the size and the ordering of the pores; (ii) the composition and crystallinity of the functional scaffold; (iii) the macroscopic shape such as thin films, bulk, particles and fibers. Moreover, we are interested in even more complex hierarchical morphologies combining different types of porosity and crystallinity. One important goal is the synthesis of macroporous materials with a pore size beyond 50 nm, as this scale is required by several of the applications studied. The developed materials were examined as anodes in dye-sensitized solar cells (titania) and as cathodes in lithium-sulfur batteries (carbon) in order to evaluate the role of the morphology on the device performance.

A main strategy employed here for the fabrication of the macroporous materials is based on the use of poly(methyl methacrylate) (PMMA) beads as shape-persistent sacrificial templates in a one-step (negative replication) or a two-step (reverse replication) procedure. A part of this thesis was devoted to the synthesis of monodisperse PMMA beads of different size. In chapter 3 we describe the synthesis of PMMA particles by emulsion polymerization. We have

optimized this synthesis to be able to generate particles with different sizes ranging from 40 nm to 320 nm and with narrow size distribution by adjusting the monomer/surfactant/initiator ratio.

We have investigated the formation of 3-D macroporous TiO_2 films by a one-step co-deposition of PMMA particles and different titania precursors (chapter 4). To control the crystallinity, an amorphous molecular precursor, or crystalline anatase nanoparticles (4, 6, or 18 nm), or their combination (brick and mortar approach) were used for a negative replication of the PMMA template. Further improvement was achieved by a post-synthetic humidity treatment leading to improved film quality, reduced shrinkage of the pores and increased crystallinity of the titania walls.

We have also used a more elaborate two-step replication of a pre-assembled PMMA template to obtain even more complex hierarchical morphologies or to generate different macroscopic shapes. In this way, we have developed a novel hierarchical periodic nanostructure composed of a macroporous titania crystalline scaffold and a mesoporous titania phase (chapter 5). In the first step, a macroporous titania scaffold was obtained by a negative replication of the PMMA bead array, which was subsequently filled with surfactant-containing titania precursors to obtain a mesostructured titania phase. The formation of mesostructure in the confined space of the macroporous scaffold upon thermal treatment was investigated with in-situ grazing incidence small angle X-ray scattering (GISAXS). The macroporous scaffold strongly influences the mesostructure assembly and leads to much larger structural parameters of the formed mesostructure, this effect becoming more pronounced with decreasing pore size of the macroporous host. Furthermore, the inverse opal scaffold acts as a stabilizing matrix, limiting the shrinkage of the mesopores upon heating. This effect is coupled with an enhanced crystallization of the mesophase, which is attributed to the crystalline walls of the

macroporous host. The hierarchical titania was implemented as anode in dye-sensitized solar cells (DSCs).

This replication procedure was also adapted for the synthesis of mesoporous titania spheres that can be considered as a positive mesoporous replica of the PMMA particles. In a first step macroporous silica with tunable pore sizes was obtained, which was used in a second step as a sacrificial hard template for spherical titania (chapter 6). For that purpose, the silica voids were filled with a mixture of the surfactant Pluronic P123 and tetraethyl orthotitanate leading to the mesoporous crystalline titania after calcination, and silica was etched afterwards with NaOH to produce polycrystalline titania balls.

A similar templating strategy was used for the formation of spherical hexagonally ordered mesoporous carbon (300 nm, chapter 7) and colloidal nanosized mesoporous carbon (60 nm, chapter 9). Both materials feature high surface area and high pore volume. To obtain colloidal nanosized mesoporous carbon, the macroporous silica inverse opal template was filled with a triconstituent precursor mixture of Pluronic F127 as a soft template, tetraethyl orthosilicate and resol oligomers as carbon source. After thermopolymerization and carbonization at 900 °C in nitrogen a composite mesoporous carbon/silica material was formed. All the silica, both in the macroscopic scaffold and in the carbon phase, was removed afterwards with HF to obtain a bimodal porosity.

We have also adapted this protocol to obtain mesoporous carbon fibers (chapter 8). This was achieved by replacing PMMA templates in the first step with dense carbon fibers, and the resulting tubular silica template was filled and post-treated in a way similar to the carbon sphere approach. Again we observed a confinement effect of the larger template, resulting in a reduced shrinkage of the mesophase and larger structural parameters.

The obtained carbon nanomaterials were further investigated in two different applications. The beneficial influence of the spherical and fiber morphology of the mesoporous carbon on performance in lithium-sulfur batteries was demonstrated in our collaboration with Guang He and Prof. Linda Nazar (chapter 7 and 8). These promising nanostructured cathodes enabled very high initial capacities and excellent cycling stability performance.

For the first time colloidal nanosized carbon spheres (NCS, ca. 60 nm) were loaded in a solution with calcein as model drug and were efficiently sealed with a stable supported lipid bilayer (SLB) cap system (chapter 9). Molecular release experiments showed the efficiency of our system, which is tight until the addition of the surfactant Triton X-100, destabilizing the lipid bilayer and initiating a complete and controlled release of the fluorescent dye from the highly porous carbon.

Table of Contents

1. Introduction

1.1. Goals of Study

This thesis is focused on developing templating strategies for mesoporous and macroporous titania and carbon morphologies in different morphologies that can serve in applications where porous structure is essential for optimized functionality. Especially, nano-morphologies used in devices required for energy generation and storage – mainly solar cells and batteries – need to be improved continuously by developing new efficient synthetic techniques and by implementing abundant raw materials.

Specifically, macro- and/or mesoporosity was introduced into 3D titania and carbon architectures by the direct replication of hard and soft templates, colloidal poly(methylmetacrylate) and block-copolymers, respectively.

We also aimed at gaining high synthetic flexibility for controlling the structural parameters of new nanostructures. These include (i) the size of the macropores and size and the ordering of the mesopores; (ii) the composition and crystallinity of the functional scaffold; (iii) the macroscopic shape such as thin films, bulk, particles and fibers.

For the development of defined macroporous oxides it was essential to polymerize uniform colloidal PMMA in emulsions. These sacrificial templates – variable in size – were deposited in combination with metal alkoxide precursors and crystalline building blocks to create macroporous titania films and bulk silica by using different techniques.

Another purpose of this study deals with the creation of more complex hierarchical systems and the investigation of mesostructure formation in the confined space of macroporous hosts

acting as hard template. This templating approach could also be transferred to obtain a novel tubular macroporous silica hard template, showing comparable dimensions to anodic alumina membranes. This was achieved by using dense carbon fibers, in contrast to colloidal PMMA, as initial hard template in a silica matrix.

We finally investigated the physical properties of these materials with a view on diverse applications, i.e., the performance of dye-sensitized solar cells (DSCs), rechargeable lithium-sulfur batteries and controlled drug delivery and studied the influence of the nanostructures on the device performance.

1.2. Colloidal Templates

Colloids are defined particles with sizes from the micrometer down to the nanometer scale and their movement in a liquid dispersion can be described by Brownian motion. Various synthetic approaches were reported to obtain organic and inorganic colloids with uniform properties, such as size, shape, surface chemistry and chemical composition.[1]

Colloidal silica[2] can be as small as several nanometers, it is available through lab scale synthesis[3] and at industrial scale, e.g. Ludox®. One of the most common inorganic colloids is represented by the so-called Stöber spheres. They are composed of amorphous silica and can be made in a size-range from about 2 μm to 50 nm.[4-6] In basic solutions the Stöber spheres feature a negative surface charge resulting from the deprotonation of silanol groups. These colloids are stable upon thermal treatment and can be fused at around 800 °C.[7] Silica spheres with diameters from about 150 to 400 nm can also be naturally found in opals, where spheres

are periodically ordered in domains. Therefore they can interact with light and exhibit different colour effects (Figure 1.1 a), which is why they are also known as photonic crystals. Figure 1.1 b shows an SEM image of the close packed face-centered cubic (fcc) opal structure schematically illustrated in Figure 1.1 c.[8]
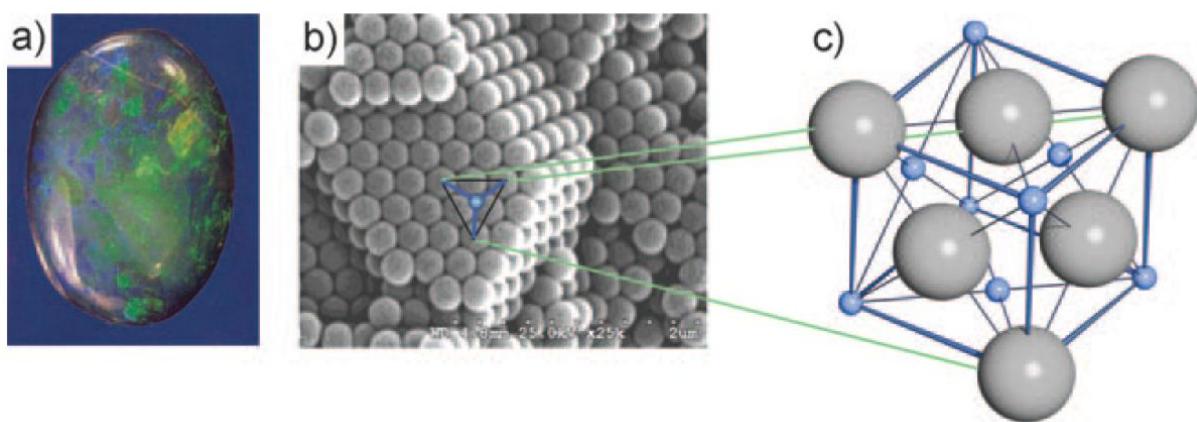
Figure 1.1: Photograph and SEM image of a natural opal (a, b) and the corresponding fcc illustration (c).[8]

Another important colloid family includes polymer particles. The most common polymer particles are spherical polystyrene (PS) or polymethyl methacrylate (PMMA) particles, which are typically prepared by emulsion polymerization of styrene (C_8H_8) and methyl methacrylate (MMA, $C_5H_8O_2$) or derivatives, respectively.[9] The colloid formation process can be separated into three main parts (Figure 1.2 a). During the first step, the organic monomer M is homogeneously emulsified by a surfactant if the concentration of the latter is above the critical micelle concentration (cmc). To this mixture an initiator I is added to initialize the polymerization with cations, anions or radicals. In case of radical polymerizations the initiator I, which usually contains a peroxo or an azo group, can be decomposed to radicals R by applying heat or light. During the initiation these radicals diffuse into the micelles and react

with the monomer. The second step describes the reaction of the generated monomeric radicals with non-consumed monomers to form dimers. The dimers react further by the same mechanism with the formation of oligomeric chains and finally the polymer particles. In the last step, the concentration of polymer chains is higher than that of the monomer, which is consumed by the remaining radicals. The recombination of two radicals leads to a termination of polymerization. The reaction mechanism of the MMA polymerization, initiated by the thermal decomposition of potassium peroxodisulfate, is shown in Figure 1.2 b.
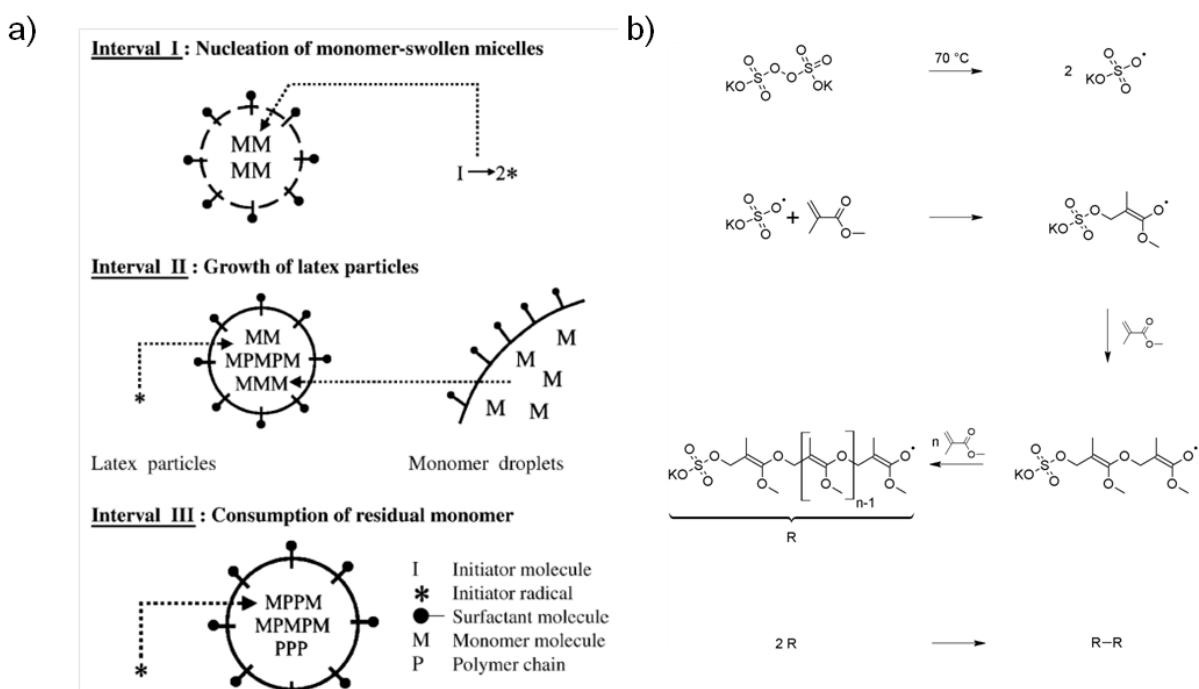
Figure 1.2: Schematic illustration of the micelle-based polymerization in aqueous solution (a) and the reaction mechanism of PMMA formation (b).[9]

The main advantage of the latex spheres is their fast and cheap preparation. Additionally, the size can be adjusted by changing the reaction parameters and composition of the reaction mixture.[1]

1.3. Colloidal Crystal Templating

Colloidal crystal templating (cct) describes a process in which colloids assemble periodically into three dimensional crystal lattices (opal). The opals can be deposited by several techniques which can be grouped into three major approaches (Figure 1.3).[8]
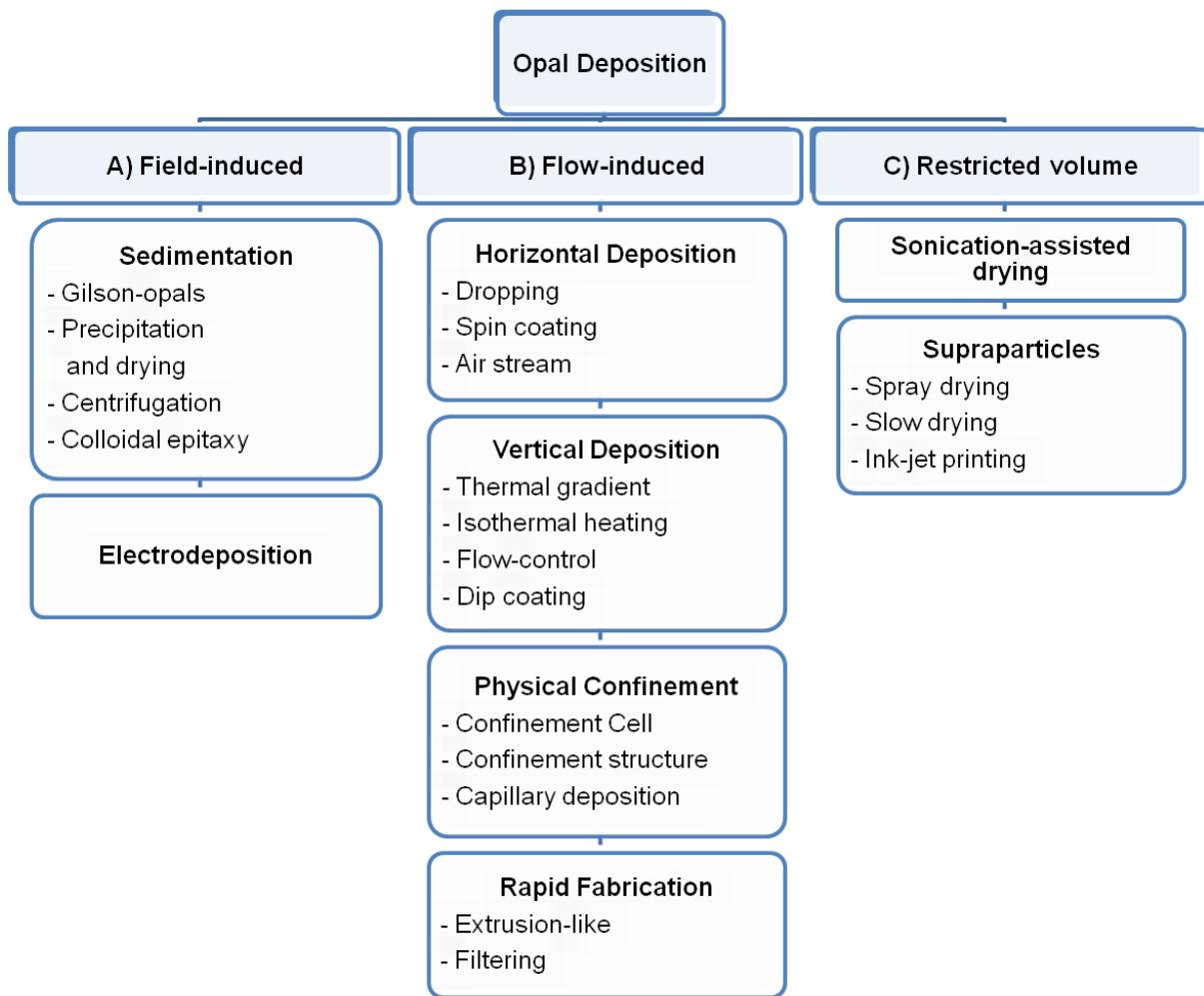
Figure 1.3: Schematic overview of different techniques for colloidal self-assembly.[8]

Field-induced deposition

Although colloidal dispersions of the latex beads are usually stable for months, they can slowly sediment to the bottom. The rate of sedimentation depends on the particles´ density and size, but this process is usually slow. Sedimentation can be accelerated by an additional gravity force. In practice the gravity is applied during the washing procedure of latex spheres after polymerization, which includes repeated centrifugation and redispersion steps. The external field leads to a density gradient in one direction within the dispersion, which results in a colloidal packing.[8,10] Formation of the fcc structure, which is also present in natural grown opals, is usually more favoured than a hexagonal closed-packing (hcp).[11] Advanced scattering measurements performed under microgravity conditions have demonstrated that PMMA particles (508 nm) can also crystallize into a random hcp structure.[12]

Flow-induced deposition

Two typical examples for flow-induced deposition are horizontal and vertical deposition of colloids from a solution on a substrate.

The simplest case of horizontal deposition is drop casting of the dispersion of beads. This process usually results in non-uniform coatings having a thicker ring at the outside and a flat part in the middle. A variation of this method is the spin-coating deposition.[13]

Vertical deposition is usually made by placing a substrate close to vertically into the colloidal dispersion and letting it dry, but it can also be achieved by dip-coating. Alternatively, cct can be obtained by blade coating. In this method, some amount of bead dispersion is pulled by a blade over a fixed substrate using a motor (Figure 1.4; a-c).[14]
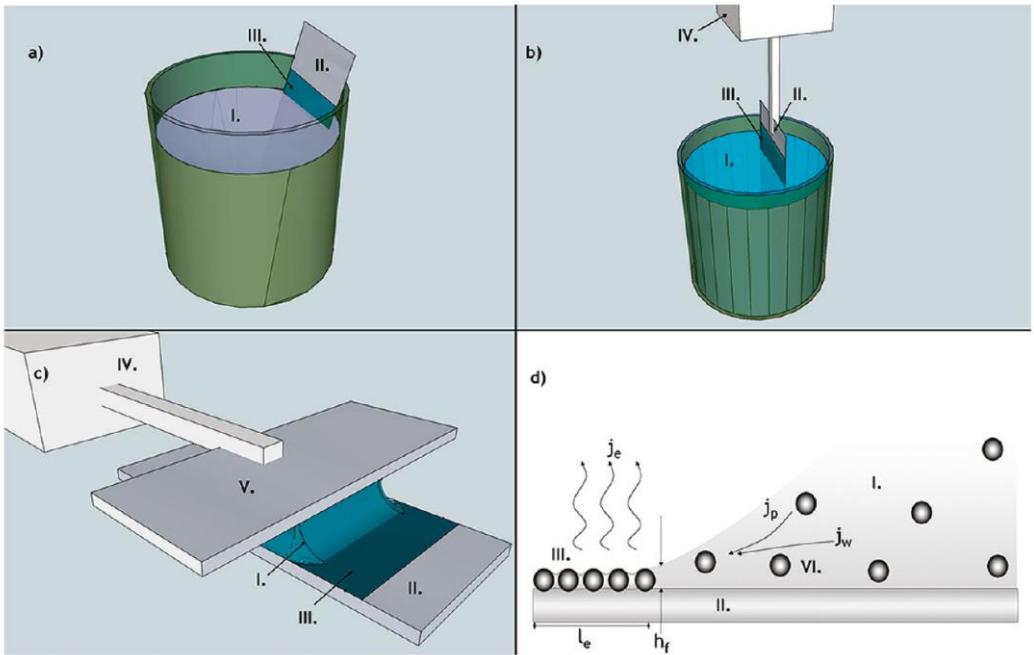
Figure 1.4: Colloidal crystal deposition using vertical drying (a), dip-coating (b) and blade coating (c). Illustration of the processes of colloidal packing taking place at the meniscus (d).[14]

Generally, a flow is induced by the evaporation of the solvent at the evaporation front (meniscus), which forces the arrangement of disordered colloids into a solid fcc structure.[6] It is reported that the shape and the height of the meniscus mainly influence local particle concentration and thus the growth of the colloidal crystal. Figure 1.4 d illustrates the processes which take place during flow-induced deposition; this mechanism is similar for all the deposition techniques described above. Drying of the wet particle film (III) with the length (l_e) and height (h_f) causes an evaporative flux of the water (j_e) and a dragging of the colloids. This leads to a convective flux (VI) from the bulk reservoir (I) into the cct, which includes a particle flux (j_p) and a water flux (j_w).[14]

Restricted volume deposition

Similar to the field induced deposition, the colloidal crystallization in the restricted volume deposition method is caused by the increase in the particle concentration beyond the critical concentration. In the restricted volume deposition process this is achieved by a volume reduction and an applied ultrasonic field, which generates a colloidal film faster and in higher quality compared to the reference prepared just by sedimentation.[15] It is suggested that the sonication-assisted homogenous drying helps to avoid formation of a lateral deposition front. As a consequence, the evaporation leads to a lateral concentration gradient and a lateral deposition front perpendicular to the substrate. The restriction of a volume, e.g. during the drying of dispersion droplet, leads to so called supraparticles, which are composed of (often disordered) packed smaller spheres.[6]

Stacking faults

The quality of the colloidal crystals strongly depends on the experimental conditions during the assembly such as temperature, humidity, air flow and vibrations. Stacking faults are often observed during the colloidal crystal assembly,[8,16,17] and their reduction is a key issue in the fabrication of ordered opals. Different point defects can arise within the crystal lattice, for example if a bead is missing (Schottky defect, Figure 1.5 a) or if smaller beads are incorporated into the lattice (Frenkel defect, Figure 1.5 b). Additionally, the long range order can be distorted by empty volumes which originate from the inclusion of large spheres or by local rearrangements (Figure 1.5 c, d).
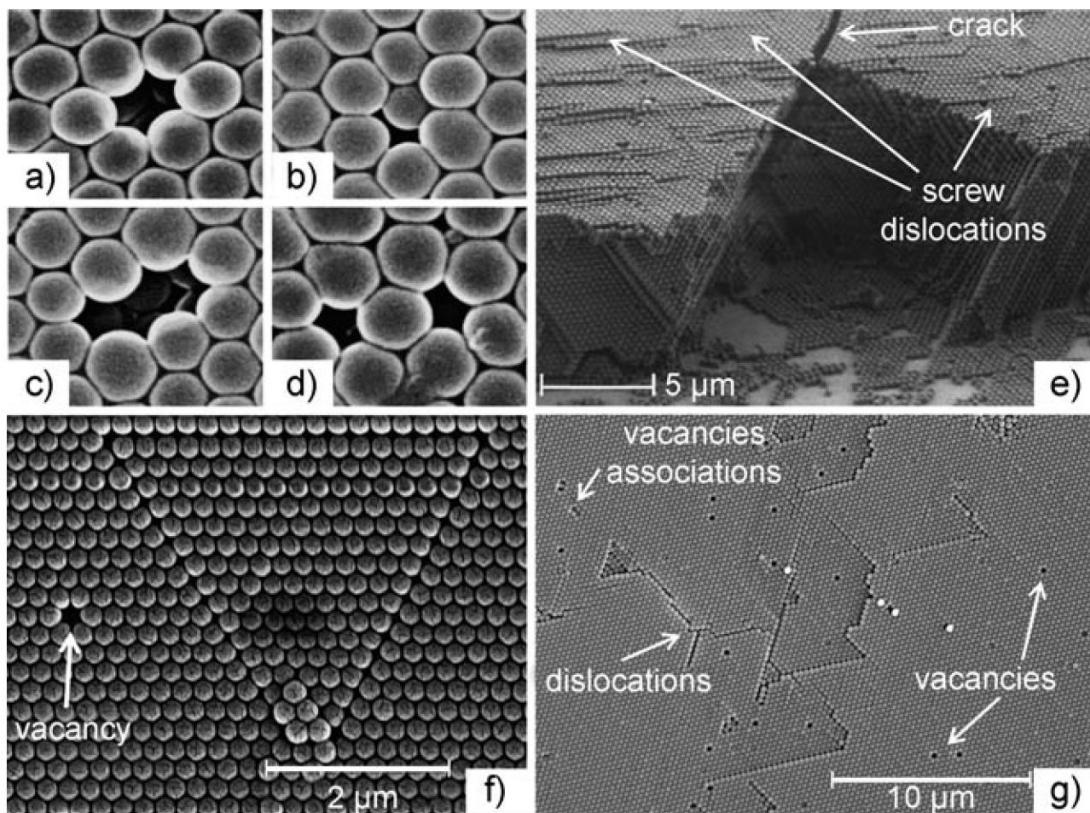
Figure 1.5: SEM images (a-g) show examples of possible defect types in colloidal crystals.[6]

Furthermore, displacements of lattice planes leading to step or screw dislocations can be caused by growth, slip and twinning defects. Lattice shrinkage during the drying process often leads to crack formation, which is frequently observed at the edges of the crystalline domains (Figure 1.5 a). Segregated domains (triangular part) are probably formed due to reduction of stress which is induced by edge dislocations (Figure 1.5 f). The expansion of point defects within the lattice leads to line defects (Figure 1.5 g).

1.4. Three-Dimensionally Ordered Macroporous Materials

Three-dimensionally ordered macroporous (3DOM) materials exhibit a structure having a long-range order of interconnected pores with the size larger than 50 nm (IUPAC). 3DOM materials can be prepared by the structural replication of ordered colloidal crystal (opals) and are also known as inverse opals. After replication, the former connection points (whose size can be tuned by a temperature treatment in case of polymer templates) lead to the formation of interconnection windows within the closed packed array of air spheres (macropores). These windows ensure a good accessibility and mass transport through the 3DOM bulk or film material. An ideal fcc pore structure features pore connections to twelve neighboring pores.[18-20] In general, three main approaches are used for synthesis of 3DOM materials by using colloidal spheres as hard templates (Figure 1.6).[1,21-24] The walls of 3DOM materials can be composed of amorphous or crystalline inorganic oxides, phosphates, hybrid composites,[20,25-27] carbon[28-30], metals[31-33], alloys[34-36] and metal-organic frameworks.[37]

The most common route to the fabrication of 3DOM materials is infiltration of a preformed colloidal crystal template with a precursor solution. Infiltration induced by capillary forces can be done e.g. by drop casting, spin-coating or dip-coating (Figure 1.6, top). Other techniques such as chemical vapor deposition (CVD)[38], atomic layer deposition (ALD)[39] or electrodeposition[1] can also be applied. A key factor in this process is the filling fraction of the interstitial voids, which can be improved by multiple infiltration steps and the application of vacuum. After solidification of the precursor the colloidal template can be removed. Silica templates are usually removed by etching with hydrofluoric acid or a strong base such as potassium hydroxide. In contrast, polymer spheres can be easily removed by thermal decomposition or extraction, which leads to the final macroporous structure. Advantages of

this method include the direct replication of the highly ordered template and, in the case of polymer spheres, the size control of the interconnection windows. (Figure 1.6, first row).
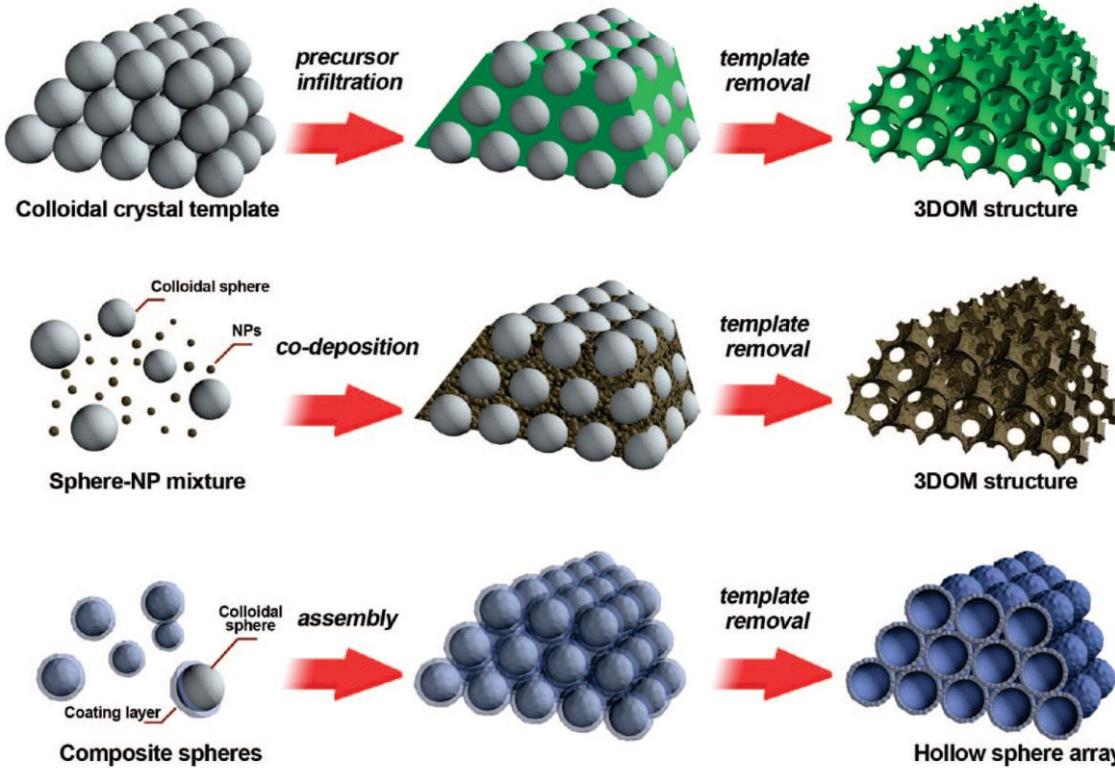
Figure 1.6: Illustration of three main approaches for fabrication of 3D ordered macroporous materials: infiltration of a preformed colloidal crystal template with a precursor (first row), a co-deposition of nanoparticle (NP) building blocks and colloids (second row), and the assembly of core-shell colloids (third row).[22]

Another approach to the fabrication of 3DOM materials is a so called 'one-pot' deposition process. In this method pre-formed inorganic nanoparticles (NPs) or sol-gel precursor solutions are common precursors for the templated material. For example, a colloidal dispersion of nanoparticles is mixed with the colloidal dispersion of latex beads, and the resulting mixture is deposited on a substrate with the formation of ordered composite

material. In order to form a solid stable scaffold after the template removal the NPs have to be connected, which can be achieved by sintering. The morphology of the resulting scaffold and its characteristics such as the size of the interconnecting windows and the wall thickness depend mainly on the relative ratios (mass or volume) of the nanoparticles and the latex beads. Wall thickness can be controlled by changing the relative concentration of the nanoparticles or other precursors. There is however a certain range of ratios where the formation of an interconnected porous scaffold is possible. Too high relative concentrations of nanoparticles lead to formation of isolated macropores that are not interconnected; the connection between the pores is realized only by an additional porosity within the scaffolds´ walls. One-pot deposition is a very advantageous approach for the fabrication of macroporous materials as it offers an easy control of the morphology parameters, is easily processable and enables fabrication of homogeneous layers. Thus, one-pot deposition was also applied for the fabrication of large-area crack-free 3DOM films by co-assembly of colloidal beads and a sol-gel precursor using vertical deposition and a film growing rate of 2 cm/ day.[40] However, this method is not universal. One of the main prerequisites is the colloidal dispersibility of the nanoparticles acting as the precursors for the macroporous material, which is not always achievable. Additionally, the colloidal dispersions of the nanoparticles and the latex beads have to be compatible, without possible flocculation and/ or phase separation (Figure 1.6, second row).

An alternative approach for the fabrication of 3 DOM materials is the deposition of composite core-shell particles. This method implies a high control over the wall thickness in the resulting scaffold by tuning the thickness of the shells. However, depending on the material of the shell, this method involves the risk of generating isolated air spheres within the bulk after

template removal, if the density of the shell is high or if it gets too thick (Figure 1.6, third row).

1.5. Sol-gel Precursors for 3DOM Materials

The sol-gel process is a general route for the preparation of colloidal dispersions of different materials.[41-45] The sol-gel dispersions can be composed of oxides, oxide-based hybrids, inorganic and organic-inorganic hybrid materials. Sol-gel reactions proceed at low processing temperatures and enable homogeneous mixing of different precursor compounds on a molecular level. Sol-gel dispersions can be processed to obtain different macroscopic morphologies such as thin films, fibers, monoliths and powders. The sol-gel reactions with the formation of metal-oxygen compounds usually involve several hydrolysis and condensation steps. The formation of a solid metal-oxygen framework by sol-gel reactions may proceed via six main steps which are described below (Figure 1.7). During the first step a sol is formed, which contains a stable solution of completely or partially hydrolyzed or solvated metal oxide precursors. Typical metal oxide precursors are easily hydrolysable metal compounds such as halogenides, alkoxides or metal salts. In the second step, the sol is gelated by a polycondensation or polyesterfication of the oxide- or alcohol bridged network leading to an increase in the solutions´ viscosity. During the third step (syneresis) the formed gel is further condensed and solidified leading to gel contraction, which is accompanied by a solvent exclusion from the porous network.

The degree of gelation is essential for the future applications as it influences the degree of shrinkage of the formed metal oxide network upon drying and heating. Additionally, the properties of the sol-gel solutions during the aging can also be influenced by some other processes such as Ostwald ripening and phase transformations. Figure 1.7 describes in detail

the corresponding hydrolysis and condensation reactions under acidic and basic condition, respectively.

The complete drying of the gel (step 4) leads to the removal of volatile products and the structural changes of the metal oxide network. The product formed by thermal evaporation is called xerogel. Drying under supercritical conditions (typically in CO_2) leads to the formation of a very light porous material with a huge surface area called aerogel. Dehydration and stabilization of the gel is observed in step 5 at temperatures up to 800 °C, where surface-bound hydroxyl groups are removed.

At higher temperatures the gel densifies further, the pores collapse and organic residues are volatilized (step 6).[46]

In this work two metal alkoxide precursors were used for the infiltration of colloidal crystal templates and the fabrication of the macroporous titania and silica, respectively. For that purpose, clear ethanolic solutions of tetraethylorthotitanate (TEOT) and tetraethylorthosilicate (TEOS) were hydrolyzed with hydrochloric acid. For the preparation of 3DOM bulk materials, the pieces (several mm^3 in size) of colloidal template assembled from PMMA beads were placed on a filter paper in a Büchner funnel. The sol-gel precursor solution was cast on the template, the remaining solution was removed by vacuum.[18,47] For the film formation, the colloidal template was deposited on the desirable substrate. After drying, the deposited template was infiltrated with the precursor sol-gel solution using dip-coating.[48]

Hydrolysis reaction under acidic condition
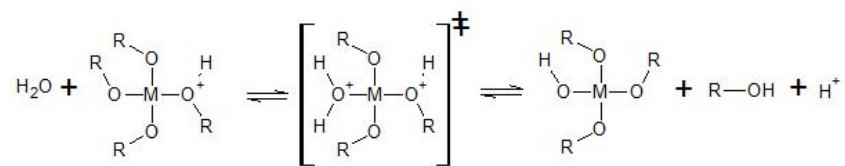
Hydrolysis reaction under basic condition
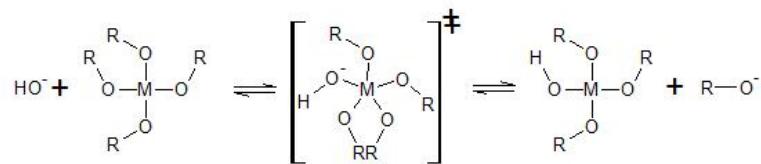
Catalyzed condensation reaction under acidic condition
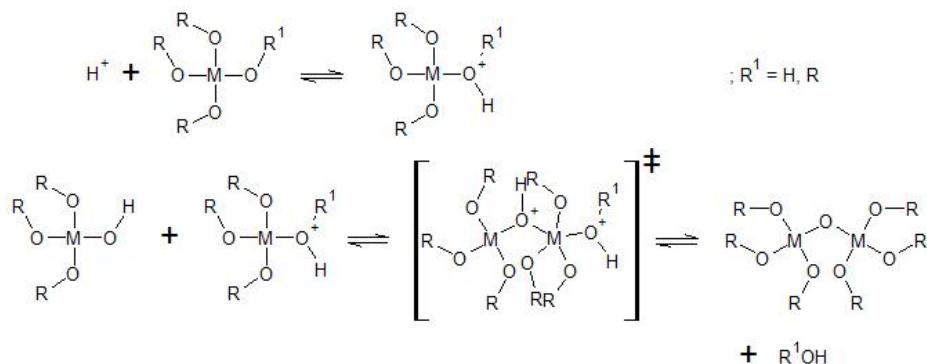
Catalyzed condensation reaction under basic condition
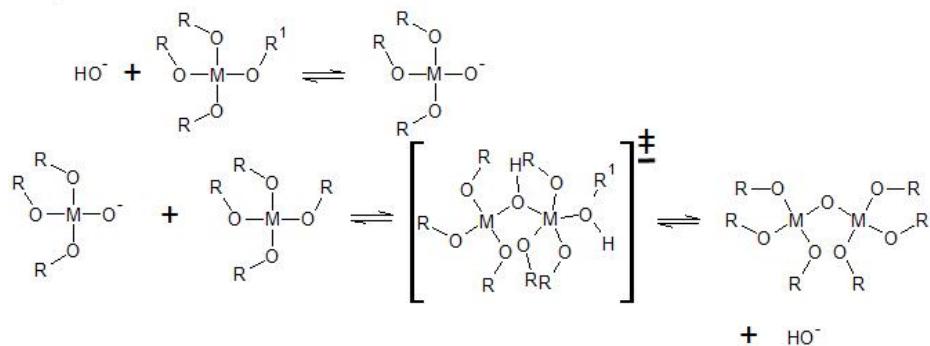
Figure 1.7: Hydrolysis and condensation of metal (M) alkoxide precursor under acidic and basic conditions.

1.6. Titanium Dioxide for Photovoltaic Applications

1.6.1. Working Principle of Dye-Sensitized Solar Cells

In comparison to the solar cells based on highly pure silicon (first generation), amorphous silicon or non silicon thin film solar cells[49], such as cadmium telluride (CdTe), and copper indium gallium diselenide (CIGS) (second generation), dye-sensitized solar cells (DSCs) can offer several advantages. This includes a reduction of the preparation cost, due to the application of titanium(IV) oxide as semiconducting electrode material. Furthermore, they provide an improved performance under diffuse light and at higher operating temperatures. For the application the cells´ transparency and availability in various colors are additional beneficial features, too.

Dye-sensitized solar cells (DSCs) are photoelectrochemical cells, which convert solar energy to electrical energy. DSCs were introduced in 1991 by Micheal Grätzel and Brian O´Reagan.[50]

The working principle of a classical DSC sandwich device is presented in Figure 1.8 a.[51] The anode is usually composed of a nanocrystalline mesoporous titania (TiO_2) covered by a monolayer of light-absorbing dye. The SEM top-view image (Figure 1.8 b) shows a typical titania layer, which is composed of randomly packed and sintered anatase crystals. The titania nanoparticle size ranges commonly between 10-30 nm, but in this example a broad grain size distribution from 10 – 80 nm was estimated by Grätzel et al..[51] The titania layers prepared in this way have a textural porosity of ca. 50-60 %. The titania layers are coated on transparent conducting substrates by doctor blading, screen printing, dip- or spin-coating; the typical thickness of the layers is in the range of 10 μm. Transparent conducting substrates for DSCs

are float glasses coated with a few hundred nanometer thick layer of tin-doped indum oxide (ITO) or fluorine-doped tin oxide (FTO), typically with a sheet resistance from 7-15 Ω/sq..
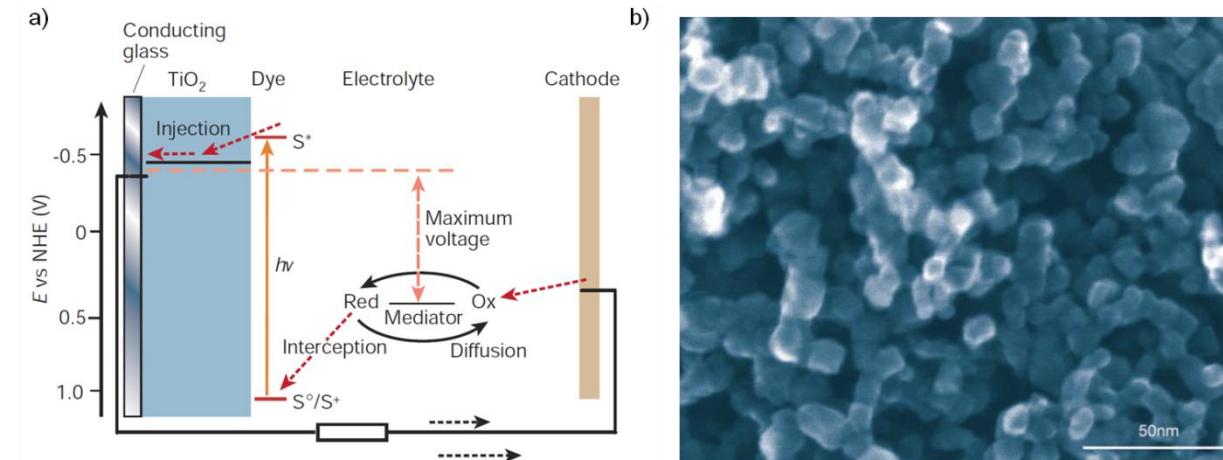
Figure 1.8: Operation principle of a dye sensitized solar cell (a) and SEM image of mesoporous titania composed of sintered anatase nanoparticles (ca. 7 to 20 nm) (b).[51]

The walls of the mesoporous titania layer are coated by a monolyer of dye covalently attached to the titania surface. Several classes of organic dyes are known to be efficient sensitizers (N3, N719, black dye, etc.), the most common dyes are ruthenium bipyridyl complexes, which exhibit a broad absorption range in the visible, but weak absorption in near IR regime (750-950 nm). But supply of ruthenium is limited, and for this reason research also focuses on the development of purely organic dyes with higher extinction coefficients and extended absorption spectra.[52] The dyes typically bear carboxylic acid residues acting as the anchoring groups for the titania surface. The dyes are usually deposited by chemical bath deposition by soaking of the titania layers in the dye solutions. Under illumination the dye (S^0) is photoexcited (S^*) and an electron is injected into the conduction band of the titania. The oxidized dye (S^+) can be regenerated by a redox active electrolyte, which is usually an iodide/ triiodide (I^-/I_3^-) mixture in organic solvents. The I_3^- that is formed in this reaction diffuses

through the electrolyte to the cathode, where it is regenerated to I⁻ at the cathode surface. The cathode consists of a platinum layer acting as a catalyst for triiodide reduction deposited on transparent conductive oxide (TCO) substrate. The maximum voltage depends on the potential difference between the redox potential of the electrolyte and the conduction band of the titania semiconductor.

The efficiency of DSCs is affected by several recombination processes. One of the possible processes is the recombination of the excited state of the dye (S*) to its ground state. The most important recombination processes that can seriously affect the efficiency of the DSCs are the recombination of the injected electrons within TiO_2 with acceptors of the electrolyte or with the oxidized dye molecules (S⁺). To avoid a possible electron transfer between the I_3^- and the TCO surface at the anode side, an additional thin blocking layer can be deposited between the TCO and the nanocrystalline titania layer.[53,54]

The performance of DSCs is tested under standard conditions and involves irradiation of the cell using simulated sunlight with a 1.5 air mass spectrum (AM) and an intensity of 100 Wm². The DSC is built up as a sandwich device, for this a spacer is applied between the cathode and anode for avoiding a short circuit. The spacer, usually a 25 μm thick thermopolymeric foil (Surlyn, DuPont), also seals the cell against electrolyte leakage and offers protection against environmental conditions, e.g. humidity.

The electrolyte is typically infiltrated by a vacuum backfilling of the sealed cell through a small hole drilled in the cathode, which is in turn sealed after the filling.[55] Figure 1.9 shows a typical layout of the DSC sandwich cell device. For increasing the cell performance by enlarging the pathway for the light within in the anode, a backscattering layer can be put on the top of the nanocrystalline TiO_2 layer. This additional layer can be composed of large

anatase crystals, typically about 400 nm in size[55], assembled titania spheres[56] or of macroporous TiO_2[38].
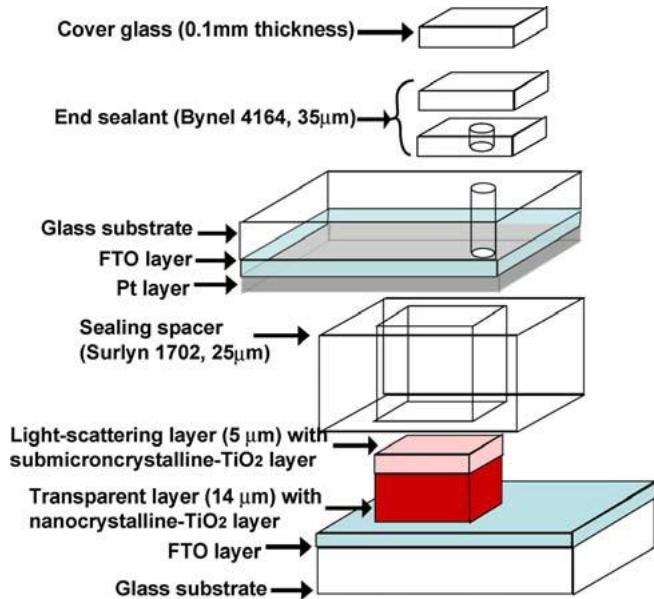
Figure 1.9: Schematic illustration of a DSC sandwich cell device.[55]

There exist various approaches to optimize each component of the DSCs, thus leading to an improvement of the performance or leading to a cost reduction.[52] This was achieved by new organic or inorganic dyes or their mixtures, for an improved light absorption in the visible and near IR regime.[57-66] Also the influence of electrolyte composition[67-70] and alternative counter electrodes[69,71-73] on the DSC performance has been intensively studied. Optimization of the morphology of the porous nanocrystalline anode is also one of the ways to improve the cells' efficiency, being in the focus of recent research.[53,54,74] In 2008 an efficiency of 11.1 % was achieved with a ruthenium sensitizer (N 719) and an I^-/I_3^- electrolyte, and these components are still used for device comparison.[55] In 2011 a record efficiency up to 12.3 % was obtained for a DSC sensitized with a porphyrin dye and utilizing a cobalt(II/III)-based electrolyte.[52,75] Although the number of published studies on DSCs increases rapidly every year, the increase

in the efficiency of the DSCs is comparably slow.[76] In every case, such studies are important

for a further and deeper understanding of the involved physical and chemical processes.

1.6.2. Synthesis and Properties of Mesoporous and Macroporous Titania

Titanium dioxide (TiO_2) can be naturally found in three different modifications: brookite

(orthorhombic), anatase (tetragonal) and rutile (tetragonal), in which one titanium atom is

coordinated by six oxygen atoms. Two additional high pressure modifications of rutile with

monoclinic and orthorhombic structure have been found in the Ries crater.[77,78]

Anatase is rarely found in a white colorless state, but is mostly coloured by inclusion of

impurities (Figure 1.10 a, b).

Figure 1.10: Photographs of naturally grown anatase crystals with dimensions of 3.3 x 2.7 x

2.3 cm (a),[79,]ca. 1 cm (b)[80] and TEM image of a homemade anatase nanocrystal with a size of

ca. 30 x 16 nm (c).[55]

Titania can be prepared synthetically by a variety of procedures including physical and

chemical vapor deposition (PVD, CVD), electrodeposition and microwave-assisted synthesis.

Other known approaches are solvothermal or hydrothermal syntheses, direct oxidation and sol-gel chemistry.[81] Titania is chemically stable and has a high refractive index (2.5 – 3.1). Due to that it is widely used in paints as a white pigment. TiO_2 is a semiconductor that absorbs in the UV regime and has band gap energies of 3.0 eV (rutile) and 3.2 eV (anatase), respectively. Therefore it is also commonly used for photocatalytic water splitting and photocatalytic decomposition of organic compounds under UV irradiation (water purification).[82,83]

Mesoporous titania became increasingly important as anode material, as described before, and can be prepared in different ways. The common approach to fabrication of mesoporous titania is sintering of pre-formed titania nanoparticles, as described above. The porosity in such materials arises from the random packing of the nanoaprticles (so called textural porosity), and the pore size directly depends on the nanoparticle size (Figure 1.8 b, 1.10 c).

Mesoporous titania with organized periodic porosity can be prepared by soft templating techniques using surfactants as structure directing agents. Typically, a solution containing an inorganic titania precursor and amphiphilic molecules such as block co-polymers is coated as thin film on a substrate. Under certain stoichiometric ratios, block copolymers form micelles that act as soft templates. The mesostructuration occurs by an evaporation-induced self-assembly (EISA) of the micelles into an ordered structure (Figure 1.11 b). After drying, a film composed of periodically alternating organic and inorganic phases is formed. The removal of the organic polymer phase, which is typically made by calcination (thermal decomposition), leaves a periodic porous titania replica. The sol-gel derived titania precursors can be used for thin film deposition on substrates. The titania films obtained in this way are completely or partially amorphous and have to be heated additionally in order to complete transformation of the amorphous titania into the polycrystalline anatase. This process is accompanied by significant density changes leading to the shrinkage or even collapse of the corresponding

mesostructure. To reduce this shrinkage, mixtures of an alkoxide sol-gel precursor with small

titania nanoparticles have been used in a so called 'brick and mortar' approach to crystallize

the amorphous titania at lower temperatures, which further stabilizes the mesostructure upon

heating.[84,85] Porous titania films were also structured with the block copolymer template

poly(ethylene-*co*-butylene)-*block*-poly(ethylene oxide) (KLE). The pore size of these films

was shown to be 14 – 19 nm.[86] The final pore size can be easily adjusted by the choice of the

polymer template.[87]

Alternatively, the surfactant can be coated on a substrate where it can form a liquid crystal

mesophase, which is infiltrated afterwards with the precursor (Figure 1.11 a).
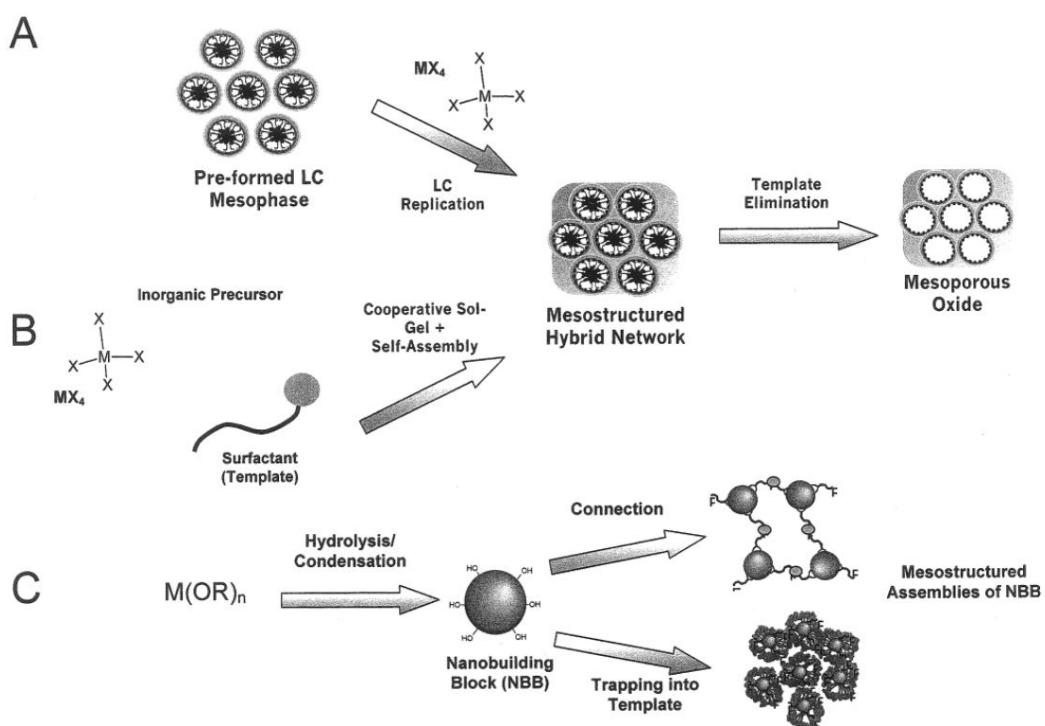
Figure 1.11: Illustration of three approaches for mesostructured materials. In route A a

preformed liquid crystal is replicated, while in route B an evaporation-induced self-assembly

is used for mesostructuration. Route C generates porosity by assembling preformed

nanobuilding blocks.[88]

Titania nanoparticles for application in DSCs can be prepared by different techniques. Most commonly the anatase nanoparticles are synthesized hydrothermally by a hydrothermal treatment of hydrolyzed $TiCl_4$ in a titanium autoclave at temperatures up to 250 °C.[55] Another known approach is a non-aqueous solvothermal reaction in benzyl alcohol, which acts as a solvent and as an oxide source. This reaction enables fabrication of very small crystalline anatase nanoparticles with a size of about 5 nm.[89] The solubility and surface functionality of the nanoparticles can be tuned by an addition of different capping agents directly to the reaction mixture,[90] and nanoparticles can be assembled into anisotropic structures[91]. The drawbacks of this approach are the low dispersibility of the nanoparticles and the presence of aromatic benzyloxy groups on the surface, which can be hardly removed. As alternative to aromatic benzyl alcohol, *tert*-butanol was developed in our group as a promising alternative reaction medium for a microwave assisted synthesis of ultrasmall titania nanoparticles (3 nm).[92]

1.6.3. Macroporous Titania for Applications in DSCs

Macroporous titania is also used as active anode material in dye-sensitized solar cells.[93-101] In comparison to mesoporous anodes, they provide larger pore diameters (> 50 nm, IUPAC) and correspondingly lower surface areas for the covalent anchoring of a sensitizer. These films are usually prepared by infiltrating a performed colloidal crystal with a titania precursor or by co-deposition. Possible precursors are similar to the ones used for mesoporous films, and originate from sol-gel solutions or nanocrystalline building blocks.[20,22,40,102]

The 3D ordered macroporous titania is also called an inverse opal or photonic crystal, because it is composed of a closed-packed array of air spheres that can appear coloured much as natural opals.

Periodic photonic crystals are also known as photonic band gap materials, because light can be diffracted from the lattice planes and generate photonic stop bands. The stop bands cause coloured reflections over a band of frequencies and the 3DOM material can act as an optical filter or reflector. The stop bands depend on the lattice diameter *d* of the inverse opal, the refraction indices *n* of the wall and the void material, usually air or a solvent. A linear equation, obtained by an extended combination of the Bragg´s law and Snell´s law, gives the position of the wavelength *λ*.

$$\lambda = \frac{2d_{hkl}}{m}\Phi n_{walls} + \frac{2d_{hkl}}{m}(1-\Phi)n_{void\ material}$$

The order of the Bragg diffraction is given by *m*, while *Φ* represents the volume fraction of the solid wall material, which is 0.26 in the case of a perfect face centered cubic structure.

As an example, the diffuse-reflectance UV-vis spectra in Figure 1.12 (top) show different stop-band minima that can be attributed to the wavelengths of maximum reflection of 3DOM zirconia powders filled with methanol (ZrO_2, bottom). An increasing pore diameter from 200 nm (A) up to 250 nm (C) and 285 nm (E) leads to red shifts of the stop band positions from violet over blue to green. The effect of changing the void materials, and thus a different refractive index, is obvious in case of D and E. These samples are similar in size to B and C, respectively, but now the air voids (*n* = 1.000) are infiltrated with methanol (*n* = 1.329), which caused a shift to orange and red, respectively (Figure 1.12, photographs of powders).[103]
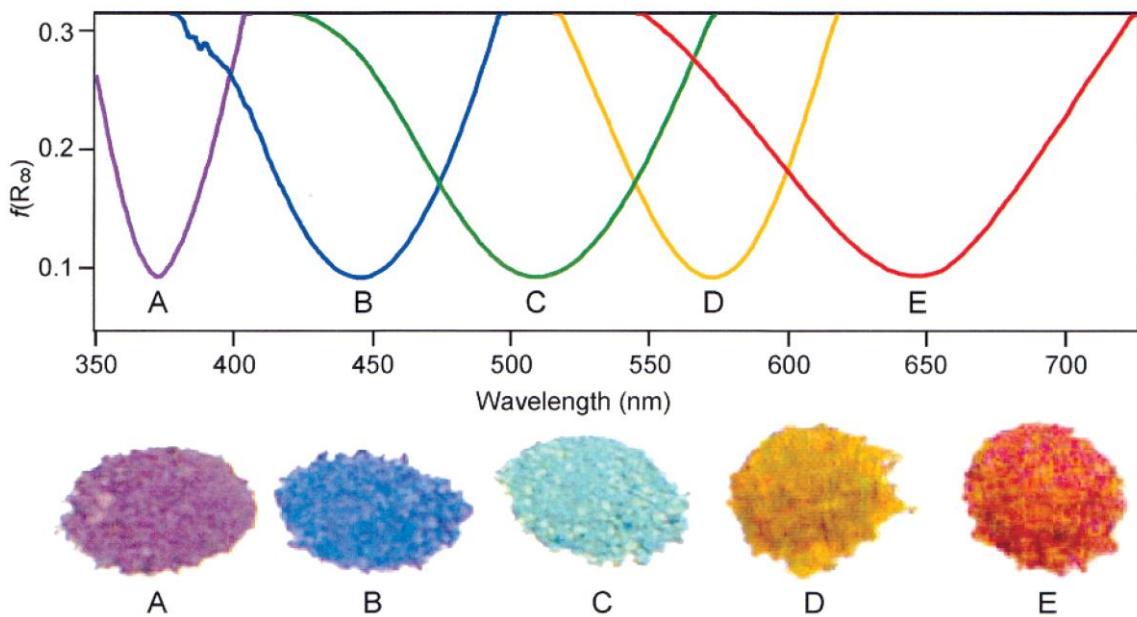
Figure 1.12: Diffuse-reflectance UV-vis spectra (top) and photographs (bottom) of macroporous ZrO_2 powders in air with pore sizes of 200, 250 and 285 nm (A, B, C). D and E are similar to B and C, but the voids were filled with methanol.[103]

Macroporous titania is mainly used in DSCs in combination with a mesoporous titania layer to improve the light harvesting. Ordered macroporous titania with photonic crystal properties acts as a dielectric mirror and increases the optical path length within the more photactive dye sensitized mesoporous titania layer.[38,104-116]

There are also reports about fabrication of titania with a bimodal porosity. Such materials are composed of macroporous titania with walls of mesoporous titania. Bimodal porous titania is prepared using two types of templates, polymer beads to generate macropores and

amphiphilic polymers to make mesopores.[117] Usually, the voids of closely packed polymer beads are infiltrated with the surfactant-containing titania precursor used for mesoporous materials. Such a structure obtained after thermal decomposition of both templates is shown in the TEM image in Figure 1.13 a.[118] This morphology was modified with graphene, incorporated by *in situ* reduction of graphene oxide, which was added to the precursor mixture. The arrows highlight the formed anatase mesostructure, using Pluronic P123 as soft template and $TiCl_4$ as precursor. This morphology shows a high BET surface area of 298 m^2g^{-1} and pore sizes of 3 nm.[118]
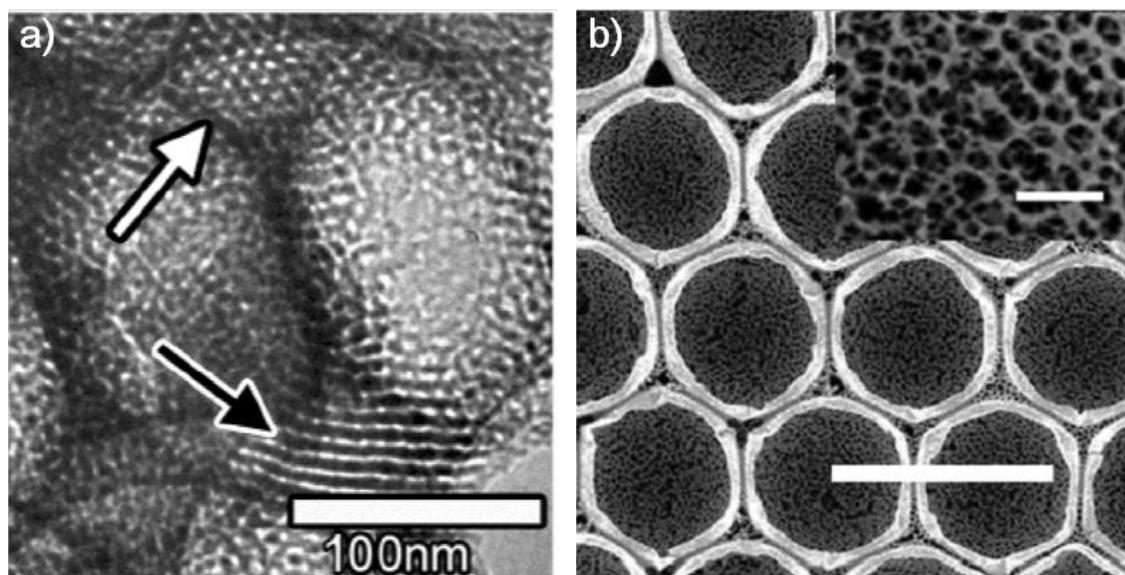
Figure 1.13: TEM image of 3DOM anatase with mesopores within the walls of the macroporous scaffold; the macropore diameter is about 200 nm (a).[118] SEM images (plan view) of titania with a hierarchical twin scale morphology. The macroporous scaffold has a diameter of ca. 1.7 μm, which is filled up with mesostructured titania phase with a pore size of about 35 nm (b). The scale bars correspond to 5 μm and 300 nm (inset).[93]

Recently, there was a report about the application of hierarchical twin-scale inverse opal (ts-IO) as electrode in DSC. For this, firstly titania inverse opal films with a macropore diameter

of 1.7 μm were prepared. In the following step the macropores were filled with 40, 60 or 80 nm sized polystyrene spheres by colloidal crystal templating. The voids between these small spheres were also impregnated with an ethanolic solution of $TiCl_4$ as precursor. After calcination at 500 °C the spheres were removed and mesoporous anatase replica was obtained (Figure 13 b). The sizes of the pores depend on the initial template size and were about 35, 55 and 70 nm, respectively. The best DSC operating with a ruthenium dye N719 and a volatile I^-/I_3^- redox electrolyte had an anode with 35 nm large pores. This cell provided an open circuit potential of 0.79 V (V_{OC}), a short-circuit current of 13.18 mAcm^{-2} (I_{SC}) and a corresponding efficiency of 6.9 %. In this case the thickness was about 12 μm, while a thickness of 8 μm gave an efficiency of 5.14 % that was mainly attributed to the decreased photocurrent density (10 mAcm^{-2}).[93]

Macroporous titania scaffolds and hierarchical materials on their base were recently used as photoanodes in CdS quantum dot (QD) sensitized solar cells.[119] The schematic synthetic procedure is illustrated in Figure 1.14 a. Hierarchical ordered nanobushes were made by growing ZnO nanowires within the empty voids of the titania macropores. The morphology is shown in the SEM cross section and the TEM image (Figure 1.14 b). The growth of nanowires starts from a previously deposited ZnO seed layer covering the titania scaffold. The bushes were finally decorated with the CdS QDs (Figure 1.14 c). The motivation of this work was firstly to increase the sensitizer concentration in comparison to a purely macroporous scaffold, secondly to improve light harvesting by scattering effects, and finally to increase the reaction sites with the electrolyte. In total this led to an increase of photocurrent.
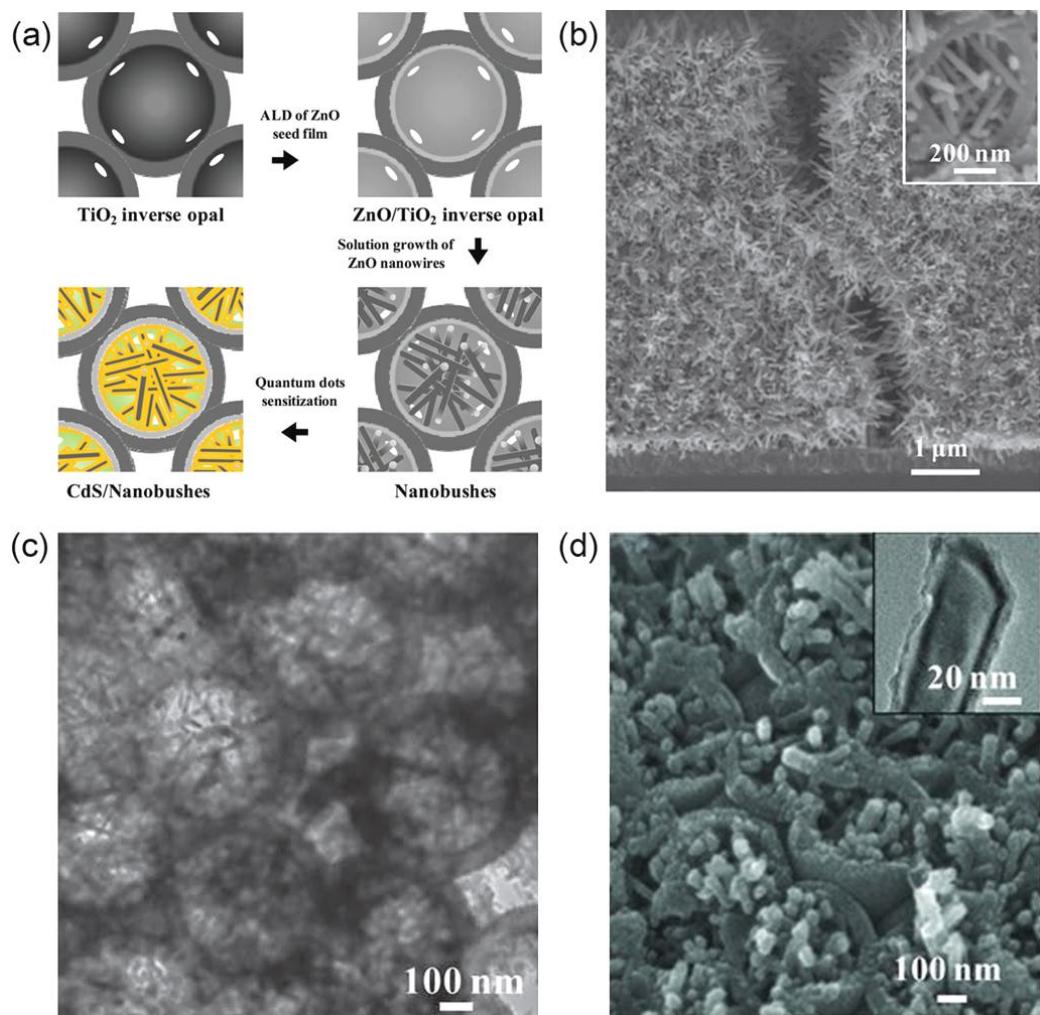
Figure 1.14: Schematic procedure for nanobushes decorated with QDs (a), SEM cross section (b) and TEM (c) images of a macroporous TiO$_2$ film, whose voids are filled with ZnO nanowires. SEM and TEM (inset) images show the hierachical composite material after sensitization with CdS QDs.[119]

1.7. Mesoporous Carbon for Applications in Lithium Sulfur Batteries

1.7.1. Working Principle of Lithium Sulfur Batteries

Lithium sulfur batteries are a promising alternative to existing Li ion batteries (LIB´s)[120], because of their very high theoretical energy densities of 2800 WhL^{-1} or 2500 $Whkg^{-1}$. Additionally, these batteries can be stored at temperatures from -40 up to $+50$ °C and cycled from -20 to +45 °C.[121] The classical battery set-up consists of an elemental lithium anode, which requires a proper sealing. The anode is separated from the cathode (elemental sulfur) by an organic electrolyte. Sulfur is generally a very attractive battery material due to its low price and high availability. However, sulfur has a low electronic conductivity. This drawback can be overcome by blending sulfur with carbon acting as conducting matrix and a corresponding organic binder.[122]

Figure 1.15 shows the schematic working principle of a Li-S battery.[123] The reduction of sulfur by lithium metal occurs in three steps depending on the applied voltage, which is accompanied by the formation of intermediate polysulfides (Li_2S_n; n = 8, 6, 4, 3, 2). Here, the final discharge product is Li_2S, because the long polysulfide anionic chains become shorter by further sulfur reduction. The detailed reduction mechanism is still being discussed in the literature, especially the exact amounts of polysulfides and the presence of the radical anion $S_3^{\cdot-}$. The formation of soluble polysulfides, which show a concentration dependency on the overall elemental sulfur concentration, includes equilibrium reactions.[124] During the battery charging the intermediate polysulfide anions are re-oxidized, finally into sulfur.
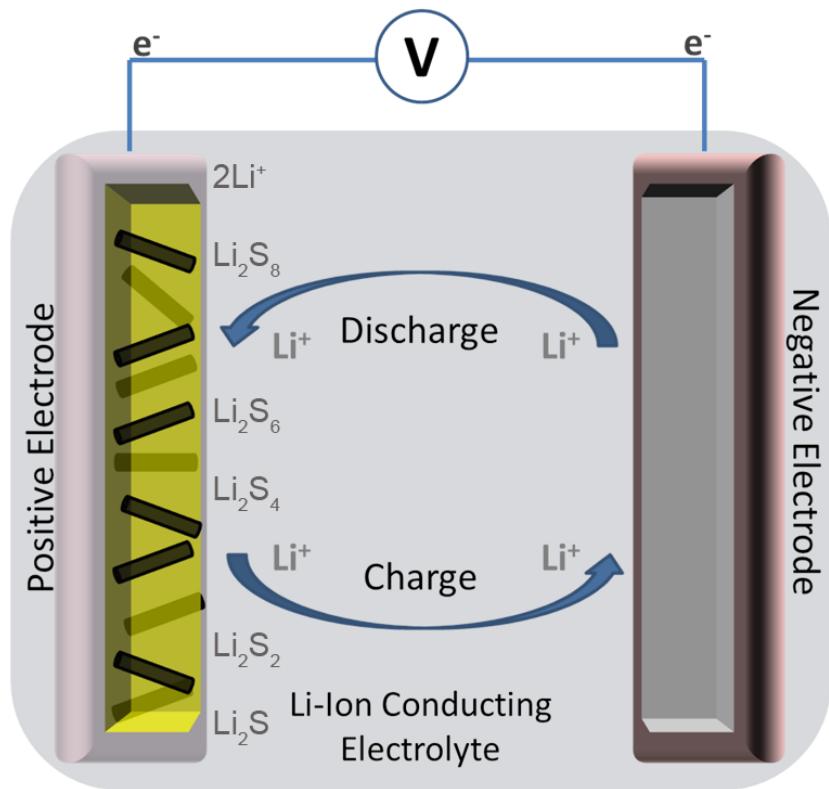
Figure 1.15: Basic working principle of a Li-S battery, composed of structured C/S cathode and Li foil anode, which are electrochemically connected via an electrolyte.[123]

Polar organic solvents are typically used as electrolytes in sulfur batteries. Common electrolytes contain a solution of lithium hexafluorophosphate ($LiPF_6$) in ethyl methyl sulfone ($C_2H_5SO_2CH_3$).[125] The polar solvent is beneficial for the dissociation of the salt and thus for the good ionic conductivity.

The main challenges involving lithium-sulfur batteries include the solubility of the polysulfides formed during electrochemical reduction of sulfur, and formation of solid lithium salts such as Li_2S and Li_2S_2, generated by reduction. These salts are stable and unreactive, also at the anode site, and cause a loss of active mass by a sulfur-depleted cathode. This changes the cathode composition and induces a volume change. The lower density of the

precipitated lithium salts can cause degradation and ohmic resistance at the cathode site, which alters the battery performance.

Several chemical approaches were found to improve the performance of Li-S batteries. For example, different polymers were used to cover the carbon/sulfur composite. Hydrophilic polyethyleneglycol (PEG) was attached to the carboxy-functionalized carbon surface of the mesoporous carbon/sulfur composite, which shows the effect of polysulfide trapping by generating a concentration gradient in the electrolyte. Additionally, it influences the mechanism of the redox reaction, which leads to a decreased deposition of insoluble Li_2S at the anode. In this approach, the silica material SBA-15 was used as hard template to make the carbon CMK-3 material.[125] The same system was also coated with the conducting polymer poly(3,4-ethylenedioxythiophene)-poly(styrene sulfonate) (PEDOT:PSS) for achieving an improved cycling stability of the Li-S battery. The approach is illustrated in Figure 1.16 on the left, and the TEM image on the right shows the polymer coated C/ S composite.[126]
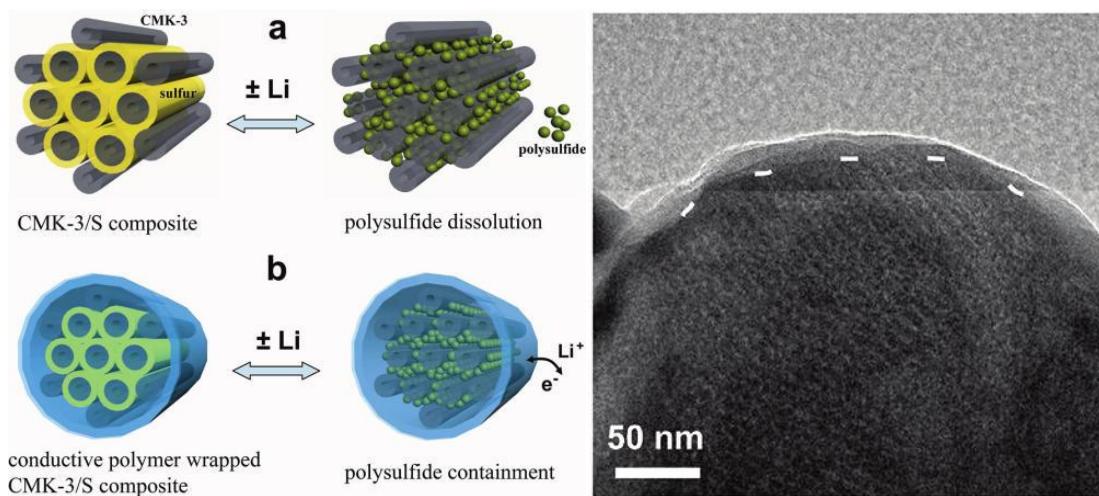
Figure 1.16: (left) Scheme of polysulfide formation within the carbon (CMK-3)/sulfur composite (a). Illustration of polysulfide trapping by an additional polymer coating (b). (right)

TEM image of CMK-3/sulfur composite having a thin PEDOT:PSS-layer on top, which still permits Li-ion diffusion.[126]

Hollow carbon nanofibers with diameters ranging from 200 to 300 nm were also used as cathode material.[127] The fibers were prepared as free standing membranes by a replication of a commercial anodic alumina membrane (AAO, Whatman) (Figure 1.17 c, upper photograph).
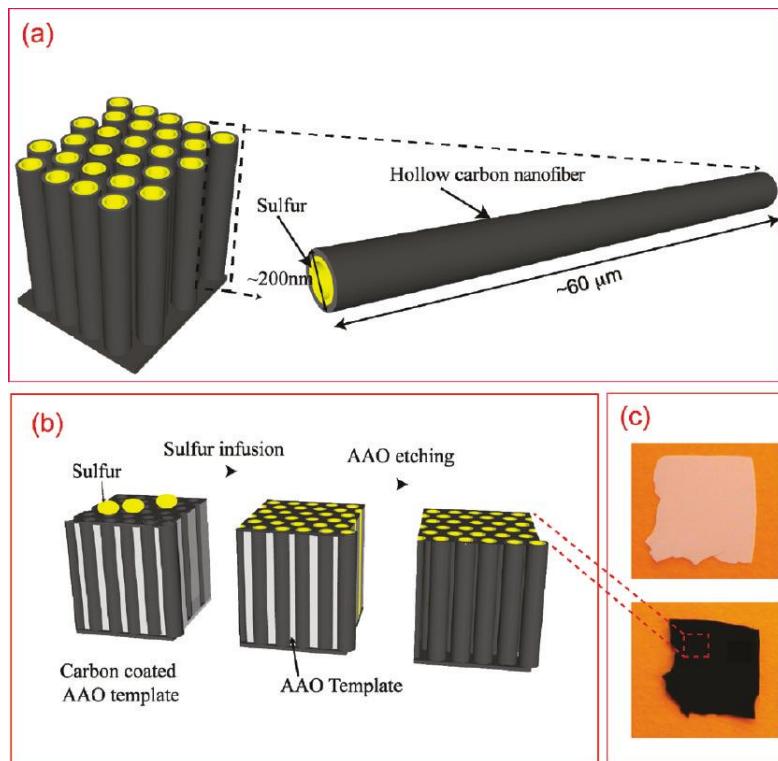
Figure 1.17: Schematic design of hollow carbon/sulfur fibers (a), and illustration of preparation process (b). Photographs show a piece of AAO membrane before (top) and after loading with sulfur and carbon (bottom) (c).[127]

For that purpose, the walls of AAO were coated first with polystyrene (PS) that was subsequently carbonized. Afterwards the alumina was removed by etching with phosphoric acid to obtain hollow fibers with a length of about 60 µm (Figure 1.17 a). For the

implementation in the batteries, the hollow carbon fibers were filled with sulfur (Figure 1.17 c, bottom photograph). The corresponding synthesis procedure is shown in Figure 1.17 b. In this study the performance was also improved by adding $LiNO_3$ to the electrolyte, which apparently passivated the lithium electrode.

Recently, double-shelled hollow carbon spheres were prepared by a facile synthetic route by using hollow tin oxide spheres in the range of 300 to 500 nm. For that purpose, the exterior surface of the hard templates was coated with a polysaccharide. During this process the textural pores between the tin oxide nanocrystals were filled with the carbon precursor. The polysaccharide was transformed to carbon by pyrolysis, while the tin oxide was reduced to tin under these temperatures by applying a hydrogen/ nitrogen atmosphere. After removing the tin particles with hydrochloric acid, the hollow carbon spheres with porous walls were formed. Figure 1.18 a shows a TEM image of hollow carbon spheres that were filled with sulfur, and corresponding elemental mappings for carbon (b) and sulfur (c). The hollow carbon spheres show improved cycling stabilities in Li-S batteries in comparison to dense carbon spheres (carbon black). This difference was mainly attributed to a trapping of the polysulfide in the interior.[128] Carbon black nanoparticles of about 40 nm were also used as cathodes in combination with oxidized graphene layers to cover submicrometer sized sulfur particles. Graphene was used to improve the conductivity and trap the mobile polysulfides. Additionally the composite was encapsulated by a layer of polyethyleneglycol (PEG) to further reduce the leakage of polysulfides. This flexible polymer also improved the cathode stability upon the volume changes during the battery cycling.[129] Recently, pure graphene nanosheets prepared by reduction of graphene oxide with hydrazine and mixed with sulfur were applied as cathode material in combination with carbon black (10 wt%) and organic binders (10 wt%). The batteries show very high initial discharge capacities of 1580 mAhg^{-1} and a good cycling stability, obtained at 0.05 C.[130]
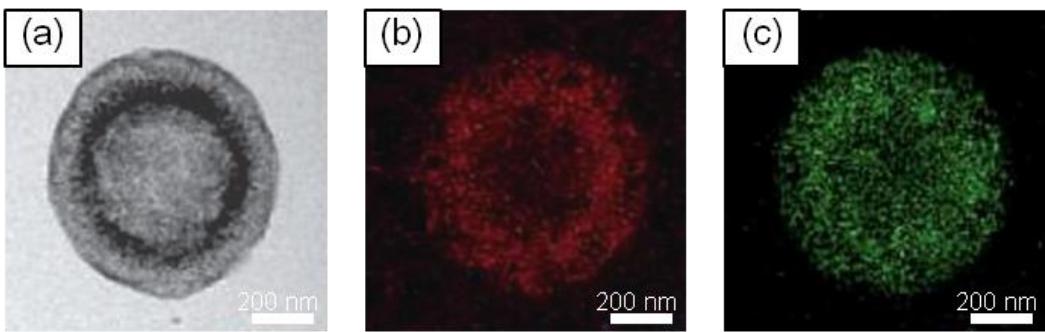
Figure 1.18: TEM image (a) of a hollow double shelled carbon sphere filled with sulfur. The elemental mapping of carbon (b) and sulfur (c) indicate homogeneous distribution of both elements in the shell.[128]

1.7.2. Synthesis and Properties of Nanosized Carbon Materials

Elemental carbon exists in various allotropes. Cubic diamond (transparent; isolating) and graphite (black metallic, conductive) are naturally found and are built up by sp^2 – and sp^3 hybridized atoms forming three dimensional networks. A rarely found mineral, Lonsdaleite, also known as hexagonal diamond, represents a translucent and yellowish additional carbon allotrope. A more prominent carbon compound is graphite.[131,132] Other carbon allotropes (0D) include the fullerenes, with the best-known member, the C_{60} molecule. Higher fullerenes such as C_n (n = 74, 76, 78, 80, 84, 90, 94) are also synthetically available. The existence of even larger ones was discussed and structures for C_{240} and C_{540} fullerenes were calculated.[133-137] The carbon allotropes can be transformed into each other under certain conditions; thus, diamond can be formed by a thermal activation of graphite[138,139] or by crushing of C_{60}.[140] Recently C_{60} was also crushed under high pressure conditions (60 GPa) to form amorphous

carbon clusters, which were ordered with long range order to produce a crystalline material.[141] Carbon nanotubes (CNTs) are additional very important carbon allotropes, they are structurally similar to graphene[142] and fullerenes[143,144]. Figure 1.19 summarizes the structure models of the allotropes described above.[136] Additionally, there are also theoretical and experimental studies describing the electronic structure of amorphous carbons.[145,146]
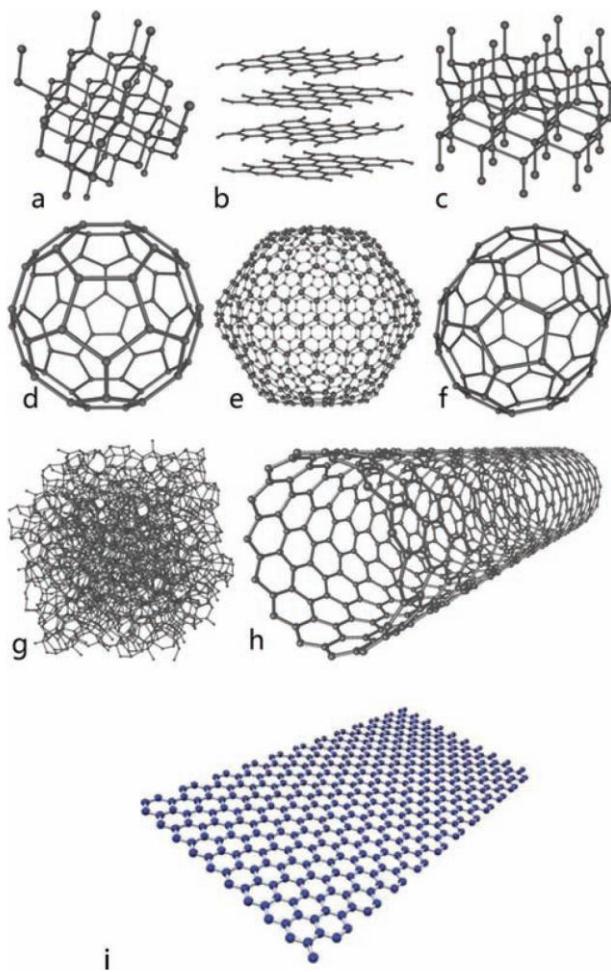
Figure 1.19: Carbon allotrope structures: cubic diamond (a), graphite (b), londsdaleilite (c), C_{60}, C_{540}, C_{70} (d, e, f), amorphous carbon (g), carbon nanotube (h), and graphene (i).[136]

Different carbon allotropes have very different chemical and physical properties. Therefore they find use in a large variety of different applications. As an example, thermal conductivity

increases by several orders of magnitude from amorphous carbon to graphene and CNTs.[147] Carbon allotropes can be prepared by a series of techniques. Generally, carbon can be prepared by processes including gas or liquid phase and solid-state reactions using many different precursors. For example, hydrocarbons can be transformed to carbon by condensation, polymerization or pyrolysis. Thermoplastic polymers can be molten and then carbonized, while thermosetting polymers can be transformed to carbon by thermal decomposition.[148] Moreover there are several approaches available to modify the polymers´ morphology by creating meso- or macroporosity.[149-151] Another common technique involves hydrothermal reactions to achieve a full carbonization of the precursor.[152,153]

Despite the many techniques available to form carbon phases, it is still fundamentally important to control and tune carbons´ morphology and structure from the macroscale, e.g. fibers[154] and colloids[155], down to the nanoscale. There are already several reports about graphene quantum dots derived from carbon fibers[156], the passivation of carbon quantum dots[157], as well as the efforts to make them soluble in water[158]. Additionally, amorphous spherical carbon nanoparticles in the range of 4 to 30 nm are also present in carbohydrate containing food.[159] Several approaches exist for the fabrication of submicrometer-sized carbon spheres. Thus, hollow or mesoporous spheres with uniform size distributions can be obtained by soft or hard templating approaches.[160] Carbon spheres can also be made dense[158], microporous[161,162] or mesoporous[163].

Solid carbon spheres are commonly prepared from spherical polymer resin built by carbon rich precursors, which can be converted with high yield into carbon by high temperature pyrolysis. Such precursors are often made by the reaction of phenol derivatives with aldehydes under basic conditions.[160,164,165] During the first reaction step a phenyl alcohol,

2,4,6-tris(hydroxymethyl)phenol, is formed by nucleophilic addition of formaldehyde in the α and β positions of phenol.

Such carbon precursors can be used in combination with hard or soft templates to generate porosity within the resulting carbon material that can have different macroscopic morphologies. Typical soft templates are micelles of block copolymers, while silica colloids usually act as hard templates. The use of hard templates enables the formation of larger pores with sizes over 50 nm. Additionally, it reduces thermally induced shrinkage and subsequently minimizes formation of defects or cracks. Recently the hard templating approach was used for the fabrication of mesoporous carbons with large pore size. For that purpose, silica spheres with a size of about 10, 20, 30 and 40 nm were used as hard templates. Figure 1.20 a-c show the SEM images of the obtained carbon bulk material, while in Figure 1.20 d the spherical pore geometry of the mesostructure is illustrated. High resolution nitrogen (77.4 K) and argon (87.3 K) sorption measurements on these materials show type IV isotherms exhibiting a H1 hysteresis. A new model was applied that correlates to the surface rougness and is based on quenched solid density functional theory (QSDFT), to calculate the spherical pore size geometry. Figure 1.20 e, f represents the obtained pore size distributions, which are in good agreement with the SEM images.[166]
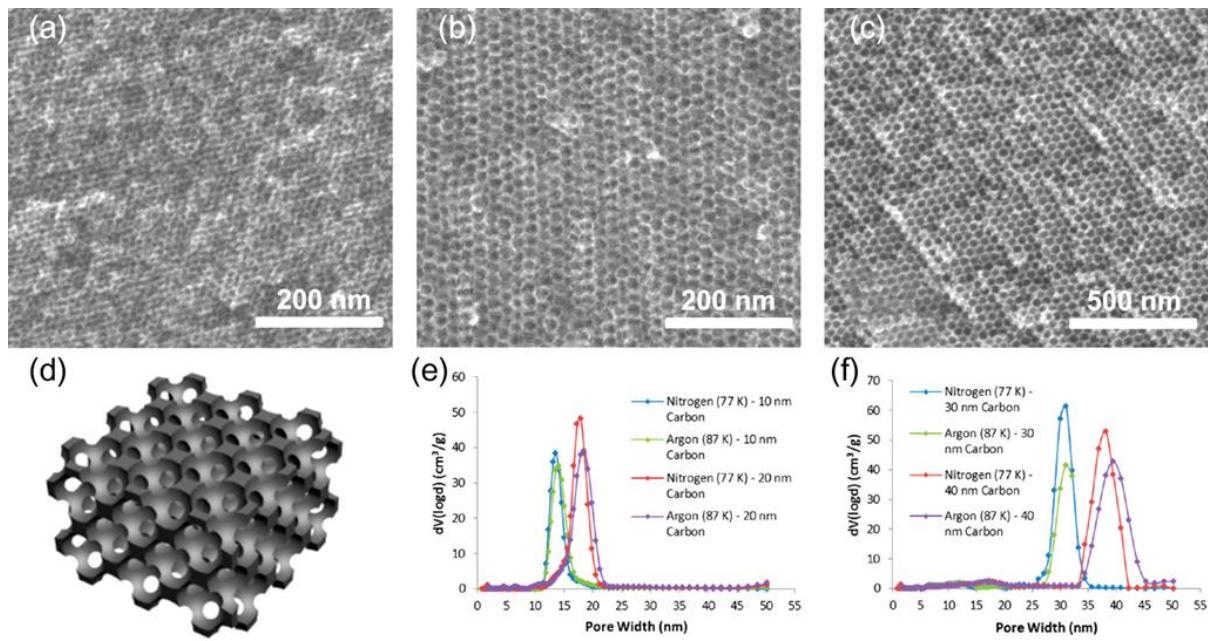
Figure 1.20: SEM images (a-c) and schematic illustration (d) of mesoporous carbon obtained by hard templating using spherical silica beads with size of 10, 20 and 40 nm. The pore size distribution obtained from isotherms, which results from nitrogen and argon sorption measurements, exhibits peaks at around 13 and 18 nm (e) and 28, 38 nm (f), respectively.[166]

Besides silica beads as described above, mesoporous silica made as bulk or as thin films[167] was used as hard template for the fabrication of mesoporous carbon. Mesoporous carbon can also be made by soft templating in the evaporation-induced self-assembly (EISA) process using micelles of amphiphilic polymers as the soft templates. The mechanism of mesophase formation from amphiphilic block copolymer Pluronic F127 and a carbon precursor (resol) resulting in mesoporous carbon particles[168] or free standing mesoporous thin carbon films[169] was recently studied.[170] In our group we have investigated the effect of temperature-induced self-assembly of Pluronic P123 and F127 with resol by in situ small-angle X-ray scattering (SAXS) measurements.[171] There are also efforts to synthesize carbon with large mesopores using poly(styrene-block-ethylene oxide) (PS-b-PEO) as structure directing agent, to generate bulk material or thin films. The corresponding parameters of the mesostructure could be

changed by using polystyrene as swelling agent. This agent was incorporated into the core of the micelle to obtain carbon with large pores of up to 38 nm.[172,173]

Carbon fibers can be prepared with different macroscopic size as well as pore dimensions and morphology. Examples include activated mesoporous carbon fibers with diameters up to 35 μm.[174] Generally, an additional anisotropic template is needed to obtain a final fiber structure. Such templates can be found in nature or are synthetically available to provide suitable dimensions. A possible natural template is a special site found in crab shells.[175] More often, however, macroporous anodic aluminum oxide (AAO) is used as the anisotropic template.[176-178] Commercial AAO membranes also act as a hard template for a series of different materials, and provide a confined environment for mesostructuration of inorganic and organic materials.[179-188] AAO can feature a fairly ordered periodicity and mainly tubular channels with lengths up to 60 μm, while the channel diameter is usually in the range of 200 nm.

Figure 1.21 a illustrates a synthetic procedure for mesoporous carbon fibers. Colloidal silica nanoparticles of ca. 30 nm (Stöber NPs) were infiltrated into the AAO membrane and used as the hard template (Silica at AAO). During the next steps, phenol was infiltrated into the interstitial voids of the packed silica colloids before the composite was exposed to paraformaldehyde at 131 °C to form a resin. Afterwards the AAO membrane was removed by etching with hydrochloric acid (5 M) at 50 °C. The resin within the fibers was finally carbonized at 700 °C. Figure 1.21 b shows a TEM of the resulting mesoporous carbon nanofibers (MCBF) obtained after etching the silica with hydrofluoric acid (48 %).[189]

In our group we have demonstrated the formation of highly ordered hexagonal mesoporous carbon fibers in the channels of an AAO membrane using Pluronic F127 as structure-directing agent and soft template (Figure 1.21 c).[180] A similar approach also enabled the formation of

free-standing arrays consisting of mesoporous carbon fibers. The membrane thickness is between 50 to 60 μm corresponding to the thickness of the AAO.[190]

Electrospinning is an alternative technique to obtain mesoporous carbon fibers.[191] With this technique it is also possible to prepare fibers containing inorganic nanoparticles (Ag, Fe_3O_4, $ZnFe_2O_4$)[192] or dense rectangular rods.[193]
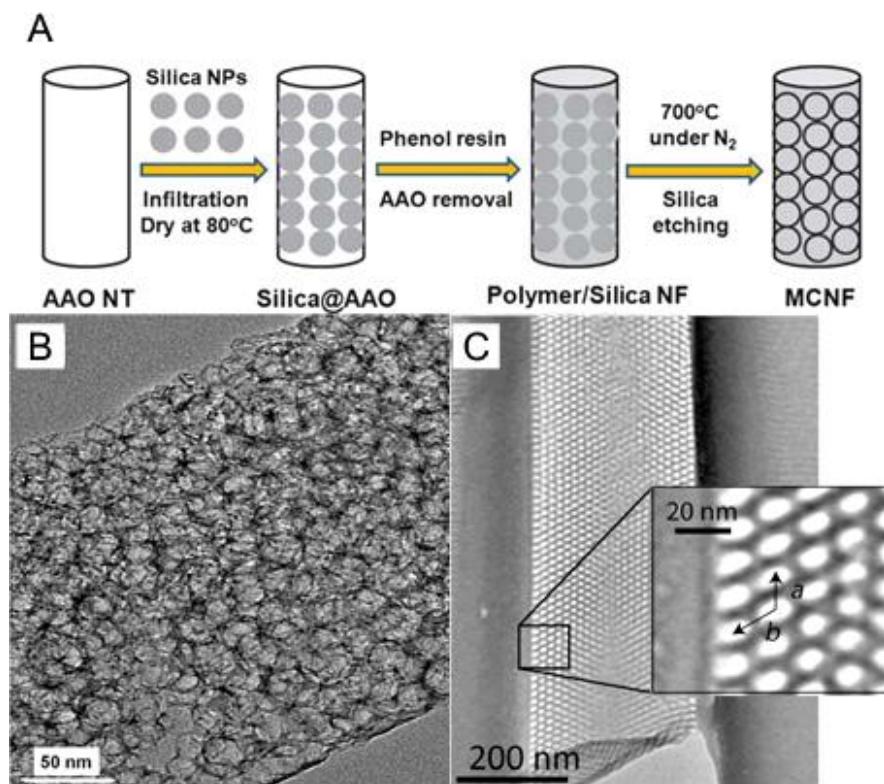
Figure 1.21: Schematic synthesis procedure (a) and TEM image (b) of a mesoporous carbon fiber derived by a hard templating approach (AAO, silica spheres).[189] TEM cross section image (c) of mesoporous carbon within a pore of AAO prepared with Pluronic F127 as the template for mesoporosity.[180]

An additional approach for the fabrication of highly porous carbon with greatly increased surface area and pore volume but without changing the mesopore size involves a

triconstituent evaporation-induced co-assembly of a mixture of a carbon (PF), silica precursor and amphiphilic polymer. A schematic illustration of this approach is given in the Figure 1.22. Using a mixture of resol, hydrolyzed tetraethoxy orthosilicate (TEOS) and Pluronic F127, bulk silica/carbon nanocomposites,[194] stable centimeter sized monoliths[195] and thin films[196,197] were prepared. The composite was thermopolymerized at 100 °C to condense the resol precursor molecules and to dry silica sol-gel, which also stabilizes the already mesostructured network. A subsequent heating procedure in a nitrogen atmosphere removes Pluronic polymer to gain mesoporosity. Finally temperatures up to 900 °C induce a full carbonization. A bimodal porosity and thus an increase in the surface area can be achieved by introducing porosity within the walls of the highly ordered hexagonal mesoporous material by etching the silica within the walls with hydrofluoric acid. The high resolution TEM images in Figure 1.22 represent the mesoporous character of carbon (top) and silica (bottom).

The addition of silica is also beneficial for a reduced shrinkage of the mesostructure compared to a pure carbon material. Additionally, with an increase of the aging time of the TEOS/carbon precursor mixture prior to deposition, the degree of silica polycondensation increases, which further stabilizes the mesophase.[198]
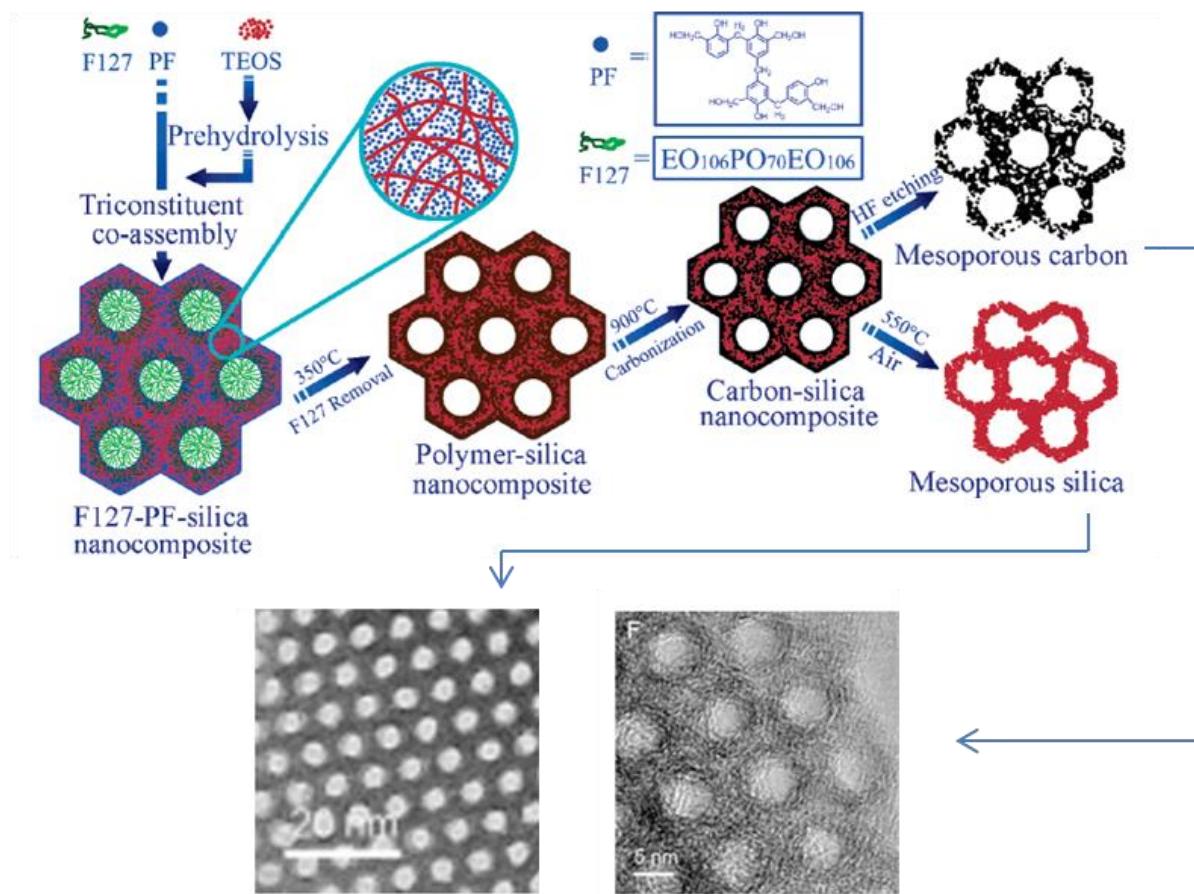
Figure 1.22: Schematic drawing of individual steps for highly porous carbon (TEM image, top) and silica (TEM image, bottom) with a hexagonal structure that was obtained by triconstituent co-assembly of TEOS, a carbon precursor (resol) and a triblock copolymer (Pluronic F127).[194]

Instead of silica alkoxides, further precursors were co-condensed with carbon precursors to tune the properties of mesoporous carbon. Metal sources such as cobalt and vanadyl acetylacetonate complexes ($Co(acac)_2$, $VO(acac)_2$) led individually or in combination to formation of cobalt oxide (CoO) and vanadium oxide (V_2O_5) nanoparticles dispersed in the carbon mesostructure. This modification can increase the electrical conductivity up to a maximum metal concentration of 10 wt%. Moreover, mesoporous carbon containing titania (TiO_2), magnesia (MgO), manganese oxide (MnO_2) and iron oxide (Fe_2O_3) nanoparticles can be prepared by triconstituent co-assembly.[199,200]

1.8. Chapter References

(1)   Caruso, F. *Colloids and colloid assemblies synthesis, modification, organization and utilization of colloid particles*; Wiley-VCH: Weinheim, 2004.

(2)   *The Colloid Chemistry of Silica*; American Chemical Society, 1994; Vol. 234.

(3)   Hartlen, K. D.; Athanasopoulos, A. P. T.; Kitaev, V. *Langmuir* **2008**, *24*, 1714.

(4)   Howard, A. G.; Khdary, N. H. *Analyst* **2005**, *130*, 1432.

(5)   Nozawa, K.; Gailhanou, H.; Raison, L.; Panizza, P.; Ushiki, H.; Sellier, E.; Delville, J. P.; Delville, M. H. *Langmuir* **2005**, *21*, 1516.

(6)   Stöber, W.; Fink, A.; Bohn, E. *J. Coll. Interf. Sci.* **1968**, *26*, 62.

(7)   Jones, J. B.; Sanders, J. V.; Segnit, E. R. *Nature* **1964**, *204*, 990.

(8)   Marlow, F.; Muldarisnur; Sharifi, P.; Brinkmann, R.; Mendive, C. *Angew. Chem. Int. Ed.* **2009**, *48*, 6212.

(9)   Chern, C. S. *Prog. Polym. Sci.* **2006**, *31*, 443.

(10)   Beckham, R. E.; Bevan, M. A. *J. Chem. Phys.* **2007**, *127*.

(11)   Woodcock, L. V. *Nature* **1997**, *385*, 141.

(12)   Zhu, J.; Li, M.; Rogers, R.; Meyer, W.; Ottewill, R. H.; Crew, S. T. S. S. S.; Russel, W. B.; Chaikin, P. M. *Nature* **1997**, *387*, 883.

(13)   Lee, K.; Yalamanchili, H.; Rodak, L. E.; Kadiyala, A.; Dawson, J.; Korakakis, D. *Microelec. Eng.* **2012**, *96*, 45.

(14)   Born, P.; Blum, S.; Munoz, A.; Kraus, T. *Langmuir* **2011**, *27*, 8621.

(15)   Li, Y.; Kunitake, T.; Fujikawa, S. *Coll. Surf. A: Physicochem. Eng. Aspects* **2006**, *275*, 209.

(16)   Hoogenboom, J. P.; Derks, D.; Vergeer, P.; van Blaaderen, A. *J. Chem. Phys.* **2002**, *117*, 11320.

(17)   Hilhorst, J.; van Schooneveld, M. M.; Wang, J.; de Smit, E.; Tyliszczak, T.; Raabe, J.; Hitchcock, A. P.; Obst, M.; de Groot, F. M. F.; Petukhov, A. V. *Langmuir* **2012**, *28*, 3614.

(18)   Holland, B. T.; Blanford, C. F.; Stein, A. *Science* **1998**, *281*, 538.

(19)   Blanford, C. F.; Carter, C. B.; Stein, A. *J. Microscopy* **2004**, *216*, 263.

(20)   Holland, B. T.; Blanford, C. F.; Do, T.; Stein, A. *Chem. Mater.* **1999**, *11*, 795.

(21)   Stein, A.; Schroden, R. C. *Curr. Opin. Solid State Mat. Sci.* **2001**, *5*, 553.

(22)   Stein, A.; Li, F.; Denny, N. R. *Chem. Mater.* **2008**, *20*, 649.

(23)   Ozin, G. A.; Arsenault, A. C.; Cademartiri, L. *Nanochemistry a chemical approach to nanomaterials*; 2. ed. ed.; RSC Publ.: Cambridge, 2009.

(24)   Aguirre, C. I.; Reguera, E.; Stein, A. *Adv. Funct. Mater.* **2010**, *20*, 2565.

(25)   Sadakane, M.; Sasaki, K.; Kunioku, H.; Ohtani, B.; Abe, R.; Ueda, W. *J. Mater. Chem.* **2010**, *20*, 1811.

(26)   Lytle, J. C.; Yan, H.; Ergang, N. S.; Smyrl, W. H.; Stein, A. *J. Mater. Chem.* **2004**, *14*, 1616.

(27)   D'Arienzo, M.; Armelao, L.; Cacciamani, A.; Mari, C. M.; Polizzi, S.; Ruffo, R.; Scotti, R.; Testino, A.; Wahba, L.; Morazzoni, F. *Chem. Mater.* **2010**, *22*, 4083.

(28)   Lee, S. H.; Kim, H. W.; Hwang, J. O.; Lee, W. J.; Kwon, J.; Bielawski, C. W.; Ruoff, R. S.; Kim, S. O. *Angew. Chem. Int. Ed.* **2010**, *49*, 10084.

(29)   Woo, S.-W.; Dokko, K.; Nakano, H.; Kanamura, K. *J. Mater. Chem.* **2008**, *18*, 1674.

(30)   Lee, K. T.; Lytle, J. C.; Ergang, N. S.; Oh, S. M.; Stein, A. *Adv. Funct. Mater.* **2005**, *15*, 547.

(31)   Kulinowski, K. M.; Jiang, P.; Vaswani, H.; Colvin, V. L. *Adv. Mater.* **2000**, *12*, 833.

(32)   Jiang, P.; Cizeron, J.; Bertone, J. F.; Colvin, V. L. *J. Am. Chem. Soc.* **1999**, *121*, 7957.

(33) Yan, H.; Blanford, C. F.; Lytle, J. C.; Carter, C. B.; Smyrl, W. H.; Stein, A. *Carbon* **2001**, *13*, 4314.

(34) Yan, H.; Blanford, C. F.; Smyrl, W. H.; Stein, A. *Chem. Commun.* **2000**, 1477.

(35) Woo, S.-W.; Okada, N.; Kotobuki, M.; Sasajima, K.; Munakata, H.; Kajihara, K.; Kanamura, K. *Electrochim. Acta* **2010**, *55*, 8030.

(36) Ke, F. S.; Huang, L.; Wei, H. B.; Cai, J. S.; Fan, X. Y.; Yang, F. Z.; Sun, S. G. *J. Power Sources* **2007**, *170*, 450.

(37) Wu, Y. N.; Li, F. T.; Zhu, W.; Cui, J. C.; Tao, C. A.; Lin, C. X.; Hannam, P. M.; Li, G. T. *Angew. Chem. Int. Ed.* **2011**, *50*, 12518.

(38) Guldin, S.; Hüttner, S.; Kolle, M.; Welland, M. E.; Müller-Buschbaum, P.; Friend, R. H.; Steiner, U.; Tétreault, N. *Nano Lett.* **2010**, *10*, 2303.

(39) Liu, L.; Karuturi, S. K.; Su, L. T.; Tok, A. I. Y. *Energy Environ. Sci.* **2011**, *4*, 209.

(40) Hatton, B.; Mishchenko, L.; Davis, S.; Sandhage, K. H.; Aizenberg, J. *Proc. Natl. Acad. Sci. USA* **2010**, *107*, 10354.

(41) Hench, L. L.; West, J. K. *Chem. Rev.* **1990**, *90*, 33.

(42) Bilecka, I.; Niederberger, M. *Electrochim. Acta* **2010**, *55*, 7717.

(43) Livage, J. *Curr. Opin. Solid State Mat. Sci.* **1997**, *2*, 132.

(44) Livage, J.; Lemerle, J. *Annu. Rev. Mater. Sci.* **1982**, *12*, 103.

(45) Livage, J.; Henry, M.; Sanchez, C. *Prog. Solid State Chem.* **1988**, *18*, 259.

(46) Cao, G. *Nanostructures & nanomaterials synthesis, properties & applications*; Reprint. ed.; Imperial College Press: London, 2008.

(47) http://www.chem.umn.edu/groups/stein/abstracts/InverseOpal.Guide.pdf.

(48) Galusha, J. W.; Tsung, C.-K.; Stucky, G. D.; Bartl, M. H. *Chem. Mater.* **2008**, *20*, 4925.

(49) Peter, L. M. *Phil. Trans. R. Soc. A* **2011**, *369*, 1840.

(50)   O'Regan, B.; Gratzel, M. *Nature* **1991**, *353*, 737.

(51)   Gratzel, M. *Nature* **2001**, *414*, 338.

(52)   Hardin, B. E.; Snaith, H. J.; McGehee, M. D. *Nature Photon.* **2012**, *6*, 162.

(53)   Hagfeldt, A.; Boschloo, G.; Sun, L.; Kloo, L.; Pettersson, H. *Chem. Rev.* **2010**, *110*, 6595.

(54)   Kalyanasundaram, K. *Dye-sensitized solar cells*; 1. ed. ed.; EPFL Press: Lausanne, 2010.

(55)   Ito, S.; Murakami, T. N.; Comte, P.; Liska, P.; Grätzel, C.; Nazeeruddin, M. K.; Grätzel, M. *Thin Solid Films* **2008**, *516*, 4613.

(56)   Park, Y.-C.; Chang, Y.-J.; Kum, B.-G.; Kong, E.-H.; Son, J. Y.; Kwon, Y. S.; Park, T.; Jang, H. M. *J. Mater. Chem.* **2011**, *21*, 9582.

(57)   McCall, K. L.; Jennings, J. R.; Wang, H.; Morandeira, A.; Peter, L. M.; Durrant, J. R.; Yellowlees, L. J.; Robertson, N. *Eur. J. Inorg. Chem.* **2011**, *2011*, 589.

(58)   Moorcraft, L. P.; Jack, L. A.; Jennings, J. R.; Peter, L. M.; Yellowlees, L. J.; Robertson, N. *Polyhedron* **2009**, *28*, 4084.

(59)   McCall, K. L.; Jennings, J. R.; Wang, H. X.; Morandeira, A.; Peter, L. M.; Durrant, J. R.; Yellowlees, L. J.; Woollins, J. D.; Robertson, N. *J. Photochem. Photobiol. A* **2009**, *202*, 196.

(60)   Blackburn, O. A.; Coe, B. J.; Hahn, V.; Helliwell, M.; Raftery, J.; Ta, Y. T.; Peter, L. M.; Wang, H. X.; Anta, J. A.; Guillen, E. *Dyes Pigments* **2012**, *92*, 766.

(61)   Zhao, H. C.; Harney, J. P.; Huang, Y. T.; Yum, J. H.; Nazeeruddin, M. K.; Gratzel, M.; Tsai, M. K.; Rochford, J. *Inorg. Chem.* **2012**, *51*, 1.

(62)   Chang, D. W.; Tsao, H. N.; Salvatori, P.; De Angelis, F.; Gratzel, M.; Park, S. M.; Dai, L.; Lee, H. J.; Baek, J. B.; Nazeeruddin, M. K. *RSC Adv.* **2012**, *2*, 6209.

(63)   Calogero, G.; Yum, J. H.; Sinopoli, A.; Di Marco, G.; Gratzel, M.; Nazeeruddin, M. K. *Sol. Energy* **2012**, *86*, 1563.

(64)   Tsao, H. N.; Yi, C.; Moehl, T.; Yum, J. H.; Zakeeruddin, S. M.; Nazeeruddin, M. K.; Gratzel, M. *Chem. Sus. Chem.* **2011**, *4*, 591.

(65)   Shi, Y. R.; Hill, R. B. M.; Yum, J. H.; Dualeh, A.; Barlow, S.; Gratzel, M.; Marder, S. R.; Nazeeruddin, M. K. *Angew. Chem. Int. Ed.* **2011**, *50*, 6619.

(66)   Katono, M.; Bessho, T.; Wielopolski, M.; Marszalek, M.; Moser, J.-E.; Humphry-Baker, R.; Zakeeruddin, S. M.; Grätzel, M. *J. Phys. Chem. C* **2012**, *116*, 16876

(67)   Wang, H. X.; Nicholson, P. G.; Peter, L.; Zakeeruddin, S. M.; Gratzel, M. *J. Phys. Chem. C* **2010**, *114*, 14300.

(68)   Haid, S.; Marszalek, M.; Mishra, A.; Wielopolski, M.; Teuscher, J.; Moser, J. E.; Humphry-Baker, R.; Zakeeruddin, S. M.; Gratzel, M.; Bauerle, P. *Adv. Funct. Mater.* **2012**, *22*, 1291.

(69)   Ahmad, S.; Bessho, T.; Kessler, F.; Baranoff, E.; Frey, J.; Yi, C. Y.; Graetzel, M.; Nazeeruddin, M. K. *Phys. Chem. Chem. Phys.* **2012**, *14*, 10631.

(70)   Sauvage, F.; Chhor, S.; Marchioro, A.; Moser, J. E.; Graetzel, M. *J. Amer. Chem. Soc.* **2011**, *133*, 13103.

(71)   Wu, M. X.; Lin, X.; Wang, Y. D.; Wang, L.; Guo, W.; Qu, D. D.; Peng, X. J.; Hagfeldt, A.; Gratzel, M.; Ma, T. L. *J. Amer. Chem. Soc.* **2012**, *134*, 3419.

(72)   Burschka, J.; Brault, V.; Ahmad, S.; Breau, L.; Nazeeruddin, M. K.; Marsan, B.; Zakeeruddin, S. M.; Gratzel, M. *Energy Environ. Sci.* **2012**, *5*, 6089.

(73)   Kavan, L.; Yum, J. H.; Gratzel, M. *Nano Lett.* **2011**, *11*, 5501.

(74)   Tetreault, N.; Arsenault, E.; Heiniger, L. P.; Soheilnia, N.; Brillet, J.; Moehl, T.; Zakeeruddin, S.; Ozin, G. A.; Gratzel, M. *Nano Lett.* **2011**, *11*, 4579.

(75)   Yella, A.; Lee, H. W.; Tsao, H. N.; Yi, C. Y.; Chandiran, A. K.; Nazeeruddin, M. K.; Diau, E. W. G.; Yeh, C. Y.; Zakeeruddin, S. M.; Gratzel, M. *Science* **2011**, *334*, 629.

(76)   Peter, L. M. *J. Phys. Chem. Lett.* **2011**, *2*, 1861.

(77)   Goresy, A. E.; Chen, M.; Dubrovinsky, L.; Gillet, P.; Graup, G. *Science* **2001**, *293*, 1467.

(78)   El Goresy, A.; Chen, M.; Gillet, P.; Dubrovinsky, L.; Graup, G.; Ahuja, R. *Earth Planet. Sci. Lett.* **2001**, *192*, 485.

(79)   http://www.irocks.com/db_pics/new2012/Anatase-Norway-33mm-JB663-09.jpg.

(80)   Foto: Rupert Hochleitner, A., Fundort Alp Lärcheltini, Binntal, Schweiz, Größe 1 cm, Mineralogische Staatssammlung, München.

(81)   Chen, X.; Mao, S. S. *Chem. Rev.* **2007**, *107*, 2891.

(82)   Fujishima, A.; Honda, K. *Nature* **1972**, *238*, 37.

(83)   Kubacka, A.; Fernandez-Garcia, M.; Colon, G. *Chem. Rev.* **2012**, *112*, 1555.

(84)   Szeifert, J. M.; Fattakhova-Rohlfing, D.; Rathousky, J.; Bein, T. *Chem. Mater.* **2012**, *24*, 659.

(85)   Szeifert, J. M.; Fattakhova-Rohlfing, D.; Georgiadou, D.; Kalousek, V.; Rathousky, J.; Kuang, D.; Wenger, S.; Zakeeruddin, S. M.; Gratzel, M.; Bein, T. *Chem. Mater.* **2009**, *21*, 1260.

(86)   Fang, J.; Reitz, C.; Brezesinski, T.; Nemanick, E. J.; Kang, C. B.; Tolbert, S. H.; Pilon, L. *J. Phys. Chem. C* **2011**, *115*, 14606.

(87)   Ortel, E.; Fischer, A.; Chuenchom, L.; Polte, J.; Emmerling, F.; Smarsly, B.; Kraehnert, R. *Small* **2012**, *8*, 298.

(88)   Soler-illia, G. J. D.; Sanchez, C.; Lebeau, B.; Patarin, J. *Chem. Rev.* **2002**, *102*, 4093.

(89)   Niederberger, M.; Bartl, M. H.; Stucky, G. D. *Chem. Mater.* **2002**, *14*, 4364.

(90) Niederberger, M.; Garnweitner, G.; Krumeich, F.; Nesper, R.; Cölfen, H.; Antonietti, M. *Chem. Mater.* **2004**, *16*, 1202.

(91) Polleux, J.; Pinna, N.; Antonietti, M.; Niederberger, M. *Adv. Mater.* **2004**, *16*, 436.

(92) Szeifert, J. M.; Feckl, J. M.; Fattakhova-Rohlfing, D.; Liu, Y.; Kalousek, V.; Rathousky, J.; Bein, T. *J. Am. Chem. Soc.* **2010**, *132*, 12605.

(93) Cho, C. Y.; Moon, J. H. *Langmuir* **2012**, *28*, 9372.

(94) Shin, J. H.; Kang, J. H.; Jin, W. M.; Park, J. H.; Cho, Y. S.; Moon, J. H. *Langmuir* **2011**, *27*, 856.

(95) Seo, Y. G.; Woo, K.; Kim, J.; Lee, H.; Lee, W. *Adv. Funct. Mater.* **2011**, *21*, 3094.

(96) Liu, L. J.; Karuturi, S. K.; Su, L. T.; Tok, A. I. Y. *Energy Environ. Sci.* **2011**, *4*, 209.

(97) Han, S. H.; Lee, S.; Shin, H.; Jung, H. S. *Adv. Energy Mater.* **2011**, *1*, 546.

(98) Yip, C. H.; Chiang, Y. M.; Wong, C. C. *J. Opt. Soc. Am. B* **2010**, *27*, 920.

(99) Qi, L.; Sorge, J. D.; Birnie, D. P. *J. Am. Ceram. Soc.* **2009**, *92*, 1921.

(100) Kwak, E. S.; Lee, W.; Park, N. G.; Kim, J.; Lee, H. *Adv. Funct. Mater.* **2009**, *19*, 1093.

(101) Ruani, G.; Ancora, C.; Corticelli, F.; Dionigi, C.; Rossi, C. *Sol. Energ. Mat. Sol.* **2008**, *92*, 537.

(102) Kavan, L.; Zukalova, M. T.; Kalbac, M.; Graetzel, M. *J. Electrochem. Soc.* **2004**, *151*, A1301.

(103) Schroden, R. C.; Al-Daous, M.; Blanford, C. F.; Stein, A. *Chem. Mater.* **2002**, *14*, 3305.

(104) Mihi, A.; Miguez, H. *J. Phys. Chem. B* **2005**, *109*, 15968.

(105) Huisman, C. L.; Schoonman, J.; Goossens, A. *Sol. Energ. Mat. Sol.* **2005**, *85*, 115.

(106) Hore, S.; Nitz, P.; Vetter, C.; Prahl, C.; Niggemann, M.; Kern, R. *Chem. Commun.* **2005**, 2011.

(107) Halaoui, L. I.; Abrams, N. M.; Mallouk, T. E. *J. Phys. Chem. B* **2005**, *109*, 6334.

(108) Nishimura, S.; Abrams, N.; Lewis, B. A.; Halaoui, L. I.; Mallouk, T. E.; Benkstein, K. D.; van de Lagemaat, J.; Frank, A. J. *J. Am. Chem. Soc.* **2003**, *125*, 6306.

(109) Miguez, H.; Tetreault, N.; Hatton, B.; Yang, S. M.; Perovic, D.; Ozin, G. A. *Chem. Commun.* **2002**, 2736.

(110) Ferber, J.; Luther, J. *Sol. Energ. Mat. Sol.* **1998**, *54*, 265.

(111) Mihi, A.; Calvo, M. E.; Anta, J. A.; Miguez, H. *J. Phys. Chem. C* **2008**, *112*, 13.

(112) Jin, M.; Kim, S. S.; Yoon, M.; Li, Z.; Lee, Y. Y.; Kim, J. M. *J. Nanosci. Nanotech.* **2012**, *12*, 815.

(113) Mihi, A.; Zhang, C.; Braun, P. V. *Angew. Chem. Int. Ed.* **2011**, *50*, 5711.

(114) Tao, C.-a.; Zhu, W.; An, Q.; Li, G. *J. Phys. Chem. C* **2010**, *114*, 10641.

(115) Colodrero, S.; Mihi, A.; Anta, J. A.; Ocana, M.; Miguez, H. *J. Phys. Chem. C* **2009**, *113*, 1150.

(116) Lee, S.-H. A.; Abrams, N. M.; Hoertz, P. G.; Barber, G. D.; Halaoui, L. I.; Mallouk, T. E. *J. Phys. Chem. B* **2008**, *112*, 14415.

(117) Fu, Y. A.; Jin, Z. G.; Xue, W. J.; Ge, Z. P. *J. Am. Ceram. Soc.* **2008**, *91*, 2676.

(118) Du, J.; Lai, X. Y.; Yang, N. L.; Zhai, J.; Kisailus, D.; Su, F. B.; Wang, D.; Jiang, L. *ACS Nano* **2011**, *5*, 590.

(119) Karuturi, S. K.; Luo, J.; Cheng, C.; Liu, L.; Su, L. T.; Tok, A. I. Y.; Fan, H. J. *Adv. Mater.* **2012**, *24*, 4157.

(120) Hayner, C. M.; Zhao, X.; Kung, H. H. *Ann. Rev. Chem. Biomol. Eng.* **2012**, *3*, 445.

(121) http://sionpower.com/pdf/articles/LIS%20Spec%20Sheet%2010-3-08.pdf.

(122) Ji, X.; Nazar, L. F. *J. Mater. Chem.* **2010**, *20*, 9821.

(123) Evers, S.; Nazar, L. F. *Acc. Chem. Res.* **2012**.

(124) Barchasz, C.; Molton, F.; Duboc, C.; Leprêtre, J.-C.; Patoux, S.; Alloin, F. *Anal. Chem.* **2012**, *84*, 3973.

(125) Ji, X.; Lee, K. T.; Nazar, L. F. *Nature Mater.* **2009**, *8*, 500.

(126) Yang, Y.; Yu, G.; Cha, J. J.; Wu, H.; Vosgueritchian, M.; Yao, Y.; Bao, Z.; Cui, Y. *ACS Nano* **2011**, *5*, 9187.

(127) Zheng, G.; Yang, Y.; Cha, J. J.; Hong, S. S.; Cui, Y. *Nano Lett.* **2011**, *11*, 4462.

(128) Zhang, C.; Wu, H. B.; Yuan, C.; Guo, Z.; Lou, X. W. *Angew. Chem. Int. Ed.* **2012**, *51*, 9592.

(129) Wang, H.; Yang, Y.; Liang, Y.; Robinson, J. T.; Li, Y.; Jackson, A.; Cui, Y.; Dai, H. *Nano Lett.* **2011**, *11*, 2644.

(130) Wang, B.; Li, K.; Su, D.; Ahn, H.; Wang, G. *Chem. Asian J.* **2012**, *7*, 1637.

(131) Mao, W. L.; Mao, H.-k.; Eng, P. J.; Trainor, T. P.; Newville, M.; Kao, C.-c.; Heinz, D. L.; Shu, J.; Meng, Y.; Hemley, R. J. *Science* **2003**, *302*, 425.

(132) Zhou, R.; Zeng, X. C. *J. Am. Chem. Soc.* **2012**, *134*, 7530.

(133) Cahn, R. W.; Harris, B. *Nature* **1969**, *221*, 132.

(134) Schaetz, A.; Zeltner, M.; Stark, W. J. *ACS Catal.* **2012**, *2*, 1267.

(135) Hirsch, A. *Nature Mater.* **2010**, *9*, 868.

(136) Qin, F.; Brosseau, C. *J. Apl. Phys.* **2012**, *111*.

(137) Calaminici, P.; Carmona-Espindola, J.; Geudtner, G.; Köster, A. M. *Int. J. Quant. Chem.* **2012**, *112*, 3252.

(138) Palnichenko, A. V.; Jonas, A. M.; Charlier, J. C.; Aronin, A. S.; Issi, J. P. *Nature* **1999**, *402*, 162.

(139) Khaliullin, R. Z.; Eshet, H.; Kuhne, T. D.; Behler, J.; Parrinello, M. *Nature Mater.* **2011**, *10*, 693.

(140) Regueiro, M. N.; Monceau, P.; Hodeau, J. L. *Nature* **1992**, *355*, 237.

(141) Wang, L.; Liu, B.; Li, H.; Yang, W.; Ding, Y.; Sinogeikin, S. V.; Meng, Y.; Liu, Z.; Zeng, X. C.; Mao, W. L. *Science* **2012**, *337*, 825.

(142) Novoselov, K. S.; Geim, A. K.; Morozov, S. V.; Jiang, D.; Zhang, Y.; Dubonos, S. V.; Grigorieva, I. V.; Firsov, A. A. *Science* **2004**, *306*, 666.

(143) Rietmeijer, F. J. M. *Natural Fullerenes and Related Structures of Elemental Carbon*; Springer: Dordrecht, 2006.

(144) Terrones, M. *Annu. Rev. Mater. Res.* **2003**, *33*, 419.

(145) Sebastian, A.; Pauza, A.; Rossel, C.; Shelby, R. M.; Rodriguez, A. F.; Pozidis, H.; Eleftheriou, E. *New J. Phys.* **2011**, *13*.

(146) Robertson, J.; O'Reilly, E. P. *Phys. Rev. B* **1987**, *35*, 2946.

(147) Balandin, A. A. *Nature Mater.* **2011**, *10*, 569.

(148) Serp, P. *Carbon materials for catalysis*; Wiley: Hoboken, NJ, 2009.

(149) Liang, C. D.; Li, Z. J.; Dai, S. *Angew. Chem. Int. Ed.* **2008**, *47*, 3696.

(150) Wu, D.; Xu, F.; Sun, B.; Fu, R.; He, H.; Matyjaszewski, K. *Chem. Rev.* **2012**, *112*, 3959.

(151) Wu, X. Y.; Wang, K. X.; Chen, J. S. *Prog. Chem.* **2012**, *24*, 262.

(152) Titirici, M.-M.; Antonietti, M. *Chem. Soc. Rev.* **2010**, *39*, 103.

(153) Funke, A.; Ziegler, F. *Bioffpr* **2010**, *4*, 160.

(154) Jeffries, R. *Nature* **1971**, *232*, 304.

(155) Paraknowitsch, J. P.; Thomas, A.; Antonietti, M. *Chem. Mater.* **2009**, *21*, 1170.

(156) Peng, J.; Gao, W.; Gupta, B. K.; Liu, Z.; Romero-Aburto, R.; Ge, L.; Song, L.; Alemany, L. B.; Zhan, X.; Gao, G.; Vithayathil, S. A.; Kaipparettu, B. A.; Marti, A. A.; Hayashi, T.; Zhu, J.-J.; Ajayan, P. M. *Nano Lett.* **2012**, *12*, 844.

(157) Li, X.; Wang, H.; Shimizu, Y.; Pyatenko, A.; Kawaguchi, K.; Koshizaki, N. *Chem. Commun.* **2011**, *47*, 932.

(158) Li, H. T.; He, X. D.; Kang, Z. H.; Huang, H.; Liu, Y.; Liu, J. L.; Lian, S. Y.; Tsang, C. H. A.; Yang, X. B.; Lee, S. T. *Angew. Chem. Int. Ed.* **2010**, *49*, 4430.

(159) Sk, M. P.; Jaiswal, A.; Paul, A.; Ghosh, S. S.; Chattopadhyay, A. *Sci. Rep.* **2012**, *2*.

(160) Lu, A.-H.; Hao, G.-P.; Sun, Q.; Zhang, X.-Q.; Li, W.-C. *Macrom. Chem. Phys.* **2012**, *213*, 1107.

(161) Nieto-Marquez, A.; Romero, R.; Romero, A.; Valverde, J. L. *J. Mater. Chem.* **2011**, *21*, 1664.

(162) Yoo, H.; Moon, J. H. *RSC Adv.* **2012**, *2*, 8934.

(163) Guo, L. M.; Zhang, J. M.; He, Q. J.; Zhang, L. X.; Zhao, J. J.; Zhu, Z. Y.; Wu, W.; Zhang, J.; Shi, J. L. *Chem. Commun.* **2010**, *46*, 7127.

(164) Meng, Y.; Gu, D.; Zhang, F.; Shi, Y.; Cheng, L.; Feng, D.; Wu, Z.; Chen, Z.; Wan, Y.; Stein, A.; Zhao, D. *Chem. Mater.* **2006**, *18*, 4447.

(165) Meng, Y.; Gu, D.; Zhang, F.; Shi, Y.; Yang, H.; Li, Z.; Yu, C.; Tu, B.; Zhao, D. *Angew. Chem. Int. Ed.* **2005**, *44*, 7053.

(166) Cychosz, K. A.; Guo, X. F.; Fan, W.; Cimino, R.; Gor, G. Y.; Tsapatsis, M.; Neimark, A. V.; Thommes, M. *Langmuir* **2012**, *28*, 12647.

(167) Park, K.-Y.; Jang, J.-H.; Hong, J.-E.; Kwon, Y.-U. *J. Phys. Chem. C* **2012**, *116*, 16848.

(168) Schlienger, S.; Ducrot-Boisgontier, C.; Delmotte, L.; Guth, J. L.; Parmentier, J. *J. Phys. Chem. C* **2012**.

(169) Feng, D.; Lv, Y.; Wu, Z.; Dou, Y.; Han, L.; Sun, Z.; Xia, Y.; Zheng, G.; Zhao, D. *J. Am. Chem. Soc.* **2011**, *133*, 15148.

(170) Brinker, C. J.; Lu, Y.; Sellinger, A.; Fan, H. *Adv. Mater.* **1999**, *11*, 579.

(171) Schuster, J.; Köhn, R.; Döblinger, M.; Keilbach, A.; Amenitsch, H.; Bein, T. *J. Amer. Chem. Soc.* **2012**, *134*, 11136.

(172) Deng, Y.; Liu, J.; Liu, C.; Gu, D.; Sun, Z.; Wei, J.; Zhang, J.; Zhang, L.; Tu, B.; Zhao, D. *Chem. Mater.* **2008**, *20*, 7281.

(173) Labiano, A.; Dai, M.; Young, W.-S.; Stein, G. E.; Cavicchi, K. A.; Epps, T. H.; Vogt, B. D. *J. Phys. Chem. C* **2012**, *116*, 6038.

(174) Tamai, H.; Ikeuchi, M.; Kojima, S.; Yasuda, H. *Adv. Mater.* **1997**, *9*, 55.

(175) Liu, H.-J.; Wang, X.-M.; Cui, W.-J.; Dou, Y.-Q.; Zhao, D.-Y.; Xia, Y.-Y. *J. Mater. Chem.* **2010**, *20*, 4223.

(176) Che, G. L.; Lakshmi, B. B.; Fisher, E. R.; Martin, C. R. *Nature* **1998**, *393*, 346.

(177) Kyotani, T.; Tsai, L. F.; Tomita, A. *Chem. Mater.* **1995**, *7*, 1427.

(178) Wang, K. X.; Birjukovs, P.; Erts, D.; Phelan, R.; Morris, M. A.; Zhou, H. S.; Holmes, J. D. *J. Mater. Chem.* **2009**, *19*, 1331.

(179) Schuster, J.; Kohn, R.; Doblinger, M.; Keilbach, A.; Amenitsch, H.; Bein, T. *J. Am. Chem. Soc.* **2012**, *134*, 11136.

(180) Schuster, J.; Keilbach, A.; Kohn, R.; Doblinger, M.; Dorfler, T.; Dennenwaldt, T.; Bein, T. *Chem. Eur. J.* **2011**, *17*, 9463.

(181) Platschek, B.; Keilbach, A.; Bein, T. *Adv. Mater.* **2011**, *23*, 2395.

(182) Muhlstein, L.; Riederer, M.; Platschek, B.; Bein, T. *J. Mater. Chem.* **2009**, *19*, 9195.

(183) Keilbach, A.; Doblinger, M.; Kohn, R.; Amenitsch, H.; Bein, T. *Chem. Eur. J.* **2009**, *15*, 6645.

(184) Platschek, B.; Petkov, N.; Himsl, D.; Zimdars, S.; Li, Z.; Kohn, R.; Bein, T. *J. Am. Chem. Soc.* **2008**, *130*, 17362.

(185) Platschek, B.; Kohn, R.; Doblinger, M.; Bein, T. *Langmuir* **2008**, *24*, 5018.

(186) Platschek, B.; Kohn, R.; Doblinger, M.; Bein, T. *Chem. Phys. Chem.* **2008**, *9*, 2059.

(187) Platschek, B.; Petkov, N.; Bein, T. *Angew. Chem. Int. Ed.* **2006**, *45*, 1134.

(188) Cott, D. J.; Petkov, N.; Morris, M. A.; Platschek, B.; Bein, T.; Holmes, J. D. *J. Am. Chem. Soc.* **2006**, *128*, 3920.

(189) Fang, B.; Kim, M.; Fan, S.-Q.; Kim, J. H.; Wilkinson, D. P.; Ko, J.; Yu, J.-S. *J. Mater. Chem.* **2011**, *21*, 8742.

(190) Wang, K.; Zhang, W.; Phelan, R.; Morris, M. A.; Holmes, J. D. *J. Am. Chem. Soc.* **2007**, *129*, 13388.

(191) Zhang, X. B.; Chen, M. H.; Zhang, X. G.; Li, Q. W. *Acta Phys-Chim. Sin.* **2010**, *26*, 3169.

(192) Xie, J. S.; Wu, Q. S.; Zhao, D. F. *Carbon* **2012**, *50*, 800.

(193) Bo, X. J.; Zhu, L. D.; Wang, G.; Guo, L. P. *J. Mater. Chem.* **2012**, *22*, 5758.

(194) Liu, R.; Shi, Y.; Wan, Y.; Meng, Y.; Zhang, F.; Gu, D.; Chen, Z.; Tu, B.; Zhao, D. *J. Am. Chem. Soc.* **2006**, *128*, 11652.

(195) Wei, H.; Lv, Y. Y.; Han, L.; Tu, B.; Zhao, D. Y. *Chem. Mater.* **2011**, *23*, 2353.

(196) Song, L. Y.; Feng, D.; Lee, H. J.; Wang, C. Q.; Wu, Q. Y.; Zhao, D. Y.; Vogt, B. D. *J. Phys. Chem. C* **2010**, *114*, 9618.

(197) Song, L. Y.; Feng, D.; Campbell, C. G.; Gu, D.; Forster, A. M.; Yager, K. G.; Fredin, N.; Lee, H. J.; Jones, R. L.; Zhao, D. Y.; Vogt, B. D. *J. Mater. Chem.* **2010**, *20*, 1691.

(198) You, B.; Zhang, Z. D.; Zhang, L. L.; Yang, J.; Zhu, X. L.; Su, Q. D. *RSC Adv.* **2012**, *2*, 5071.

(199) Dai, M. Z.; Song, L. Y.; LaBelle, J. T.; Vogt, B. D. *Chem. Mater.* **2011**, *23*, 2869.

(200) Sun, Z.; Sun, B.; Qiao, M.; Wei, J.; Yue, Q.; Wang, C.; Deng, Y.; Kaliaguine, S.; Zhao, D. *J. Am. Chem. Soc.* **2012**.

2. Characterization Methods

In this thesis the morphology and properties of porous titania, silica and carbon were studied by various methods. This chapter describes different methods, mainly used for the characterization of particles, thin films and bulk.

2.1. Dynamic Light Scattering

In the field of colloid chemistry particle size is of major interest and dynamic light scattering (DLS) is a sensitive technique for rapid characterization of particles in solution.[1-6] If colloids, which need to be dispersed in quartz or PMMA cuvettes, are illuminated with a laser beam, light scattering occurs and the fluctuations of the scattering intensity are detected. Therefore DLS is also known as photon correlation spectroscopy.

The random Brownian motion describes the spontaneous motion of the colloids in solution, caused by collisions between individual particles and the solvent molecules. A size dependent influence on the diffusion of particles is given by the following Stokes-Einstein equation. Thus an ideal spherical shape is assumed.

$$D = \frac{k_B T}{6\pi\eta r} = \frac{k_B T}{3\pi\eta d}$$

The diffusion coefficient (translation) D is proportional to the Boltzmann constant k_B and the temperature and decreases with the viscosity η of the liquid and the particles´ radius r. The obtained hydrodynamic diameter d is not exactly equal to the diameter of the colloidal core, because the particle volume is also affected by a shell of solvent molecules and hydrated counter ions.

During laser irradiation particles permanently change their position, which causes a time dependent change of the scattering intensity. This scattered laser light undergoes a positive or negative interference, which leads to the detection of a speckle pattern. DLS instruments use an internal correlator to transform the fluctuating scattering intensity. In theory large particles undergo a slower Brownian motion, causing a decreased change in scattering intensity and for this a lower exponential decay of the correlation function $G(\tau)$.

$$G(\tau) = A\left[1 + Be^{(-2\Gamma\tau)}\right]$$

$$\Gamma = Dq^2$$

$$q = \frac{4\pi n}{\lambda_0}\sin\frac{\theta}{2}$$

Here A and B describe the correlation function baseline and the intercept of $G(\tau)$. The decay is also dependent on the solvents´ refractive index n, the wavelength of the incoming laser beam λ_0 and the scattering angle θ.

A Zetasizer Nano S (Malvern Instruments, UK), operated with a 4mW He-Ne ($\lambda = 633$ nm) laser, was used in this work to determine the particle size. Commonly a semi-micro PMMA cuvette (1.5 mL, Brand Gmbh and CoKG) was filled with transparent colloidal solutions.

The final particle sizes are obtained after a few minutes, depending on the repetition number and measurement time. For DLS the PMMA particles were typically dispersed in water (~ 0.1 wt%) and measured at room temperature.

2.2. X-Ray Diffraction

X-ray diffraction (XRD) is a common technique to characterize the crystallinity, phase composition and structural properties of metals, oxides and mesoporous materials.[7]

X-rays (10^{-12}-10^{-9} m) can be emitted by an evacuated X-ray tube, which was invented by C.W. Röntgen.[8] Within an X-ray tube, a current and high voltages are applied to a filament, which causes electron emission into vacuum. These electrons bombard an anode and X-rays are emitted over a continuous spectrum of energies (Bremsstrahlung), which are not higher than the acceleration voltage. Common anode materials are copper or molybdenum, which additionally emit characteristic X-rays, e.g. Cu-$K_{\alpha 1}$ (λ = 0.154 nm) and Mo- $K_{\alpha 1}$ (λ = 0.702 nm), respectively. These X-rays are applied for XRD measurements and need to be aligned and focused on the specimens´ surface, where they interfere with the specimen. Depending on its crystallinity or structure a corresponding pattern can be detected. In the case of a constructive interference, the relationship between the incoming X-ray beam with its wavelength λ, the lattice distance d and the angle of incidence θ is given by the following Bragg´s equation, where n represents the order of interference.[9,10]

$$n\lambda = 2d\sin\theta$$

The geometric description of Bragg´s law is shown in Figure 2.1.

Depending on the detection angle, one can distinguish between small angle X-ray scattering (SAXS) and wide angle X-ray scattering (WAXS). A pattern is usually recorded in SAXS experiments at values from 0.5 up to 5 $2\theta°$, and WAXS between 5 and 100 $2\theta°$, respectively. Thus SAXS experiments are suitable for the characterization of periodic and mesoporous matter, while WAXS gives information about the materials´ crystallinity and phase.
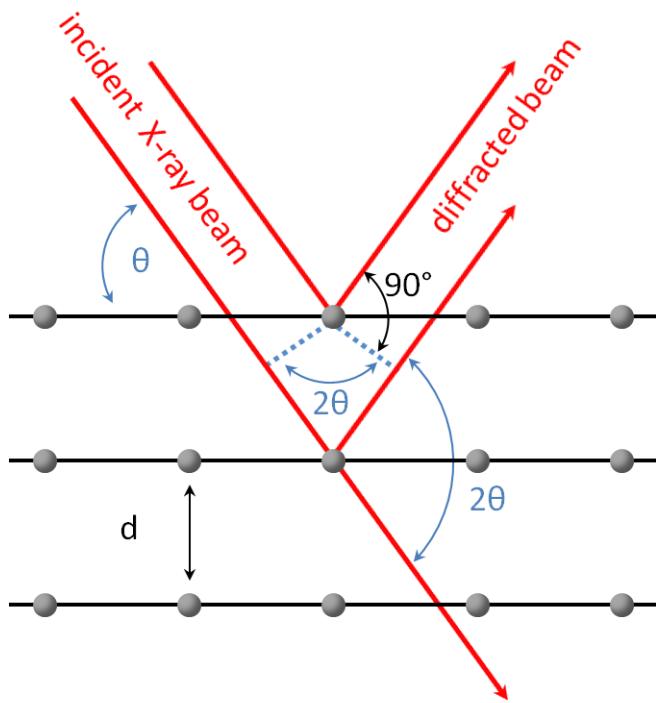
Figure 2.1: Illustration of Bragg´s law and the corresponding geometry of the X-ray diffraction at the lattice planes.

With XRD the average crystalline domain size up to 100-200 nm can also be estimated, which is important for the characterization of dense material and powders composed of single nanocrystals. The Scherrer equation describes the relationship between the crystalline domain size D and the corresponding peak broadening in the XRD pattern.[11]

The form factor k, with its dependence on the particle shape, is in most experiments 0.9, while the peak broadening β is given by a corrected full width at half maximum (FWHM).[12,13]

With decreasing domain size and small sample amounts the measurements need to be improved, because very broad peaks have to be distinguished from the background and low initial intensities require long measurement times. For this reason, small particles and their textural porosity are also often characterized by transmission electron microscopy and gas sorption experiments (see below).[14] A common reference material for XRD measurements is silver behenate, which shows well-defined reflections in the range of 1.5 to 20 degrees two theta[15], while glassy carbon is also widely used for SAXS.[15,16]

In this thesis, a Bruker diffractometer (D8 Discover, Cu-K$_{\alpha 1}$) including a VÅNTEC-1 detector was used for XRD and SAXS measurements of powders and thin films.

Two-dimensional grazing incidence small angle X-ray scattering (2D-GISAXS) is an advanced method for studying mesoporous materials (films, powders) with regard to their periodicity and orientation. The 2D detector also detects reflections that are not only perpendicular to the specimens' surface, which leads to more detailed structural information compared to 1D-SAXS measurements. X-ray sources with very high energy densities are available at synchrotrons. Such sources are advantageous for small specimen amounts and materials having a low X-ray contrast. The SAXS beamline at the Elettra synchrotron (B.L 5.2, Italy) provides three energies of 5.4, 8 and 16 keV, and the set up offers time-resolved measurements in the sub-millisecond regime of structural transformation. The corresponding lattice parameters can vary from 1 up to 140 nm, depending on the set up geometry.

In our studies we used 8 keV and a distance of 143 cm between the specimen, and a two-dimensional image CCD detector (Model CV 12, Photonic Science Ltd., Millham, UK). For sample heating during the in-situ studies, a modified hot stage (Model DHS 900, Anton Paar) was used.

Additionally, 2D-GISAXS was also carried out in the lab (Cu $K_{\alpha 1}$ at 40 keV), using a SAXSess mc^2 instrument (Anton Paar) and a 2D CCD detector.

2.3. Sorption Measurements

Micro- and mesoporous materials have pores below 2 and 50 nm, respectively and can be analyzed by gas adsorption experiments, which is a suitable technique[17] to determine porosity[18] and surface area[19,20].

Thus physisorption describes the interaction between the adsorptive (gas) and adsorbent (solid), which is of fundamental importance to get information about the adsorbents´ morphology. This process is reversible due to the weak Van-der-Waals interactions involved[21]. In contrast, chemisorption is often an irreversible process, because of the formation of a chemical bond between the adsorptive and the adsorbent.

Adsorption is an exothermic process and proceeds preferably at higher pressures and lower temperatures. Usually a gas such as nitrogen, krypton or argon is used as adsorptive. Kr is favorable for small amounts and/ or low surface areas and therefore is used for porous films. Argon is also widely used for microporous materials. These gases are more expensive than nitrogen, which is commonly used for mesoporous samples. Prior to every measurement, the adsorbent has to be properly outgassed under vacuum for several hours at temperatures above

100 °C to obtain a complete desorption of residual molecular contaminations, e.g. water or solvents, from the surface. The measuring vessel, usually a glass flask with a small volume, is finally cooled with a constant volume of liquid nitrogen (-196 °C) during the measurement.

Depending on the adsorbents´ porosity, the absorber gas has different ways for the penetration into the adsorbent bulk. Thus gas interacts with the surface, and depending on the specimens' porosity characteristic layer formation is observed. The International Union of Pure and Applied Chemistry (IUPAC) has classified six types of sorption isotherms (I – VI), represented in Figure 2.2.
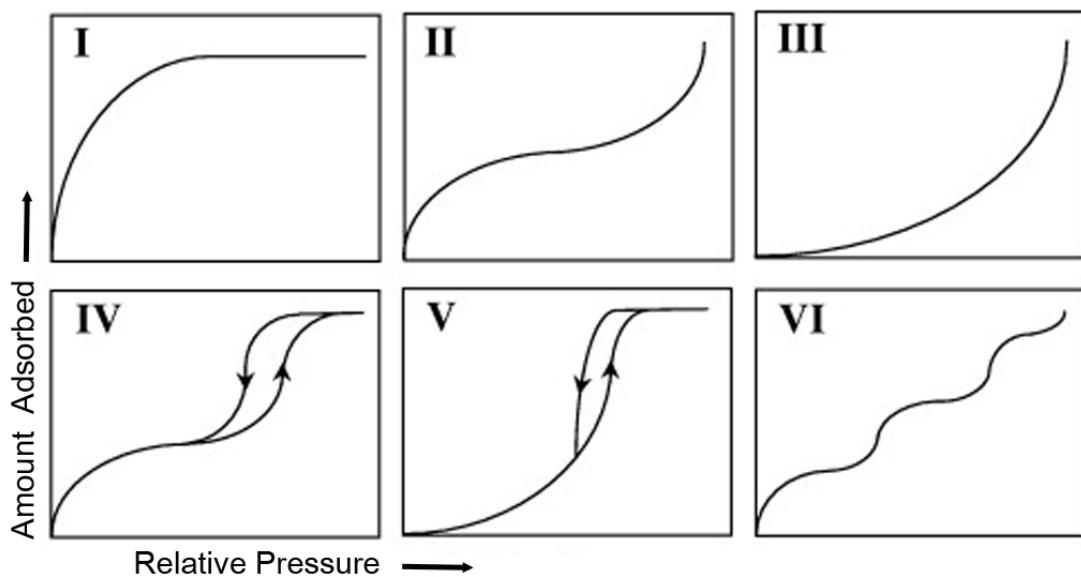
Figure 2.2. Schematic description of the UIPAC isotherms (type I to VI).[23]

A type I isotherm is obtained by a reversible ad- and desorption process within a microporous material, which has typical pore widths of up to 2 nm. If the pore dimensions have a similar

66

scale than the adsorbate, the formation of a monolayer correlates to a complete pore filling. For this reason a plateau is formed at higher relative pressures. The relative pressure represents the ratio between the applied pressure p and the saturation vapor pressure of the gas, p_0.

If the material is dense or has macropores (> 50 nm) a type II isotherm is formed, which shows the development from a closed gaseous monolayer to multilayers. The type III isotherm is not so common, here the interactions between the individual absorber molecules are strong and layer formation on the surface is unfavorable.

Furthermore there are a series of mesoporous materials, which have a defined pore width in the range of 2 to 50 nm. Their sorption behavior is represented in the shape of type IV, where the isotherm is similar to type II at lower relative pressures. However, an additional appearance of a hysteresis loop between the branches is observed at higher relative pressures. The loop is attributed to the effect of capillary condensation within the mesopores, and desorption of the multilayers often occurs at lower relative pressures.

The type V isotherm represents a system with very low interactions between the adsorbate molecules and the existence of mesoporosity. Type VI shows a stepwise adsorption of multilayers on a dense surface, but also different pore widths can be present in this material.

There exist different models for the description of sorption isotherms. The Langmuir model describes the monolayer formation of the adsorptive on a solid surface. The Brunauer-Emmett-Teller (BET) theory is based on the Langmuir model but assumes infinite multilayer formation; it is commonly used for a detailed evaluation of the isotherms. Thus the Langmuir model is used for describing the individual gas layers, and physical absorption of the gaseous adsorptive on a solid surface is also assumed. Additionally, there is no interaction between the

adsorptive molecules within one layer. The following linear BET equation is used for isotherm modeling.

$$\frac{p}{n^a(p_0 - p)} = \frac{1}{n_m^a C} + \frac{(C-1)}{n_m^a C} \frac{p}{p_0}$$

p_0: saturation pressure of the adsorptive

n^a: amount of adsorbate at relative pressure p/p_0

n_m^a: monolayer capacity

C: BET constant with an exponential relation to the adsorption enthalpy

The total surface area A_s(BET) and specific surface area a_s(BET), or just S_{BET}, can also be calculated with the BET theory.

$$A_s(\text{BET}) = n_m^a N_A a_m$$

$$a_s(\text{BET}) = \frac{A_s(BET)}{m}$$

a_m: molecular cross-sectional area; for N_2 it is 0.162 nm^2 at 77 K

N_A: Avogadro constant, $6.022*10^{-23}$ mol^{-1}

m: mass of adsorbent

Another important information about the porous material is provided with the pore size distribution, which is accessible by applying the Barret-Joyner-Halender (BJH) method. For the description of the pore volume distribution with respect to the pore size, the Kelvin equation is used.

$$\frac{1}{r_1} + \frac{1}{r_2} = -\frac{RT}{\sigma^{1g} v^{1}} \ln \frac{p}{p_0}$$

r_n, n = 1, 2: principal curvature radii of the liquid meniscus in the pores at the relative pressure

σ^{1g}: surface tension of the condensate

v^{1}: molecular volume of the condensate

R: ideal gas constant, 8.324 Jmol^{-1}K^{-1}, produkt of N_A and k_B

T: temperature in Kelvin

Additionally, Density Functional Theory (DFT) can be used to determine pore diameters. This specific calculation gives more correct values for microporous and mesoporous materials with small pore diameters, in comparison with the BJH method. Here, models are available that consider the pore geometry as well as the adsorbent. Depending on the material, pores can be more cylindrical, spherical or slit shaped. The models are applicable to the adsorption and the desorption branch of the isotherm.[17,23] A new Quenched Solid Density Functional Theory (QSDFT) can be applied to carbon materials, and considers the specimens heterogeneity and roughness, which makes it difficult to compare results with literature values based on the previous methods.[24,25]

For macroporous solid materials other techniques for surface determination are suitable and based on liquid intrusion and extrusion, commonly performed with mercury.[26]

In this thesis a Quantachrome Instruments NOVA 4000e at 77 K was used in combination with nitrogen for all sorption measurements.

2.4. Scanning Electron Microscopy

Scanning electron microscopy (SEM) is widely used and an important tool to characterize organic and inorganic materials regarding their morphology and structural composition. SEM implies a rapid and easy specimen preparation, which is widely used for detailed studies of titania anodes[27-30] and cathodes for lithium-sulfur batteries[31,32].

The basic principle involves an incident electron beam, which scans the specimen linewise with a certain frequency (raster scanning). The interaction of the incoming beam with the specimen generates a series of signals, which provides detailed information about the morphology and chemical composition.[33]

The primary electron beam can be generated in different ways, typically by thermal emission. Here, a wire of tungsten or lanthanum hexaboride is heated and the emitted electrons are accelerated within an applied electric field under high-vacuum conditions ($\sim 10^{-8}$ Pa; $\sim 10^{-6}$ mbar). Field-emission guns are popular sources in modern instruments. Here a potential difference, between an anode and a sharp metal tip (e.g. W), causes an electric field and electron emission. Thus higher resolutions, due to smaller beam diameters and higher current densities, are accessible.

The beam can be accelerated by applying voltages from 0.1 to 30 kV. Additionally several electromagnetic condenser lenses are used to align and stabilize the beam. To achieve a 2D image, a scan in x and y direction requires two sawtooth-wave generators to control the magnetic fields of coils, which drive the beam at certain frequencies. A high resolution also requires small beam diameters in the range of 1 to 10 nm and focusing by the objective lens. This electron beam interacts with the matter of the specimen and the different generated

electrons and X-rays are collected by detectors and the amplified signal is finally transferred into an image or a spectrum. Figure 2.3 summarizes the individual parts of an SEM.
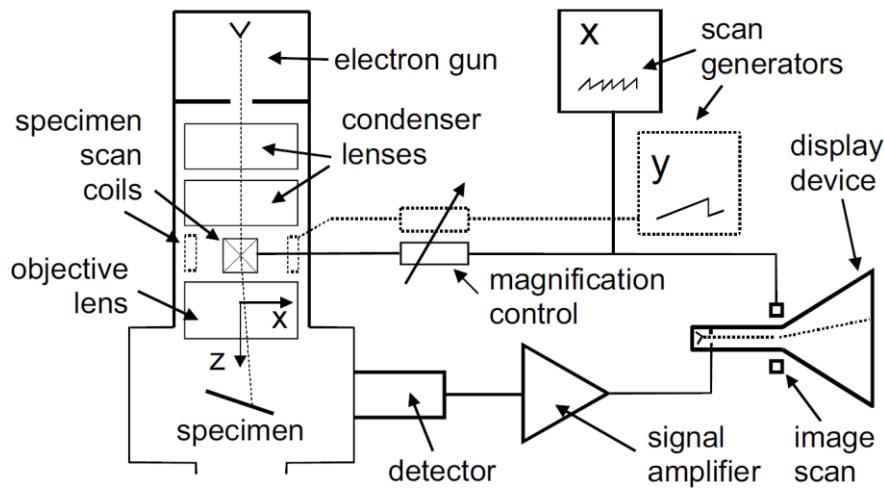
Figure 2.3: Schematic illustration of a scanning electron microscope.[33]

Different electrons are emitted from the specimen (Figure 2.4), which can be usually detected by a Everhart-Thornley detector and the signals used for further imaging and characterization. Secondary electrons (SE) (< 50 eV) are used for detailed images of the surface morphology, they are only emitted from the specimens' surface. X-rays are emitted from a larger interaction volume, which depends on the penetration depth (Figure 2.4). In energy-dispersive X-ray (EDX) spectroscopy, characteristic X-ray lines of elements present are detected and used for a quantitative chemical analysis. In EDX mapping experiments, a spatially-resolved elemental distribution of a defined area is obtained point by point.

The formation of backscattered electrons (BSE) occurs also in the interaction volume. They have high energies above 50 eV, and the detection reveals a high contrast difference between different elements of the specimen. The Auger electron (AU) spectroscopy is an additional technique to study the surface composition and observe different contrast of elements. These

electrons are emitted from a very small volume at the surface, which is favorable for very thin specimen.
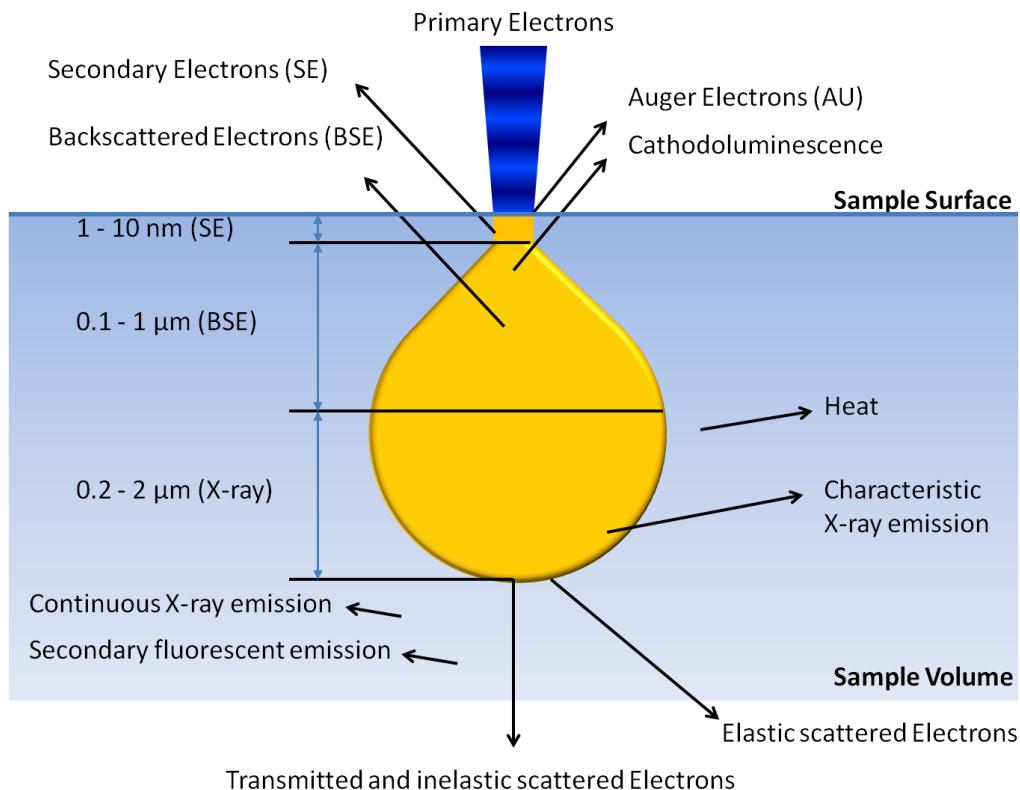
Figure 2.4: Schematic illustration of the emitted electromagnetic radiation and particles, generated by the interaction of a highly energetic incident electron beam with the specimens' matter.[33,34]

SEM studies were carried out with a JEOL JSM-F6500 microscope (field emission gun), which is operating at 0.5-30 kV and equipped with BSE, SE and EDX detectors. Powders and films were fixed on an aluminum sample holder with a conductive carbon tape or silver lacquer. In some cases the samples required conducting carbon coatings, prepared by sputter deposition.

2.5. Transmission Electron Microscopy

In contrast to SEM, transmission electron microscopy (TEM) uses higher accelerating voltages, usually from 80 up to 400 kV (or higher), which also enables very high resolution, down to the atomic scale. TEM is advantageous for detailed morphological and crystallographic studies of mesoporous and nanocrystalline materials. This also implies the observation of void arrangements in highly ordered macroporous oxides[35] and the development of grain formation in the walls of macroporous metals and oxides using in-situ heating experiments from room temperature up to 1000 °C.[36,37]

However, in TEM the specimen preparation, especially cross-sectioning of thin films, is very time consuming and implies several steps, e.g. embedding into an epoxy resin, slicing, grinding, dimpling and ion polishing. In the case of thin films, small parts can be scratched from the substrate and directly transferred to the sample holder. The observation of nanoparticles implies the transfer of solutions (dropwise) on the sample holder, which can be copper grid having a dense or holey carbon layer, by dropcasting and drying of diluted particle suspension in pure and volatile solvents. The resulting sample should be very thin to enable the electron transmission. High resolution TEM (HRTEM) requires thicknesses of only a few tens of nm. Similar to SEM, the electrons can be generated by thermal emission or by field emission guns, and CCD cameras or fluorescence screens can be used for signal detection.

In the case of bright field imaging, the transmitted electron beam is detected directly, while dark field imaging is based on the detection of the diffracted/scattered electron beam. Another common operation mode, the scanning transmission electron microscopy (STEM), generates images by scanning the beam linewise. Typically the detector only measures electrons that are

scattered at high angles (High Angle Annular Dark Field mode, HAADF). The detected electrons enable a high resolution based on mass contrast.

Complimentary to XRD, the crystallinity and phase composition of the specimen can be determined in electron microscopy by applying a technique called selected area electron diffraction (SAED). Corresponding diffraction patterns of single crystals or very small crystalline domains can be obtained. The patterns display spots or diffuse rings in the reciprocal space, which can be attributed to electron diffraction at the lattice planes if crystalline matter is present.[33,38]

In this thesis TEM images were obtained with a JEOL 2011 transmission electron microscope operating at 200 kV and a FEI Titan operating at 300 kV, which is additionally equipped with an EDX detector. In both instruments CCD cameras are used for imaging and DigitalMicrograph and ImageJ softwares are used for data processing.

2.6. I-V Measurements of Solar Cells

For the characterization of solar cell devices it is of fundamental importance to determine their performance.[39,40] One major method is determination of the current-voltage characteristics (I-V curve).

For this purpose different potentials are applied to the solar cell in the dark und under illumination, and the resulting current response is measured. From these data the maximum power point P_{max} can be determined. To avoid cell damage it is important to choose suitable edge potentials, and a typical scan rate of 10 mVs^{-1} enables good data collection. Usually xenon lamps are used as light sources to obtain the AM 1.5 standard illumination (100 Wcm^{-2},

25 °C). The power conversion efficiency η_{global} is defined as the ratio between maximum electrical power P_{max} and the incoming power P_{in}, which is also depending on the incoming light intensity I.

$$\eta_{global} = \frac{P_{max}}{P_{in}} = \frac{V_{oc}I_{SC}ff}{I}$$

The fill factor *ff* is often used for comparison of solar cell devices and defined as the ratio between the maximum power and the product of the open circuit potential and short circuit current.

$$ff = \frac{V_{max}I_{max}}{V_{oc}I_{SC}} = \frac{P_{max}}{V_{oc}I_{SC}}$$

A high fill factor indicates that losses from serial or shunt resistances are minimal. Figure 2.5 shows a typical IV-curve of a photovoltaic device. Usually the detected photocurrent is normalized to the active illuminated cell area, which is realized by masking the solar cell.
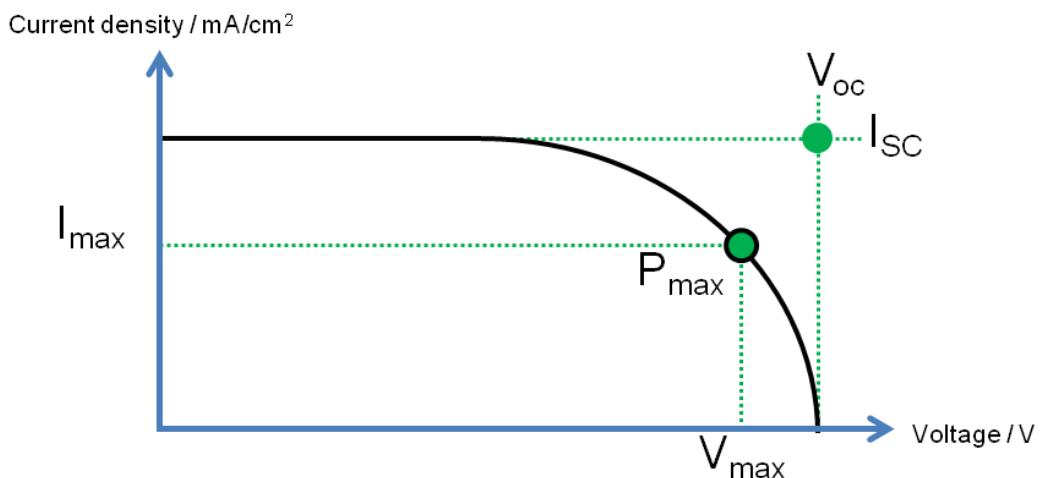
Figure 2.5: Schematic illustration of a current / voltage curve (IV) of a DSC including characteristic points.

To obtain standard illumination a calibration of the solar simulator is required. A common technique for measuring the solar irradiation is based on the conversion of heat generated by the solar irradiation into an electronic signal, which correlates to the solar radiation flux density ($mWcm^{-2}$). For this reason, a thermopile is the major part of standardized pyranometers. Certified measurements are performed by several organizations, such as the U.S. Department of Energy's National Renewable Energy Laboratory (NREL) or the Fraunhofer-Institute for solar energy systems (ISE), which also provides a certified reference solar cell. This reference cell adheres to the international standard (World PV Scale), and is again commonly used to calibrate silicon diodes, acting as frequently used reference.

In this thesis I-V-curves were measured with a ZAHNER Electric IM6ex potentiostat, controlled by a ZAHNER Electric software Thales 4.05 USB. Photovoltaic measurements were done with an AM 1.5 sun simulator. A Solar Light Co. Xenon lamp (model: 16S-300-V3, 100 mW/cm^2) was used as light source and driven by a XPS-400 power supply. Solar irradiance was detected by a pyranometer (PMA2144, Solar Light Co.)

2.7. External Quantum Efficiency

Measuring the external quantum efficiency (EQE) of a solar cell device is a common method to quantify the ratio between the short circuit current density I_{SC} and the product of incident photon flux I_0 and the elementary charge q. This technique is equivalent to the so called spectral incident-photon-to-collected-electron efficiency (IPCE).

$$IPCE(\lambda) = \frac{I_{SC}}{qI_0} = \eta_{lh}(\lambda)\eta_{inj}(\lambda)\eta_{col}(\lambda)$$

The EQE or IPCE of a dye-sensitized solar cell is strongly dependent on the irradiation wavelength λ, and is the product of different efficiencies, such as the light-harvesting efficiency η_{lh}, the electron-injection efficiency η_{inj} from the sensitizer (HOMO) into the semiconducting oxide (CB) and the electron collection efficiency η_{col}.

In this thesis a 150 W xenon lamp (Lot Oriel Xenon lamp) was used as primary light source. The white light passed a monochromator (Horiba Jobin Yvon microHR; slit opening fixed at 1.5 mm), equipped with appropriate long-pass filters. The primary beam was chopped at a frequency of 2 Hz. The secondary illumination source is given by a solar simulator and the provided bias illumination was reduced to about 10 mW/cm² using a neutral density filter. Finally a signal recovery dual-phase lock-in amplifier was used for signal detection (model: 7265). EQE measurements were referenced to a silicon photodiode with known spectral response.

2.8. Chapter References

(1)   Bantle, S.; Schmidt, M.; Burchard, W. *Macromolecules* **1982**, *15*, 1604.

(2)   Eshuis, A.; Harbers, G.; Doornink, D. J.; Mijnlieff, P. F. *Langmuir* **1985**, *1*, 289.

(3)   Tuzun, U.; Farhadpour, F. A. *Part. Part. Syst. Char.* **1986**, *3*, 151.

(4)   Wagner, J. *Chem.-Ing.-Tech.* **1986**, *58*, 578.

(5)   Barth, H. G.; Sun, S. T. *Anal. Chem.* **1991**, *63*, R1.

(6)   Pecora, R. *J. Nano. Res.* **2000**, *2*, 123.

(7)   Fernández-García, M.; Martínez-Arias, A.; Hanson, J. C.; Rodriguez, J. A. *Chem. Rev.* **2004**, *104*, 4063.

(8)   Underwood, E. A. *Proc. Roy. Soc. of Medicine-London* **1945**, *38*, 697.

(9)   Strong, W. W. *Science* **1914**, *40*, 709.

(10)   Pfluger, C. E. *Anal. Chem.* **1972**, *44*, R563.

(11)   Holzwarth, U.; Gibson, N. *Nature Nanotechn.* **2011**, *6*, 534.

(12)   Jiang, H. G.; Ruhle, M.; Lavernia, E. J. *J. Mater. Res.* **1999**, *14*, 549.

(13)   Zhang, Z.; Zhou, F.; Lavernia, E. J. *Metall. Mater. Trans. a* **2003**, *34A*, 1349.

(14)   Weibel, A.; Bouchet, R.; Boulc'h, F.; Knauth, P. *Chem. Mater.* **2005**, *17*, 2378.

(15)   Huang, T. C.; Toraya, H.; Blanton, T. N.; Wu, Y. *J. Appl. Crystallogr.* **1993**, *26*, 180.

(16)   Perret, R.; Ruland, W. *J. Appl. Cryst.* **1972**, *5*, 183.

(17)   Rouquerol, J.; Avnir, D.; Fairbridge, C. W.; Everett, D. H.; Haynes, J. H.; Pernicone, N.; Ramsay, J. D. F.; Sing, K. S. W.; Unger, K. K. *Pure Appl. Chem.* **1994**, *66*, 1739.

(18)   Schull, C. G. *J. Am. Chem. Soc.* **1948**, *70*, 1405.

(19)   Brunauer, S.; Emmett, P. H.; Teller, E. *J. Am. Chem. Soc.* **1938**, *60*, 309.

(20)   Barrett, E. P.; Joyner, L. G.; Halenda, P. P. *J. Am. Chem. Soc.* **1951**, *73*, 373.

(21)   Brunauer, S.; Deming, L. S.; Deming, W. E.; Teller, E. *J. Am. Chem. Soc.* **1940**, *62*, 1723.

(22)   Carmody, O.; Frost, R.; Xi, Y.; Kokot, S. *Surf. Sci.* **2007**, *601*, 2066.

(23)   Sing, K. S. W.; Everett, D. H.; Haul, R. A. W.; Moscou, L.; Pierotti, R. A.; Rouquerol, J.; Siemieniewska, T. *Pure Appl. Chem.* **1985**, *57*, 603.

(24)   http://www.quantachrome.com/technical/dft.html.

(25)   Gor, G. Y.; Thommes, M.; Cychosz, K. A.; Neimark, A. V. *Carbon* **2012**, *50*, 1583.

(26) Rouquerol, J.; Baron, G. V.; Denoyel, R.; Giesche, H.; Groen, J.; Klobes, P.; Levitz, P.; Neimark, A. V.; Rigby, S.; Skudas, R.; Sing, K.; Thommes, M.; Unger, K. *Micropor. Mesopor. Mat.* **2012**, *154*, 2.

(27) Tonejc, A. M.; Turkovic, A.; Gotic, M.; Music, S.; Vukovic, M.; Trojko, R.; Tonejc, A. *Mater. Lett.* **1997**, *31*, 127.

(28) Ito, S.; Chen, P.; Comte, P.; Nazeeruddin, M. K.; Liska, P.; Pechy, P.; Gratzel, M. *Prog. Photovoltaics* **2007**, *15*, 603.

(29) Chen, X.; Mao, S. S. *Chem. Rev.* **2007**, *107*, 2891.

(30) Ito, S.; Nazeeruddin, M. K.; Zakeeruddin, S. M.; #233; chy, P.; Comte, P.; Grätzel, M.; Mizuno, T.; Tanaka, A.; Koyanagi, T. *Int. J. Photoenergy* **2009**, *2009*.

(31) Ji, X.; Lee, K. T.; Nazar, L. F. *Nature Mater.* **2009**, *8*, 500.

(32) Oleshko, V.; Scordilis-Kelley, C.; Xiao, A. *Microsc. Microanal.* **2009**, *15*, 718.

(33) Egerton, R. F.; *Physical Principles of Electron Microscopy*, Springer Science+Business Media, Inc: 2005.

(34) http://serc.carleton.edu/details/images/9673.html

(35) Blanford, C. F.; Carter, C. B.; Stein, A. In *EMAG-NANO 2005: Imaging, Analysis and Fabrication on the Nanoscale*; Brown, P. D., Baker, R., Hamilton, B., Eds. 2006; Vol. 26, p 264.

(36) Denny, N. R.; Li, F.; Norris, D. J.; Stein, A. *J. Mater. Chem.* **2010**, *20*, 1538.

(37) Blanford, C. F.; Carter, C. B.; Stein, A. *J. Mater. Sci.* **2008**, *43*, 3539.

(38) Fultz, B.; Howe, J. M.; Springer-Verlag Berlin Heidelberg: 2008.

(39) Oregan, B.; Gratzel, M. *Nature* **1991**, *353*, 737.

(40) Hagfeldt, A.; Boschloo, G.; Sun, L.; Kloo, L.; Pettersson, H. *Chem. Rev.* **2010**, *110*, 6595.

3. Colloidal Poly(methyl methacrylate) Templates

3.1. Introduction

Colloids are widely used and can be composed of a range of inorganic and organic materials.[1] Prominent organic colloids are monodisperse polymer beads, which are essential for this work. Large poly(methyl methacrylate) (PMMA) microparticles (1 μm to 250 μm) are often used for medical applications, which can be attributed to a good biocompatibility and a possible drug or particle encapsulation. For this purpose many techniques are reported for the PMMA functionalization, addressing the particle solubility, stability and loading behavior.[2-4] For example polymer cross-linking, dye incorporation and steric stabilization also enables the application in apolar media.[5]

For other purposes a reduction of the bead size can be essential. Such systems can be obtained by emulsion polymerization[6,7], which is a suitable technique to obtain polymers with spherical shape.[8]

In this thesis we use PMMA beads as shape-persistent sacrificial templates to develop macroporous materials, which are further applied as hard templates for more complex morphologies. This requires a gram-scale synthesis of monodisperse PMMA beads of different sizes. In general it was shown by Zou D. et al. that emulsion polymerization of methyl methacrylate ($C_5H_8O_2$) can produce uniform PMMA particles (ca. 313 nm), without further stabilizing the monomer droplets within a water phase.[9] The final particle size can be controlled by the ratio of surfactant to monomer, which is usually much smaller than 1. Based on this work, it was reported by Wang et al. that the particle diameter can be further decreased to 170 to 190 nm by stabilizing monomer droplets with an anionic surfactant, here sodium

dodecyl sulfate (SDS, $NaC_{12}H_{25}SO_4$). Moreover, the diameter was also reduced to 90 to 100 nm by changing the ratio between the monomer (MMA) and the radical initiator (potassium persulfate, $K_2S_2O_8$), accompanied by a five times higher SDS concentration.[10]

The work of Wang et al. also applied PMMA beads as hard template for the synthesis of macro- and mesoporous materials. Here, macroporous oxide powders (CeO_2) with pore diameters ranging from 200-240 nm, 70-80 nm (macropores) and 30-40 nm (large mesopores), respectively, were obtained by the use of the previously mentioned PMMA templates. This dimensions also clearly show the effect of temperature-induced shrinkage, noted to be around 29, 58 and 63 %. The temperature-induced shrinkage was observed after calcination at high temperatures, e.g. 450 °C, which was required to achieve a complete removal of the PMMA template.[10]

An alternative technique (which was not further used in this thesis) involves the use of microemulsions. In this case the monomer-to-surfactant weight ratio is larger or equal to 1. For example, small PMMA particles from 98 nm down to 21 nm and polystyrene particles (20 – 30 nm) were obtained.[11-13]

3.2. Experimental Section

Emulsion Polymerization

In a typical synthesis 98 mg water was degassed by flushing nitrogen through a three-necked flask (250 mL) with reflux condenser for 1 h. MMA (6.89 g, 68.8 mmol) and SDS (196 mg, 0.68 mmol) was added and the mixture was magnetically stirred for 1 h in nitrogen at 90 °C

(oil bath). For reaction initiation a solution of $K_2S_2O_8$ (227.2 mg, 0.84 mmol) in degassed water (2 mL) was injected into the emulsion. After a polymerization time of ca. 2 h the reaction was stopped by removing heat, exposing to ambient air and cooling to room temperature. The PMMA bead solution was stirred for ca. 12 h in air at room temperature, filtered and washed three times by centrifugation and redispersion in ultrapure water (Millipore Q). The resulting solution contains stable PMMA particles of $30 - 50$ nm (SEM, Table 3.1).

The synthesis of the larger PMMA particles is similar and is further described in the following chapters (4 - 6, 9).

3.3. Results and Discussion

In this thesis highly monodisperse PMMA particles were used as hard templates for 3D macroporous structures. The particle synthesis procedures are based on the work of Wang et al.[10] and were slightly modified, and the resulting aqueous colloidal solutions are stable for months. All procedures were adjusted to a fixed total volume of 100 mL water and did not require KPG-stirrers. During emulsion polymerizations, a permanent control of the stirring is necessary to achieve a homogenous particle size distribution. The clear homogenous mixtures become turbid white and viscous after the injection of the initiator solution. The reactions and final PMMA particle sizes are sensitive to parameter changes in the processing such as a change of the stirring bar size and shape in relation to the flask size. The resulting colloidal solutions need to be washed, usually 3-4 times by centrifugation and redispersion in water.

Because of the rather low PMMA density (1.18 - 1.20 g/cm^{-3}), the time for pellet formation can vary from around 15 minutes for large particles up to several hours for smaller ones, using a centrifuge at 20500 rpm (50228 rcf). After washing, the spheres can be stored as stable stock solutions or dry powders, which are redispersible by ultrasonic treatment.

The PMMA particle diameter is mainly dependent on the surfactant (SDS), monomer (MMA) and initiator concentrations, which are summarized in Table 3.1. The listed colloids are further used and described in the following chapters (4-6, 9) of this thesis.

Table 3.1. Overview on surfactant, monomer and initiator concentrations, and their influence on the PMMA particle size.

Sample description	SDS (mol/l)	MMA (mol/l)	$K_2S_2O_8$ (mol/l)	Size* (nm)
T.Wang et al.[10]	-	0.895	5.0×10^{-4}	300 - 320
	1.7×10^{-4}	0.688	2.1×10^{-3}	170 - 190
	8.5×10^{-4}	0.688	2.1×10^{-3}	90 - 100
Chapter 4, 5	1.7×10^{-4}	3.55	2.1×10^{-3}	300 - 320
Chapter 6	1.7×10^{-4}	1.78	2.1×10^{-3}	~ 200
Chapter 6	8.5×10^{-4}	0.688	2.1×10^{-3}	~ 100
Chapter 9	6.8×10^{-3}	2.752	8.4×10^{-3}	60 - 70
Chapter 3	6.8×10^{-3}	0.688	8.4×10^{-3}	30 - 50

* Estimated by SEM.

The SEM images in Figure 3.1 clearly demonstrate the homogeneous size distribution obtained from the individual polymerizations, which provide PMMA particles in the range from around 320 nm down to 30 nm. For SEM imaging the PMMA films (colloidal crystals)

were prepared by a horizontal-deposition technique of aqueous colloidal solutions under vibration free conditions. Figure 3 c and d show colloidal crystal templates that were slightly physically connected by applying a thermal treatment at 80 °C for 2 h. This treatment has no influence on the size estimation by SEM. In contrast, Figure 3 a shows loosely packed non-connected PMMA particles, which were only dried at 60 °C for 1 h. In this case the PMMA particle positions were sensitive to the electron beam irradiation time in the SEM, causing partial particle movements and rearrangements, and the observed plan view can be different to the real one.
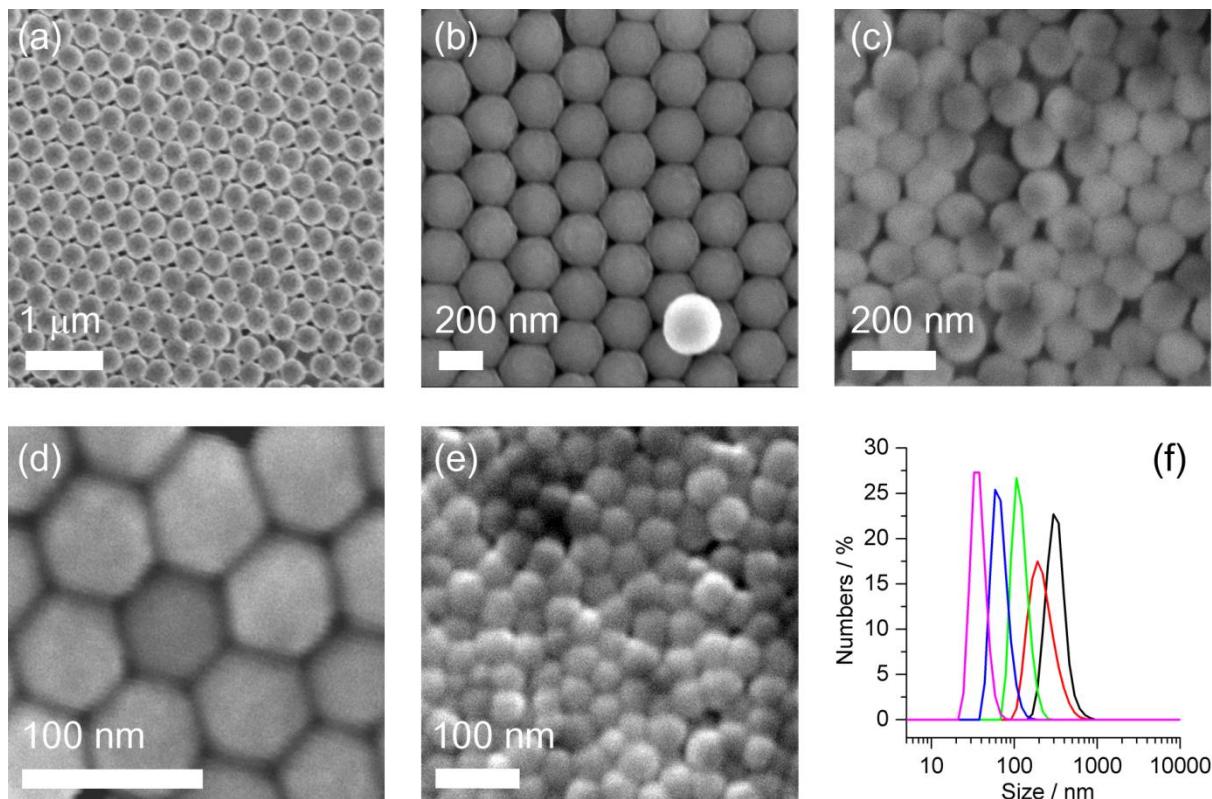
Figure 3.1: SEM top-view images of washed PMMA particles having particle diameters in the range of 320 (a), 200 (b), 100 (c), 60-70 nm (d) and 30-50 nm (e). (f) Summary of corresponding particle sizes (hydrodynamic sizes) estimated by DLS measurements of diluted solutions. The peak maxima occur at 324, 223, 143, 91, and 46 nm, respectively.

Dynamic light scattering (DLS) is a very sensitive technique to estimate particle sizes in solutions. It is known that the observed diameters are often somewhat larger than the ones obtained by electron microscopy (where shrinkage can also occur under high vacuum conditions), which is attributed to the measured hydrodynamic diameter.[11] All five colored graphs show only one distinct peak, correlating to a monodisperse and uniform size distribution, which is a critical criterion for the development of ordered nanostructures (Figure 3.1 f).

The observed peak maxima in DLS were attributed to 324, 223, 143, 91 nm and 46 nm, respectively, and are in very good agreement with particle sizes estimated by SEM (a-e).

In general the PMMA particles can be used as hard templates for macroporous (> 50 nm) inorganic and organic materials, and different synthetic approaches are suitable for template deposition and application of the scaffold precursor.[14,15]

3.4. Conclusions

This chapter describes a suitable emulsion polymerization technique that allows high control of both the final size of PMMA particles and a narrow size distribution. For this purpose we used known procedures and modified them to achieve very stable colloidal solutions of particles in the range of about 320 to 40 nm. These solutions provide the essential templates for further colloidal crystal templating approaches and the preparation of macroporous materials such as titania and silica. In the following our focus is on different deposition techniques: (i) one step co-deposition of PMMA templates with different titania precursors,

(ii) and a two step replication requiring prior assembly of PMMA spheres, which are further infiltrated with hydrolyzed alkoxyprecursors, such as tetraethyl orthotitanate and –silicate, respectively. The latter scaffolds are the prerequisite for the development of more complex hierarchical structures. This technique is useful to create new templated titania and carbon nanostructures having a distinct porosity and spherical or fibrous morphology. These morphologies are beneficial for diverse applications in the fields of energy generation, energy storage and for controlled drug delivery and release.

We anticipate that there is nearly no limit regarding the scaffold precursor interacting with the spherical templates, which generally opens the way to new macroporous materials, as long as the used solvent is compatible with PMMA and the molecular precursor or building block fits into the confined space between the spheres. Furthermore, to avoid destruction of the templated structure, the solidified precursor should not exhibit large volume changes during the processing.

In this context it is worth noting that the developed PMMA particles are part of various recent research projects of Dr. Yujing Liu (Dissertation, 2012), Erika Mühlbauer (Master thesis, LMU, 2012), Enrico Greul (Master thesis, 2013), Ilina Kondofersky, Dr. Markus Waibel and Prof. Dr. Dina Fattakhova-Rohlfing, all at the LMU, respectively. These studies contain unpublished results and are not further presented in this thesis.

Furthermore, several macroporous structures developed with these templates turned out to be interesting model systems with complex percolation pathways, and the charge transport in the resulting TiO_2 films was investigated by our collaboration partners Hynek Němec et al. (Academy of Sciences of the Czech Republic) by time-resolved terahertz spectroscopy.[17]

3.5. Chapter References

(1)   Lekkerkerker, H. N. W.; Tuinier, R.; Springer Netherlands: 2011.

(2)   Bettencourt, A.; Almeida, A. J. *Journal of Microencapsul.* **2012**, *29*, 353.

(3)   Matijevic, E., Ed.; Springer-Verlag New York: 2008.

(4)   Partch, R.; Stamper, A.; Ford, E.; Bawab, A. A.; Odeh, F. In *Fine Particles in Medicine and Pharmacy*; Matijević, E., Ed.; Springer US: 2012, p 309.

(5)   Peng, B.; van der Wee, E.; Imhof, A.; van Blaaderen, A. *Langmuir* **2012**, *28*, 6776.

(6)   Hawkett, B. S.; Napper, D. H.; Gilbert, R. G. *J. Chem. Soc., Faraday Trans. 1* **1975**, *71*, 2288.

(7)   Hawkett, B. S.; Napper, D. H.; Gilbert, R. G. *J. Chem. Soc., Faraday Trans. 1* **1981**, *77*, 2395.

(8)   Tait, P. J. T.; Rooney, J. M.; Young, R. N.; Bevington, J. C.; Blackley, D. C.; Tidswell, B. M. In *Macromolecular Chemistry: Volume 3*; Jenkins, A. D., Kennedy, J. F., Eds.; The Royal Society of Chemistry: 1984; Vol. 3, p 3.

(9)   Zou, D.; Ma, S.; Guan, R.; Park, M.; Sun, L.; Aklonis, J. J.; Salovey, R. *J. Polym. Sci. A Polym. Chem.* **1992**, *30*, 137.

(10)   Wang, T. W.; Sel, O.; Djerdj, I.; Smarsly, B. *Colloid Polym.Sci.* **2006**, *285*, 1.

(11)   Pilcher, S. C.; Ford, W. T. *Macromolecules* **1998**, *31*, 3454.

(12)   O'Donnell, J. M. *Chem. Soc. Rev.* **2012**, *41*, 3061.

(13)   Guo, J. S.; El-Aasser, M. S.; Vanderhoff, J. W. *J. Polym. Sci. A Polym.* **1989**, *27*, 691.

(14)   Holland, B. T.; Blanford, C. F.; Stein, A. *Science* **1998**, *281*, 538.

(15)   Stein, A.; Li, F.; Denny, N. R. *Chem. Mater.* **2008**, *20*, 649.

(16)   Guldin, S.; Huttner, S.; Tiwana, P.; Orilall, M. C.; Ulgut, B.; Stefik, M.; Docampo, P.;

Kolle, M.; Divitini, G.; Ducati, C.; Redfern, S. A. T.; Snaith, H. J.; Wiesner, U.; Eder,

D.; Steiner, U. *Energy Environ. Sci.* **2011**, *4*, 225.

(17)   H. Němec, V. Z., I. Rychetský, D. Fattakhova-Rohlfing, B. Mandlmeier, T. Bein, Z.

Mics, and P. Kužel *IEEE Trans. Terahertz Sci. Technol.* **2013**, *invited paper*.

4. Tuning of Crystallinity Parameters in Macroporous Titania Films

The following chapter is based on collaborative research with Norma K. Minar and Johann M. Feckl (both LMU), who prepared well-defined titania nanoparticles of 6 and 4 nm, respectively. The work was also supported by Prof. Dr. Dina Fattakhova-Rohlfing.

4.1. Introduction

Macroporous crystalline titania offers specific morphological benefits[1-4]. The open architecture exhibits a high accessibility and in principle enables efficient mass transport into the structure via pores (> 50 nm) that are also interconnected by smaller windows. These pore dimensions enable an interaction of the high refractive index titania scaffolds with light, which can increase the light harvesting efficiency for photoprocesses by scattering, and in the case of ordered arrays photonic effects can be exploit. Macroporous titania is a very attractive system for chemical sensing of molecules[5,6], insertion of lithium ions,[7,8] photocatalytic decomposition of organic compounds[9-13] and photoanodes in solar cell devices.[14-23] The preparation of macroporous titania usually follows a time-consuming two step replication approach, which starts with the deposition of polymer spheres[24,25] and the subsequent infiltration of molecular titania precursors or titania nanoparticles into the interstitial voids of the preformed colloidal crystal template[26-28]. The infiltration of anatase nanoparticles can be improved by adjusting the polymer bead size, titania particle size and concentration, by tuning parameters such as temperature and number of infiltration steps, or by surface modifications

of the titania surface.[20,22,23] Alternatively, a one-step co-deposition of the template and precursor has been applied using spray deposition[29,30], doctor-blading[31], vertical deposition[32,33] and sedimentation[34] methods. These techniques can shorten the fabrication time of macroporous titania films, accompanied by enhanced control over the final wall thickness depending on the template/precursor ratio.

In a final step, polymer templates are usually removed by thermal decomposition, which is accompanied by further densification and crystallisation of the precursors within walls of the 3D open macroporous materials. Precursors for the titania scaffold applied in the above techniques can either be sol-gel processed or nanocrystalline building blocks, and they are similar to the ones used for the preparation of various titania materials in the form of mesoporous films[35-45] and mesoporous particles,[46-48] powders[49] and nanocrystals.[50] The choice of precursor influences the crystallinity parameters such as phase composition, crystal shape, crystal size and interconnectivity of the crystals. In addition, mesoscopic features of the macroporous films such as porosity, pore size, pore connectivity and the surface area, as well as the macroscopic properties such as thickness and homogeneity of films or their optical behavior are expected to have a great impact on the performance of such films in different devices.

The crystallization behavior not only strongly depends on the calcination temperature but it can also be influenced by a post-synthetic hydrothermal treatment of soft-templated metal oxide films. With this so-called delayed humidity treatment (DHT) highly ordered mesostructures can be obtained that are more stable against shrinkage and collapse of the structure.[51]

Here we present a comparative study of macroporous titania films based on the co-deposition of monodisperse PMMA spheres (~ 320 nm) with a variety of titania precursors using spin-

coating and drop-casting techniques. We show that the crystalline domain size within the pore walls can be tuned by a selection of different titania precursors – molecular or particulate – and the variation of the calcination temperature (400 and 500 °C). These parameters influence the crystal growth and the macroscopic properties of the films, such as homogeneity and texture. The utilized precursors exhibit different initial crystallinity, from amorphous sol-gel[52] to crystalline particles, having sizes of 4,[44] 6,[53] and 18[54] nm, respectively. Additionally, a combination of sol-gel precursors with nanoparticles in a so-called brick and mortar approach was investigated. Depending on the described parameters we are able to tune the crystal domain sizes in the macropore walls from about 9 to 26 nm.

In addition to the choice of the precursor, we have investigated the influence of post-synthesis treatment of the assembled films on the crystallization behavior and final properties. As such, thermal treatment at different temperatures and a hydrothermal treatment of the PMMA-titania composites before calcination at 450 °C were explored. Additionally, this treatment shows a profound beneficial influence on the heating-induced shrinkage of the structures, thus stabilizing the desired porous scaffolds.

4.2. Experimental Section

Chemicals

All chemicals are commercially available and were used without further purification. Methyl methacrylate (99%, MMA), sodium dodecyl sulfate (SDS), tetraethyl orthotitanate, titanium iso-propoxide, titanium tetrachloride, hydrochloric acid (conc.), nitric acid (conc.), potassium chloride and the organic solvents were obtained from Sigma-Aldrich or from an in-house supplier. Pure water was obtained from a Millipore Q system.

Synthesis of PMMA nanoparticles

The PMMA spheres were synthesized via an emulsion polymerization route,[55] yielding an aqueous colloidal solution. Clean water (98.0 mL, milipore Q) was degassed in a three-necked flask (250 mL) for 1 h by a stream of nitrogen, before sodium dodecylsulfate (5.6 mg, 0.017 mmol, SDS) and methylmethacrylate (35.5 g, 0.35 mmol, MMA) were added. The monomer mixture was stirred magnetically (Heidolph MR 3001K) for 1 h at 90 °C (external oil bath) in nitrogen atmosphere to obtain a homogenous emulsion. A solution of potassium peroxodisulfate (56 mg, 0.2 mmol, $K_2S_2O_8$) in water (2 mL) was injected to initiate the polymerization. The solution turned white within 5 minutes, indicating the formation of particles. The reaction was continued for 2 h at 90 °C, before the flask was exposed to air and cooled with an ice bath. The colloidal solution was stirred over night, filtered over glass wool and washed three times by centrifugation and redispersion in water.

Since an aqueous medium is unfavorable for a controlled hydrolysis of titanium alkoxides[56] the PMMA was dried in air at room temperture and redispersed in ethanol to prepare mixtures with various titania precursors. The size of the PMMA spheres was estimated at around 320 nm from field emission (FE) SEM images, which is in good agreement with the average size of 324 nm measured by dynamic light-scattering (DLS) (Figure S1 a, b).

Synthesis of macroporous titania

All following mixtures contained 325 mg of ground PMMA powder, and the amount of titania precursors was adjusted to transform to 100 mg anatase after calcination.

Sol-gel

The titania sol-gel solution corresponds to the one we used for dip-coating infiltration of PMMA colloidal crystal template films.[52] 325 mg PMMA powder was well dispersed in 4 mL ethanol by the use of an ultrasonic bath for several hours at room temperature. Tetraethyl orthotitanate (0.36 g, 1.25 mmol, TEOT) was added and the solution was stirred for another hour at room temperature. To this mixture 230 μL (37%, 2.8 mmol) of HCl was added. The solution is ready for use after additional stirring for 10 minutes. We note that a direct addition of the prehdrolyzed TEOT solution to the PMMA solution led to a strong increase of viscosity, which would be unfavorable for further use.

NP-18

Crystalline anatase nanoparticles were prepared according to literature reports.[57] To 9.47 g titanium iso-propoxide (33.0 mmol) was added drop wise within 15 minutes 1.90 ml acetic acid (33.0 mmol) under stirring at room temperature. To the faint-yellow solution 48.5 ml water was added to form a white precipitate. The mixture was stirred for 1 h before 4 ml of nitric acid (conc.) was added. An additional refluxing at 80 °C for 75 minutes was applied. Prior to the hydrothermal treatment in an autoclave (100 mL, PTFE) at 250 °C for 12 hours, 0.44 ml of water was added. After reaction, 0.40 ml of 65 % nitric acid was added to the precipitate, which was treated with ultrasound for 60 minutes. The resulting solution was concentrated by rotary evaporation and the titania nanoparticles were washed three times with absolute EtOH by centrifugation and redispersion (19000 rpm; 20 minutes).

For film preparation (NP-18), 100 mg of the titania NPs were redispersed in 4 mL absolute ethanol by ultrasonic treatment, than 325 mg fine PMMA particle powder added, and the solution stirred over night.

NP-6

Titania nanoparticles (NP-6) were synthesized by a route described by Niederberger et al..[42,53] Here, 1.5 mL titanium tetrachloride (13.7 mmol) was cautiously dropped into 10 mL toluene under stirring. Then 30 mL benzyl alcohol (290.8 mmol) was added to the solution, which was further heated in a plastic autoclave at 60 °C for 20 h. After the reaction, the nanoparticle solution was centrifuged (50000 rcf ; 30 minutes) and the titania content within the pellet was estimated by gravimetry. Finally, 100 mg of titania nanoparticles were redispersed in 4 mL ethanol and used according to the film preparation in NP-18.

NP-4

The preparation is similar to NP-6, but in contrast 30 mL *tert*-butyl alcohol (320 mmol)[44] was used instead of benzyl alcohol.

A twofold microwave heating procedure (Synthos 3000, Anton Paar) was performed in 100 mL autoclaves. One step involved heating up to 80 °C within one minute, followed by cooling to and dwelling at 50 °C for another 20 minutes. The resulting titania nanoparticle solution was washed by a successive particle flocculation using a mixture of n-heptane/ *tert*-butyl alcohol (2 : 1, vol.), and centrifugation (50000 rcf; 15 minutes). The final particles were redispersed in absolute ethanol, and the titania content was estimated by gravimetry. Typically, 100 mg of titania nanoparticles (NP-4) were dispersed in 1 mL ethanol and added to 3 mL of an ethanolic PMMA particle (325 mg) dispersion. Prior to use, the final solution was stirred over night.

NP18 & Sol-gel

This titania mixture was prepared by mixing an ethanolic solution of 70 mg nanoparticles (NP18) and 325 mg PMMA particles over night before 108 mg of TEOT (0.37 mmol) was

added. The solution was stirred for 1 h at room temperature and finally 69 μL HCl (37%, 0.8 mmol) was added to obtain the final mixture with a total amount of 4 mL ethanol.

Film preparation

Typically all PMMA/titania precursor solutions were spin coated (2000 rpm) or drop-casted on silicon wafer (15 μL on 2.25 cm^2). After drying at room temperature under vibration-free conditions (ca. 1 d), films were calcined in air up to 400, 450 and 500 °C, respectively. The heating ramp was 1 °C/ min and dwell time defined to 1 h.

Humidity treatment

PMMA/ NP-6 composite films were also treated according to a procedure reported elsewhere.[51] First they were dried in air at room temperature, than stored in a desiccator and exposed to water vapor at 100 °C for 1 d or 7 d, by placing the desiccator in an oven at this temperature. The bottom of the desiccator was filled with a saturated aqueous KCl solution. Afterwards a calcination at 450 °C in air was applied. The heating ramp was 1 °C/ min and dwell time was defined to 1 h.

4.3. Results and Discussion

The aim of this study is the development of a one-pot fabrication of crystalline macroporous titania films using a direct co-deposition of colloidal titania precursors and poly (methylmethacrylate) (PMMA) beads. We are especially interested in synthetic means to control the crystallinity and morphology of the films. Although many of the applications based on semiconducting titania such as sensors[5,6], photocatalysts[9-13] and solar cells[14-23] profit from high crystallinity of the titania morphology, different applications have specific requirements regarding the crystallinity parameters such as phase composition, crystal shape and facetting, crystal size and interconnectivity of the crystals. In addition, mesoscopic features of the macroporous films such as porosity, pore size, pore connectivity and the surface area, as well as the macroscopic properties such as overall thickness and homogeneity of films or their optical behavior have a great impact on the performance of such films in different devices.

In order to address these issues we have performed, to the best of our knowledge and for the first time, a direct comparison of several titania precursors in the film assembly to study their influence on the properties of the macroporous films, and thus provide a direct comparison of the crystallinity and the morphology of the resulting films. We have used several precursors offering different crystallinity and crystal sizes. One of the most common precursors for the assembly of titania morphologies is amorphous colloidal sol-gel titania (assigned **SG**).[13,14,35,39] We have used this precursor as a known benchmark for the film fabrication. The SG precursor for our study was prepared by adding tetraethyl orthotitanate (TEOT) and some amount of HCl to a dispersion of PMMA beads with the size of ca. 320 nm (Figure S1, Supplementary information) in ethanol. Additionally, we have examined colloidal dispersions of already

crystalline titania nanoparticles with different particle sizes. The smallest particles (assigned **NP-4**) were prepared by a microwave-assisted synthesis in *tert*-butanol.[44] The particles prepared in this way have a size of about 3–4 nm with a narrow size distribution, they are largely crystalline corresponding to the anatase phase with an amorphous shell, and are well dispersible in ethanol. Slightly larger particles of ca. 5–6 nm in size (assigned **NP-6**) were obtained by a solvothermal synthesis in benzyl alcohol.[42,53] These particles are poorly dispersible in ethanol resulting in turbid dispersions of agglomerated nanoparticles. The largest fully crystalline anatase particles (assigned **NP-18**) of ca. 18 nm in size were prepared by hydrothermal treatment of hydrolyzed tetraisopropyl orthotitanate.[57,58] All particles were charcterized after synthesis by SAED and TEM and are shown in Figure S2 a, b (NP-6), c, d (NP-4) and in Figure S4 b (NP-18), respectively.

All the macroporous titania films described in this work were made by a similar procedure. Typically, ethanolic dispersions of titania precursors (25 mg/mL) were mixed with an ethanolic dispersion of the PMMA beads in a PMMA / TiO_2 weight ratio of 3.25 to 1. The resulting white colloidal dispersions were spin coated or drop casted on substrates. The composite films were heated in air at 400 °C or 500 °C using the same heating procedure. The similarity of the heat treatment procedure for different films makes possible a direct evaluation of the role of different precursors in the crystallization mechanism and the final crystallinity of the films obtained from different precursors.

Coating of all the described precursor solutions on a substrate leads to the formation of thin semitransparent, rough and slightly scattering films after calcination. The average thickness of the films is about 1 μm. The thickest films are obtained with the amorphous **SG** precursor, while the use of larger crystalline **NP-18** precursor results in the thinnest films. Although the

films obtained from different precursors look similar at the first glance, they show a striking difference in their mechanical stability and the adhesion to the substrate depending on the nature of the precursor. The **SG** precursor provides homogeneous coatings with a good adhesion to the substrate. The coatings become more fragile with the increasing crystal size of the crystalline precursor. The films assembled from **NP-4** and **NP-6** precursors still have rather good mechanical stability and substrate coverage, but the films obtained from **NP-18** nanoparticles are very fragile and do not cover the substrate completely. Thicker **NP-18** films strongly contract after drying into single small flakes lying loose on the substrate (Figure S6 b, Supplementary information). However, the wetting and adhesion properties of the crystalline precursor dispersions are drastically improved when some amount of sol-gel titania is added to the nanocrystal dispersion. This so called 'Brick and Mortar' approach, developed by us earlier for block-copolymer-templated mesoporous titania assembled from nanoparticles, was shown to be a very promising method to obtain fully crystalline porous layers at relatively low temperatures.[42] This approach also seems to be applicable to larger pore dimensions and to other types of templates. Thus, mixing of the **NP-18** particle dispersion with some amount of **SG** precursor (in the ratio 30 : 70 wt % of SG : NP-18 drastically changes the properties of the resulting films (assigned as **NP-18-SG**). This ratio is based on the assumption that the sol-precursor completely transforms after calcination into antase and that it is present within the architecture at a fraction of 30 wt% (Ti). The films completely cover the substrate and they have a much better adhesion and mechanical stability (Fig. S6 a).

SEM images (Fig. 1) demonstrate that the films assembled from all the precursors examined here have an open macroporous morphology with a uniform pore size but rather low periodicity of the pore ordering. The specific parameters of porosity such as pore size, pore

connectivity, wall thickness and, importantly, the change in the pore size (shrinkage) after calcination depend strongly on the origin of the used precursors. The sol-gel sample **SG** (Fig. 4.1a, b) shows the highest degree of pore ordering. This scaffold shows individual macropores with diameters of about 235 nm that are interconnected by ca. $50 - 120$ nm windows. The thickness of the titania walls is about $20 - 40$ nm. The morphology obtained by this one-pot co-precipitation is in fact very similar to that obtained by a two-step infiltration approach, but its fabrication is more simple and less time-demanding.[52]

When crystalline nanoparticulate building blocks are used instead of the amorphous molecular precursor, the size of the single crystals matters. Basically, the bigger the size of the used particles, the less perfect is the replication of the curvature of the original PMMA beads. The films assembled from small **NP-4** and **NP-6** precursor crystals show less periodic pore ordering compared to the **SG** sample (Fig. 4.1a and 4.1f), but much better regularity compared to films obtained from the large crystalline **NP-18** precursor. Surprisingly, the films assembled from the larger **NP-6** particles show more regular pore packing compared to the smaller **NP-4** precursor. We tentatively attribute this effect to different hydrophilicity/ hydrophobicity of the particles obtained by different reactions, and consequently different interaction with the PMMA beads. The pores of films assembled from the **NP-4** precursor are rather rough and irregular. Sample **SG** and **NP-4** have a similar pore size of around 240 nm, which corresponds to shrinkage with respect to the original template size of 320 nm by about 25 %. The **NP-6** films show rather regular pore packing comparable to that of the sol-gel sample, but a larger pore diameter of 270 to 290 nm and a significantly reduced shrinkage of about 10-16 %. In contrast, the **NP-18** sample assembled from large crystalline nanoparticles is very rough, completely disordered and is composed of non-uniform pores with a broad variety in shape and size (Fig. 1c, d) separated by about 100 nm thick walls. Due to the large

size and high crystallinity of the 18 nm anatase precursor particles the shrinkage of the pore size in **NP-18** samples is furthermore reduced to approximately 3 to 10 %.
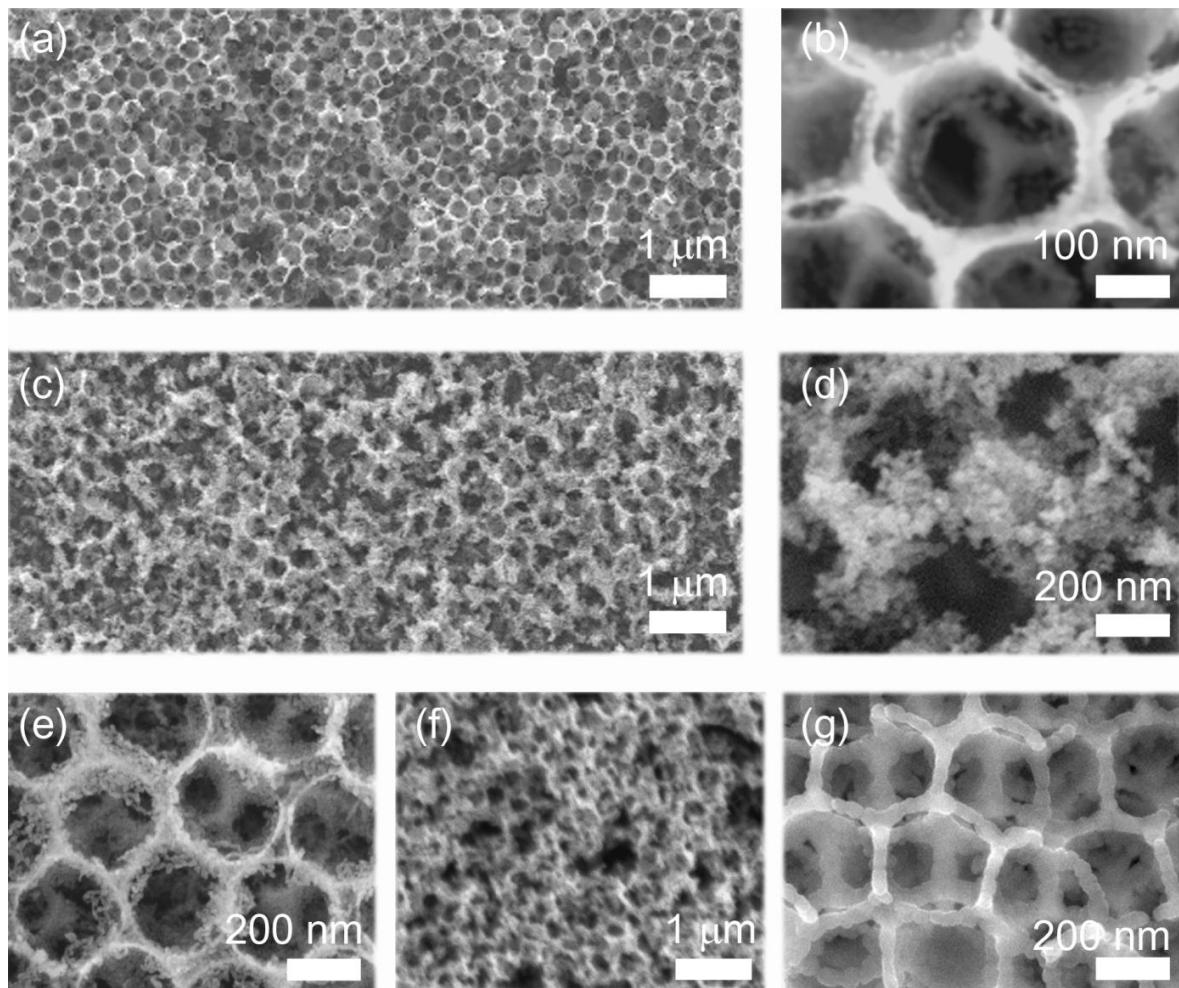
Figure 4.1: SEM top view images of macroporous titania films prepared by spin-coating and calcined at 500 °C: (a, b) sol-gel derived TiO_2, (c, d) NP-18, (e) NP-6, (f) NP-4 and (g) 'brick and mortar' combination of NP-18-SG.

As mentioned before, the addition of an amorphous sol-gel 'mortar' to the **NP-18** precursor changes the properties of the films completely. The morphology of the **NP-18-SG** resembles much more that of the **SG** films with nice uniform pores with a smooth surface and dense interconnecting walls (Figure 4.1g). In contrast to the **NP-18** sample, the pores are even

partially ordered with a size ranging from 250 to 270 nm and wall thicknesses of $25 - 45$ nm. We view this strategy as a successful extension of our previous 'brick and mortar' approach to a large-scale hard templating method and much larger TiO_2 precursor nanoparticles.

The second important issue we investigate beside morphology is the crystallinity of the films and the texture of the titania walls in the macroporous structure as controlled by the type of precursor. The TEM images in Figure 4.2 illustrate the composition of the scaffold walls and the interconnectivity of the resulting anatase crystals with respect to the different precursors. Complementary to the TEM studies, we further investigated the TiO_2 crystallization process by XRD measurements, focusing on the 101 anatase reflection and extracting the mean crystallite size from the signal broadening (Figure 4.3). No XRD data at 60 °C are shown for the samples **SG** (Figure 4.3 b) and **NP-18-SG** (Figure 4.3 d), because drying causes no obvious increase in crystallinity of the initial amorphous sol-gel derived sample, and for **NP-18-SG** it should correlate to the crystallite size of the used titania nanoparticles. As shown in Figure S3 e, precursor **NP-18** consists of already uniformly grown crystals after hydrothermal synthesis. The corresponding SAED pattern (Figure S3 a) proves the high crystallinity of the anatase particles. Applied in macroporous films, these NP18 particles were randomly packed in the walls of the scaffolds and exhibit a certain textural porosity (Figure S3 d) after calcination at 400°C. From the corresponding TEM image (Figure S3 f) we can conclude that a higher sintering temperature of 500 °C formed a higher packing density of particles, but no distinct change of particle size was observed. The higher calcination temperature had also no effect on the type of the titania phase present (anatase), which was derived from the similar SEAD pattern (Figure S3 c, e).

We now consider the other extreme of the synthetic methods presented here, that is, starting with amorphous sol-gel precursors. Due to the amorphous nature of the SG precursor the

walls of the macroporous titania **SG** films are dense and compact after calcination (SEM images, Figure 4.1 b, S2 b). TEM investigations proof the polycrystallinity within the walls (Figure S5 a-c), which is in good agreement to reported 10 to 40 nm large anatase crystals observed in other macroporous sol-gel derived TiO_2 structures.[2,18,45,52,59] For the **SG**, **NP-4** and **NP-6** films additional bright spots in the SAED pattern are observed after 500 °C calcination due to the transformation of small randomly oriented particles into larger crystalline anatase domains.

In contrast to the smooth and dense walls of the SG sample (Figure 4.1 a, b), the walls of all nanoparticle samples (**NP-4**, **NP-6**, **NP-18**) show a distinct particulate texture due to the used crystalline solid building blocks. This way the surface area compared to the dense **SG** scaffold is increased, which can be advantageous for applications requiring a high surface area.
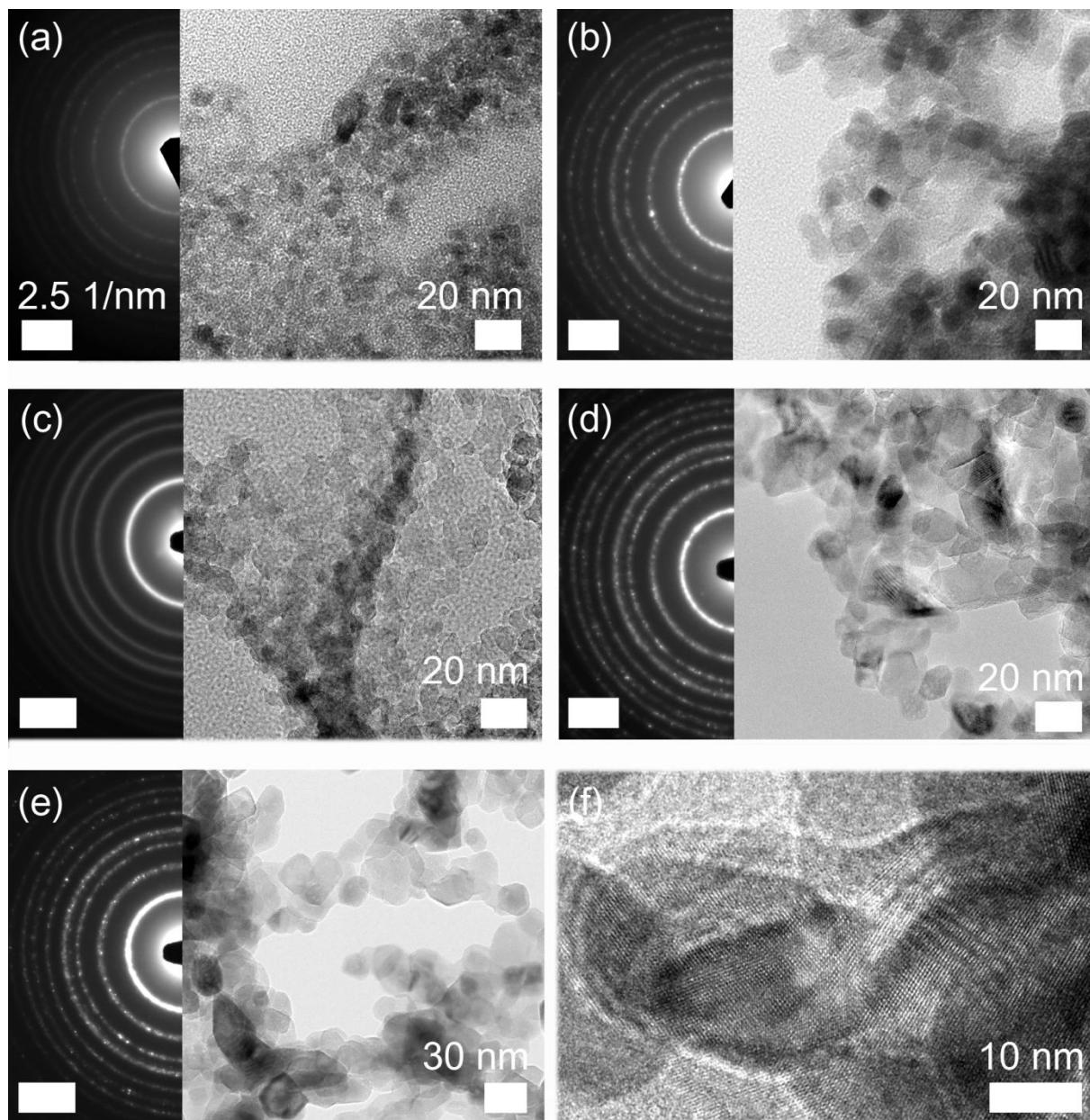
Figure 4.2: Selected area electron diffraction patterns (SAED) and TEM images of powders scratched off from films after calcination. (a) NP-6 400 °C, (b) NP-6 500 °C, (c) NP-4 400 °C, (d) NP-4 500 °C, (e, f) NP-18-SG 500 °C at different magnifications.

The most significant change of the crystal size with treatment temperature due to grain growth was observed for NP-4. For the initially ca. 3–4 nm particles an anisotropic growth was estimated to 10 ± 3 nm x 8 ± 2 nm and 21 ± 10 nm x 15 ± 4 nm at 400 °C and 500 °C,

respectively (Figure 4.2 c, d). A similar trend can be seen for the initially 5–6 nm large **NP-6** building-blocks.[42,53] After calcination, the resulting crystals exhibit an average length of 13 ± 2 nm and width of 10 ± 3 nm after 400 °C, and 16 ± 4 nm and 14 ± 2 nm after heating at 500 °C, respectively (Figure 4.2 c, d). Thus for both samples the linear crystallite size increased by a factor of 2 for 400 °C and even a factor of 3 upon heating at 500 °C. The increase in the crystal size after calcination can be explained by a solid-state diffusion (Ostwald ripening) of the **NP-4** and **NP-6** precursors, which is greatly enhanced for the very small nanoparticles. In comparison, **NP-18** exhibits nearly no grain growth after calcination, which is attributed to the bigger size and smaller surface area of the crystals at the beginning[57,58] (Figure 4.3 e, f, S4 a, b). The TEM images of the **NP-18** films after calcination at 400 and 500 °C demonstrate that the walls are composed of very loosely packed crystals whose size practically does not change compared to the precursor particles (Figure S4 d, f).

As discussed above, the morphology can be dramatically improved by the addition of some amount of titania sol-gel precursor (compare Figure 4.1 d, g). This amorphous 'mortar' containing some HCl apparently has the effect that the individual **NP-18** building blocks are more homogeneously distributed in the casting solution of sample **NP-18-SG**.[64] As a result it was possible to achieve a high titania infiltration into the PMMA interstitials and to reduce textural porosity. The TEM image in Figure 4.2 e, f displays macroporous titania with highly dense walls where crystalline domains similar to the precursor NP-18 particles can be observed. TEM, SAED and XRD data show fully crystalline titania without any indication of the amorphous phase. Therefore we can conclude that the already crystalline **NP-18** particles assist in the crystallization of the initially amorphous molecular precursor by acting as crystalline seeds, similar to the effect observed by us earlier for mesoporous titania.[42,43,52]

Both sol-gel precursor mixtures - **SG** (Figure 4.3 b) and especially **NP-18-SG** (d) - which both contained hydrolyzed TEOT feature the largest crystalline domains at 500 °C (see XRD line shapes in Figure 4.3 f). The largest mean crystallite sizes for both calcination temperatures and compared to all studied precursors could be observed for the **NP-18-SG** sample. This result clearly demonstrates the incorporation and crystallization of sol-gel derived titania around the already crystalline large hydrothermally processed anatase particles (NP-18, Fig. S3; NP-18-SG, Fig. 4.2 f).

To compare the crystallization behavior with respect to morphology, the crystallinity of some of the above precursors was also studied in mesoporous systems.[45] In the course of this study a linear dependence of grain size with calcination temperature was observed for a TEOT based precursor (similar to **SG**) between 400 – 700 °C, exhibiting grains of 12 nm (400 °C), 14 nm (500 °C) and 23 nm (700 °C), respectively.[45] Comparing with our work, the **NP-4** building blocks show sizes of 6, 8 and 13 nm after calcination at 300, 500 and 600 °C, respectively.[44] This can be attributed to different heating protocols, resulting in different nucleation and growth rates. Furthermore, the hard templates used here (PMMA beads, ~320 nm) provide a larger confined space than the micelles of block-copolymers templates[45], which offers both a larger local reservoir for growth species and an increased space for crystal growth.
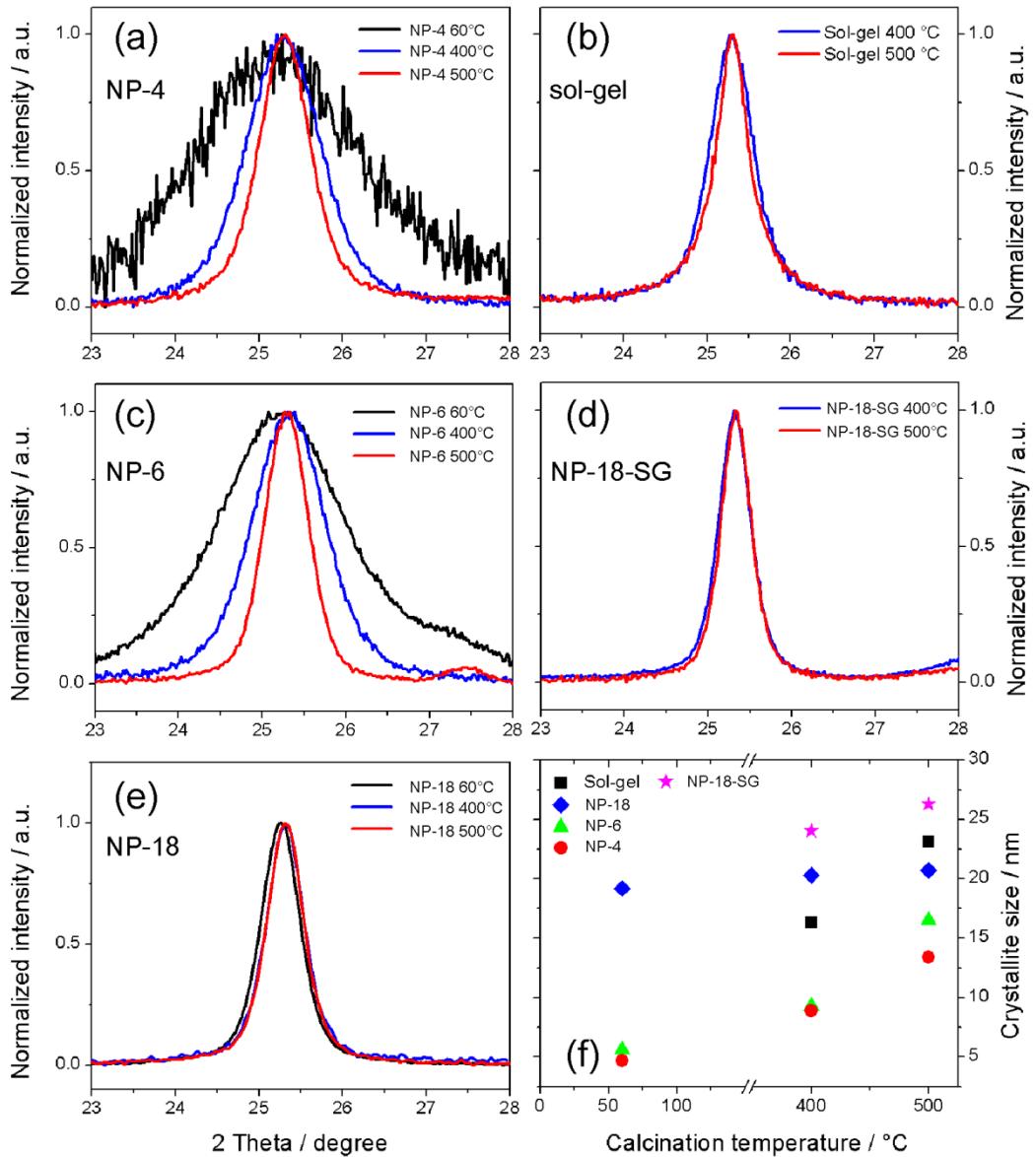
Figure 4.3: XRD study showing individual anatase (101) reflections of macroporous titania samples obtained after different treatments (after drying at 60 °C for 1 h and calcination). The normalized reflections of macroporous titania samples obtained with nanocrystalline building blocks NP-4, NP-6 and NP-18 are shown in (a), (c) and (e). The samples containing a molecular and initially amorphous precursor, sol-gel (b) and NP-18-SG (d), were only characterized for 400 and 500 °C. (f) Graphical summary and development of grain growth with temperature (from line broadening; Scherrer equation). (e) additional 110 reflection indicates some rutile present (27.5 °2θ).

The properties of the different macroporous samples are summarized in Table 4.1.

Table 4.1. Crystallite domain size from macroporous titania treated at different temperatures.

Sample	size* (nm) after heat treatment (°C)			Comments		
	60	400	500	technique	morphology	Shrinkage⊥
Sol-gel	n.a.	16.3	23.1	sc	ordered**	~ 26 %
NP-18	19.2	20.3	20.7	sc, dc	random	~ 3 -10 %
NP-18-SG		24.0	26.3	sc, dc	ordered**	~ 16 - 22 %
NP-6	5.6	9.3	16.5	sc	less ordered	~ 10 - 16 %
NP-4	4.7	8.9	13.4	sc	ordered**	~ 25 %

* Estimated by XRD using Scherrer equation.

** Locally ordered in domains, but no photonic effects were observed.

⊥ Difference of macropore diameter in relation to initial PMMA sphere size of ca. 320 nm.

sc: spin-coating; dc: drop-casting

Enhancing crystallization through processing

In addition to the choice of the precursor and the temperature treatment as the means to tune the crystallinity and the morphology of the films, we have investigated an alternative strategy to affect the final crystal size, morphology and macroscopic film quality. For that purpose, an additional post-synthetic delayed humidity treatment (DHT) of the assembled PMMA/titania composites was performed prior to the films' calcination. A similar method is known for sol-gel derived mesoporous titania and tin-oxide films, where it improved the mesostructure formation and induced the crystal growth of the amorphous precursors.[51,52,65,66]

Figure 4.4 shows TEM images of three identically prepared macroporous titania films with the **NP-6** precursor but treated differently before calcination in air at 450 °C (Figure 4.4 a – c). The first sample **NP-6** was calcined directly after film formation (a), while the two other samples were stored for 1 day (b) or 7 days (c) within a desiccator at 100 °C at around 90% relative humidity (**NP-6-1d**, **NP-6-7d**). The TEM image in Figure 4.4 a represents a magnified area of a macropore interconnection, which looks similar to the one calcined at 500 °C (Figure 4.2 d). The SAED pattern of **NP-6** (Fig. 4.4. d) reveals the polycrystalline composition, and an anisotropic shape of the particles being 17 ± 7 nm long and 12 ± 4 nm wide can be extracted from the TEM image (Fig. 4.4. a), which is similar to the size and shape obtained after 500 °C (Fig. 4.2 b). For this reason we assume that for the sample **NP-6** no significant further crystal growth takes place above 450 °C.
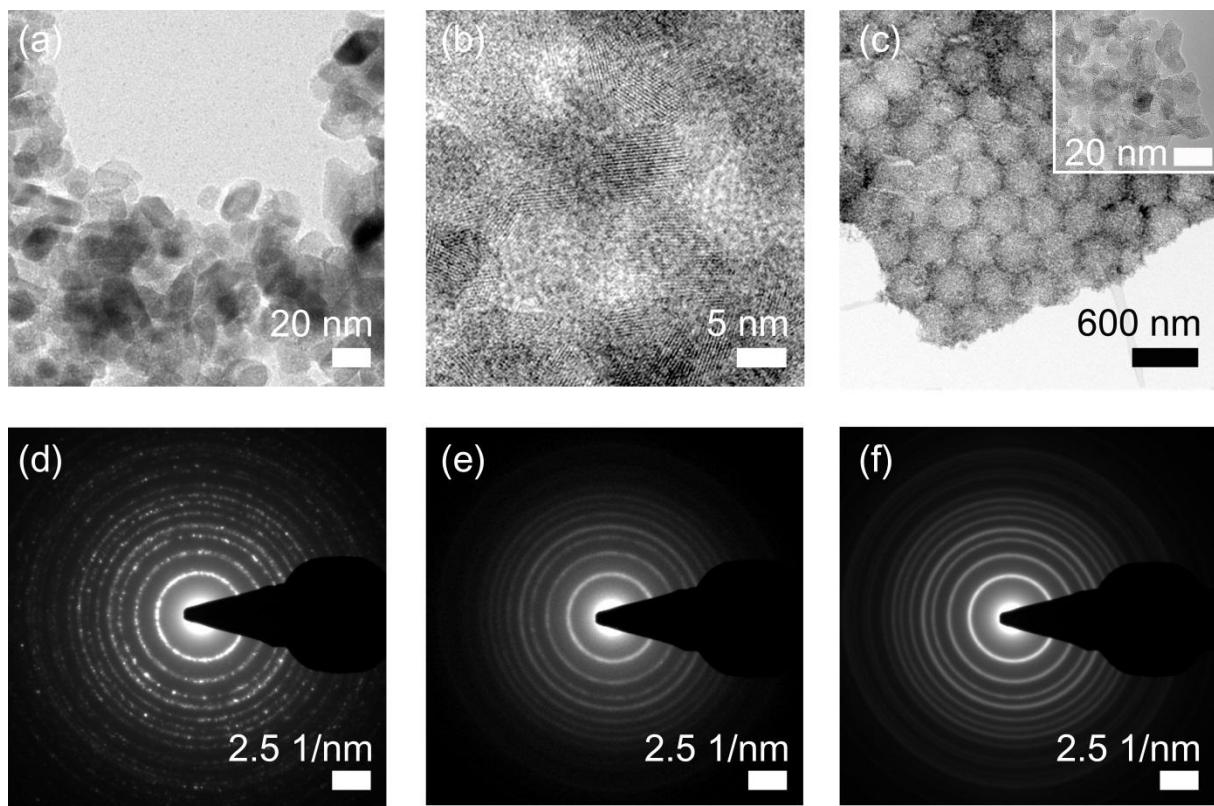
Figure 4.4: HR-TEM images and SAED patterns of macroporous titania using NP-6 as building blocks and a PMMA hard template. Samples were calcined at 450 °C and show the influence of a post-synthetic humidity treatment (DHT). (a, d) particles after calcination (NP-6); (b, e) particles and morphology after calcination, but previously applied humidity (DHT) treatment at 100 °C at 90 % RH for 1 d (b, e; NP-6-1d) and 7 days (c, f; NP-6-7d), respectively.

The applied post-synthetic humidity treatment (DHT) leads to particle sizes (Figure 4.4 b, c inset) of 10 ± 2 nm (length) and 8 ± 1 nm (width) which corresponds more to a calcination at 400 °C (Figure 4.2 c). The related SAED patterns (e, f) are attributed to anatase[60,61] and underline the smaller size by featuring mainly diffuse rings compared to the non-treated, calcined sample, which exhibits additional bright spots (d). Additionally, we observed that a 7 d humidity treatment significantly improves the macrostructure ordering and stabilized the

PMMA/ titania building-block architecture upon temperature induced shrinkage. The TEM overview image in Figure 4.4 c shows a small magnification of a highly ordered part of the scaffold, which was scratched off the substrate. It represents a excellent replication of the inverse structure of the PMMA spheres, which indicates a good adhesion of the nanoparticles to the templates´ surface. Furthermore, the architecture, looking more like an array of titania hollow spheres rather than a macroporous scaffold, is stabilized dramatically regarding heating-induced shrinkage. The corresponding TEM image in Figure 4.4 c shows wall-to-wall distances of around 315 nm, which is nearly the size of the initial PMMA particles (~ 320 nm).

4.4. Conclusions

In this study we have presented the co-deposition of uniform PMMA hard templates with a variety of titania precursors to create macroporous films by spin coating and drop-casting and compared the scaffolds´ crystallinity, originating from sol-gel, three different crystalline titania nanoparticles and a combination of both (brick & mortar method). The precursors exhibit characteristic crystal domain growth upon calcination at 400, 450 and 500 °C. As a result, crystalline domains within the anatase scaffolds can be adjusted up to about 26 nm. The individual grain size and morphological differences were studied in detail by FE-SEM, HR-TEM, SAED and XRD.

Moreover, a post-synthetic humidity treatment strongly influences the further crystal growth of nanoparticle-derived scaffolds upon calcination at 450 °C. As a result the macroporous structure was stabilized against heating-induced shrinkage.

4.5. Supporting Information
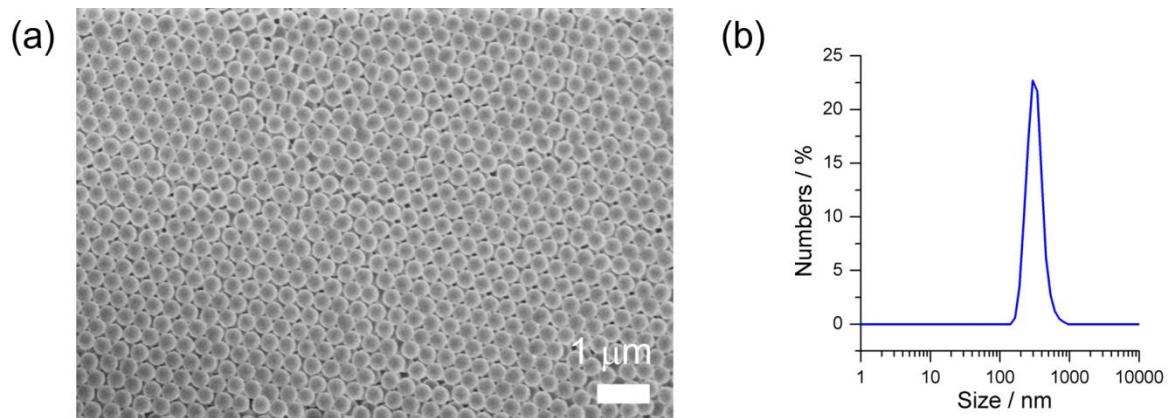
Figure S1: SEM top-view image of washed and loosely packed PMMA particles dried on a flat silicon wafer. Particle diameters are in the range of 320 nm (a, SEM) and a peak maximum of 324 nm was estimated by DLS (b).
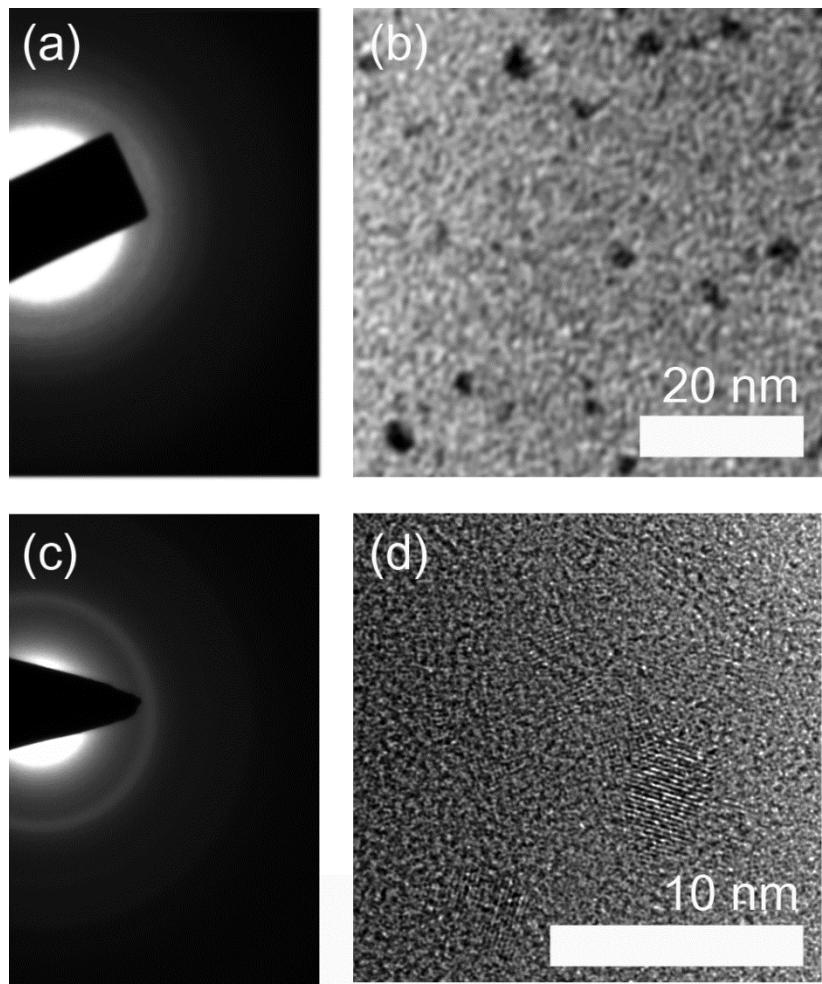
Figure S2: SAED and TEM images of small titania nanoparticles NP-6 (a, b) and NP-4 (c, d)

obtained after synthesis. Particles were transferred from solutions to the TEM grids.
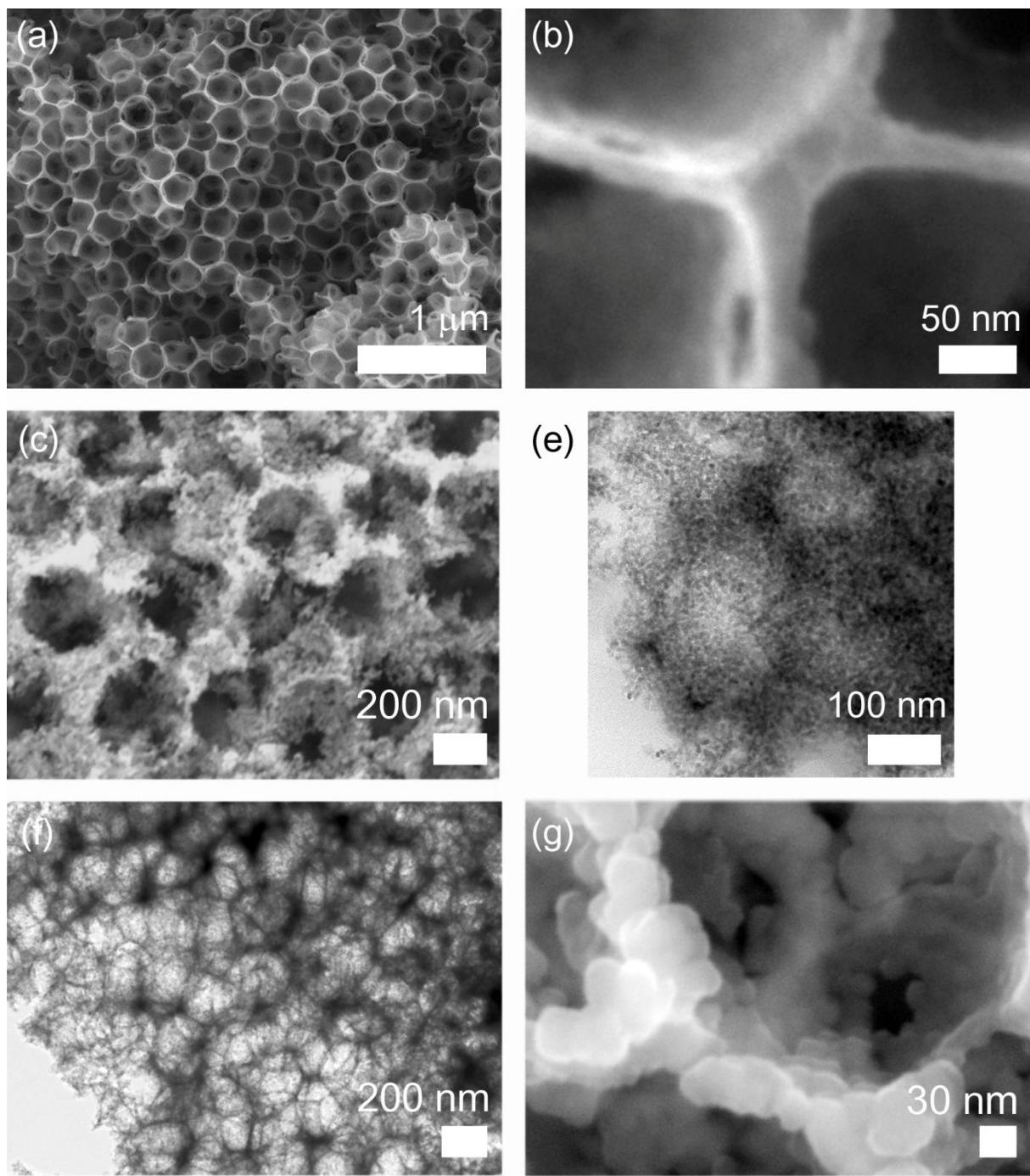
Figure S3: FE-SEM top-view images (a, b, c, g) and TEM images of films removed from substrates (e, f) obtained after calcination at 400 °C. The following precursors were used: sol-gel derived TiO$_2$ (a, b), NP-18 (c), NP-6 (e), NP-4 (f) and brick and mortar combination of NP-18/sol-gel (g).
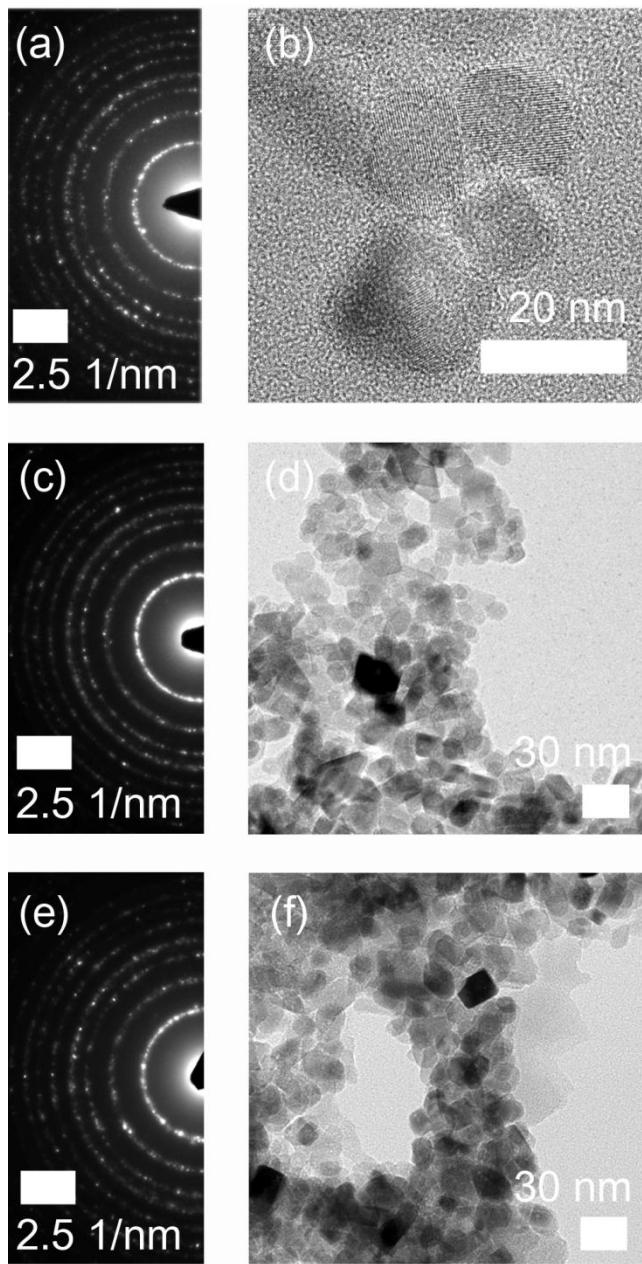
Figure S4: Detailed characterization of NP-18 using SAED (a, c, e) and TEM (b, d, f). Washed and dried anatase particles after synthesis (a, b). Packed particles in the walls of the macroporous architectures after calcination at 400 °C (c, d) and 500 °C (e, f), respectively. For TEM investigations titania was removed from the films by scratching. Titania powders were collected, redispersed in ethanol and transferred to the TEM grids (dropwise).
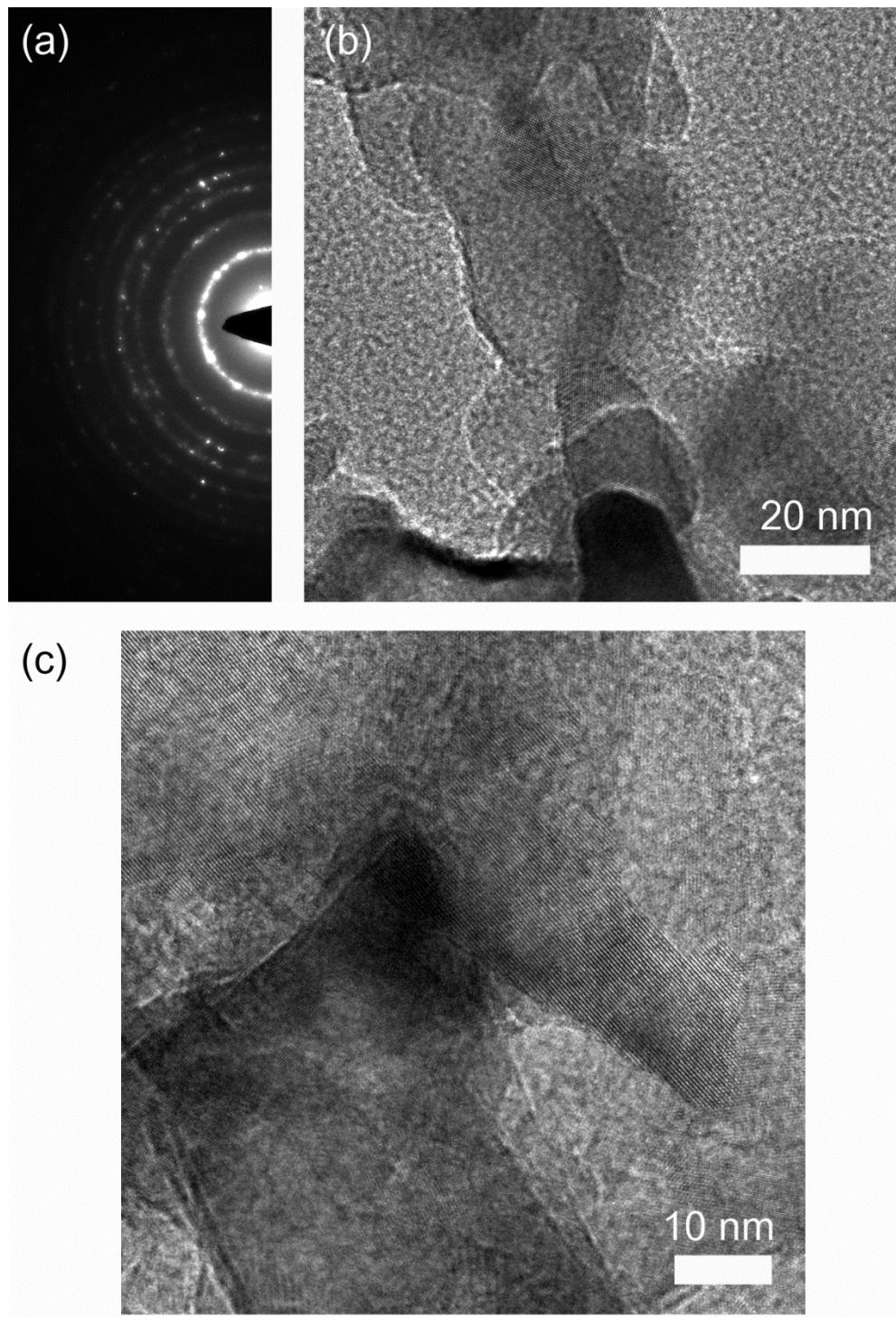
Figure S5: SAED of sol-gel derived macroporous anatase (a) and TEM images of dense polycrystalline walls (b, c). The sample was collected from a film that was calcined at 500 °C in air.
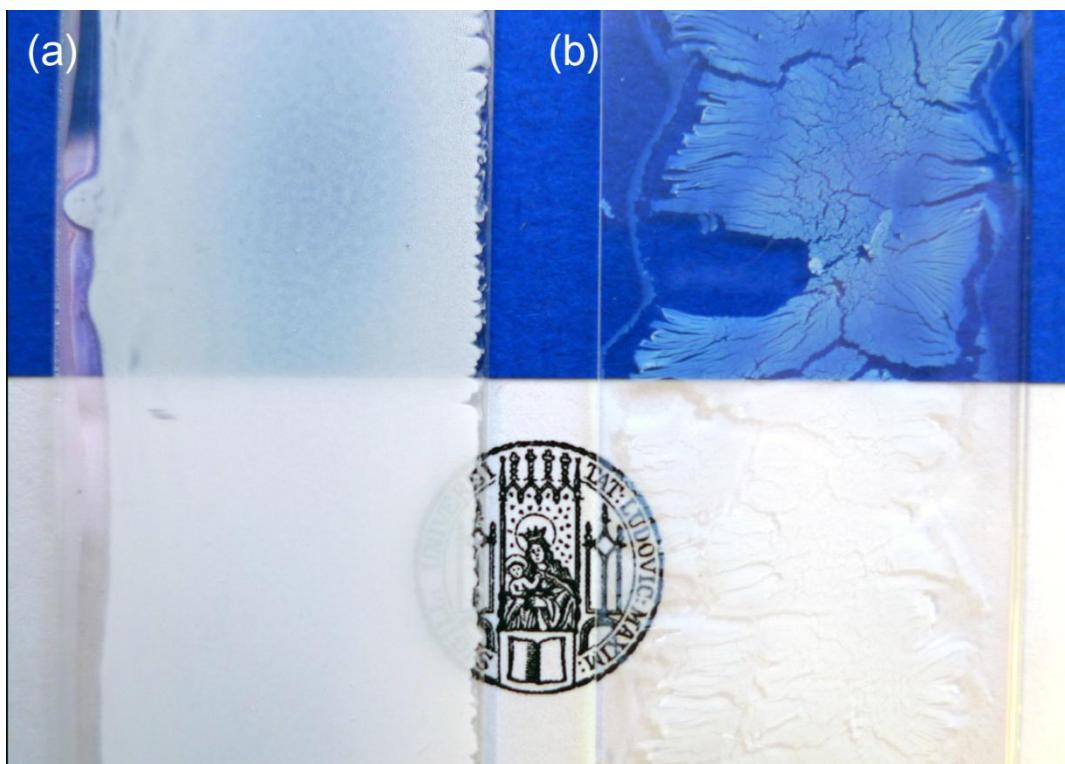
Figure S6: Macroporous layers composed of NP-18/ sol gel (a) and only NP-18 (b) after calcination at 500°C for 1 h in air. For NP-18/ sol-gel a twice higher volume of precursor solution was simply drop-casted on a common microscope slide.

4.6. Chapter References

(1)   Holland, B. T.; Blanford, C. F.; Stein, A. *Science* **1998**, *281*, 538.

(2)   Holland, B. T.; Blanford, C. F.; Do, T.; Stein, A. *Chem. Mater.* **1999**, *11*, 795.

(3)   Turner, M. E.; Trentler, T. J.; Colvin, V. L. *Adv. Mater.* **2001**, *13*, 180.

(4)   Wijnhoven, J. E. G. J.; Bechger, L.; Vos, W. L. *Chem. Mater.* **2001**, *13*, 4486.

(5)   Chandra, D.; Bekki, M.; Nakamura, M.; Sonezaki, S.; Ohji, T.; Kato, K.; Kimura, T. *J. Mater. Chem.* **2011**, *21*, 5738.

(6)   Li, J.; Zhao, X.; Wei, H.; Gu, Z.-Z.; Lu, Z. *Anal. Chim. Acta.* **2008**, *625*, 63.

(7)   Kavan, L.; Zukalova, M. T.; Kalbac, M.; Graetzel, M. *J. Electrochem. Soc.* **2004**, *151*, A1301.

(8)   Kim, H.; Kim, M. G.; Cho, J. *Adv. Energy Mater.* **2012**, *2*, 1425.

(9)   Natoli, A.; Cabeza, A.; De La Torre, Á. G.; Aranda, M. A. G.; Santacruz, I. *J. Am. Ceram. Soc.* **2012**, *95*, 502.

(10)   Wu, M.; Li, Y.; Deng, Z.; Su, B.-L. *ChemSusChem* **2011**, *4*, 1481.

(11)   Chen, H.; Nanayakkara, C. E.; Grassian, V. H. *Chem. Rev.* **2012**, *112*, 5919.

(12)   Lim, M.; Zhou, Y.; Wood, B.; Guo, Y.; Wang, L.; Rudolph, V.; Lu, G. *J. Phys. Chem. C* **2008**, *112*, 19655.

(13)   Chen, J. I. L.; von Freymann, G.; Choi, S. Y.; Kitaev, V.; Ozin, G. A. *Adv. Mater.* **2006**, *18*, 1915.

(14)   Halaoui, L. I.; Abrams, N. M.; Mallouk, T. E. *J. Phys. Chem. B* **2005**, *109*, 6334.

(15)   Mihi, A.; Calvo, M. E.; Anta, J. A.; Miguez, H. *J. Phys. Chem. C* **2008**, *112*, 13.

(16)   Colodrero, S.; Mihi, A.; Anta, J. A.; Ocana, M.; Miguez, H. *J. Phys. Chem. C* **2009**, *113*, 1150.

(17)   Mihi, A.; Zhang, C.; Braun, P. V. *Angew. Chem. Int. Ed.* **2011**, *50*, 5711.

(18)   Nishimura, S.; Abrams, N.; Lewis, B. A.; Halaoui, L. I.; Mallouk, T. E.; Benkstein, K. D.; van de Lagemaat, J.; Frank, A. J. *J. Am. Chem. Soc.* **2003**, *125*, 6306.

(19)   Toyoda, T.; Shen, Q. *J. Phys. Chem. Lett.* **2012**, *3*, 1885.

(20)   Shin, J.-H.; Kang, J.-H.; Jin, W.-M.; Park, J. H.; Cho, Y.-S.; Moon, J. H. *Langmuir* **2010**, *27*, 856.

(21)   Shin, J.-H.; Moon, J. H. *Langmuir* **2011**, *27*, 6311.

(22)   Yip, C.-H.; Chiang, Y.-M.; Wong, C.-C. *J. Phys. Chem. C* **2008**, *112*, 8735.

(23)   Kwak, E. S.; Lee, W.; Park, N. G.; Kim, J.; Lee, H. *Adv. Funct. Mater.* **2009**, *19*, 1093.

(24)   Pilcher, S. C.; Ford, W. T. *Macromolecules* **1998**, *31*, 3454.

(25)   Xia, Y. N.; Gates, B.; Yin, Y. D.; Lu, Y. *Adv. Mater.* **2000**, *12*, 693.

(26)   Galusha, J. W.; Tsung, C.-K.; Stucky, G. D.; Bartl, M. H. *Chem. Mater.* **2008**, *20*, 4925.

(27)   Orilall, M. C.; Abrams, N. M.; Lee, J.; DiSalvo, F. J.; Wiesner, U. *J. Am. Chem. Soc.* **2008**, *130*, 8882.

(28)   Stein, A.; Li, F.; Denny, N. R. *Chem. Mater.* **2008**, *20*, 649.

(29)   Sokolov, S.; Paul, B.; Ortel, E.; Fischer, A.; Kraehnert, R. *Langmuir* **2011**, *27*, 1972.

(30)   Nandiyanto, A. B. D.; Iskandar, F.; Okuyama, K. *Chem. Eng. J.* **2009**, *152*, 293.

(31)   Ruani, G.; Ancora, C.; Corticelli, F.; Dionigi, C.; Rossi, C. *Sol. Energ. Mat. Sol.* **2008**, *92*, 537.

(32)   Hatton, B.; Mishchenko, L.; Davis, S.; Sandhage, K. H.; Aizenberg, J. *Proc. Natl. Acad. Sci. USA* **2010**, *107*, 10354.

(33)   Dionigi, C.; Greco, P.; Ruani, G.; Cavallini, M.; Borgatti, F.; Biscarini, F. *Chem. Mater.* **2008**, *20*, 7130.

(34)   Kim, M.-A.; Seo, Y. G.; Lee, S.-S.; Lee, W.; Lee, H. *J. Nanosci. Nanotechnol.* **2012**, *12*, 3247.

(35)   Alberius, P. C. A.; Frindell, K. L.; Hayward, R. C.; Kramer, E. J.; Stucky, G. D.; Chmelka, B. F. *Chem. Mater.* **2002**, *14*, 3284.

(36)   Crepaldi, E. L.; Soler-Illia, G. J. d. A. A.; Grosso, D.; Cagnol, F.; Ribot, F.; Sanchez, C. *J. Am. Chem. Soc.* **2003**, *125*, 9770.

(37)   Fattakhova-Rohlfing, D.; Wark, M.; Brezesinski, T.; Smarsly, B. M.; Rathouský, J. *Adv. Funct. Mater.* **2007**, *17*, 123.

(38) Rawolle, M.; Sarkar, K.; Niedermeier, M. A.; Schindler, M.; Lellig, P.; Gutmann, J. S.; Moulin, J.-F.; Haese-Seiller, M.; Wochnik, A. S.; Scheu, C.; Müller-Buschbaum, P. *ACS Appl. Mater. Interfaces* **2012**, Article ASAP, Publication Date (Web): December 31, 2012.

(39) Yang, P. D.; Zhao, D. Y.; Margolese, D. I.; Chmelka, B. F.; Stucky, G. D. *Nature* **1998**, *396*, 152.

(40) Ortel, E.; Fischer, A.; Chuenchom, L.; Polte, J.; Emmerling, F.; Smarsly, B.; Kraehnert, R. *Small* **2012**, *8*, 298.

(41) Liu, Y.; Szeifert, J. M.; Feckl, J. M.; Mandlmeier, B.; Rathousky, J.; Hayden, O.; Fattakhova-Rohlfing, D.; Bein, T. *ACS Nano* **2010**, *4*, 5373.

(42) Szeifert, J. M.; Fattakhova-Rohlfing, D.; Georgiadou, D.; Kalousek, V.; Rathousky, J.; Kuang, D.; Wenger, S.; Zakeeruddin, S. M.; Gratzel, M.; Bein, T. *Chem. Mater.* **2009**, *21*, 1260.

(43) Szeifert, J. M.; Fattakhova-Rohlfing, D.; Rathousky, J.; Bein, T. *Chem. Mater.* **2012**, *24*, 659.

(44) Szeifert, J. M.; Feckl, J. M.; Fattakhova-Rohlfing, D.; Liu, Y.; Kalousek, V.; Rathousky, J.; Bein, T. *J. Am. Chem. Soc.* **2010**, *132*, 12605.

(45) Guldin, S.; Huttner, S.; Tiwana, P.; Orilall, M. C.; Ulgut, B.; Stefik, M.; Docampo, P.; Kolle, M.; Divitini, G.; Ducati, C.; Redfern, S. A. T.; Snaith, H. J.; Wiesner, U.; Eder, D.; Steiner, U. *Energy Environ. Sci.* **2011**, *4*, 225.

(46) Zhang, Y. X.; Li, G. H.; Wu, Y. C.; Luo, Y. Y.; Zhang, L. D. *J. Phys. Chem. B* **2005**, *109*, 5478.

(47) Macwan, D. P.; Dave, P.; Chaturvedi, S. *J. Mater. Sci.* **2011**, *46*, 3669.

(48) Li, H.; Bian, Z.; Zhu, J.; Zhang, D.; Li, G.; Huo, Y.; Li, H.; Lu, Y. *J. Am. Chem. Soc.* **2007**, *129*, 8406.

(49) Barringer, E. A.; Bowen, H. K. *J. Am. Ceram. Soc.* **1982**, *65*, C.

(50) Wang, C.-C.; Ying, J. Y. *Chem. Mater.* **1999**, *11*, 3113.

(51) Shao, S.; Dimitrov, M.; Guan, N.; Kohn, R. *Nanoscale* **2010**, *2*, 2054.

(52) Mandlmeier, B.; Szeifert, J. M.; Fattakhova-Rohlfing, D.; Amenitsch, H.; Bein, T. *J. Am. Chem. Soc.* **2011**, *133*, 17274.

(53) Niederberger, M.; Bartl, M. H.; Stucky, G. D. *Chem. Mater.* **2002**, *14*, 4364.

(54) Ito, S.; Chen, P.; Comte, P.; Nazeeruddin, M. K.; Liska, P.; Pechy, P.; Gratzel, M. *Prog. Photovoltaics* **2007**, *15*, 603.

(55) Schuster, J.; He, G.; Mandlmeier, B.; Yim, T.; Lee, K. T.; Bein, T.; Nazar, L. F. *Angew. Chem., Int. Ed.* **2012**, *124*, 3651.

(56) Yoldas, B. *J. Mater. Sci.* **1986**, *21*, 1087.

(57) Ito, S.; Murakami, T. N.; Comte, P.; Liska, P.; Grätzel, C.; Nazeeruddin, M. K.; Grätzel, M. *Thin Solid Films* **2008**, *516*, 4613.

(58) Barbé, C. J.; Arendse, F.; Comte, P.; Jirousek, M.; Lenzmann, F.; Shklover, V.; Grätzel, M. *J. Am. Ceram. Soc.* **1997**, *80*, 3157.

(59) Choi, S. Y.; Mamak, M.; Speakman, S.; Chopra, N.; Ozin, G. A. *Small* **2005**, *1*, 153.

(60) Chen, X.; Mao, S. S. *Chem. Rev.* **2007**, *107*, 2891.

(61) http://webmineral.com/data/Anatase.shtml.

5. Formation of Interpenetrating Hierarchical Titania Structures by Confined Synthesis in Inverse Opal

This chapter is based on the following publication.

5.1. Introduction

Metal oxides with periodic porous architecture have shown great potential in processes involving interface- and transport-related phenomena, such as adsorption, catalysis, energy conversion[1-3] and storage,[4-6] or biomaterials.[7-9] Tuning the chemical functionality and the morphology of the pore network provides a flexible means to optimize the performance of such materials. However, for specific applications such as those based on transport phenomena it would be highly desirable to implement a hierarchical organization of different scales of porous frameworks in one material.

The majority of reports on the fabrication of the hierarchical porous metal oxides deal with systems containing different scales of pores. Such materials, which combine large pores with walls that consist of the small ones[7,10-12] are of interest for applications involving molecular adsorption and diffusion phenomena, and whose functionality is therefore largely governed by the properties of the pores.[7,11]

Another type of hierarchical systems involves different length scales of two different physical properties, for example pore diameter and crystal size of a larger backbone. Such hierarchical morphologies have been much less investigated, but they are of significant interest for various applications, for example those involving charge transfer and charge transport properties, in which the performance is determined by the electronic properties and the size of the inorganic backbone in addition to the dimensions of the porous network. Examples for these applications are new forms of hybrid or dye-sensitized solar cells, where the charge carrier diffusion length is one of the important performance-limiting factors[13-15] and whose efficiency strongly depends on the morphology of the titania layer acting as an n-conductor.[1,16,17] These devices are expected to benefit from hierarchical structures, because the latter provide the combination of both larger structural elements for high carrier conductivity over greater length scales and very small ones for achieving large interface areas. Moreover, an additional possible increase in the light harvesting efficiency can be achieved due to photonic or backscattering effects resulting from periodic macroscopic structures,[18-21] However, these effects were not a focus of the present study. Nanotube arrays, rods and inverse opals are examples for such large macroscopic titania morphologies that demonstrate excellent electron transport properties due to optimized orientation with respect to the current collector, or large crystal size with few grain boundaries.[6,22-28] On their own, however, these structures feature interface areas that are too low for efficient electrodes in photovoltaic applications. On the other hand, sensitized mesoporous crystalline titania films show impressively high light absorption in thin layers[29-33] but limited electron transport characteristics due to the small size of the crystals (and grain boundaries) composing the mesoporous scaffold.[34]

Therefore, a hierarchical architecture combining advantages of both mesoscale and macroscale morphologies, that is, efficient light harvesting and charge separation in mesoporous phases and fast transport of photogenerated electrons through interpenetrating

macroscale scaffolds is expected to offer (i) new insights into the impact of morphology on charge carrier dynamics, and (ii) new opportunities for the design of efficient DSCs.

Reports concerning the fabrication of crystalline hierarchical titania are scarce, and are mostly based on the control of growth conditions leading to the simultaneous formation of hierarchical titania frameworks.[2,22,35,36] An alternative approach is a combination of individual strategies for the fabrication of large-scale and mesoscopic materials. This general method would offer the possibility to individually vary both the macro- and the mesostructures' morphologies and dimensions, as was demonstrated for hybrid hierarchical oxides obtained by infiltration of mesoporous amorphous silica in macroporous ceramic[37] or titania backbones.[38] This strategy has not yet been applied to the fabrication of fully crystalline hierarchical titania. In this context the following questions will be important: How to ascertain that the desired mesoporous structures can be formed in a confined space? How to ensure the crystallization of a mesophase, when the regular mesostructure without a confining backbone collapses upon heating to the critical temperature for crystallization? What is the connectivity of porous systems and the accessibility of pore volume deep within the layers?

Here we report the fabrication of hierarchical structures based on the preparation of a highly crystalline, macroporous inverse opal backbone that is formed by colloidal crystal templating using polymethyl methacrylate (PMMA) spheres, and a titania precursor solution for impregnation. These macropores are afterwards filled with a mesoporous titania phase by impregnation with a titania precursor solution containing a polymer template (Figure 1). The development of the mesostructure from this surfactant-directed evaporation-induced self-assembly method was monitored by *in-situ* GISAXS measurements, and correlated with electron microscopy data. An interesting confinement effect of the macroporous backbone on the mesostructure leads to enhanced temperature stability, less shrinkage and generally large mesopore sizes, as observed for the two investigated pore sizes of the macroporous scaffold.

Furthermore, we found that the highly crystalline backbone of the macroporous titania scaffold synergistically affected the crystallization behaviour of the sol-gel derived mesoporous filling. The resulting hierarchical structures were also investigated as anodes in dye-sensitized solar cells, demonstrating the large difference between the individual components and the combined hierarchical titania structure with respect to photon to electron conversion efficiency.

5.2. Experimental Section

Materials

Methyl methacrylate (99%, MMA), sodium dodecyl sulfate (SDS), tetraethyl orthotitanate (technical grade), concentrated HCl (37% in water), Pluronic P123 and the organic solvents were obtained from Aldrich and used without further purification. Bidistilled water (Millipore Q) was used for synthesis.

An overview on the different structured titania films is summarized in Table 5.1.

Preparation of PMMA spheres and macroporous titania inverse opals (Macro)

Polymethyl methacrylate (PMMA) spheres of 200 nm were synthesized by emulsion polymerization according to a procedure described elsewhere.[39] Briefly, MMA (17.8 g) and SDS (5.0 mg) were added under stirring into water (98.0 mL), which had been deoxygenated by purging of nitrogen at 40 °C for 15 min under reflux conditions. The emulsion was heated at 90 °C for 1 h, afterwards the polymerization was initialized by injection of solution of

potassium peroxydisulfate (56.0 mg) in water (2 mL) and the reaction mixture was heated at 90 °C for additional 2.5 h. The reaction was stopped by external ice cooling, and the reaction mixture was further stirred under atmospheric conditions for 30 min. The suspension of PMMA spheres was filtered and washed by repeated steps of centrifugation and ultrasonic redispersion in water. A stock solution (10 wt%) was stored at room temperature for further deposition. For the synthesis of ca. 100 nm large PMMA spheres MMA (6.9 g) and SDS (24.5 mg) were dissolved in 98 mL water and $K_2S_2O_8$ (56.8 mg) in 2 mL water. MMA was polymerized and PMMA washed accordingly.

Colloidal crystal films were obtained by deposition of the PMMA spheres from aqueous solutions (1-5 wt %) on various substrates by horizontal sedimentation under vibration-free conditions. The substrates were first cleaned by ultrasonication for 30 min in a mixture of acetone and ethanol (1:1 v/v) and then in water, and dried in a stream of nitrogen.

Titania inverse opals were fabricated by dip coating (immersion time 30 seconds, withdrawal speed 1.3 mm s^{-1}) of the colloidal crystal films into a titania precursor solution prepared by addition of 1.08 mL (37%, 13.2 mmol) HCl to 1.68 g (7.36 mmol) of tetraethyl orthotitanate under ice cooling and moderate stirring, followed by addition of 4.8 g (104.2 mmol) of ethanol. The impregnated films were dried at 60 °C for 1 h and then calcined in two sequential steps at 300 °C and 450 °C (the heating rate and dwell time for each step are 2 °C min^{-1} and 2 h, respectively).

Preparation of mesoporous titania films (Meso)

The solution for deposition of mesoporous titania films was prepared by a procedure described elsewhere.[46] Briefly, a solution of Pluronic P123 (0.5 g, 0.1 mmol) in ethanol (6 g) was added to a mixture of hydrochloric acid (37%, 1.05 mL, 12.8 mmol) and tetraethyl orthotitanate (1.5 mL, 7.06 mmol) at room temperature under continuous stirring for 1 h. The prepared solution was then cast on a silicon substrate (Meso-ca) or dip-coated (Meso-dc) under ambient conditions, dried at room temperature and individually calcined up to 450 °C in air.

Preparation of hierarchical titania films (Hier)

The templated titania precursor solution (Meso solution, see above) was cast on the inverse opal film and allowed to dry horizontally at ambient conditions at room temperature. The amount of solution used was estimated from the volume of the voids in the initial macroporous host film, taking into account the porosity and thickness of the macroporous film, and the porosity and density of the mesoporous titania phase formed after calcination. As an example, for a macroporous film of 1 cm^2 area and 1 μm thickness, the void volume can be estimated as 7.5×10^{-5} cm^3. The mesoporous phase after calcination is assumed to have 50 % porosity,[31] therefore, taking into account the density of crystalline anatase of 4 g cm^{-3}, the amount of titania formed in the macropores should be 0.15 mg (1.9×10^{-3} mmol), which corresponds to 1.34×10^{-3} mL of 1.42 mol/L precursor titania solution. The films were dried at 60 °C for 1 h and the surfactant was removed by calcination at 450 °C for 30 min (ramp: 0.7 °C min^{-1}).

Table 5.1. Overview on the used sample codes and the corresponding preparation characteristics.

Sample code	Structure	Template	Film preparation
Meso	mesoporous	Pluronic P123	casting
Macro-100	macroporous	PMMA spheres (ca. 100 nm)	CCT
Macro-200	macroporous	PMMA spheres (ca. 200 nm)	CCT
Hier-100-ca	hierarchical	1. PMMA spheres (ca. 100 nm)	1. CCT
		2. Pluronic P123	2. casting
Hier-200-ca	hierarchical	1. PMMA spheres (ca. 200 nm)	1. CCT
		2. Pluronic P123	2. casting
Hier-200-dc	hierarchical	1. PMMA spheres (ca. 200 nm)	1. CCT
		2.Pluronic P123	2. dip-coating

CCT: colloidal crystal templating

For photovoltaic measurements,[47] the titania films were fabricated on FTO-coated glass substrates coated with a dense titania blocking layer. The blocking layer was prepared by spin coating (4000 rpm) of the solution obtained from hydrochloric acid (37%, 0.75 mL, 9.13 mmol), tetraethyl orthotitanate (1.05 mL, 5.06 mmol) and tetrahydrofuran (14 mL), and calcination to 450 °C (ramp: 0.7 °C min^{-1}). After preparation and final calcination of the different porous titania structures, the films were cooled to ca. 80 °C, immersed into a dye solution at room temperature, and kept there for 12 h. The dye solution contains 0.5 mM of

ruthenium 535 bis-TBA dye (N 719) in acetonitrile and *tert*-butyl alcohol (volume ratio: 1:1). The dye-coated mesoporous TiO_2 films were assembled and sealed with a thin transparent hot-melt Surlyn 1702 ring with an open area of 0.196 cm² (DuPont) to the counter electrodes (Pt on FTO glass, chemical deposition from 0.5 mM hexachloroplatinic acid in ethanol, heated at 400 °C for 15 min). The electrolyte was injected into the inner electrode space from the counter electrode side through a pre-drilled hole, and then the hole was sealed with a Surlyn sheet and a thin glass cover slide by heating. The volatile electrolyte contains butylmethylimidazolium iodide (BMII, 0.536 mL, 3.0 mmol) iodine (38.1 mg, 0.3 mmol), guanidinium thiocyanate (59.1 mg, 0.5 mmol), and 4-*tert*butylpyridine (837.8 mg, 6.2 mmol) dissolved in valeronitrile (0.75 mL, 7.2 mmol) and acetonitrile (4.25, 80.7 mmol).

Further hierarchical titania materials

Analogue to the previous imbibition of a sol-gel precursor (Meso), we additionally used different titania building-block templated solutions[30,31] to create hierarchical titania films. The synthesis of the particles is identical to the procedures for NP-6 and NP-4, previously described in chapter 4 and were not further explained in this section.

Solution containing 6 nm large anatase particles and a sol-gel precursor.[30]

A non-aqueous solvothermal processing was used for particle synthesis. To obtain a homogeneous solution, NP-6 titania particles (0.1 g, 0.55 mmol) were stirred at room temperature for 12 h in a solution a of Pluronic P123 (0.1 g, 0.02 mmol) in THF (2 mL).

Finally a second sol-gel solution was added. Thereby tetraethyl orthotitanate (3.6 mL, 17.1 mmol) was stirred at room temperature and hydrolyzed by adding hydrochloric acid (37%, 2.55 mL, 31.0 mmol).[30]

Solution containing 4 nm large anatase particles.[31]

A microwave heating protocol was used to obtain smaller titania nanocrystals and a clear particle solution was obtained by dispersing NP-4 (0.1 g, 0.55 mmol) in ethanol (1 mL), which was combined under stirring at with an additional solution of Pluronic P123 (0.05 g, 0.01 mmol) in THF (1 mL).[31]

Hirarchical films were prepared according to the procedure used for Hier-200-ca. Both templated precursor solutions were cast on macroporous crystalline titania films (Macro-200). After drying at 60 °C the films were calicined at 450 °C for 30 min (ramp: 0.7 °C min^{-1}).

Characterization

Scanning electron microscopy (SEM) was performed on a JEOL JSM-6500F scanning electron microscope equipped with a field emission gun, at 4-10 kV and an Oxford analysis system. High-resolution transmission electron microscopy (HRTEM) and scanning transmission electron microscopy in high-angle annular dark-field mode (STEM-HAADF) were performed using a FEI Titan 80-300 equipped with a field-emission gun operated at 300 kV. Cross sections of the films were prepared by epoxy glue embedding, dimple grinding and polishing with Argon ions.

The film thickness was measured by profilometry (Veeco Dektak 156) and SEM cross-section analysis.

X-ray diffraction analysis was carried out in reflection mode using a Bruker D8 diffractometer, using Ni-filtered CuK$_\alpha$-radiation (wavelength: 1.5406 Å) with theta/theta geometry, operating at 40 kV and 40 mA, and a scintillation detector.

Grazing-incidence small-angle X-ray scattering (GISAXS) experiments were performed at the Austrian SAXS beamline BL 5.2 L facility at Synchrotrone Elettra (Trieste, Italy). The wavelength of the incident beam was 0.15498 nm (8 keV), and the sample-detector distance was set to 1430 mm. The detector was a two-dimensional image intensified CCD detector (Model CV 12, Photonic Science Ltd., Millham, UK). The samples were heated on a modified hot stage (Model DHS 900, Anton Paar).

Nitrogen sorption measurements were performed on all samples with a Quantachrome Instruments NOVA 4000e at 77 K. Pore size distribution and volume were calculated with a NLDFT equilibrium model of N_2 on silica. The specific surface area was estimated using a BET model.

Photovoltaic measurements were done with an AM 1.5 sun simulator. A Solar Light Co. Xenon lamp (model: 16S-300-V3, 100 mW/cm^2) was used as light source. I-V-curves were measured with a ZAHNER Electric IM6ex potentiostat and the ZAHNER Electric software Thales 4.05 USB.

External quantum efficiency measurements were performed using a 150 W Xenon lamp (Lot Oriel Xenon lamp) and a monochromator (Horiba Jobin Yvon microHR; slit opening fixed at 1.5 mm) with appropriate long-pass filters as the primary illumination source and a bias illumination provided by a solar simulator, which was reduced to about 10 mW/cm² using a neutral density filter. The primary beam was chopped at 2 Hz. The signal was detected using a Signal Recovery dual-phase lock-in amplifier (model: 7265). EQE measurements were referenced to a silicon photodiode with known spectral response.

5.3. Results and Discussion

The individual synthetic steps are for the development of a hierarchical titania scaffold is illustrated in Figure 5.1, beginning form an ordered colloidal crystal template (left), the generation of a macroporous inverse opal titania replica (middle), which is again interpenetrated with a additional mesoporous titania phase (right).

For the preparation of the macroporous host scaffold, first opal films of PMMA spheres were assembled on different substrates by a horizontal deposition from aqueous colloidal dispersions. The size of the PMMA spheres can be controllably varied from around 100 to 400 nm by selection of surfactant concentration and reaction time in emulsion polymerization synthesis,[39] and the thickness of the opal layers by the concentration of the PMMA spheres and the amount of the applied dispersion.
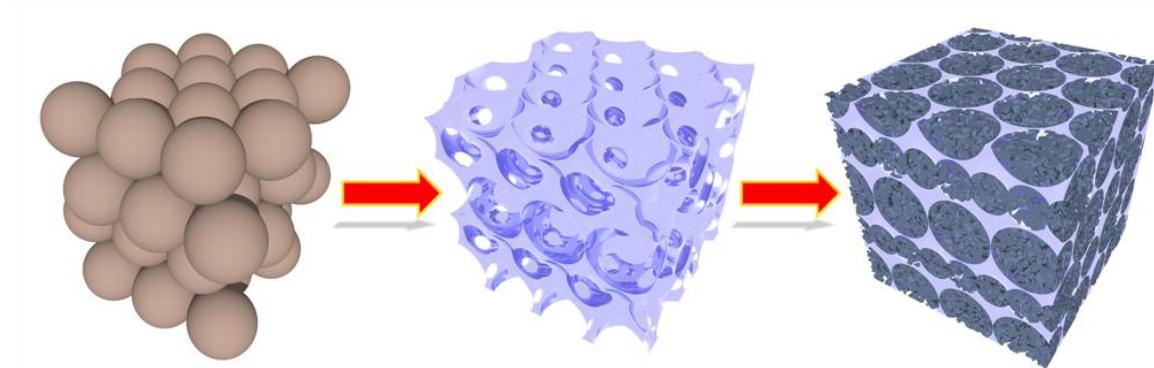
Figure 5.1: A strategy for the preparation of hierarchical titania frameworks: a colloidal crystal template is impregnated with a titania precursor solution and forms a three-dimensional ordered macroporous material (3 DOM) after template removal. The inverse opal host is filled with the surfactant-containing solution of hydrolyzed titania leading to the formation of a hierarchical titania framework after calcination.

The dried films obtained in this way show an ordered close packing of the larger PMMA spheres and a more loose packing for the smaller ones, as can be seen from the SEM images (Figure 5.2 a,b). In a second step, the negative replica of the opal material was fabricated by infiltration of the films with a solution of titania sol using a dip-coating technique according to a known procedure.[40] As can be seen from the EDX-mapping of the films' cross-sections (Figure 5.2 c,d), a single impregnation step already leads to a complete filling of the interstitial voids between the PMMA spheres. The good filling quality can be attributed to a good wetting behavior of the sulfonated PMMA spheres, causing the transport of the titania precursor into the voids by capillary forces. For the latter, the intensity of Titanium $K\alpha1$ rays correlates with the brightness of blue and is homogeneously distributed over the entire sample area (white rectangle). The blue area is therefore slightly interrupted, which can be attributed to present vacuum and a dense thin TiO_2 layer, acting as intermediate layer between silicon and the PMMA/ titania sol-gel composite layer on top.
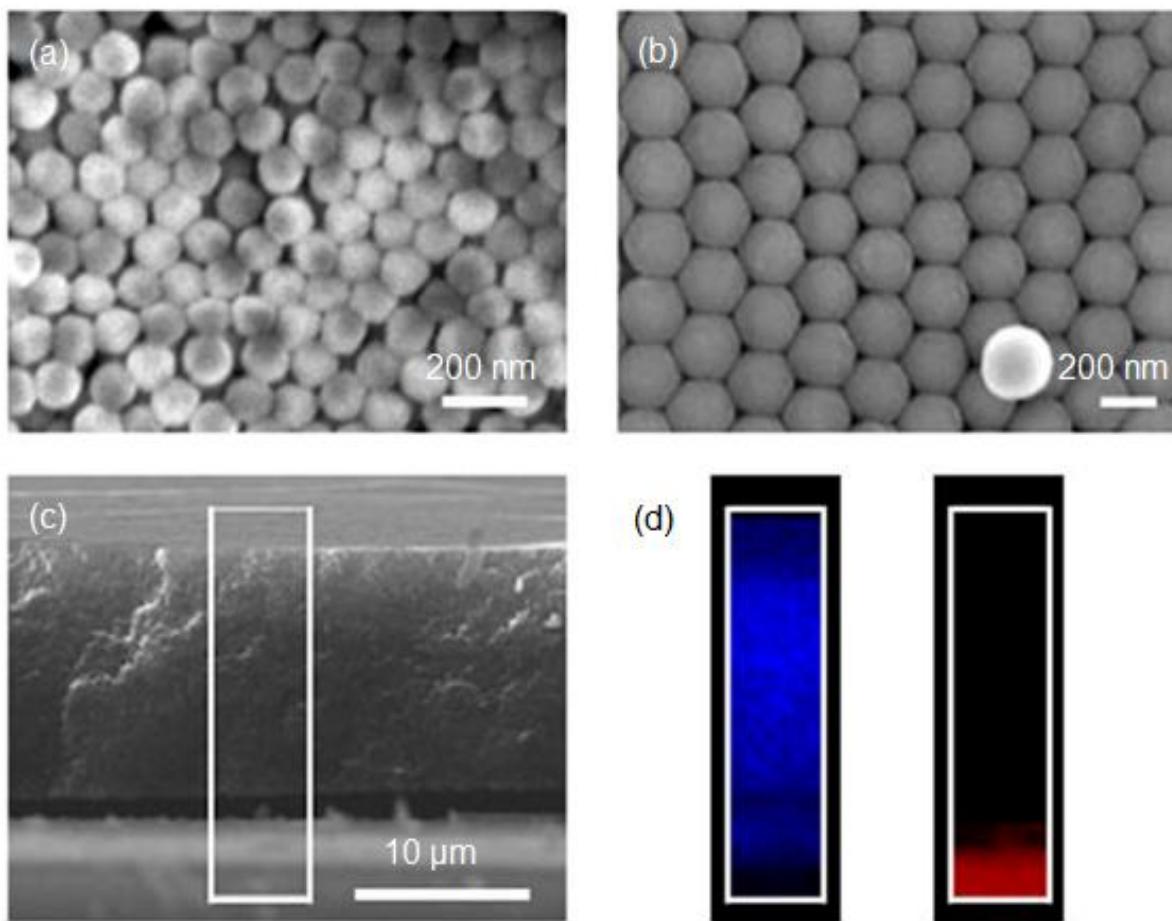
Figure 5.2: Scanning electron microscopy (SEM) images along the [111] direction of the films assembled from PMMA beads of around 100 nm and 200 nm as prepared (a, b). The cross-section image (c) shows the area (white rectangle) used for EDX spectroscopy (elemental mapping) of a densely packed film, consisting of the larger spheres acting as template, after impregnation with a titania sol—gel solution before calcination. A homogeneous intensity distribution of titanium (blue) was found within in the film prepared on a silicon wafer (red) (d).

After drying the infiltrated films, the PMMA spheres were removed by calcination in air at 400 °C, which also leads to the crystallization of the titania scaffold. The inverse opals obtained in this way are assigned further as Macro-X, with X standing for the diameter of the

parent PMMA spheres in nm (see Table 5.1.). A close investigation of sol-gel derived macroporous titania is shown in the TEM images, which confirms the polycrystalline wall composition (Figure 5.3 a, b).
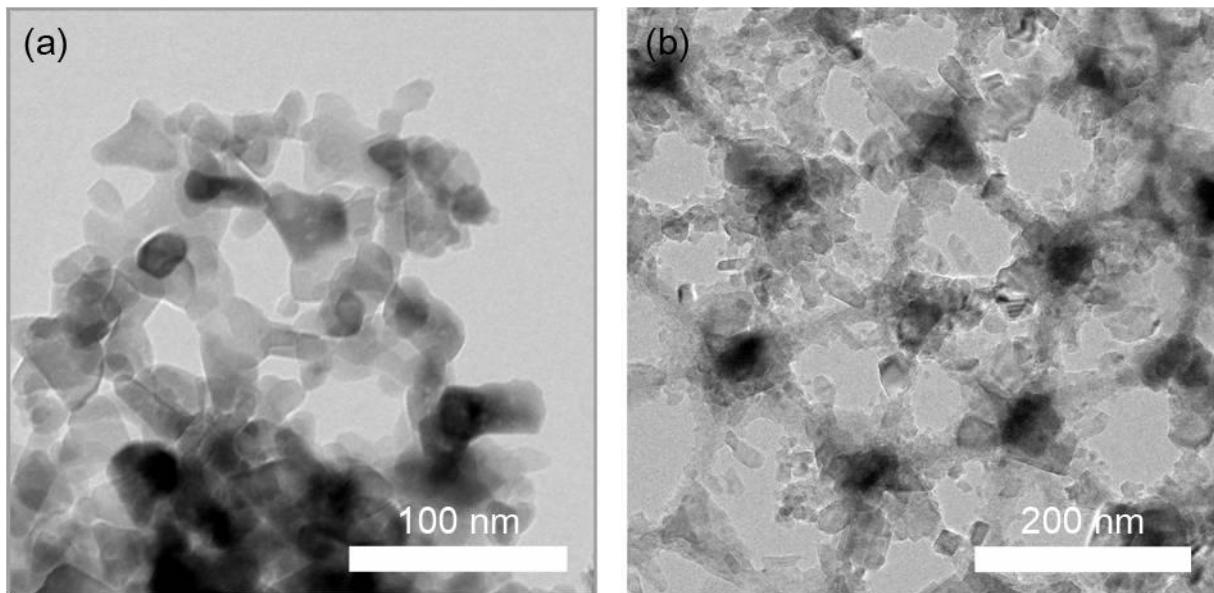
Figure 5.3: TEM images of the different macroporous titania scaffolds after calcination at 400 °C in air. Polycrystalline cages have formed around the removed PMMA templates with diameters of around 100 nm (a, Macro-100) and 200 nm (b, Macro-200).

SEM and TEM images of the films obtained in this way using the 200 ± 25 nm PMMA spheres reveal the presence of 3 DOM macroporous structure of a highly ordered crystalline titania scaffold containing interconnected spherical voids with a diameter of around 200 nm and intervoid connections of around 50-70 nm (Macro-200, Figure 5.4 a, b).
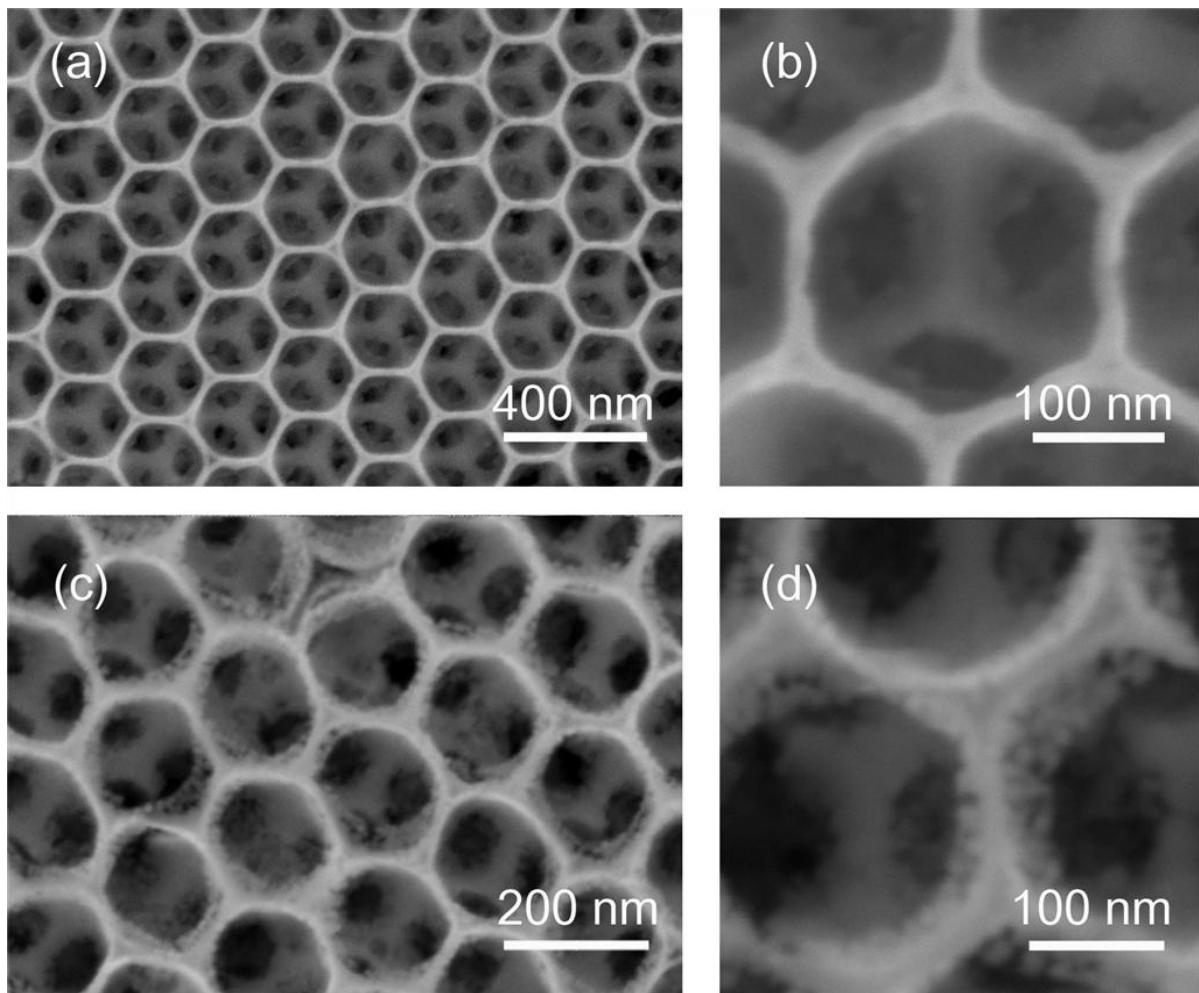
Figure 5.4: FESEM micrographs (top view) show the morphology of the macroporous titania inverse opal prepared by the 200 nm large PMMA spheres before (a, b, sample Macro-200) and after a single dip coating step with a Pluronic P123-containing titania sol-gel solution, leading to the formation of a thin mesoporous titania layer on the crystalline inverse opal backbone (c, d, sample Hier-200-dc). All films were prepared on silicon substrates and calcined at 400 °C.

For the fabrication of the hierarchical structure, the macroporous titania films were filled with a surfactant-containing solution (Pluronic P123) of hydrolyzed titania using different techniques. Casting of this solution by dip coating and an additional calcination results in an

open hierarchical structure containing the macroporous scaffold homogeneously covered by an additional layer of mesoporous titania (assigned as Hier-200-dc, Figure 5.4 c-d).

In order to achieve complete filling of the macropores, the solution for the mesoporous phase was drop-cast into the inverse opal host layer. The amount of the solution was calculated from the available macropore volume in the inverse opal scaffold as estimated from the pore diameter and the films' thickness (see detailed description in the Experimental Part). The filled films were dried in air and calcined at temperatures of $200 - 450\,°C$ applying a fast calcination ramp ($10\,°C\ min^{-1}$). SEM top view and TEM cross-section images show that this procedure leads to filling of each macropore throughout the whole film thickness, resulting in the formation of mesoporous films periodically interpenetrated with the macroporous scaffold, such that both mesoscale and macroscale repeating units are observed in the electron microscopy images (assigned as Hier-200-ca, Figure 5.5 a, b). The thickness of the films is determined by the thickness of the parent macroporous scaffold (about 5.5 μm). We note that coating of the solutions for the mesoporous film preparation alone enables fabrication of no more than 1 μm thick films on a flat substrate - attempts to increase the film thickness further result in the films' cracking and peeling off the substrates.[33,41] The fact that the thickness of mesoporous films can reach several micrometers in a hierarchical structure is attributed to good adhesion between the crystalline titania meso-phase and the dense polycrystalline three-dimensional macroporous titania. The hierarchical titania films are completely crystalline after calcination in air at $450\,°C$ and consist of anatase, as follows from their wide-angle X-ray scattering (WAXS) patterns, high resolution TEM (HR-TEM) images and selected area electron diffraction (SAED) patterns of the films' cross-sections (Figure 5.6). The HR-TEM images reveal that the obtained hierarchical structure is composed of two types of crystalline anatase, with crystal sizes of over 20 nm in the macroporous titania walls (Figure 5.6 a) and

4-6 nm in the walls of mesoporous material. The corresponding SAED pattern (Figure 5.4 d) proves the existence of these two size populations of the anatase crystals in the hierarchical sample. In addition to the broad diffraction rings originating from many randomly oriented small crystals within the mesostructure (intensity profile over (101) anatase diffraction, number 1 in Figure 5.6 e), the large crystals in the walls of the macroporous host scaffold lead to bright spots of the same phase but with a much smaller width superimposed on the broad ring (intensity profile number 2). In WAXS, the unfilled macroporous host layer exhibits a peak broadening of the (101) anatase diffraction corresponding to a mean crystal size of about 30 nm. After filling with the mesoporous titania phase, the line broadening of the hierarchical structure becomes much larger, and the mean crystal size from the full width at half maximum can now be calculated as 18 nm.
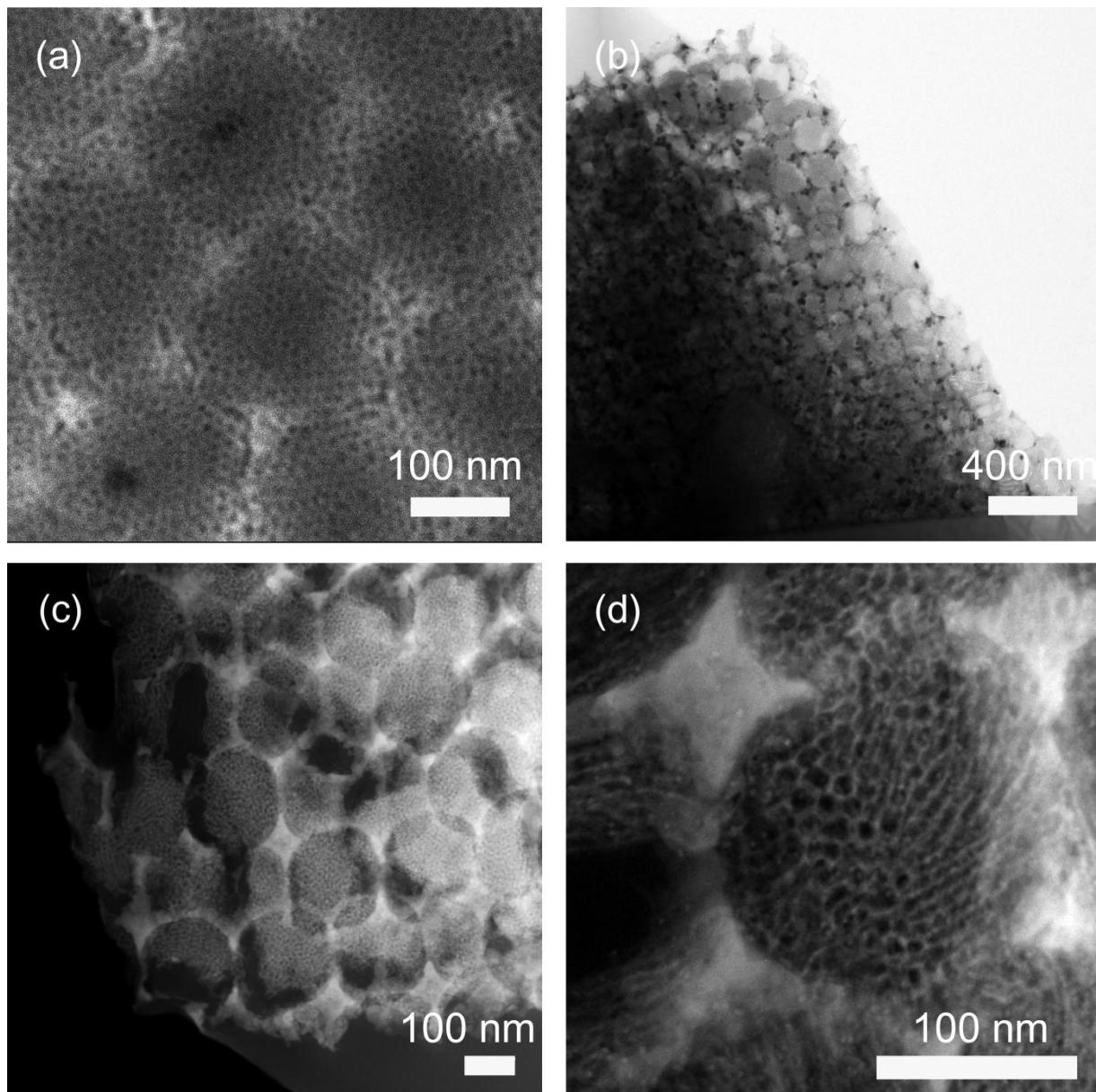
Figure 5.5: Electron micrographs of hierarchical titania frameworks fabricated using 200 nm PMMA spheres (Hier-200-ca): FESEM top-view image (a), and micrographs of the films' cross-sections in TEM (b) and HAADF-STEM (c,d). The brighter areas in (a, c, d), and the darker spots in (b) correspond to larger titania crystals in the dense walls of the inverse opal. All films were prepared on silicon substrates and calcined at 450 °C.

This supposed reduction of crystal size can be explained by the coexistence of two populations of crystal sizes in the hierarchical structure: large ones (over 30 nm) in the walls of the macroporous backbone and small ones (smaller than 10 nm) in the mesoporous filling.

Strikingly, the pure mesoporous titania (assigned further as Meso) phase prepared as a reference on a flat substrate remains amorphous as a result of the applied heating conditions (Figure 5.6 f, A) For TEM investigation at different magnification, the mesoporous reference thin film was scratched from the silicon substrate (Figure 5.7 a, d-f). It was also prepared by dip-coating the substrate into the identical templated titania sol-gel precursor solution and applying a similar calcinations procedure. The reference features well shaped and highly ordered mesostructure, confirmed by the fast Fourier transform (b). The mesopores are interconnected and d-spacings of around 10 nm were estimated. Only a few small crystallites in the network are visible in the TEM micrographs and a diffuse diffraction ring in the SAED pattern (c) indicates the generally amorphous nature of the titania mesostructure.

We conclude that the highly crystalline backbone has a strong synergistic effect on the crystallization of the mesoporous filling, acting as a nucleation site for further crystallization of the initially amorphous titania phase. We have previously observed similar effects for titania nanoparticles dispersed in a sol-gel matrix, thus it appears that this behavior can be generalized.[30]
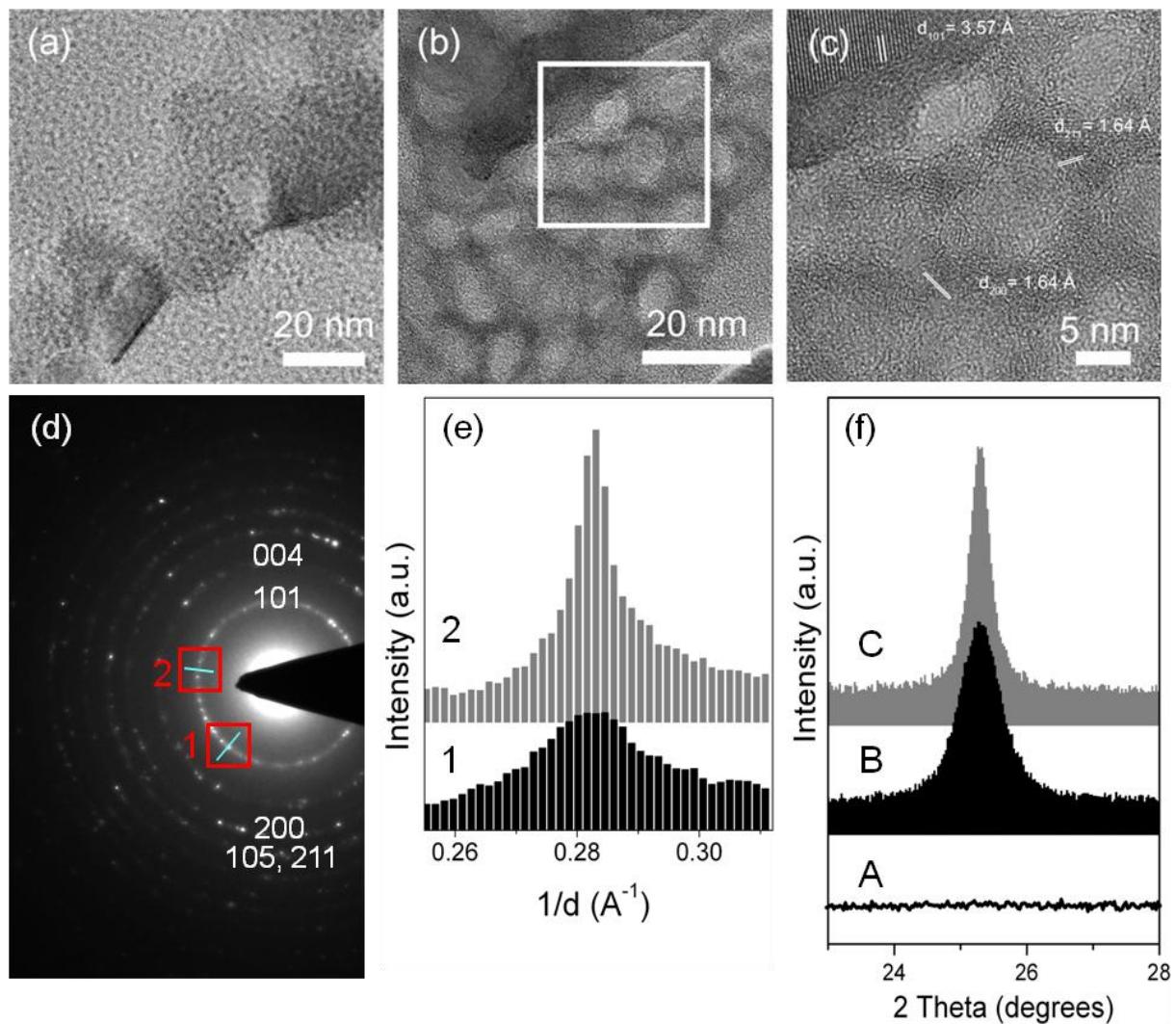
Figure 5.6: Structural characterization of titania films. TEM micrographs of the crystalline macroporous (a, Macro-200) and hierarchical titania films (b, c, Hier-200-ca) after calcination at 400 °C (a) and 450 °C (b, c). The diffraction rings in the SAED pattern (d, Hier-200-ca) could be indexed with the anatase phase. The corresponding intensity profiles of the anatase (101) reflection at two different positions (d1, d2) show the presence of two sizes of crystalline domains (e). WAXS patterns (f) of the hierarchical film (B) and individual mesoporous (A, Meso) and macroporous (C, Macro) materials prepared in the same conditions.
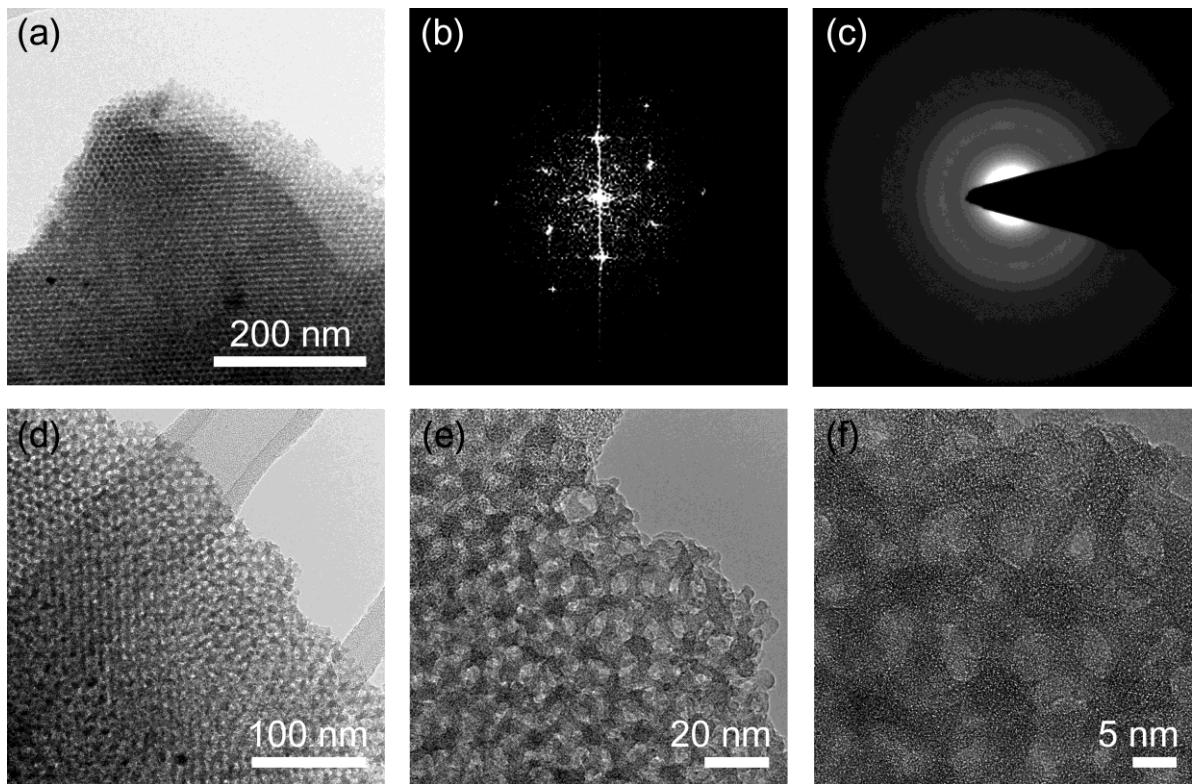
Figure 5.7: TEM images (a, d-f) and FFT (b) represent the structure of the mesoporous titania film removed from the substrate (prepared by dip-coating on a silicon substrate). After a rapid heating up to 450 °C, the SAED pattern structure shows an almost amorphous phase (c).

To further investigate the effect of this hierarchy, and especially the influence of the confined space in the macroporous material on the evaporation-induced self-assembly (EISA) based formation of a templated titania sol-gel mesostructure, we performed 2D-GISAXS monitoring of mesostructure evolution using *in-situ* heating experiments (Figure 5.8). A small amount of the solution for the mesoporous phase was drop-cast on a substrate, dried, and subsequently heated to 450 °C. A flat Si wafer was used as a reference (Meso, a-c). As substrates, we also examined two different macroporous titania films with pore sizes of about 200 nm (Macro-200, d-f), and 100 nm (Macro-100, g-i), respectively. The obtained pattern represent the structures after drying at room temperature (first column), and at calcination temperatures of

300 °C (middle) and 450°C. Note that the reflections of the periodic structures of the macroporous inverse opal are not visible because of their close proximity to the primary beam.
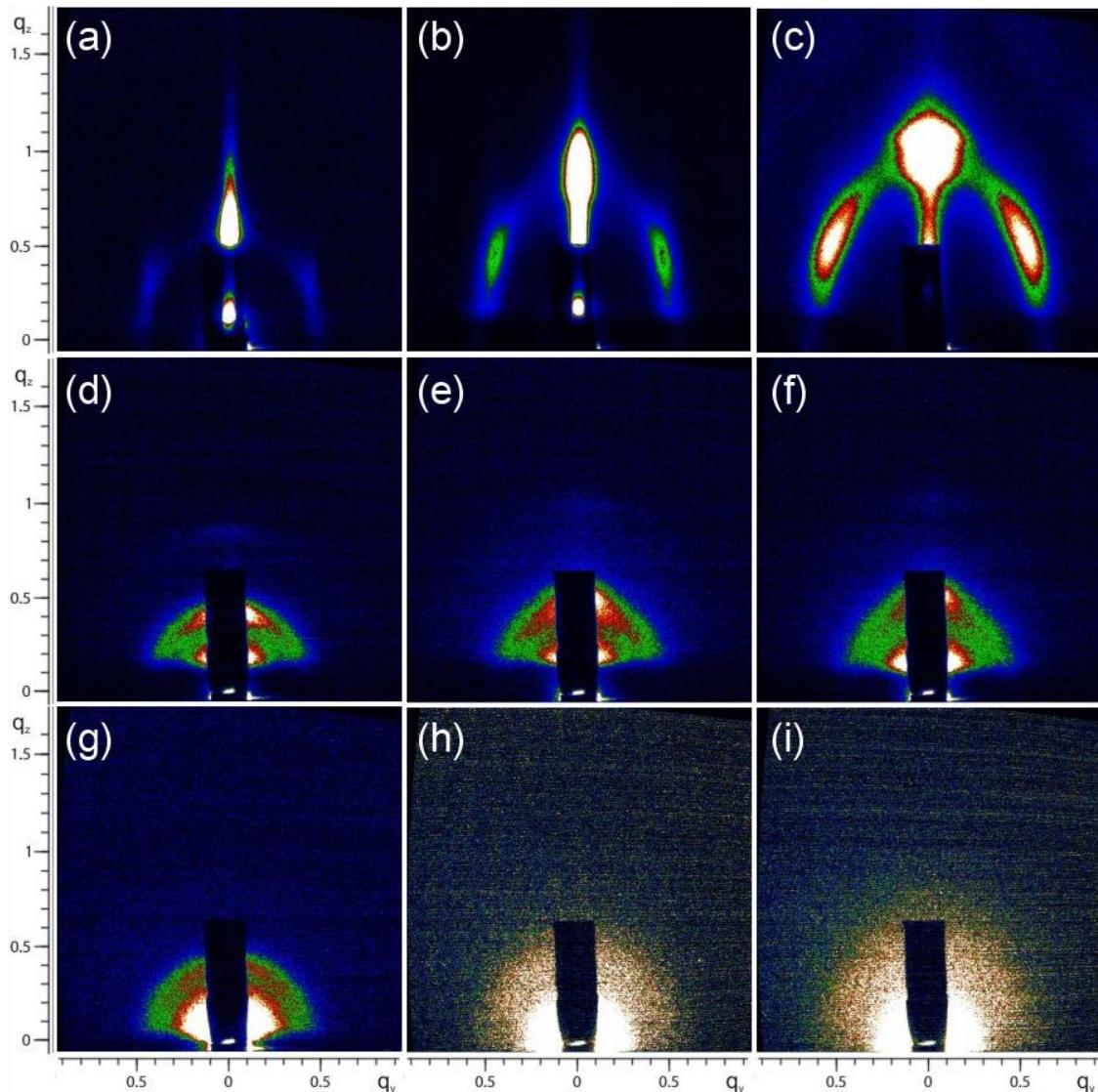
Figure 5.8: Evolution of titania structures. 2D-GISAXS patterns of samples Meso (first row, a-c), Macro-200 (second row, d-f), and Macro-100 (third row, g-i). First column: after drying at room temperature; second column: after heating to 300 °C; and third column: after heating at 450 °C.

To investigate the temperature dependent structure change in detail, the development of the scattering intensity was further investigated. Therefore the intensity was obtained from a fixed

area, highlighted in red. The 2D-GISAXS patterns of the mesoporous structure on flat silicon

(Figure 5.9 a, d) show a well-ordered cubic structure with reflections in the q_z- and q_y-plane.

The corresponding d-spacings at room temperature are 9.5 nm (in-plane, q_z) and 10.4 nm

(out-of-plane, q_y). In the confined space of a macroporous inverse opal of 200 nm pore size

(Hier-200-ca, Figure 5.9 b, e), the pattern of the mesostructure exhibits a slightly broadened

peak of a preferred in-plane (q_z) orientation only, with a significantly larger d-spacing of 12.7

nm. The mesostructure in a smaller pore inverse opal Hier-100-ca (Figure 5.9 c, f) is much

less ordered, and only an indication of a reflection in q_z plane can be seen. The shape of the

pattern and the mesostructure's dimension are similar to that of the 200 nm-inverse opal

sample.
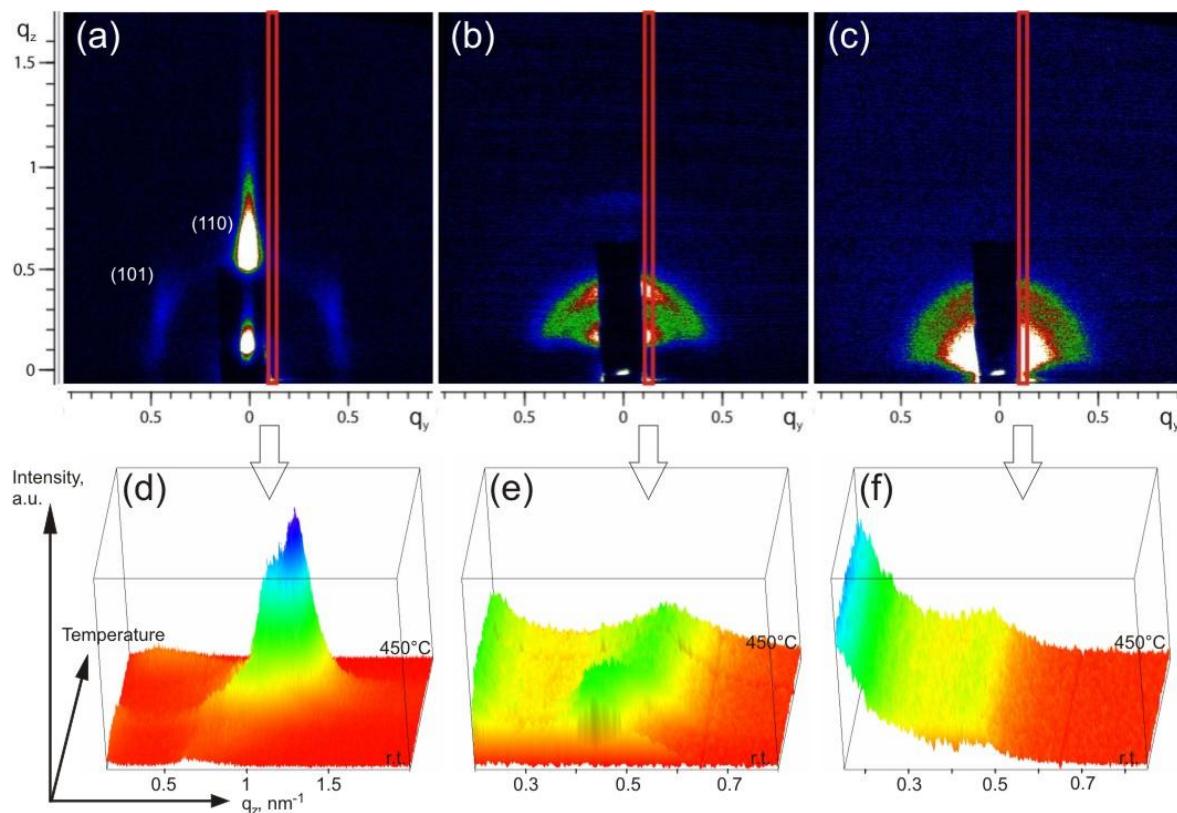
Figure 5.9: *In-situ* investigation of the evolution of hierarchical titania (Hier-200-ca, Hier-100-ca). 2D-GISAXS patterns of samples made by casting a solution of Pluronic

P123-containing titania sol on flat silicon (a), into macroporous titania with 200 nm (b, Macro-200) and 100 nm (c, Macro-100) pore size after drying at room temperature. Second row: Development of the diffraction peaks in the 2D-GISAXS patterns made visible by comparing 1D-intensity profiles at a constant q_y-value of 0.12 - 0.15 nm^{-1} (highlighted in red in 2D-images) during *in-situ* heating to 450 $^{\circ}$C: film from solution with Pluronic P123-containing titania sol cast on flat silicon (d, Meso). Same solution cast into an inverse opal with 200 nm (Macro-200, e) and 100 nm (Macro-100, f) pore size. Electron microscopy shows that the mesoporous titania completely penetrates into the macroporous scaffold and that it does not form a superficial layer (see also Figure 5.5).

Upon heating the films, they show drastically different shrinkage behaviour. This can be seen from the shifts of the diffraction peaks (3D graphs illustrating the thermal development of intensity profiles at a fixed value of q_y, Figure 5.9 d-f). Heating the mesoporous film on flat silicon results in a drastic shrinkage of the porous structure by 39 % of the in-plane, and 29 % of the out-of plane reflection, respectively (see Figure 5.5, and Table 5.2.). The mesostructures filled into the inverse opals show much less shrinkage upon heating, resulting in a structural contraction of only 21 % (Hier-200-ca) and 13 % (Hier-100-ca), respectively.

Judging from these data, the macroporous framework obviously influences the assembly of the mesostructure, and leads to much larger structures (22 % increase at room temperature) with a different orientation. A similar phenomenon has been described for the mesostructure formation in large pore anodized alumina materials, but the universality of this effect has not yet been shown concerning other macrostructures such as inverse opals.[42-45] Furthermore, the inverse opal backbone acts as a stabilizing matrix, limiting the shrinkage of the mesopores

upon heating. In this way, the final size of the mesopores in the smallest macroporous matrix is even 50 % larger than that of a structure made from the same solution on a flat substrate.

Table 5.2. Comparison of the d-spacing of the mesoporous structures on a flat Si substrate and in macroporous inverse opals with 200 nm and 100 nm pore size before and after heating to 450 °C.

		Flat substrate (Meso)		200 nm macropores (Macro-200)	100 nm macropores (Macro-100)
	Temperature	In-plane	Out-of-plane	In-plane	In-plane
d-spacing [nm]	20 °C	9.5	10.4	12.7	12.7
	450 °C	5.8	7.4	10.1	11.1
Shrinkage		39%	29%	21%	12.6%

The films monitored by GISAXS were further investigated by electron microscopy. The TEM images of the cross-sections of the hierarchical titania films reveal that a mesoporous phase is formed in each pore of the macroporous host (Figure 5.10 e). The mesoporous material shows a high order of periodicity within individual macropores, such that the mesoporous phase formed within most of the macropores can be considered as a single mesostructural domain (see orientational peaks in the Fourier transforms of highlighted sections in Figure 5.10 a-d). Between neighbouring macropores, there seems to be little orientational relationship of the mesostructure, but the observed orientations reflect some dependence with respect to the

substrate. The periodic structures, their fast Fourier transforms and the corresponding d-spacings are in good agreement with the results of the GISAXS measurements.

The TEM images of the reference mesoporous titania film obtained under the same conditions on a flat Si substrate in absence of macroporous host (Figure 5.7) show the formation of the periodic cubic mesostructure with significantly smaller d-spacing, confirming the GISAXS observations.
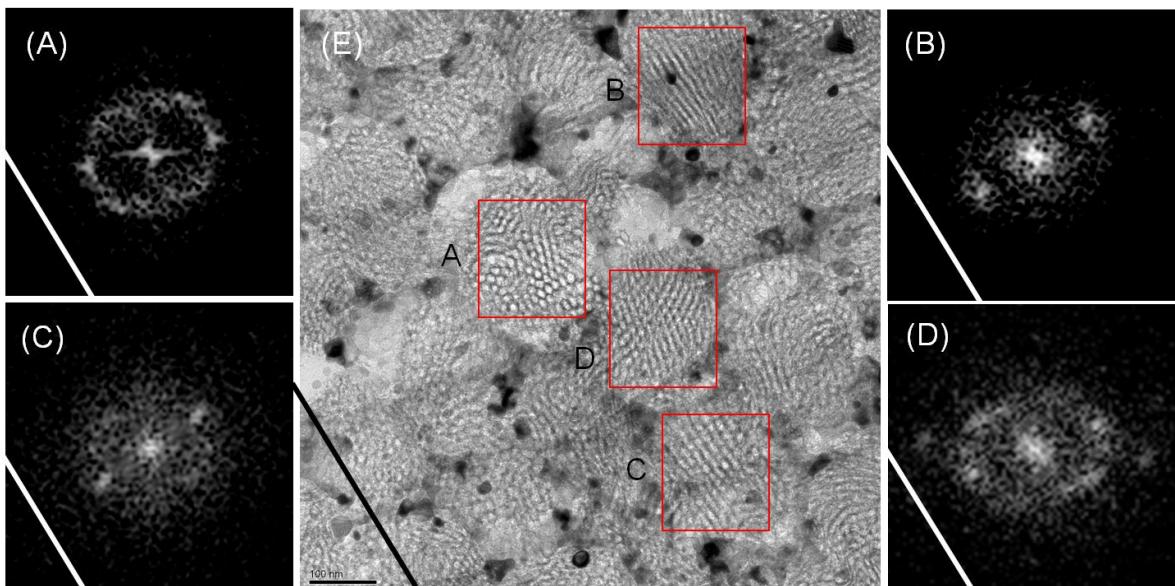
Figure 5.10: TEM image (e) of the hierarchical titania film (Hier-200-ca) prepared in macroporous titania with 200 nm pore size (Macro-200), and FFT images (a-d) of selected areas showing the periodic organization of mesopores in single macropores. The white lines show the position of substrate with respect to the film.

The porosity of the different titania materials was additionally characterized by nitrogen sorption measurements. The parent macroporous titania (Macro-200) films exhibit, as expected, type II isotherms typical for the macroporous material and a low surface area of 64

m^2/g (Figure 5.11 a). The character of porosity, however, changes completely after the filling of the macroscopic pores with the mesoporous titania. The isotherms of the resulting hierarchical films (Hier-200-ca) feature a step at relative pressures around 0.6 - 0.7 p/p$_0$ corresponding to the filling of the pores in the mesoporous range, a largely increased surface area of 154 m^2/g, and a narrow hysteresis between adsorption and desorption branches indicating the uniform pore size distribution (Figure 5.11 a, B).

On the first glance, the adsorption behavior of the hierarchical material is very similar to that of the mesoporous titania film obtained on a flat substrate without the macroporous scaffold (Figure 5.11 a, C). However, close inspection of the two latter materials reveals differences in their adsorption characteristics. The pore size calculated by a DFT method corresponds to 5.1 nm for a mesoporous film grown on a flat substrate. The pore size increases to about 6.1 nm when the same solution is cast into the macroporous support. The increase in the pore size in the hierarchical material is accompanied by an increase in the pore volume (from 0.24 to 0.28 cm^3/g) and a decrease in the surface area (from 210 to 154 m^2/g) compared to the reference mesoporous film. The increase in the pore size by 16 − 20 % for a mesoporous phase formed inside the macroporous host is in good agreement with the observations of the GISAXS and TEM methods described above. The obtained isotherms reveal the open and accessible character of porosity obtained after filling of the macropores with the solution for the mesoporous phase, and also confirm that the confined space of the macroporous host has a pronounced effect on the formation of the mesoporous phase.
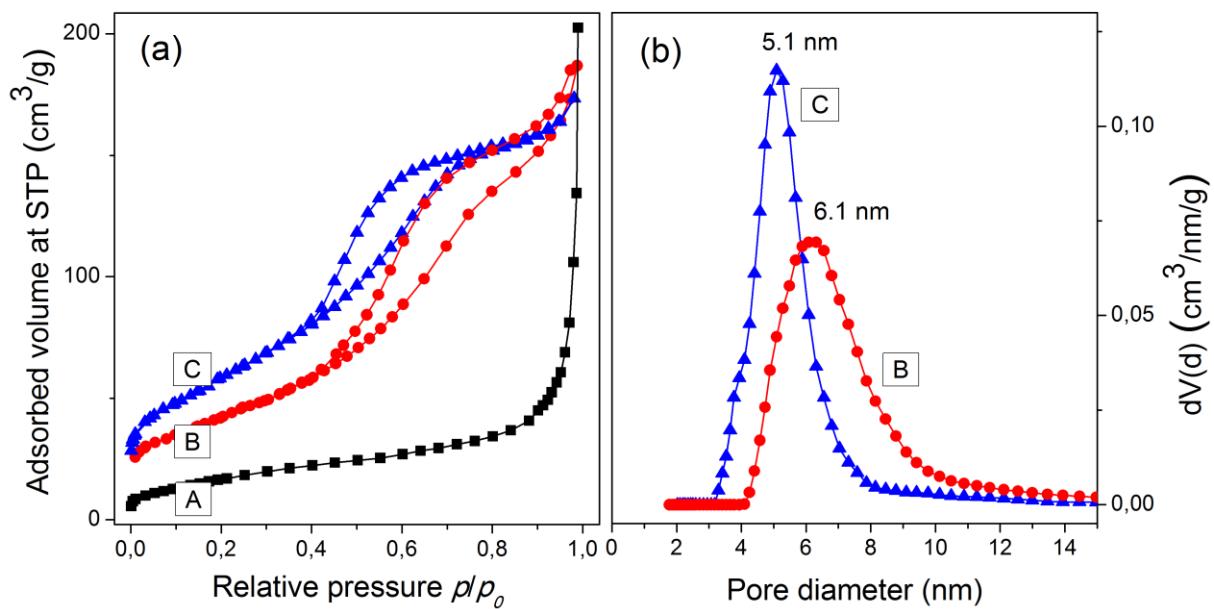
Figure 5.11: Nitrogen sorption isotherms (a) and DFT pore size distribution (b) of the macroporous film templated with the 200 nm latex spheres (A, Macro-200), corresponding hierarchical film after filling of the macropores with the mesoporous titania (B, Hier-200-ca), and the reference mesoporous film coated on the flat substrate (C, Meso). All the films were calcined at 450 $^{\circ}$C. The measurements were performed on layers removed from the substrate.

The above hierarchical titania layers (Hier-200-ca) were also employed as active electrodes in dye-sensitized solar cells (Figure 5.12) and compared to the unfilled macroporous scaffold. The macroporous scaffold exhibits a very high open circuit potential of 915 mV indicating efficient charge collection. In the hierarchical structure, this potential is reduced to 750 mV, which can be explained by the higher amount of recombination sites due to the high surface area of the mesoporous titania filling. However, this large surface area causes at the same time a drastic increase of photocurrent density from 0.97 to 7.17 mA cm^{-2} and a change in fill factor from 0.52 to 0.71. As a result, the hierarchical structure exhibits a nearly ten times higher conversion efficiency of 4.0 % compared to the unfilled macroporous DSC with an efficiency around 0.4 %.

Table 5.3. Detailed photovoltaic parameters and EQE values of the DSC device based on the inverse opal and hierarchical titania layers 5.5 μm in thickness, in combination with a N179 sensitizer and a volatile redox electrolyte under AM 1.5 sunlight at 100 mW/cm^2 full sun irradiation.

Titania layer	J_{sc}, mA/cm^2	V_{oc}, mV	FF, %	η, %	EQE$_{530nm}$, %
Hier-200-ca	7.17	780	71.4	4.0	23.6
Macro-200	0.97	910	52.6	0.46	5.2

In addition to the I-V characterization, the external quantum efficiency (EQE) of the different photoanode morphologies was determined to elucidate the influence of the macroporous backbone (Figure 5.13). The DSC hierarchical device (Hier-200-ca) has a higher density and surface area compared to the unfilled macroporous device, and shows an increased EQE in the characterized spectral range. At an illumination wavelength of 530 nm, Hier-200-ca has an EQE of about 24 %, more than four times higher than the Macro-200 sample (Table 5.3).
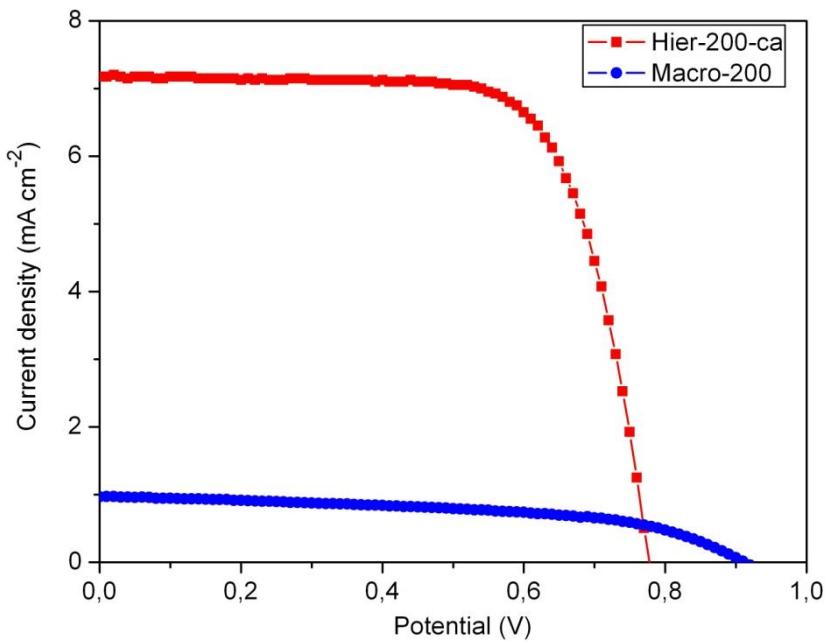
Figure 5.12: Photocurrent-voltage curve of DSC devices based on the inverse opal titania layers (blue, Macro-200) and hierarchical titania layers (red, Hier-200-ca), N179 sensitizer and a volatile redox electrolyte. The titania layer thickness was about 5.5 μm. The photovoltaic performance was measured at air mass 1.5 (100 mW/cm^2) full sunlight illumination. The active cell area was 0.196 cm^2.

The normalized spectral EQE data exhibit slightly broader and shifted features and increased relative EQE values in the blue and in the red (Figure 5.13), which could possibly be attributed to scattering effects. We note that a significant contribution of the photonic crystal structure to the EQE data is rather unlikely with the systems under study. While the hierarchical systems show good long-range order of the macropore-structure, filling the titania-based macropores with porous titania is expected to reduce the refractive index contrast such that photonic effects will be small. On this account, the most important impact of the hierarchical structure is expected to be the high surface area combined with favorable transport properties.
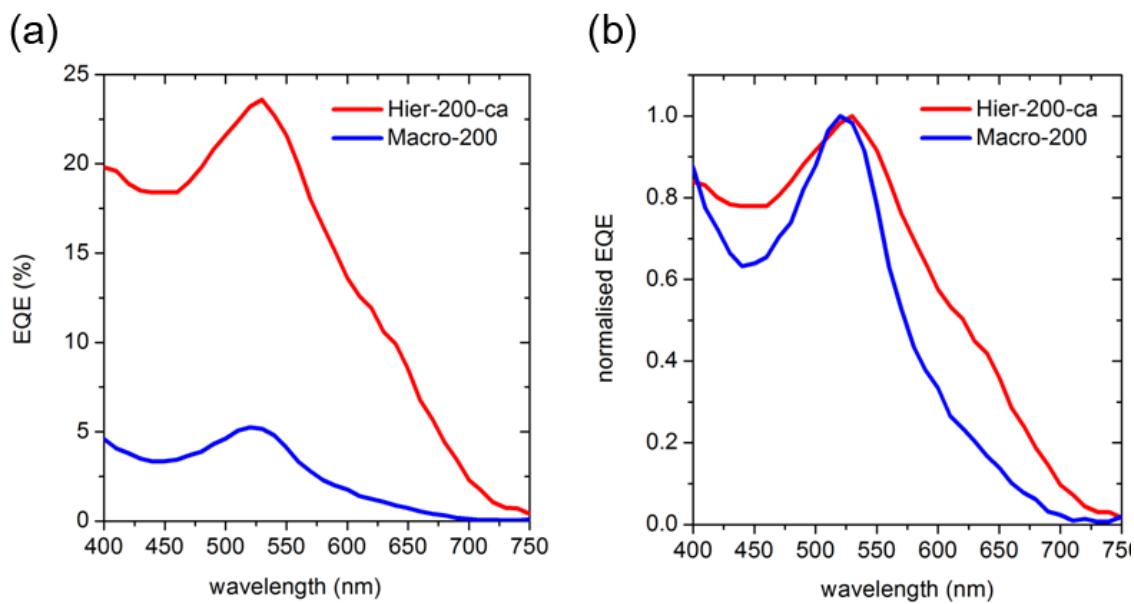
Figure 5.13: Determination of the external quantum efficiency (EQE, left) and the normalized EQE (right) of the different titania morphologies used as DSC photoanodes (N-719 sensitizer, volatile I^-/I_3^- electrolyte). The hierarchical DSC (Hier-200-ca, red line) generates a higher photocurrent, and results in an improved photon-to-electron conversion efficiency compared to the pure macroporous titania reference cell (Macro-200, blue line). Normalized EQE (right): Both measurements are normalized with respect to their maxima, which are slightly shifted (ca. 10 nm, in the green range).

As a proof of principle we further investigated additional templated titania precursors to infiltrate the sol-gel derived macroporous TiO_2 (Figure 5.4 a, b), in a method similar to the one described above. Both samples exhibit a high degree of filling of the individual macropores after calcination, which is in good agreement with Figure 5.5 a. This clearly demonstrates that templated titania nanoparticle solutions are also suitable mixtures for the creation of hierarchical titania with a distinct mesophase.

The building blocks used for the mesoporous phase in Figure 5.14 a are (i) small anatase nanoparticles prepared in a microwave-assisted solvothermal reaction (NP-4, see chapter 4), which were casted from an ethanolic solution containing additional Pluronic F127 as soft-template.[31] In contrast, the mesoporous phase in Figure 5.14 b was formed with solvothermally grown anatase particles (NP-6, see chapter 4), which were combined in a "brick and mortar" approach with some hydrolyzed molecular titania sol-gel precursor (TEOT) and were casted in combination with Pluronic P123, dissolved in THF. The final content of NPs within the total amount of TiO_2 was adjusted to 70 wt%. This solution was used as received from Johann M. Szeifert (dissertation, LMU, 2011), and was well described in the literature.[30]

It is obvious that the smaller well-dispersed NP-4 particles exhibit a homogeneous wetting of the macroporous scaffold, and nearly no shrinkage within the confined space was observed (b). The solution based on NP-6 seemed to have a higher roughness, which might be attributed to partial nanoparticle agglomeration, which was reported for this system.[30]
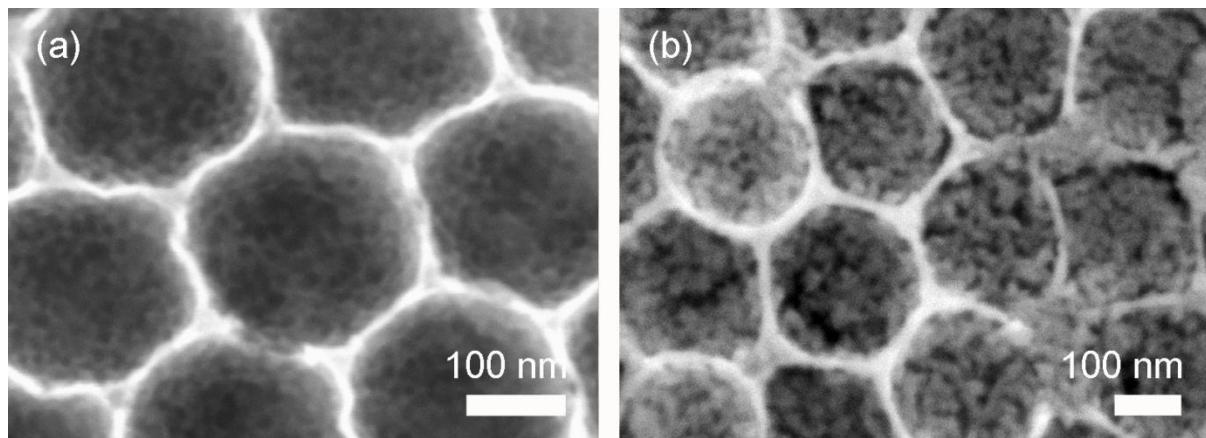
Figure 5.14: SEM top-view images of hierarchical titania films. For mesostructure formation different mixtures of crystalline building blocks, templates and solvents were used. (a) anatase nanoparticles (4 nm) and Pluronic F127 in ethanol. (b) anatase nanoparticles (6 nm), hydrolyzed sol-gel (TEOT) in THF.

5.4. Conclusions

We have developed a strategy for the preparation of a novel type of hierarchical periodic titania nanostructures, composed of a macroporous crystalline scaffold accommodating a mesoporous titania phase. The synthetic approach for these hierarchical structures involves the preparation of inverse opal titania layers followed by the impregnation of interstitial macroporous voids with surfactant-containing titania precursors. This procedure leads to filling of all macropores through the whole film thickness, and formation of a mesoporous phase in each pore of the macroporous host. As follows from *in-situ* GISAXS, TEM and nitrogen adsorption measurements, the macroporous framework significantly influences the mesostructure assembly and leads to much larger structural parameters of the mesostructure. The confinement effect of the macropores on the mesostructure formation becomes more

evident with decreasing pore size of the macroporous host. The inverse opal backbone acts as a stabilizing matrix limiting the shrinkage of the mesopores upon heating, so that the final size of the mesopores in the macroporous matrix is up to 50 % larger than that of a structure made from the same solution on a flat substrate. Furthermore, the highly crystalline macroporous backbone has a synergistic effect on the crystallization of the mesoporous filling, acting as a nucleation site for further crystallization of the initially amorphous titania phase. The hierarchical titania films are completely crystalline after calcination in air at 450 °C and consist of two types of crystalline anatase domains, with crystal sizes of over 20 nm in the macroporous titania walls and about 4-6 nm in the walls of mesoporous material. Sorption measurements of the final hierarchical layers of 5.5 μm thickness show that the resulting porous system is fully accessible, has a high total surface area of 154 m^2/g and an average mesopore size of 6.1 nm, which is about 20 % larger than the pore size of 5.1 nm for the reference mesoporous film obtained on a flat substrate.

We suggest that this hierarchical architecture combining the advantages of both mesoscale and macroscale morphologies, namely, an efficient light harvesting and charge separation in mesoporous titania, and efficient transport of photogenerated electrons through interpenetrating macroscale titania scaffold, could contribute to increasing the light conversion efficiency of dye-sensitized solar cells (DSC). Moreover, future hierarchical systems based on different materials featuring significant refractive index contrast could add additional features such as photonic crystal and backscattering effects that would additionally contribute to the enhancement of overall light conversion efficiency.

5.5. Chapter References

(1)   O'Regan, B.; Graetzel, M. *Nature* **1991**, *353*, 737.

(2)   Sauvage, F.; Di Fonzo, F.; Li Bassi, A.; Casari, C. S.; Russo, V.; Divitini, G.; Ducati, C.; Bottani, C. E.; Comte, P.; Graetzel, M. *Nano Lett.* **2010**, *10*, 2562.

(3)   Qu, Y.; Zhou, W.; Pan, K.; Tian, C.; Ren, Z.; Dong, Y.; Fu, H. *Phys. Chem. Chem. Phys.* **2010**, *12*, 9205.

(4)   Xu, J.; Wang, K.; Zu, S.-Z.; Han, B.-H.; Wei, Z. *ACS Nano* **2010**, *4*, 5019.

(5)   Chen, J. S.; Tan, Y. L.; Li, C. M.; Cheah, Y. L.; Luan, D.; Madhavi, S.; Boey, F. Y. C.; Archer, L. A.; Lou, X. W. *J. Am. Chem. Soc.* **2010**, *132*, 6124.

(6)   Kavan, L.; Zukalova, M.; Kalbac, M.; Graetzel, M. *J. Electrochem. Soc.* **2004**, *151*, A1301.

(7)   Wang, Y. J.; Caruso, F. *Adv. Funct. Mater.* **2004**, *14*, 1012.

(8)   Burazerovic, S.; Gradinaru, J.; Pierron, J.; Ward, T. R. *Angew. Chem. Int. Ed.* **2007**, *46*, 5510.

(9)   Jin, L.; Zhai, J.; Heng, L.; Wei, T.; Wen, L.; Jiang, L.; Zhao, X.; Zhang, X. *J. Photochem. Photobiol. C* **2009**, *10*, 149.

(10)   Kim, J.; Bhattacharjee, S.; Jeong, K. E.; Jeong, S. Y.; Choi, M.; Ryoo, R.; Ahn, W. S. *New J. Chem.* **2010**, *34*, 2971.

(11)   Kuang, D. B.; Brezesinski, T.; Smarsly, B. *J. Am. Chem. Soc.* **2004**, *126*, 10534.

(12)   Fan, W.; Snyder, M. A.; Kumar, S.; Lee, P. S.; Yoo, W. C.; McCormick, A. V.; Penn, R. L.; Stein, A.; Tsapatsis, M. *Nature Mater.* **2008**, *7*, 984.

(13)   Snaith, H. J.; Schmidt-Mende, L. *Adv. Mater.* **2007**, *19*, 3187.

(14)   Graetzel, M. *J. Photochem. Photobiol. C* **2003**, *4*, 145.

(15)   Graetzel, M. *Nature Mater.* **2001**, *414*, 338.

(16)   Chiba, Y.; Islam, A.; Watanabe, Y.; Komiya, R.; Koide, N.; Han, L. *Jpn. J. Appl. Phys. 2* **2006**, *45*, L638.

(17)   Guldin, S.; Huttner, S.; Kolle, M.; Welland, M. E.; Muller-Buschbaum, P.; Friend, R. H.; Steiner, U.; Tetreault, N. *Nano Lett.* **2010**, *10*, 2303.

(18)   Nishimura, S.; Abrams, N.; Lewis, B. A.; Halaoui, L. I.; Mallouk, T. E.; Benkstein, K. D.; van de Lagemaat, J.; Frank, A. J. *J. Am. Chem. Soc.* **2003**, *125*, 6306.

(19)   Mihi, A.; Miguez, H. *J. Phys. Chem. B* **2005**, *109*, 15968.

(20)   Halaoui, L. I.; Abrams, N. M.; Mallouk, T. E. *J. Phys. Chem. B* **2005**, *109*, 6334.

(21)   Mihi, A.; Calvo, M. E.; Anta, J. A.; Miguez, H. *J. Phys. Chem. C* **2008**, *112*, 13.

(22)   Liu, Z.; Subramania, V.; Misra, M. *J. Phys. Chem. C* **2009**, *113*, 14028.

(23)   Kuang, D.; Brillet, J.; Chen, P.; Takata, M.; Uchida, S.; Miura, H.; Sumioka, K.; Zakeeruddin, S. M.; Graetzel, M. *ACS Nano* **2008**, *2*, 1113.

(24)   Zhu, K.; Vinzant, T. B.; Neale, N. R.; Frank, A. J. *Nano Lett.* **2007**, *7*, 3739.

(25)   Kwak, E. S.; Lee, W.; Park, N. G.; Kim, J.; Lee, H. *Adv. Funct. Mater.* **2009**, *19*, 1093.

(26)   Pan, H.; Feng, Y. P. *ACS Nano* **2008**, *2*, 2410.

(27)   Tetreault, N.; Horvath, E.; Moehl, T.; Brillet, J.; Smajda, R.; Bungener, S.; Cai, N.; Wang, P.; Zakeeruddin, S. M.; Forro, L.; Magrez, A.; Graetzel, M. *ACS Nano* **2010**, *4*, 7644.

(28)   Jennings, J. R.; Ghicov, A.; Peter, L. M.; Schmuki, P.; Walker, A. B. *J. Am. Chem. Soc.* **2008**, *130*, 13364.

(29)   Zukalova, M.; Zukal, A.; Kavan, L.; Nazeeruddin, M. K.; Liska, P.; Graetzel, M. *Nano Lett.* **2005**, *5*, 1789.

(30)   Szeifert, J. M.; Fattakhova-Rohlfing, D.; Georgiadou, D.; Kalousek, V.; Rathousky, J.; Kuang, D.; Wenger, S.; Zakeeruddin, S. M.; Graetzel, M.; Bein, T. *Chem. Mater.* **2009**, *21*, 1260.

(31)   Szeifert, J. M.; Feckl, J. M.; Fattakhova-Rohlfing, D.; Liu, Y. J.; Kalousek, V.; Rathousky, J.; Bein, T. *J. Am. Chem. Soc.* **2010**, *132*, 12605.

(32)   Prochazka, J.; Kavan, L.; Shklover, V.; Zukalova, M.; Frank, O.; Kalbac, M.; Zukal, A.; Pelouchova, H.; Janda, P.; Mocek, K.; Klementova, M.; Carbone, D. *Chem. Mater.* **2008**, *20*, 2985.

(33)   Zukalova, M.; Prochazka, J.; Zukal, A.; Yum, J. H.; Kavan, L. *Inorg. Chim. Acta* **2008**, *361*, 656.

(34)   Chou, T. P.; Zhang, Q.; Russo, B.; Fryxell, G. E.; Cao, G. *J. Phys. Chem. C* **2007**, *111*, 6296.

(35)   Kim, D.; Ghicov, A.; Albu, S. P.; Schmuki, P. *J. Am. Chem. Soc.* **2008**, *130*, 16454.

(36)   Albu, S. R.; Kim, D.; Schmuki, P. *Angew. Chem. Int. Ed.* **2008**, *47*, 1916.

(37)   Costacurta, S.; Biasetto, L.; Pippel, E.; Woltersdorf, J.; Colombo, P. *J. Am. Ceram. Soc.* **2007**, *90*, 2172.

(38)   Angelome, P. C.; Fuertes, M. C.; Soler-Illia, G. *Adv. Mater.* **2006**, *18*, 2397.

(39)   Wang, T.; Sel, O.; Djerdj, I.; Smarsly, B. *Colloid and Polymer Science* **2006**, *285*, 1.

(40)   Galusha, J. W.; Tsung, C.-K.; Stucky, G. D.; Bartl, M. H. *Chem. Mater.* **2008**, *20*, 4925.

(41)   Prochazka, J.; Kavan, L.; Zukalova, M.; Frank, O.; Kalbac, M.; Zukal, A.; Klementova, M.; Carbone, D.; Graetzel, M. *Chem. Mater.* **2009**, *21*, 1457.

(42)   Wang, K. X.; Wei, M. D.; Morris, M. A.; Zhou, H. S.; Holmes, J. D. *Adv. Mater.* **2007**, *19*, 3016.

(43)   Keilbach, A.; Doblinger, M.; Kohn, R.; Amenitsch, H.; Bein, T. *Chem. Eur. J.* **2009**, *15*, 6645.

(44)   Platschek, B.; Petkov, N.; Himsl, D.; Zimdars, S.; Li, Z.; Kohn, R.; Bein, T. *J. Am. Chem. Soc.* **2008**, *130*, 17362.

(45)   Platschek, B.; Petkov, N.; Bein, T. *Angew. Chem. Int. Ed.* **2006**, *45*, 1134.

(46)   Alberius, P. C. A.; Frindell, K. L.; Hayward, R. C.; Kramer, E. J.; Stucky, G. D.; Chmelka, B. F. *Chem. Mater.* **2002**, *14*, 3284.

(47)   Ito, S.; Murakami, T. N.; Comte, P.; Liska, P.; Graetzel, C.; Nazeeruddin, M. K.; Graetzel, M. *Thin Solid Films* **2008**, *516*, 4613.

6. Spherical mesoporous titania

6.1. Introduction

In this chapter we describe the synthetic strategy to create mesoporous titania spheres by the use of a macroporous silica hard template. This is a two-step approach, which implies a previous replication of polymer bead arrays[1], in our case PMMA spheres, with a molecular silica precursor. This route was also successfully applied for the synthesis of mesoporous carbon spheres having different sizes (see chapter 7 and 8). Alternatively, various routes and applications were recently reported and summarized for spherical titania.[2] Hollow spheres are usually based on the direct precursor assembly on the surface of spherical hard templates, which are later removed.[3-10] Hydrothermal[11-14] and solvothermal[15-17] processing are common methods to create spherical titania. A related microwave-assisted route was also reported.[18] A further interesting technique to achieve high amounts of material is based on spraying a titania precursor solution that is transported by a carrier gas through heating zones where the formed droplets densify (aerosol-assisted self-assembly). Usually the materials are based on anatase, which was used for DSCs[19-21] and related devices[22] or photocatalysis.[23,24] Spherical titania composed of rutile was also used in a DSC.[25] For example, arrays of spherical titania beads (< 1 μm) were applied as additional scattering layer or directly as active photoanode. For the latter an increase of the surface area was intended, which was achieved by roughening of the beads´ surface[8,26-28], or by introducing a defined mesoporosity[7,29-32], which could also result from agglomerates of nanoparticles generated by phase separation in emulsions.[27,33]

We used a modified strategy of Chen et al.,[34] which we also adapted to the synthesis of mesoporous spherical carbon (chapter 7).[35] In this chapter we show a replication route for mesoporous titania. They replicated an array of monodisperse silica spheres and created a three dimensional ordered macroporous (3DOM) PMMA scaffold, after removing the silica hard template (290 nm silica spheres) with HF. The macropores were then filled by imbibition with a hydrolyzed titanium tetraisopropoxide precursor solution and Pluronic P123 as template. After calcination (400 °C for 4 h) mesoporous spherical anatase was formed, exhibiting mesopore diameters in the range of 3-5 nm and crystallite sizes of 7-10 nm. The BET surface area was determined to be 145 m^2/g, accompanied by a pore volume of 0.246 cm^3/g. However, the final sphere size was 165 nm, corresponding to strong shrinkage of around 40 %.

Here we describe the preparation of macroporous silica[36], interpenetrated with a mesoporous titania phase[37] and an investigation of the resulting crystalline mesoporous titania spheres (~ 220 nm), obtained after calcination at 300 °C and 400 °C, respectively, and subsequent removal of silica (NaOH). The samples were characterized by SEM, TEM, XRD and nitrogen sorption measurements.

6.2. Experimental Section

The used chemicals and a detailed synthesis description for emulsion polymerization of PMMA spheres and the following preparation of the macroporous silica hard template are presented in detail in chapter 7.

Synthesis of spherical TiO$_2$

Millimeter sized pieces of macroporous SiO$_2$ were collected in a petri dish, before a titania precursor solution was applied. This precursor mixture and the further calcination procedure are based on the preparation of mesoporous thin films.[37]

To tetraethyl orthotitanate (1 g, 4.38 mmol, TEOT, Ti(OCH$_2$CH$_3$)$_4$) hydrochloric acid (37%, 762 mg, 7.4 mmol) was added dropwise, and the mixture was stirred for 15 minutes at room temperature to get a clear solution. Than an ethanolic solution of Pluronic P123 (238 mg, 0.05 mmol) was dissolved in ethanol (3.6 mL) added and stirring was continued for additional 15 minutes at room temperature. The solution was cast on the mm-sized pieces of macroporous silica and dried at 60 °C. Some titania bulk material was formed at the bottom of the petri dish between interstitials between the silica pieces. This titania excess was carefully removed mechanically and only single pieces of macroporous silica containing amorphous titania/ P123 were further used. The composite was heated with 1 °C/ min and calcined in air at 300 °C or 400 °C for at least 4 h, respectively. For silica etching, the solid material was treated with an excess of NaOH (1M) at 60 °C for 1 day and was washed by centrifugation followed by two times redispersion in pure water (MilliporeQ) and one time in absolute ethanol.

TEM images and SAED patterns were acquired with a JEOL JEM-2011 electron microscope operating at 200 keV.

XRD, STEM-HAADF, and nitrogen sorption measurements were performed in a way similar to the description for previous samples in chapter 6 and are not further described in this section.

6.3. Results and Discussion

Mesoporous titania spheres were made by a two step templating approach. Our first template was bulk material consisting of dried and loosely packed PMMA spheres (~320 nm). The synthesis via emulsion polymerization is described in chapter 3. The bulk was slightly crushed, leading to rough surfaces, and collected on a filter paper (Figure 6.1. a). The PMMA spheres were only dried at room temperature and not further connected by applying thermal annealing.[38,39] A hydrolyzed solution of tetraethyl orthosilicate (TEOS; $Si(OCH_2CH_3)_4$) was cast on the PMMA bulk to fill the interstitial voids and excess precursor was removed by applying vacuum. Then a subsequent calcination at 550 °C combusted the polymer template completely, which was accompanied by consolidation of the precursor species, and a three dimensional interconnected macroporous silica bulk material was formed.[36] FE-SEM and TEM images in Figure 6.1 b, c represent the corresponding morphology, featuring a high accessibility for further material diffusion provided by macropore diameters of around 220 nm and interpore connections in the range of 50 nm. Thus a heating-induced shrinkage was

observed, similar to other studies[35,36,40], which amounts to ca. 32 % less than the initial template size.

Ordered mesoporous titania thin films were intensively studied by Alberius et al.[37] and prepared by evaporation-induced self-assembly (EISA) of the block copolymer Pluronic P123, the second template, and a hydrolyzed solution of tetraethyl orthotitanate. This mixture was adapted for lithium-insertion[41] and modified by our group and applied for the synthesis of high surface area photoanodes in dye-sensitized solar cells.[42,43] We also used this mixture to create and study hierarchical titania, composed of a highly crystalline macroporous scaffold which is interpenetrated by a mesoporous titania phase[40] (chapter 5).

In this study the precursor solution was cast on the macroporous silica hard template, dried at room temperature and calcined in air. After heating at 300 °C, Pluronic P123 was removed thus creating mesoporous titania. The TEM image in Figure 6.1 d shows good macropore filling, but also some shrinkage of the filling was observed accompanied by some beam damage during TEM investigation, which we attribute to the mainly amorphous character of sol-gel derived titania. For this reason some brighter areas around and between silica and titania were attributed to less dense matter.
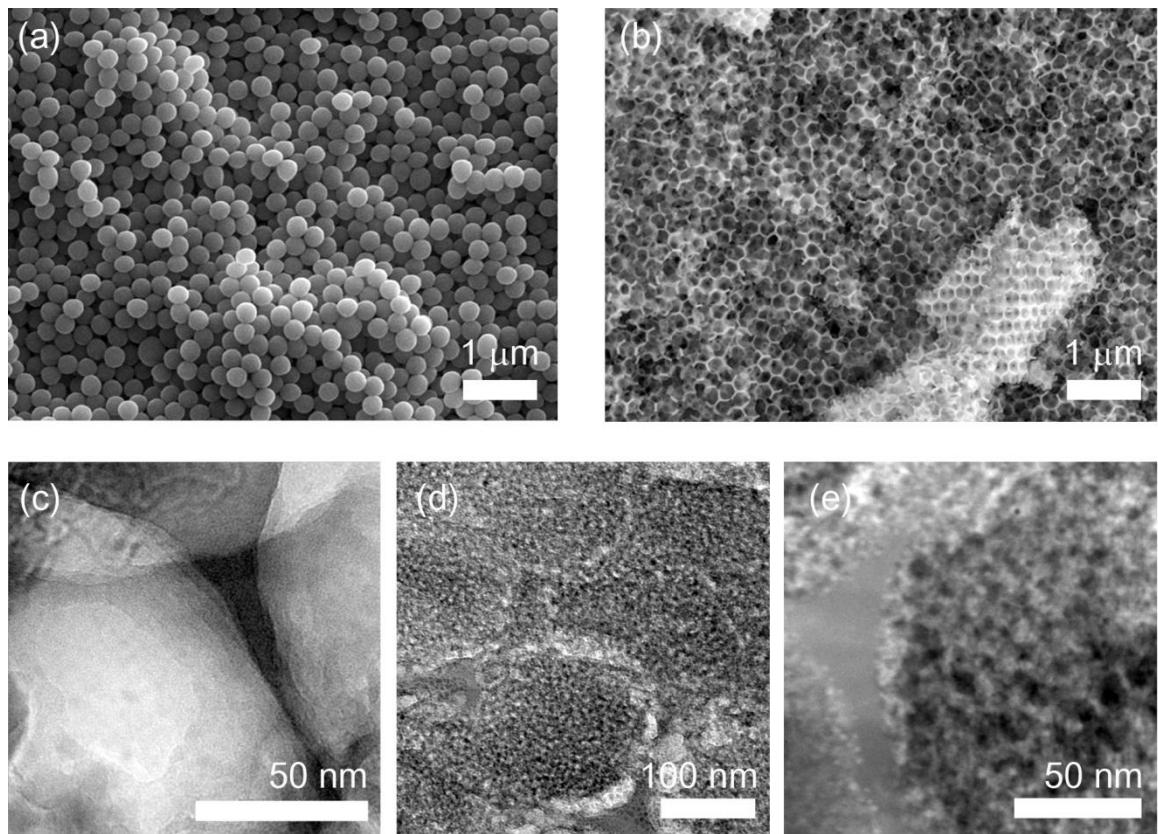
Figure 6.1: (a) SEM images of loosely packed PMMA particles of around 320 nm. (b, c) SEM and TEM image of macroporous SiO_2 replica obtained after silica precursor infiltration and calcination at 550 °C, exhibiting pore diameters of ca. 220 nm and inter pore connection windows in the range of 50 nm. (d, e) TEM and STEM-HAADF image of hierarchical macroporous silica/ mesoporous titania after precursor imbibition and final calcination at 300 °C.

The STEM-HAADF image (Figure 6.1 e) clearly demonstrates the mesoporosity and shows the contrast difference between the dense macroporous silica scaffold (homogenous grayish) and the brighter titania phase, which is interrupted by dark areas indicating mesopores (< 10 nm).

To obtain individual mesoporous spherical titania, which was calcined at 300 °C and 400°C, respectively, macroporous silica was removed by etching in NaOH (1M) at 60 °C for 1 d. The spheres were further washed in water and ethanol by centrifugation. The pellet was dispersed by stirring (ultrasonic treatment partially destroys the spheres). The resulting white and turbid ethanolic solutions contained arrays of packed mesoporos titania spheres. The TEM images (Figure 6.2 a, c) show mesoporous titania spheres after calcination (300°C) and washing. The individual spheres exhibit diameters in the range of 210 – 230 nm, comparable to the macropore diameters (Figure 6.1 b), which indicates very small heating-induced shrinkage during mesostructure formation in the confined space of the macroporous silica. The HR-TEM image (Figure 6.2 b) of the spheres shows small crystals in the range of 3-7 nm, thus leading to diffuse diffraction rings within the SAED pattern.

An EDX spectrum was recorded (white square) on a single mesoporous titania sphere, shown in the STEM-HAADF image in Figure 6.2 c. The obtained spectrum (d) shows defined peaks for titanium and oxygen suggesting the presence of TiO_2. The peaks for carbon and copper are attributed to the TEM grid. We note that peaks for Si and Na also occur, which led us conclude that one time etching and three time washing was not sufficient for full removal of residues. TEM images in 6.2 e, f show the corresponding sample (400 °C) at different magnifications. Similar to the sample calcined at 300 °C the hierarchical silica/ titania composite was treated with NaOH and finally washed. It is obvious that calcination at higher temperature improved the crystallinity, as demonstrated by the presence of anatase crystallites sized about 10 to 12 nm. This effect and the polycrystalline behavior is also represented the SAED pattern (6.2. f inset).
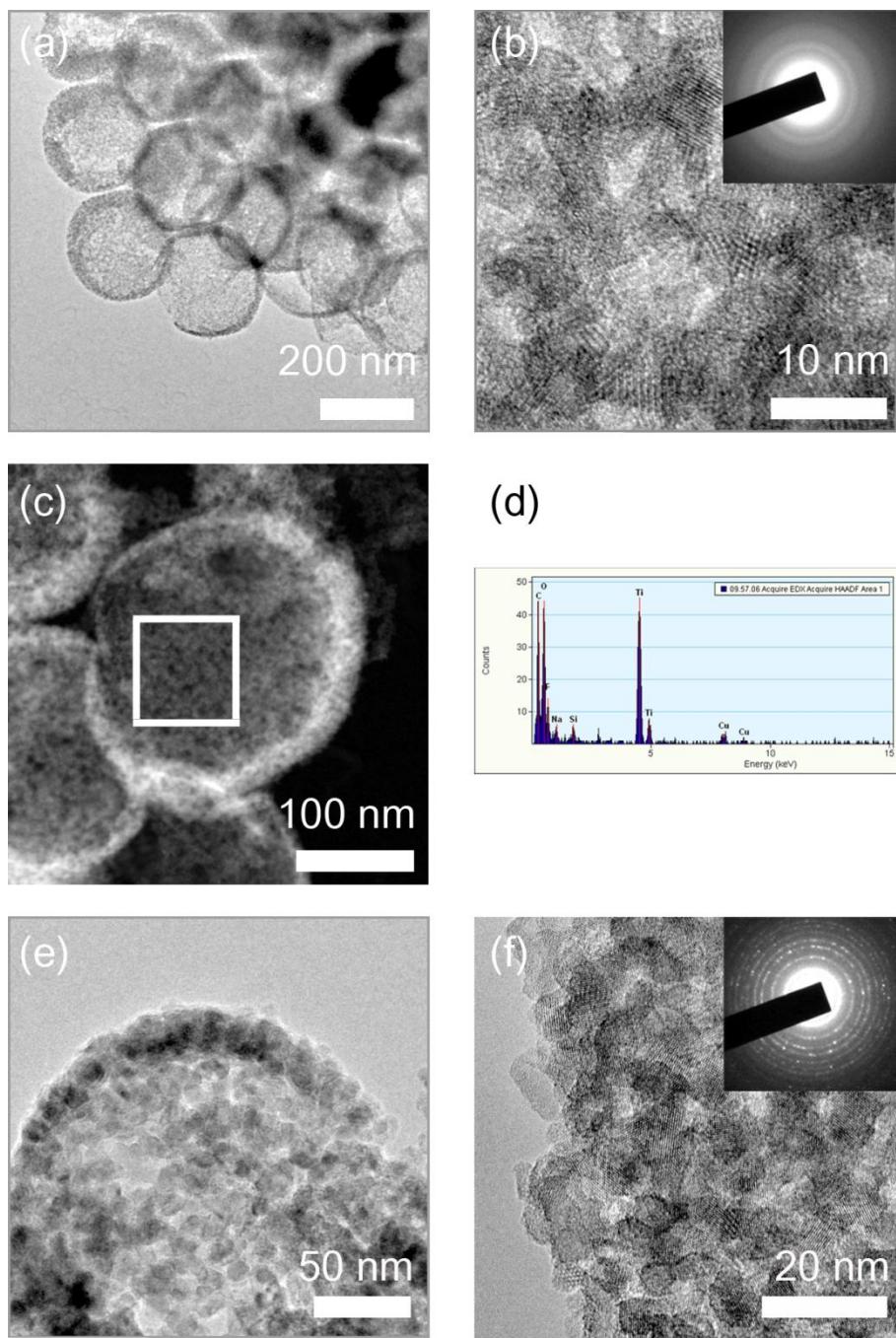
Figure 6.2: TEM and SAED (inset) of mesoporous spherical titania calcined at 300 °C (a, b) and 400°C (e, f), respectively. STEM-HAADF image (c) after calcining at 300 °C, and EDX spectrum (d) was collected from the white squared area.

Nitrogen sorption (Figure 6.3 a) was employed to estimate BET surface areas of 313 m^2/g and 119 m^2/g for the 300 and 400 °C samples, respectively. Broad pore size distributions with major peaks at 5.1 and 6.7 nm and pore volumes of 0.47 and 0.38 cm^2/g were observed for the sample calcined at 300 °C (black curves) and 400 °C (red curves), respectively. With increasing calcination temperature the randomly oriented crystals grow and present larger textural features (Figure 6.2).

The XRD pattern (Figure 6.3 b) of both samples exhibits reflections at 25.4 °/ 2θ and 37.8 °/ 2θ, which were attributed to the anatase 101 and 004 lattice planes. After heating to 300 °C only a weak broad intensity distribution indicates the 101 planes, which indicates the presence of very small crystals as shown by TEM (Figure 6.2 b) and SAED (inset), as well as a higher amorphous content.

In the literature promoted crystal growth of TEOT derived titania was induced by the presence of already crystalline titania in the form of colloidal anatase nanoparticles (NP-6, chapter 3)[42] or a polycrystalline macroporous scaffold (chapter 5)[40]. We suggest that the smooth surface of macroporous silica could also act as nucleaction site for the heating-induced crystallization of the molecular precursor (TEOT). A mean crystallite domain size of 13 nm (400 °C sample) was extracted from the XRD using the Scherrer equation, which is in good agreement with TEM measurements (Figure 6.2 d). This is also similar to the size of 12 nm observed elsewhere in thin mesoporous films, derived for a comparable precursor mixture and calcination protocol.[41]
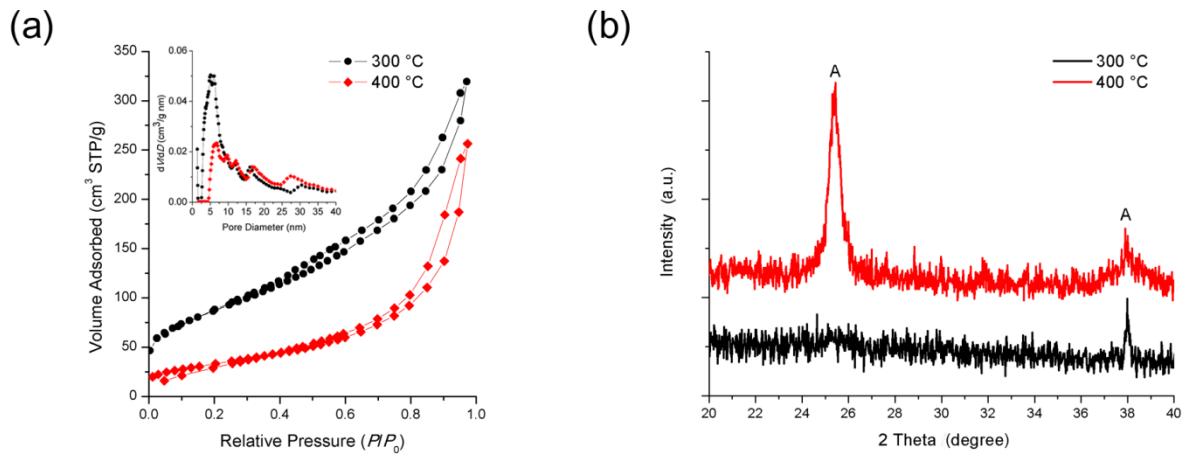
Figure 6.3: (a) Isotherms and pore size distributions (inset) obtained from nitrogen sorption measurements of spherical mesoporous titania calcined at 300 °C (black) and 400 °C (red), respectively. (b) XRD measurement of anatase (A) in the range of 20 to 40 °/ 2 Theta of these samples.

6.4. Conclusions

A two-step replication procedure to prepare crystalline mesoporous titania spheres is demonstrated. The first replication step is based on the conversion of an array of PMMA particles into macroporous silica, by infiltrating the interstitials with a silica sol-gel precursor and subsequent thermal combustion of the polymer template. Secondly the silica hard template was infiltrated with a mixture of titania sol-gel precursor solution and a block-copolymer template Pluronic P123. Calcination up to 300 °C and 400 °C induces titania crystallization and mesostructure formation by removing P123. The corresponding morphologies, hierarchical SiO_2/ TiO_2 composite and spherical titania particles, were studied before and after removal of the macroporous silica template, respectively, using a solution of sodium hydroxide. The resulting spheres are (partially) composed of nanocrystalline anatase and calcination at 300 °C lead to a highest surface area of 313 m^2/g, pores of ca. 5 nm and a pore volume of 0.47 cm^3/ g. Nitrogen sorption after calcination at 400 °C exhibit a reduction in surface area (119 m^2/g), 6.7 nm large pores and pore volume of 0.38 cm^2/g. The developed templating approach can be generalized and used for the synthesis of other spherical nanostructures, as long as the precursor solutions cause no strong dissolution of the macroporous silica hard template.

6.5. Chapter References

(1)   Ye, J., Dissertation, Johannes Gutenberg-Universität, Mainz,, 2007.

(2)   Chen, D.; Caruso, R. A. *Adv. Funct. Mater.* **2012**, Article first published online: 18 October 2012

(3)   Shi, J. W.; Zong, X.; Wu, X.; Cui, H. J.; Xu, B.; Wang, L. Z.; Fu, M. L. *ChemCatChem* **2012**, *4*, 488.

(4)   Zeng, Y.; Wang, X.; Wang, H.; Dong, Y.; Ma, Y.; Yao, J. *Chem. Commun.* **2010**, *46*, 4312.

(5)   Wang, Y.; Su, X.; Lu, S. *J. Mater. Chem.* **2012**, *22*, 1969.

(6)   Zhuang, J.; Tian, Q.; Zhou, H.; Liu, Q.; Liu, P.; Zhong, H. *J. Mater. Chem.* **2012**, *22*, 7036.

(7)   Li, W.; Zhao, D. *Adv. Mater.* **2012**, n/a.

(8)   Pan, H.; Qian, J.; Cui, Y.; Xie, H.; Zhou, X. *J. Mater. Chem.* **2012**, *22*, 6002.

(9)   Dadgostar, S.; Tajabadi, F.; Taghavinia, N. *ACS Appl. Mater. Interfaces* **2012**, *4*, 2964.

(10)   Kimling, M. C.; Caruso, R. A. *J. Mater. Chem.* **2012**, *22*, 4073.

(11)   Yang, W.; Li, J.; Wang, Y.; Zhu, F.; Shi, W.; Wan, F.; Xu, D. *Chem. Commun.* **2011**, *47*, 1809.

(12)   Liu, B.; Nakata, K.; Sakai, M.; Saito, H.; Ochiai, T.; Murakami, T.; Takagi, K.; Fujishima, A. *Catal. Sci. Technol.* **2012**, *2*, 1933.

(13)   Zhang, H.; Liu, P.; Li, F.; Liu, H.; Wang, Y.; Zhang, S.; Guo, M.; Cheng, H.; Zhao, H. *Chem. Eur. J.* **2011**, *17*, 5949.

(14)   Yu, I. G.; Kim, Y. J.; Kim, H. J.; Lee, C.; Lee, W. I. *J. Mater. Chem.* **2011**, *21*, 532.

(15)   Sun, X.; Liu, Y.; Tai, Q.; Chen, B.; Peng, T.; Huang, N.; Xu, S.; Peng, T.; Zhao, X.-Z. *J. Phys. Chem. C* **2012**, *116*, 11859.

(16)   Xu, X.; Jiang, G.; Wan, Q.; Shi, J.; Xu, G.; Miao, L. *Mater. Chem. Phys.* **2012**, *136*, 1060.

(17)   Park, Y.-C.; Chang, Y.-J.; Kum, B.-G.; Kong, E.-H.; Son, J. Y.; Kwon, Y. S.; Park, T.; Jang, H. M. *J. Mater. Chem.* **2011**, *21*, 9582.

(18)   Wang, H.-E.; Zheng, L.-X.; Liu, C.-P.; Liu, Y.-K.; Luan, C.-Y.; Cheng, H.; Li, Y. Y.; Martinu, L.; Zapien, J. A.; Bello, I. *J. Phys. Chem. C* **2011**, *115*, 10419.

(19)   Hwang, D.; Lee, H.; Seo, Y.; Kim, D.; Jo, S. M.; Kim, D. Y. *J. Mater. Chem.* **2013**, *1*, 1359.

(20)   Cha, S. I.; Koo, B. K.; Hwang, K. H.; Seo, S. H.; Lee, D. Y. *J. Mater. Chem.* **2011**, *21*, 6300.

(21)   Zhang, Y.; Shi, Y.; Liou, Y.-H.; Sawvel, A. M.; Sun, X.; Cai, Y.; Holden, P. A.; Stucky, G. D. *J. Mater. Chem.* **2010**, *20*, 4162.

(22)   Roh, D. K.; Seo, J. A.; Chi, W. S.; Koh, J. K.; Kim, J. H. *J. Mater. Chem.* **2012**, *22*, 11079.

(23)   Zhang, H.; Du, G.; Lu, W.; Cheng, L.; Zhu, X.; Jiao, Z. *CrystEngComm* **2012**, *14*, 3793.

(24)   Patra, A. K.; Das, S. K.; Bhaumik, A. *J. Mater. Chem.* **2011**, *21*, 3925.

(25)   Lan, C.-M.; Liu, S.-E.; Shiu, J.-W.; Hu, J.-Y.; Lin, M.-H.; Diau, E. W.-G. *RSC Adv.* **2013**, *3*, 559.

(26)   Wu, D.; Wang, Y.; Dong, H.; Zhu, F.; Gao, S.; Jiang, K.; Fu, L.; Zhang, J.; Xu, D. *Nanoscale* **2013**, *5*, 324.

(27)   Chen, D.; Huang, F.; Cao, L.; Cheng, Y.-B.; Caruso, R. A. *Chem. Eur. J.* **2012**, *18*, 13762.

(28)   Zhu, F.; Wu, D.; Li, Q.; Dong, H.; Li, J.; Jiang, K.; Xu, D. *RSC Adv.* **2012**, *2*, 11629.

(29)   Chen, D.; Huang, F.; Cheng, Y.-B.; Caruso, R. A. *Adv. Mater.* **2009**, *21*, 2206.

(30)   Gao, Z.; Yang, J.; Cheng, Q.; Tian, L.; Jiang, K.; Yang, L. *Mater. Chem. Phys.* **2013**, *137*, 866.

(31)   Hong, M. P.; Kim, J. Y.; Vemula, K.; Kim, H. S.; Yoon, K. B. *Chem. Commun.* **2012**, *48*, 4250.

(32)   Chen, Y.; Huang, F.; Chen, D.; Cao, L.; Zhang, X. L.; Caruso , R. A.; Cheng, Y.-B. *ChemSusChem* **2011**, *4*, 1498.

(33)   Cheng, W.-Y.; Deka, J. R.; Chiang, Y.-C.; Rogeau, A.; Lu, S.-Y. *Chem. Mater.* **2012**, *24*, 3255.

(34)   Chen, J.; Hua, Z.; Yan, Y.; Zakhidov, A. A.; Baughman, R. H.; Xu, L. *Chem. Commun.* **2010**, *46*, 1872.

(35)   Schuster, J.; He, G.; Mandlmeier, B.; Yim, T.; Lee, K. T.; Bein, T.; Nazar, L. F. *Angew. Chem.* **2012**, *124*, 3651.

(36)   Holland, B. T.; Blanford, C. F.; Stein, A. *Science* **1998**, *281*, 538.

(37)   Alberius, P.; Frindell, K.; Hayward, R.; Kramer, E.; Stucky, G.; Chmelka, B. *Chem. Mater.* **2002**, *14*, 3284.

(38)   Li, B.; Zhou, J.; Li, L.; Gui, Z. *J. Mater. Sci.* **2005**, *40*, 2611.

(39)   Kietzke, T.; Neher, D.; Landfester, K.; Montenegro, R.; Guntner, R.; Scherf, U. *Nat Mater* **2003**, *2*, 408.

(40)   Mandlmeier, B.; Szeifert, J. M.; Fattakhova-Rohlfing, D.; Amenitsch, H.; Bein, T. *J. Amer. Chem. Soc.* **2011**, *133*, 17274.

(41)   Fattakhova-Rohlfing, D.; Wark, M.; Brezesinski, T.; Smarsly, B. M.; Rathousky, J. *Adv. Funct. Mater.* **2007**, *17*, 123.

(42)   Szeifert, J. M.; Fattakhova-Rohlfing, D.; Georgiadou, D.; Kalousek, V.; Rathousky, J.; Kuang, D.; Wenger, S.; Zakeeruddin, S. M.; Gratzel, M.; Bein, T. *Chem. Mater.* **2009**, *21*, 1260.

(43)   Szeifert, J. M.; Fattakhova-Rohlfing, D.; Rathousky, J.; Bein, T. *Chem. Mater.* **2012**, *24*, 659.

7. Spherical Ordered Mesoporous Carbon Nanoparticles with Extremely High Porosity for Lithium-Sulfur Batteries

The synthetic strategy and sample preparation described here was developed in cooperation with my colleague Jörg Schuster (LMU Munich). The electrode preparation and further electrochemical characterization, TGA and nitrogen sorption of C/S composites was gratefully done in cooperation with Prof. Linda Nazar, Guang He and co-workers at the University of Waterloo (Canada)*.

This chapter is based on the following publication:

7.1. Introduction

Rechargeable lithium sulfur (Li-S) batteries are attracting increasing attention due to their high theoretical specific energy density, which is 3 to 5 times higher than that of Li-ion batteries based on intercalation chemistry.[1] Since the electronic conductivity of sulfur is extremely low,[2,3] conductive carbon materials with high accessible porosity to "wire" and contain the sulfur are an essential component of the positive electrode. During the past two decades, various attempts have been made to fabricate C/S composites using carbon black,[4] activated carbons (ACs)[5] and carbon nanotubes (CNTs).[6,7] Although some improvements resulted, the cathodes suffered from inhomogeneous contact between the active materials and the electronic conductors. A major step forward in fabricating a uniform C/S composite was

reported in 2009. Some of us employed CMK-3, an ordered mesoporous carbon (OMC) featuring high specific surface area and large pore volume as a scaffold.[8] As much as 70 wt% sulfur was incorporated into the uniform 3-4 nm mesopores, and the cells exhibited discharge capacities up to 1350 mAh/g, albeit at moderate rates. Inspired by this, another OMC, a bulk bimodal mesoporous carbon (BMC-1) was synthesized and investigated as a Li-S cathode.[9,10] The favorable pore dimensions and large pore volume greatly improved the rate performance of the sulfur cathodes. An electrode with 40 wt% S showed a high initial discharge capacity of 1135 mAh/g at a current rate of 1.0 C (defined as discharge/charge in one hour). However, similar to other reports,[11,12] the capacity is very sensitive to the sulfur ratio in the C/S composite. It drops to 718 mAh/g once the sulfur content increases to 60 wt%, which reduces the gravimetric energy density advantage. These results suggest that the texture of the mesoporous carbon could be further enhanced. Very recently, Archer et al. reported sulfur infused nanoscale hollow porous carbon spheres prepared via an elaborate vapor method.[13] Despite the relatively poor rate capability of the cathodes, they displayed remarkable cyclability and good capacity, illustrating the advantages of nano-sized porous carbon in the sulfur cathodes.

Here we report the synthesis of unique nanoscale spherical OMCs with extremely high bimodal porosities. The particles were investigated as a cathode material and sulfur host in Li-S batteries where they showed high initial discharge capacity and good cyclability without sacrificing rate capability. Unlike bulk porous carbons, these carbon-sulfur sphere electrodes did not display significant capacity fading with the increase of sulfur content in the cathodes. We show that the nanoscale morphology of these materials is of key importance for ensuring highly efficient use of the sulfur content even at high cycling rates. Morphology control is a central issue in OMC[14-16] synthesis. There are numerous examples of mesoporous bulk materials obtained either by hard-templating[17-21] or soft-templating,[22-25] including thin

films,[26-29] membranes[30-34] or free fibers.[32,35,36] Most syntheses use evaporation-induced self-assembly (EISA) followed by thermal treatment for template-removal and carbonization. It is a challenge to either create solution-based OMC nanoparticle syntheses or to adapt the established EISA methods to nanoparticles.

Only few examples of OMC nanoparticles have been reported so far which are mainly limited for application in Li-S cells due to low pore volume and/or surface area. Approaches include templating with PMMA colloidal crystals[37] or mesoporous silica nanoparticles,[38] aerosol-assisted synthesis[39], ultrasonic emulsification[40] or hydrothermal synthesis.[41] Ordered arrays of fused mesoporous carbon spheres were reported by Liu et al. using macroporous silica as template.[42] Recently Lei et al.[43] reported the synthesis of 65 nm mesoporous carbon nanospheres, with both 2.7 nm mesopores and high textural porosity (surface area of 2400 m^2/g; total pore volume of 2.9 cm^3/g). These showed promising supercapacitor properties.

Our spherical OMC nanoparticles of 300 nm in diameter, prepared by a novel method, can be dispersed in water by sonification to form stable colloidal suspensions. The spherical mesoporous carbon nanoparticles were obtained in a two-step casting process. An opal structure of PMMA spheres was cast with a silica precursor solution to form a silica inverse opal. The inverse opal was then used as template for a triconstituent precursor solution containing resol as the carbon precursor, tetraethyl orthosilicate (TEOS) as the silica precursor and the block copolymer Pluronic F127 as a structure directing agent.[22] Carbonization was followed by etching of the silica template and the silica in the carbon/silica nanocomposite, resulting in the formation of OMC with hierarchical porosity. Through the

presence of silica in the walls, shrinkage during carbonization is reduced and additional porosity is produced by its removal; therefore extremely high mesoporosity is created.

7.2. Experimental Section

Materials

Formalin (37 wt% formaldehyde in water) and the triblock copolymer Pluronic F127 (Mw = 12600, EO_{106}-PO_{70}-EO_{106}) were purchased from BASF AG, and phenol from Merck KGaA. TEOS (tetraethyl orthosilicate, $C_8H_{20}O_4Si$), SDS (sodiumdodecyl sulfate, $NaC_{12}H_{25}O_4S$), MMA (methyl methacrylate, $C_5H_8O_2$) and Potassiumpersulfate ($K_2S_2O_8$) were purchased from Sigma Aldrich GmbH. All chemicals were used without further purification. Chemicals for electrochemistry such as sulfur powders, cyclopentanone, poly(vinylidene fluoride) (PVDF), dimethoxyethane (DME), dioxolane (DOL) and bis-(trifluoromethane)sulfonimide lithium (LiTFSI) were all purchased from Sigma-Aldrich and used as is.

PMMA colloidal crystals

For the preparation of PMMA spheres 98 ml of distilled water were degassed with nitrogen for 15 minutes. 5 mg SDS (288.4 g/mol, 0.017 mmol) and 35.5 g MMA (100.1 g/mol, 0.35 mmol) were added. The mixture was held at 90 °C or 1 h under reflux conditions in nitrogen atmosphere. The initiator solution containing 56 mg $K_2S_2O_8$ (270.3 g/mol, 0.21 mmol) in 2 ml distilled water was added to the suspension. The white colloidal suspension was washed three

times by centrifugation (20 min, 20000 rpm) and redispersed in water. To remove small amounts of larger spheres (> 500 nm), an additional centrifugation and washing step was performed (2 min, 5000 rpm). The final solution exhibited a sphere concentration of about 20 wt%. The colloidal stock solution was dried in a plastic petri dish for 12 h at 60 °C. The obtained pieces of densed packed colloidal crystals had a size of several mm^3 and are directly used for further liquid impregnation of a silica sol-gel solution.

Silica inverse opal[56]

For silica sol-gel solution 4 ml of ethanol were mixed with 6 ml TEOS (26.9 mmol), 3 ml water and 1 ml concentrated hydrochloric acid (1.19 g, 12 mmol HCl). The colloidal crystal structures were crushed to powders and put on a filter paper in a Büchner funnel. While applying vacuum to the funnel, the silica sol-gel solution was dripped over the surface to completely wet the PMMA. The silica/PMMA composite was heated to 550 °C with a ramp of 1 °C/min and calcined for 5 h. The density of the silica inverse opal is much lower than for the PMMA opal, therefore the yield was only around 10 %.

Resol precursor[23]

A low molecular weight precursor for the organic framework was synthesized in a reaction of phenol and formaldehyde in a base-catalyzed process according to Meng et al.[23] For the synthesis, 6.1 g of phenol (0.064 mol) were molten in a flask with 1.3 g of 20 wt % sodium hydroxide solution (0.0065 mol). The mixture was heated up to 50 °C and then 10.5 g formalin (37 wt % formaldehyde in water, 0.1295 mol) were added dropwise. The molar ratio of phenol / formaldehyde / NaOH was 1 : 2 : 0.1. The clear, lightly yellow colored solution was stirred at 75 °C for one hour and then cooled down to room temperature. The precursor

solution was neutralized with 1 M hydrochloric acid and the water was removed by vacuum evaporation below 50 °C. The resulting product (10 g) was redissolved in ethanol to a total weight of 50 g (20 wt %).

Synthesis of Ordered Mesoporous Polymer-Silica and Carbon-Silica Nanocomposites

A precursor solution was mixed according to Liu et al.[22] for the sample MP-CS-36* with the mass ratio F127/resol/TEOS/EtOH/HCl/H_2O) 1:0.5:2.08:12:0.0073:1.0.

In a typical preparation, 1.0 g of Pluronic F127, 10.0 g of ethanol, and 1.0 g of 0.2 M HCl were mixed well at 40 °C. Then 2.08 g TEOS and 2.5 g of the 20 wt % resol solution were added, and stirring was continued for 5 h at 40 °C. The precursor solution was cast in a glass vial together with the silica inverse opal with a mass ratio for precursor solution/silica of 100:1 which is equivalent with a ratio for precursor solution to initial PMMA spheres of 10:1 for a silica yield of 10 %. The ratio is based on the assumption that the final porous carbon product has a density which is up to five times lower than the density of the non porous PMMA spheres and therefore needs up to five times more space. The OMC yield of the precursor solution is only 1.5 %. Therefore the weight ratio of the precursor solution to OMC is 66:1. Due to five times higher density of the PMMA spheres, the maximum ratio for precursor solutions to the initial PMMA spheres should be below 66:5 or 13:1. The chosen ratio of 10:1 was much lower. The solvent evaporated and the composite was thermopolymerized for 24 h at 100 °C. Afterwards, the material was carbonized at 900 °C in nitrogen, the heating sequence was 1 °C/min to 350 °C (3 h dwell time), then 1 °C/min to 600 °C and 5 °C/min to 900 °C (2 h).

Etching of the silica

After carbonization the carbon-silica nanocomposites were immersed in 10 wt% HF solution for 24 h. Afterwards the carbon was filtered and washed with water.

Ultrasonic treatment

10 mg of the OMC nanoparticles could be dispersed in 200 ml water by sonification for 60 minutes in an ice cooled ultrasonic bath and for 10 minutes with an ultrasonic generator (Vibra Cell model VC 250, 20 kHz with 13 mm tip) at 50 % power.

Preparation of BMC-1 carbon

BMC-1 was prepared as previously reported, using a similar procedure as for the OMC nanoparticles.[9]

Preparation of carbon/sulfur composites

The C/S nanocomposites were prepared following a melt-diffusion strategy.[9] The CS_2 washed sample was prepared by filtering 50 mg C/S composite (70 wt% sulfur) with 8 ml EtOH-CS_2 mixture (v:v = 9:1), washing with EtOH several times and drying at 50 °C overnight.

SiO$_x$ coating

The C/S composite with 70 wt% sulfur (100 mg) was soaked in neat TEOS (1 ml) and kept in a glove box at room temperature for 24 hours. The SiO$_x$-coated C/S composites were collected by filtration, washed twice with EtOH and dried at room temperature for one day.

Electrochemistry

Cell assembly. The C/S cathode materials were slurry-cast from cyclopentanone onto a carbon-coated aluminium current collector. Typically, 82 wt% of C/S composite, 10 wt% Super S carbon and 8 wt% PVDF were mixed with cyclopentanone. The slurries were coated on aluminium current collectors and dried at 60 °C overnight. The electrochemical performance of the prepared cathodes was evaluated in 2325 coin cells cycled galvanostatically at room temperature between 1.5 V and 3.0 V, with lithium metal foil as the anode. The electrolyte used was 1 M bis-(trifluoromethanesulfonyl)imide lithium (LiTFSI) in a mixed solvent of 1,2-dimethoxyethane (DME) and 1,3-dioxolane (DOL) with a volume ratio of 1:1. This electrolyte was chosen to optimize the high rate behaviour.[57,58] A current density of 1675 mA/g (or 1.3 mA/cm^2) equivalent to full discharge or charge in 1 h was applied in both current sweep directions.

Characterization

Transmission electron microscopy (TEM) data were obtained on a JEOL JEM 2011 microscope at an acceleration voltage of 200 kV. Scanning electron microscopy (SEM) was performed on a JEOL JSM-6500F scanning electron microscope equipped with a field emission gun, at 4 kV. Nitrogen sorption isotherms were obtained at -196 °C using a Quantachrome Autosorb-1. The sample mass in the measurement was 36.7 mg. The

calculation of the pore-size distribution was carried out with a NLDFT method using a silica kernel for cylindrical pores for the adsorption branch. This model is the best compromise for this system, as corresponding models for carbon materials do not yet exist. For better comparison with literature data the pore sizes were also determined with the BJH model, which gives maxima at 5.3 and 2 nm. Dynamic light scattering (DLS) was performed using a Malvern Zetasizer-Nano equipped with a 4 mW He-Ne laser (633 nm) and an avalanche photodiode detector. The scattering data were weighted based on particle volume. Thermal gravimetric analysis (TGA) was performed on a SDT Q600 analyzer. TEM image and elemental maps of the C/S were collected on a Hitachi HD-2000 STEM.

7.3. Results and Discussion

The scanning electron microscopy (SEM) images in Figure 7.1 depict the morphologies at different steps of the synthesis. The 400 nm PMMA spheres, close packed in an opal structure, (Figure 7.1 a) were used as the template for a silica precursor solution. A highly ordered inverse silica opal structure (Figure 7.1 b) was formed after calcination. The silica was then used in a second casting step as a template for an artificial opal made of OMC spheres (Figure 7.1 c, d). The particle size of the OMC spheres (Figure 7.1 c) is around 300 nm, indicating little shrinkage occurred at 900 °C. The OMC spheres exhibit the close packing of the PMMA spheres and the silica inverse opal. The representative TEM micrographs in Figure 7.1 d, e reveal their 2D-hexagonal mesostructure (*P6mm*). In agreement with the SEM results, the mean particle size was 300 nm ± 40 nm.
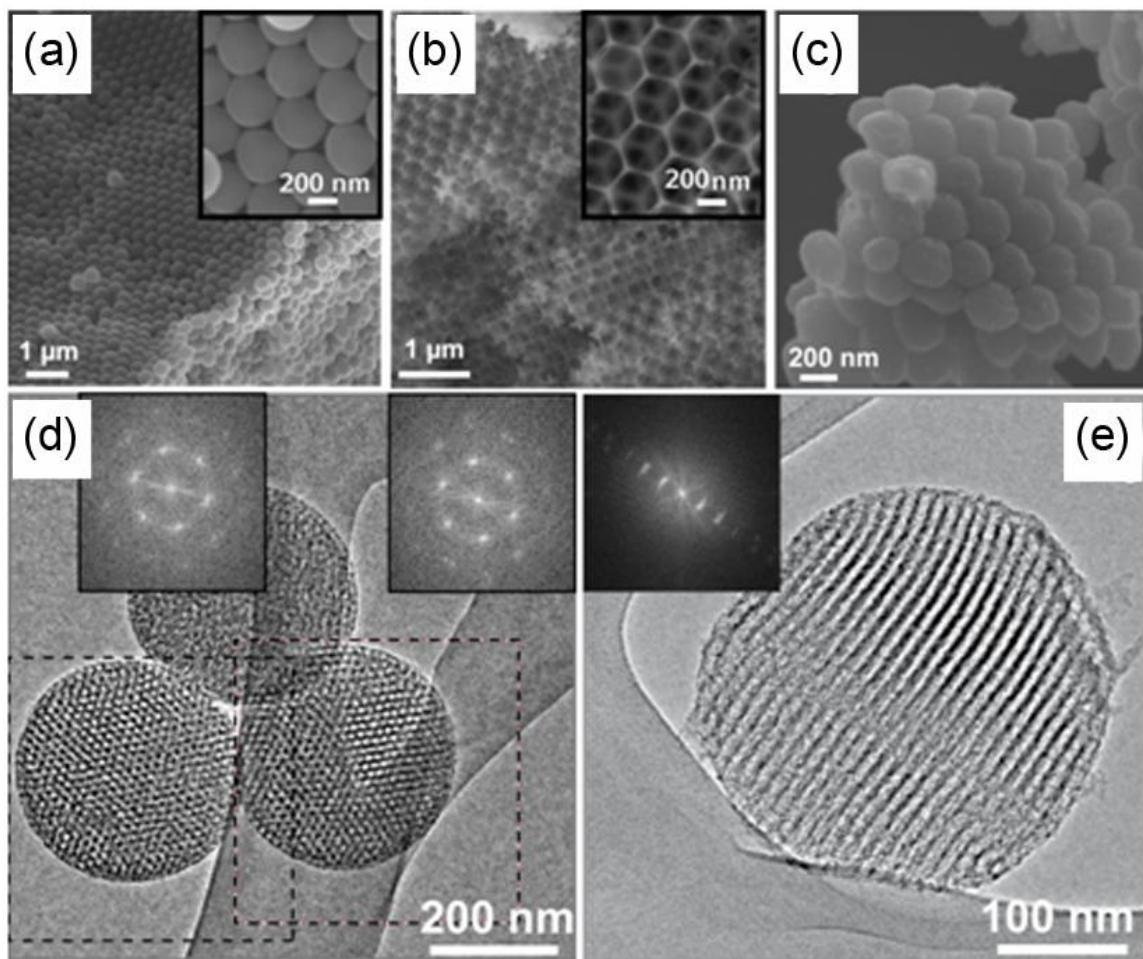
Figure 7.1: SEM images: (a) PMMA spheres ordered in close packing with an inset at higher magnification; (b) Silica inverse opal structure with an inset at higher magnification; (c) OMC spheres ordered in opal structure. TEM micrographs of spherical OMC nanoparticles showing the 2D-hexagonal structure: (d) projected along the columns, with insets of Fast Fourier Transforms (FFT) of the squares; (e) tilted out of the columnar projection with FFT inset.

Figure 7.1 d depicts the hexagonal structure projected along the columns. The FFTs clearly show the hexagonal symmetry of the projections with d-spacings of 12.5 nm. Tilting up to 30° showed no other zone axes; this excludes a 3D structure and verifies the 2D-hexagonal mesostructure. Figure 7.1 e shows the 2D-hexagonal structure tilted out of the columnar projection, where the cylindrical pores can be clearly observed. Thus the spherical

nanoparticles exhibit the same structure as the bulk material described by Liu and coworkers[22] synthesized from the same precursor solution. On grinding for TEM preparation, the OMC opal aggregates separated into small clusters (e.g. in Figure 7.1 d) or even single particles (e.g. in Figure 7.1 e), indicating that they are only loosely bound.

Complete particle separation could be achieved by sonification. The DLS measurement in Figure 7.2 a shows an average particle size of 255 nm and a narrow size distribution. The mean particle size here is even smaller than found in SEM and TEM (300 nm). Thus the spheres could be isolated from the close packing of the opal structure to form stable colloidal suspensions of single nanoparticles. The left inset shows a colloidal suspension of the spheres in water, which was still stable after one week. The TEM micrograph in the right inset shows that even after the relatively harsh ultrasonic treatment the particles still exhibit a 2D-hexagonal mesostructure. The OMC spheres show excellent porosity properties as illustrated in Figure 7.2 b. They exhibit a Type IV isotherm with a BET surface area of 2445 m^2/g, an inner pore volume of 2.32 cm^3/g ($p/p_0 = 0.82$, pores < 13 nm) and a total pore volume of 2.63 cm^3/g ($p/p_0 = 0.98$). The bimodal pore size distribution (NLDFT adsorption branch) shows a maximum for large pores of 6.0 nm and smaller pores (3.1 nm). The latter arise from the porous walls formed by etching the silica from the carbon/silica nanocomposite walls.
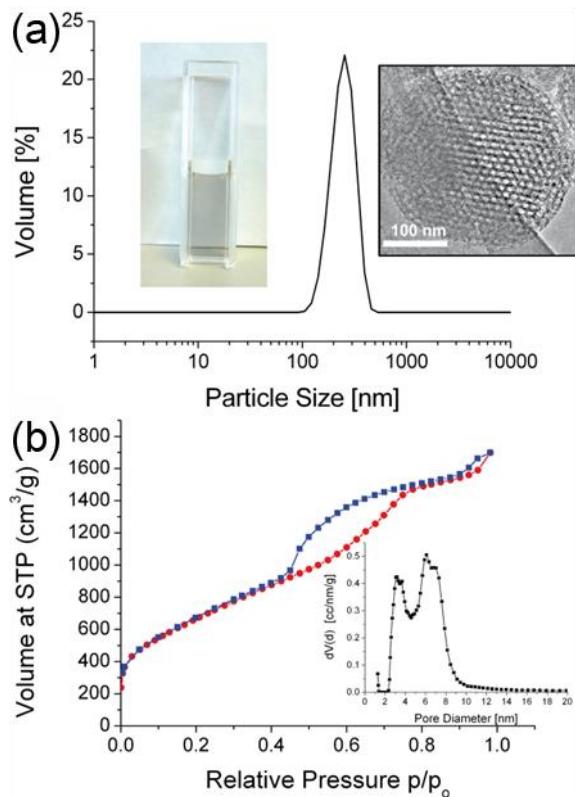
Figure 7.2: (a) DLS measurement of OMC spheres in water after sonification with insets of the stable colloidal suspension and a TEM micrograph showing the intact 2D-hexagonal mesostructure. (b) Nitrogen sorption isotherm and pore size distribution (inset, NLDFT adsorption branch) of the spherical OMC nanoparticles.

These properties make the spherical nanoparticles suitable as a scaffold and host for sulfur in Li-S batteries. Three C/S samples denoted as S-BMC/S-50, S-BMC/S-60 and S-BMC/S-70 were prepared (spherical-bimodal mesoporous carbon). The sulfur content of each sample was confirmed (Figure 7.3) by thermogravimetric analysis (TGA): 49.7 wt%, 61.4 wt% and 69.9 wt%, respectively. The composites are stable up to 200 °C, before sulfur is completely removed at around 400 °C.
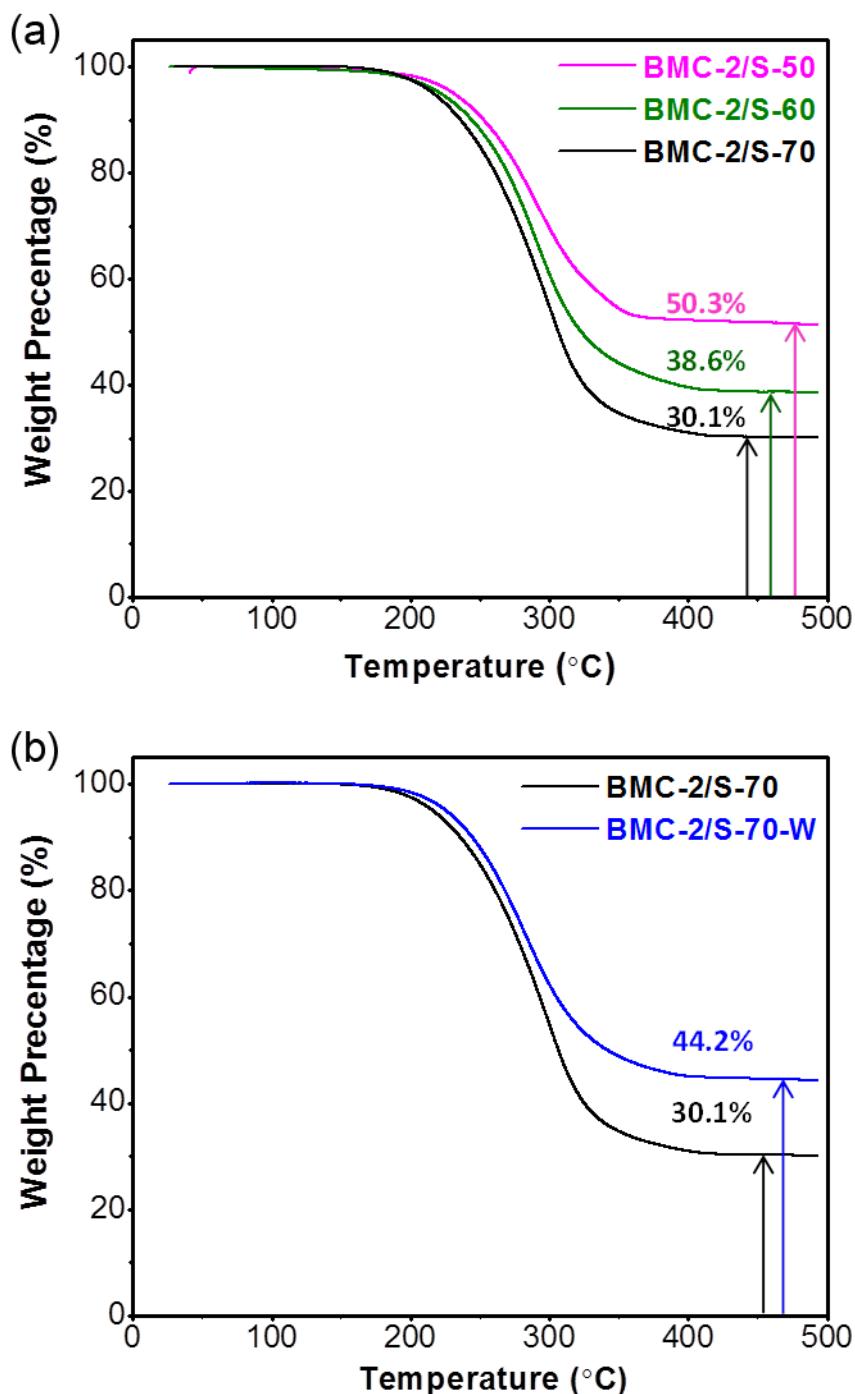
Figure 7.3: TGA data collected in N_2 at a heating rate of 10 °C/min. (a) Three samples of S-BMC/S-50, S-BMC/S-60 and S-BMC/S-70; (b) Comparison of as-prepared S-BMC/S-70 versus CS_2-washed S-BMC/S-70-W, suggesting the sulfur coated on the external surface of the particles was successfully removed.

Additionally, a successful carbon imbibition is consistent with the regarded nitrogen sorption measurements (Figure 7.4). Here, a decrease of the BET surface area from 240 m^2/g (S-BMC/S-50) to 97 m^2/g (S-BMC/S-60) and only 10 m^2/g (S-BMC/S-70) was calculated from the isotherms in figure 7. This also decreases the corresponding total pore volume from 0.46 cm^3/g to 22 cm^3/g and 0.006 cm^3/g, respectively.
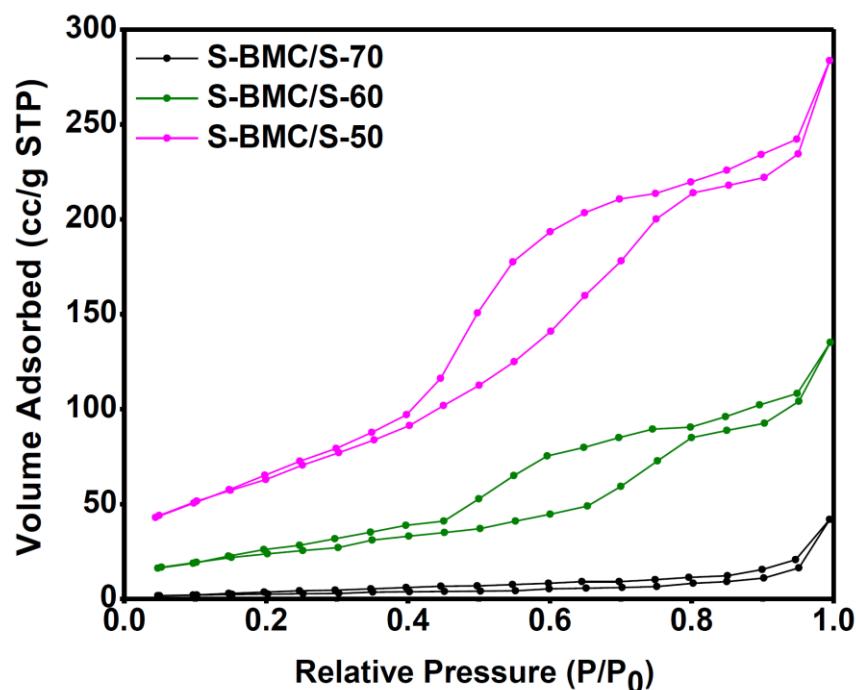
Figure 7.4: Nitrogen isotherms of the three S-BMC/ composites, indicating a successive reduction of the surface areas and pore volumes, with increasing amount of incorporated sulfur.

Moreover, a required homogenous distribution of sulphur within a single BMC particle (S-BMC/S-50) is represented by elemental mapping experiments (Figure 7.5.). The TEM image (a) still shows individual mesoporous, indicating an incomplete filling, which is consistent with the nitrogen sorption measurement (Figure 7.4). The intensity distribution of the sulphur

$K_{\alpha 1}$ rays (d) were only arising from volume of the carbon particle, which correlates with the mapping of carbon $K_{\alpha 1}$ rays (c). The detection of titanium $K_{\alpha 1}$ (b), which is not present in the sample, revealed the reference.
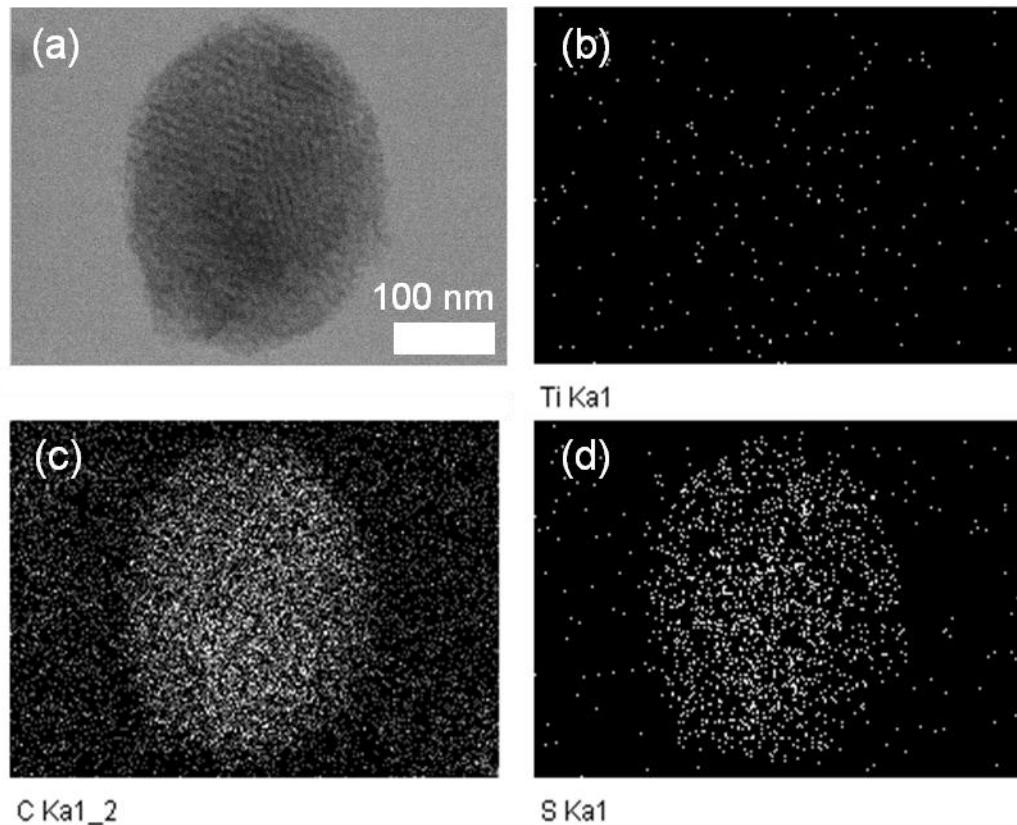
Figure 7.5: TEM image of a single S-BMC/S-50 particle (a) and the corresponding carbon (c) and sulfur (d) elemental maps showing the homogeneous distribution of sulfur; (b) is the map of titanium as a reference.

The electrochemical performance of the C/S samples as cathodes was evaluated with metallic lithium as the anode in coin cells. S-BMC/S-50 (Figure 7.7 a) shows the highest reversible discharge capacity of 1200 mAh/g. After 100 cycles this cell maintained a capacity of 730 mAh/g at a high current density of 1C (1675 mA/g). Strikingly, unlike in previous reports,[9,11,12] the electrochemical performance of the C/S nanocomposites was not strongly

affected by increasing the sulfur content to 60 wt% and 70 wt%. Both S-BMC/S-60 (Figure 7.6) displays an initial capacity of 1170 mAh/g with 700 mAh/g retained after 100 cycles, comparable to S-BMC/S-50.

All three samples show a drop in capacity during the first two cycles, followed by good stability on subsequent cycling. It is well known that both carbon and sulfur are hydrophobic and that sulfur exhibits strong affinity for porous carbons[8,44-47] This is significant since their proportion of external surface area and pore surface area is relatively large, which is more pronounced for nanospheres than for bulk, a thin sulfur layer is probable formed on the external surface of these particles.

It is also consistent with the initial charge-discharge profile of S-BMC/S-70 (Figure 7.6 b, black curve). An overcharge capacity about 150 mAh/g is observed, which we attribute to the dissolution of the reduced surface polysulfide species which engage in the shuttle mechanism during the electrode redox reactions (the results of the other two samples, which are not shown, are similar). In order to overcome this, two approaches were followed, a washing the C/S composite with CS_2 or applying a thin silica coating on its surface

First, S-BMC/S-70 was treated with CS_2 to remove excess external sulfur. This step was characterized by TGA, and data (Figure 7.3 b) confirmed that about 14% of the sulfur was extracted. Nonetheless, the S content is still relative high. [11,12] The blue curve in Figure 7.6 b shows that all of the overcharge capacity disappeared in the first cycle of the washed ("S-BMC/S-70-W") sample, indicating that the undesired shuttle processes are suppressed.

The sharp capacity drop at the 2nd cycle was also diminished (Figure 7.6 a). In spite of some sulfur loss during the washing and filtration, the sample retained a capacity above 830 mAh/g after 100 cycles at a current rate of 1 C (i.e., 83 % capacity retention). Some overcharge (ca.

95 mAhg^{-1}) appeared on the course of cycling as shown in Figure 7.6 c, similar to that reported for hollow C/S composites.[13]

The coulombic efficiency dropped from 100% on the first cycle to 92% after 10 cycles, but remained relatively constant thereafter, indicating reliable stability. Relative to S-BMC/S-50 and S-BMC/S-60 (Figure 7.7) (with similar sulfur content) it showed the best results. We anticipate even better capacity retention would be achieved with surface protection of the negative electrode.
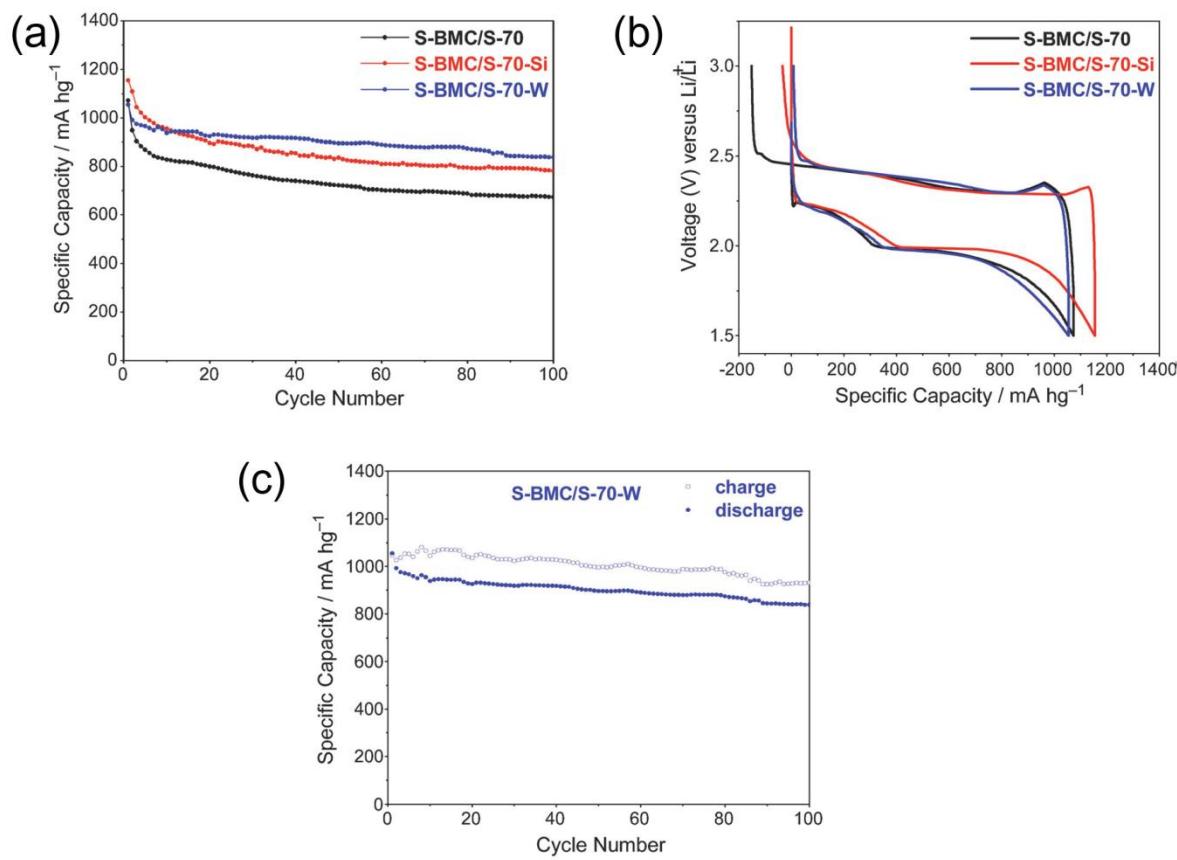
Figure 7.6: (a) Cycling stability of the three 70 wt% C/C electrodes, as prepared (S-BMC/S-70), washed (S-BMC/S-70-W), and SiO$_X$-coated (S-BMC/S-70-Si). (b) Comparison of initial charge-discharge profiles of as-prepared S-BMC/S-70 versus post-treated samples by SiO$_X$ coating or CS$_2$ washing. (c) Discharge and charge capacity of S-BMC/S-70-W as a function

of cycling number. All the cells were operated at a current rate of 1 C (1675 mAg^{-1}) at room temperature.
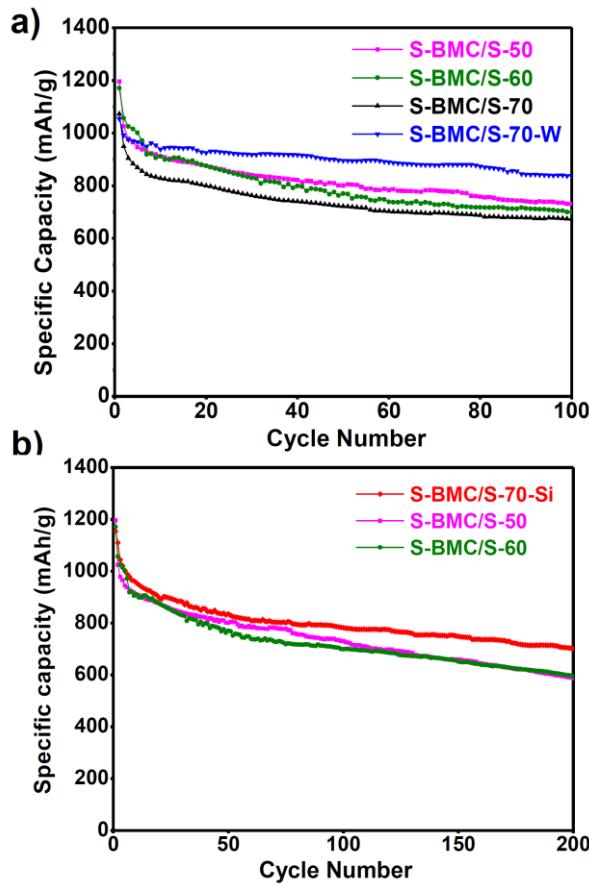
Figure 7.7: (a) Cycling stability of C/S electrodes, having sulfur contents of 50, 60 and 70 wt%. The influence of an additional CS_2 washing is also shown for S-BMC/S-70-W. (b) Cycling stability of S-BMC/S-50 and S-BMC/S-60 versus the SiO_X coated S-BMC/S-70-Si. All the cells were operated at a current rate of 1C (1675 mA/g) at room temperature.

Another approach to avoid overcharge was to modify the sample S-BMC/S-70 with a thin SiO_x coating. It has been established that additives can play important roles in the sulfur electrodes to suppress the polysulfide shuttle,[48-53] among which mesoporous silica is particularly promising.[54] Recently, Lee et al developed another facile method by creating a thin SiO_x layer on the surface of the C/S electrodes.[55]

The electrochemical data for the functionalized sample S-BMC/S-70-Si (Figure 7.6 b, c) shows that the SiO_x coating (Figure S3) was effective and that most of the over-discharge capacity was eliminated. The efficiency of the coating approach was also reflected by the cycling performance which was improved over long term cycling (200 cycles) (Figure 7.7 b).

The presence of silica coating was also confirmed by elemental mapping of a single functionalized nano sphere. Here, the intensity of the silicon and oxygen signal is homogeneous distributed over the sample volume. According, to the previous shown mapping experiment (Figure, 7.5.) sulfur is still incorporated in the carbon network.

In contrast, a complete decomposition of S-BMC/S-70-Si in oxygen, led to a remaining constant mass of around 2 wt% at temperatures above 640 °C. We attribute this ~2 wt%, to the SiO_x layer. The TGA curve is shown in Figure 7.9.
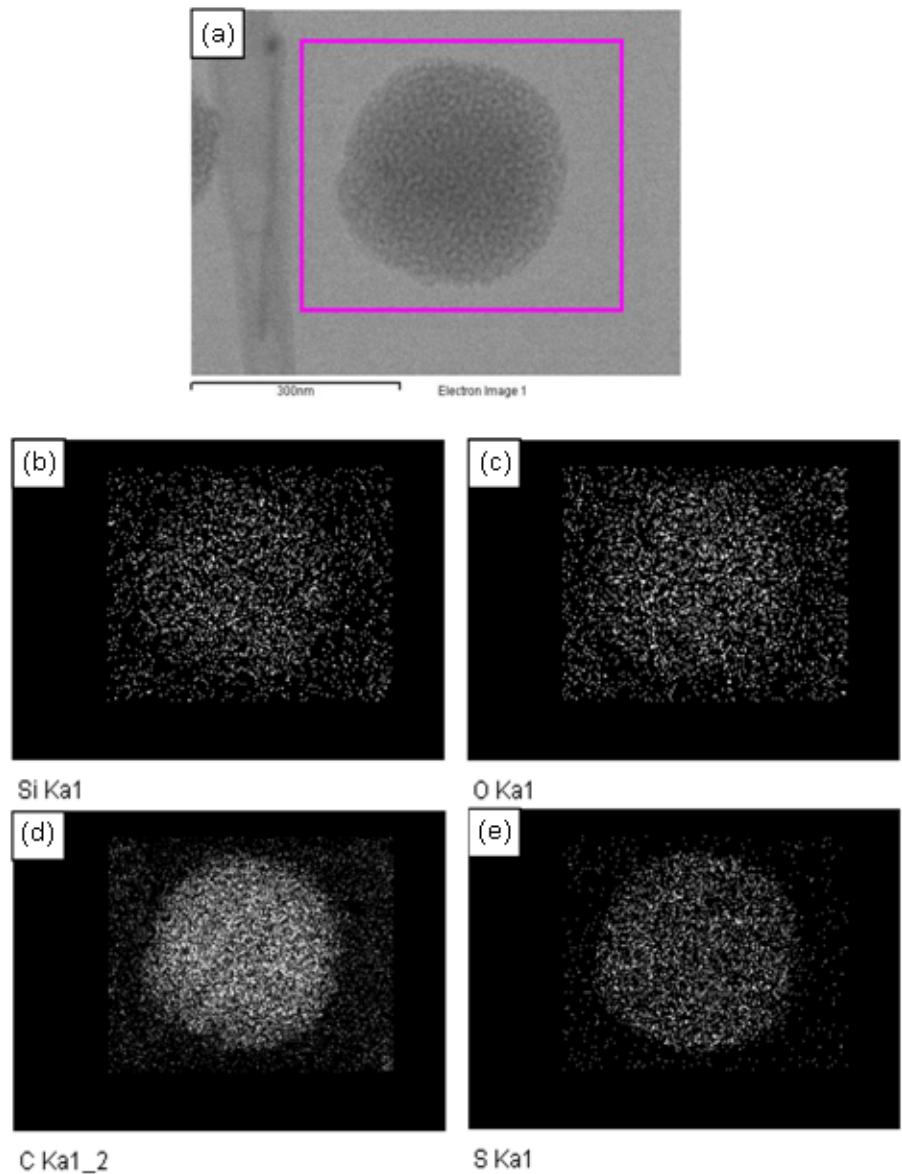
Figure 7.8: TEM image of a single S-BMC/S-70-S particle (a) and the corresponding silicon (b), oxygen (c), carbon (d) and sulfur (e) elemental maps showing the homogeneous distribution of silica on the surface.
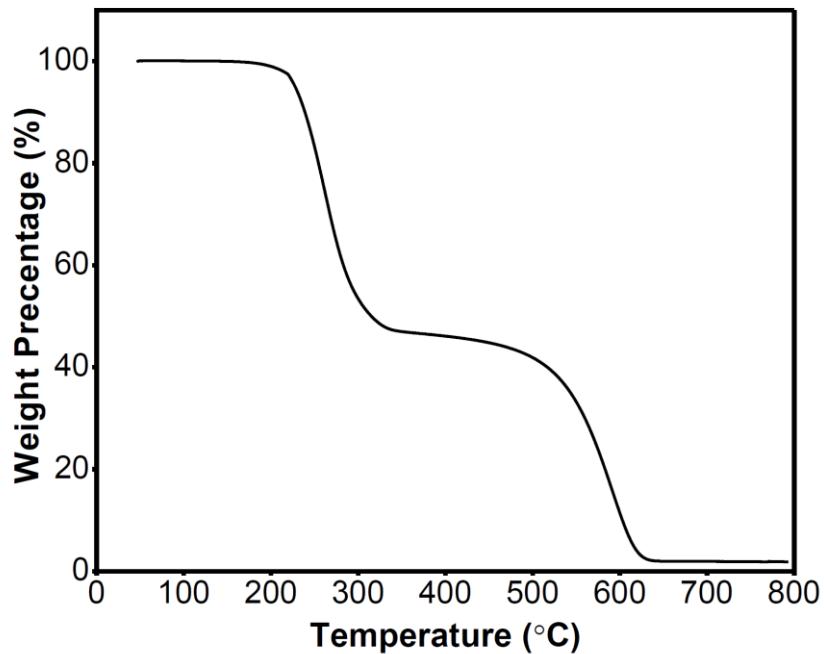
Figure 7.9: TGA data collected in O_2 showing that the SiO_X thin layer is ~ 2 wt% in the S-BMC/S-70-Si sample.

Comparison of the nano-spherical S-BMC bimodal mesoporous carbon with the previously investigated bulk material BMC-1 is illustrated in Fig. 7.10, which clearly demonstrates the advantages of S-BMC. The more sulfur is incorporated, the more obvious is the advantage. This result is attributed to the nanoscale morphology of the carbon phase. The small particle size of S-BMC allows the sulfur to distribute more homogeneously into the pores, which greatly enhances the electrochemical behaviour of the corresponding electrodes, compared with the bulk mesoporous carbon BMC-1.
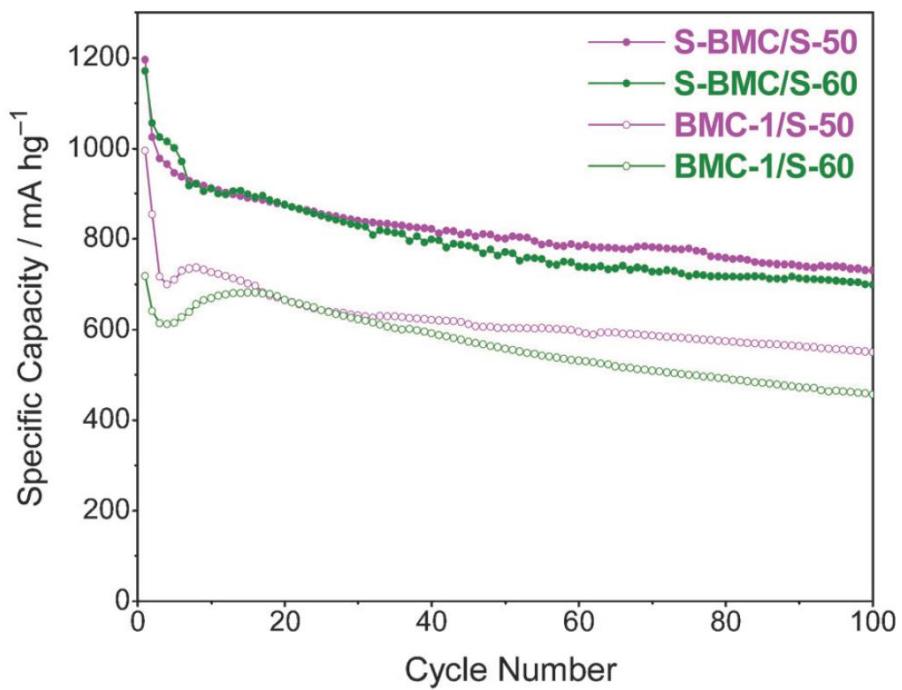
Figure 7.10: Comparison of electrodes prepared from BMC-1 and S-BMC showing the importance of nanostructured cathodes (particles), compared to a bulk geometry, on the electrochemical performance. All the cells were operated at a current of 1C (1675 mAg^{-1}) at room temperature.

7.4. Conclusions

In summary, we have demonstrated the synthesis of spherical OMC nanoparticles of 300 nm in diameter with a 2D-hexagonal mesostructure. The material shows the highest inner pore volumes for mesoporous carbon nanoparticles of 2.32 cm^3/g and also one of the highest surface areas of 2445 m^2/g with a bimodal pore size distribution of large and small mesopores of 6 nm and 3.1 nm. The nanoscale mesoporous particles were successfully utilized as host scaffold for sulfur in Li-S batteries. The C/S spherical electrodes showed high reversible charge capacity of up to 1200 mAh/g and good cycling stability. The performance of the cells could be further improved by either removing the external sulfur on the surface or by adding a thin coating of SiO_x. A comparison between nano-size and bulk carbon reveals that the excellent electrochemical properties of the cells should be attributed to the nanoscale morphology of the mesoporous carbon, which facilitates the preparation of homogeneous C/S composites and aids in charge transfer. This strategy is generally applicable to other C/S composites, as we shall show in subsequent work. For example, it also applies to other nanoscale carbon morphologies such as fibers, as long as they have comparable particle size, pore volume and surface area.

7.5. Chapter References

(1)   Ji, X.; Nazar, L. F. *J. Mater. Chem.* **2010**, *20*, 9821.

(2)   Liang, C.; Li, Z.; Dai, S. *Angew. Chem. Int. Ed.* **2008**, *47*, 3696.

(3)   Wang, J.; Chew, S. Y.; Zhao, Z. W.; Ashraf, S.; Wexler, D.; Chen, J.; Ng, S. H.; Chou, S. L.; Liu, H. K. *Carbon* **2008**, *46*, 229.

(4)   Shim, J.; Striebel, K. A.; Cairns, E. J. *J. Electrochem. Soc.* **2002**, *149*, A1321.

(5)   Wang, J.; Liu, L.; Ling, Z.; Yang, J.; Wan, C.; Jiang, C. *Electrochim. Acta* **2003**, *48*, 1861.

(6)   Han, S.-C.; Song, M.-S.; Lee, H.; Kim, H.-S.; Ahn, H.-J.; Lee, J.-Y. *J. Electrochem. Soc.* **2003**, *150*, A889.

(7)   Zheng, W.; Liu, Y. W.; Hu, X. G.; Zhang, C. F. *Electrochim. Acta* **2006**, *51*, 1330.

(8)   Ji, X.; Lee, K. T.; Nazar, L. F. *Nature Mater.* **2009**, *8*, 500.

(9)   He, G.; Ji, X.; Nazar, L. *Energy Environ. Sci.* **2011**, *4*, 2878.

(10)   Chen, S.-R.; Zhai, Y.-P.; Xu, G.-L.; Jiang, Y.-X.; Zhao, D.-Y.; Li, J.-T.; Huang, L.; Sun, S.-G. *Electrochim. Acta* **2011**, *56*, 9549.

(11)   Liang, C.; Dudney, N. J.; Howe, J. Y. *Chem. Mater.* **2009**, *21*, 4724.

(12)   Zhang, B.; Qin, X.; Li, G. R.; Gao, X. P. *Energy Environ. Sci.* **2010**, *3*, 1531.

(13)   Jayaprakash, N.; Shen, J.; Moganty, S. S.; Corona, A.; Archer, L. A. *Angew. Chem.* **2011**, *123*, 6026.

(14)   Liang, C.; Li, Z.; Dai, S. *Angew. Chem., Int. Ed.* **2008**, *47*, 3696.

(15)   Wan, Y.; Shi, Y.; Zhao, D. *Chem. Mater.* **2008**, *20*, 932.

(16)   Chang, H.; Joo, S. H.; Pak, C. *J. Mater. Chem.* **2007**, *17*, 3078.

(17)   Wu, C.-G.; Bein, T. *Science* **1994**, *266*, 1013.

(18)   Ryoo, R.; Joo, S. H.; Jun, S. *J. Phys. Chem. B* **1999**, *103*, 7743.

(19)   Lee, J.; Yoon, S.; Hyeon, T.; Oh, S. M.; Kim, K. B. *Chem. Commun.* **1999**, 2177.

(20)   Jun, S.; Joo, S. H.; Ryoo, R.; Kruk, M.; Jaroniec, M.; Liu, Z.; Ohsuna, T.; Terasaki, O. *J. Am. Chem. Soc.* **2000**, *122*, 10712.

(21)   Kruk, M.; Jaroniec, M.; Kim, T.-W.; Ryoo, R. *Chem. Mater.* **2003**, *15*, 2815.

(22)   Liu, R.; Shi, Y.; Wan, Y.; Meng, Y.; Zhang, F.; Gu, D.; Chen, Z.; Tu, B.; Zhao, D. *J. Am.. Chem. Soc.* **2006**, *128*, 11652.

(23)   Meng, Y.; Gu, D.; Zhang, F.; Shi, Y.; Cheng, L.; Feng, D.; Wu, Z.; Chen, Z.; Wan, Y.; Stein, A.; Zhao, D. *Chem. Mater.* **2006**, *18*, 4447.

(24)   Wang, X.; Liang, C.; Dai, S. *Langmuir* **2008**, *24*, 7500.

(25)   Lu, A.-H.; Spliethoff, B.; Schueth, F. *Chem. Mater.* **2008**, *20*, 5314.

(26)   Liang, C.; Hong, K.; Guiochon, G. A.; Mays, J. W.; Dai, S. *Angew. Chem. Int. Ed.* **2004**, *43*, 5785.

(27)   Tanaka, S.; Katayama, Y.; Tate, M. P.; Hillhouse, H. W.; Miyake, Y. *J. Mater. Chem.* **2007**, *17*, 3639.

(28)   Schuster, J.; Koehn, R.; Keilbach, A.; Doeblinger, M.; Amenitsch, H.; Bein, T. *Chem. Mater.* **2009**, *21*, 5754.

(29)   Song, L.; Feng, D.; Campbell, C. G.; Gu, D.; Forster, A. M.; Yager, K. G.; Fredin, N.; Lee, H.-J.; Jones, R. L.; Zhao, D.; Vogt, B. D. *J. Mater. Chem.* **2010**, *20*, 1691.

(30)   Zheng, M.; Cao, J.; Ke, X.; Ji, G.; Chen, Y.; Shen, K.; Tao, J. *Carbon* **2007**, *45*, 1111.

(31)   Steinhart, M.; Liang, C.; Lynn, G. W.; Goesele, U.; Dai, S. *Chem. Mater.* **2007**, *19*, 2383.

(32)   Wang, K.; Zhang, W.; Phelan, R.; Morris, M. A.; Holmes, J. D. *J. Am.. Chem. Soc.* **2007**, *129*, 13388.

(33)   Wang, K.; Birjukovs, P.; Erts, D.; Phelan, R.; Morris, M. A.; Zhou, H.; Holmes, J. D. *J. Mater. Chem.* **2009**, *19*, 1331.

(34)   Schuster, J.; Keilbach, A.; Köhn, R.; Döblinger, M.; Dörfler, T.; Dennenwaldt, T.; Bein, T. *Chem. Eur. J* **2011**, *17*, 9463.

(35)   Zheng, M.; Ji, G.; Wang, Y.; Cao, J.; Feng, S.; Liao, L.; Du, Q.; Zhang, L.; Ling, Z.; Liu, J.; Yu, T.; Cao, J.; Tao, J. *Chem. Commun.* **2009**, 5033.

(36)   Liu, H.-J.; Wang, X.-M.; Cui, W.-J.; Dou, Y.-Q.; Zhao, D.-Y.; Xia, Y.-Y. *J. Mater. Chem.* **2010**, *20*, 4223.

(37)   Wang, Z.; Li, F.; Stein, A. *Nano Lett.* **2007**, *7*, 3223.

(38)   Kim, T.-W.; Chung, P.-W.; Slowing, I. I.; Tsunoda, M.; Yeung, E. S.; Lin, V. S. Y. *Nano Lett.* **2008**, *8*, 3724.

(39)   Yan, Y.; Zhang, F.; Meng, Y.; Tu, B.; Zhao, D. *Chem. Commun.* **2007**, 2867.

(40)   Tonanon, N.; Intarapanya, W.; Tanthapanichakoon, W.; Nishihara, H.; Mukai, S.; Tamon, H. *J. Porous Mater.* **2008**, *15*, 265.

(41)   Fang, Y.; Gu, D.; Zou, Y.; Wu, Z.; Li, F.; Che, R.; Deng, Y.; Tu, B.; Zhao, D. *Angew. Chem.* **2010**, *122*, 8159.

(42)   Liu, H.-J.; Cui, W.-J.; Jin, L.-H.; Wang, C.-X.; Xia, Y.-Y. *J. Mater. Chem.* **2009**, *19*, 3661.

(43)   Lei, Z.; Christov, N.; Zhang, L. L.; Zhao, X. S. *J. Mater. Chem.* **2011**, *21*, 2274.

(44)   Ji, X.; Evers, S.; Lee, K. T.; Nazar, L. F. *Chem. Commun.* **2010**, *46*, 1658.

(45)   Lai, C.; Gao, X. P.; Zhang, B.; Yan, T. Y.; Zhou, Z. *J. Phys. Chem. C* **2009**, *113*, 4712.

(46)   Liu, W.; Vidić, R. D.; Brown, T. D. *Environ. Sci. Technol.* **1998**, *32*, 531.

(47)   Yang, Y.; McDowell, M. T.; Jackson, A.; Cha, J. J.; Hong, S. S.; Cui, Y. *Nano Lett.* **2010**, *10*, 1486.

(48)   Song, M.-S.; Han, S.-C.; Kim, H.-S.; Kim, J.-H.; Kim, K.-T.; Kang, Y.-M.; Ahn, H.-J.; Dou, S. X.; Lee, J.-Y. *J. Electrochem. Soc.* **2004**, *151*, A791.

(49)   Choi, Y. J.; B. S. Jung, D. J. L., J. H. Jeong, K. W. Kim, H. J. Ahn, K. K. Cho, H. B. Gu *Phys. Scripta* **2007**, *2007*, 62.

(50)   Wang, H.; Yang, Y.; Liang, Y.; Robinson, J. T.; Li, Y.; Jackson, A.; Cui, Y.; Dai, H. *Nano Lett.* **2011**, *11*, 2644.

(51)   Wang, J.; Yang, J.; Xie, J.; Xu, N. *Adv. Mater.* **2002**, *14*, 963.

(52)   Hassoun, J.; Scrosati, B. *Angew.Chem. Int. Ed.* **2010**, *49*, 2371.

(53)   Hassoun, J.; Scrosati, B. *Adv. Mater.* **2010**, *22*, 5198.

(54)   Ji, X.; Evers, S.; Black, R.; Nazar, L. F. *Nature Commun.* **2011**, *2*, 325.

(55)   Lee, K. T.; Black, R.; Yim, T.; Ji, X.; Nazar, L. F. *Adv. Energy Mater.* **2012**, *2*, 1490.

(56)   Holland, B. T.; Blanford, C. F.; Stein, A. *Science* **1998**, *281*, 538.

(57)   Peled, E.; Sternberg, Y.; Gorenshtein, A.; Lavi, Y. *J. Electrochem. Society* **1989**, *136*, 1621.

(58)   Mikhaylik, Y. V.; Kovalev, I.; Schock, R.; Kumaresan, K.; Xu, J.; Affinito, J. *ECS Trans.* **2010**, *25*, 23

8. Bimodal Mesoporous Carbon Nanofibers with High Porosity: Freestanding and Embedded in Membranes for Lithium-Sulfur Batteries

8.1. Introduction

A large number of modern applications are dependent on porous carbon materials.[1] Porous carbons are employed as sorbents for separation and gas storage, as catalyst supports and as electrode material for fuel cells, supercapacitors and batteries. A promising example for the latter is the rechargeable lithium–sulfur (Li–S) battery. This type of battery attracts increasing attention due to the high theoretical specific energy density, which is 3 to 5 times higher than that of Li-ion batteries based on intercalation chemistry.[2] The highly favorable properties of porous carbons such as high specific surface area and pore volume, chemical and thermal stability and electrical conductivity make porous carbons suitable as electrode material in such batteries. In lithium sulfur batteries the carbon acts as cathode material and host for sulfur, which is reacting to Li_2S. It has to provide electron transport to the insulating sulfur; therefore the sulfur has to be present in the range of a few nanometers from the carbon

surface. For this purpose the carbon electrodes for Li-S batteries need extremely high surface areas and high pore volumes. In addition they have to provide diffusion paths for the Li-ions.

Ordered mesoporous carbons (OMCs)[3-5] – tailor-made in terms of macroscopic morphology and properties of the periodic mesopore system – can be superior for Li-S batteries compared to classically used activated carbons.[6] Thereby the morphology of the carbon architecture is only one possibility to optimize the performance of Li-S batteries. Very recently the encapsulation of sulfur particles in combination with a yolk-type titania shell enabled the design of very stable batteries with up to 1000 cycles (0.5 C).[7] As the mass transport to the surface depends on both the pore size of the mesopores (or micropores) and the length of the diffusion paths inside those pores, hierarchical porosity is often beneficial.[8-10] Morphology control is therefore an important issue in OMC synthesis. In the literature there are numerous examples for mesoporous bulk materials made either by hard-templating[11-16] or soft-templating,[17-21] and several examples for OMCs prepared as thin films[22-28] or as nanoparticles,[29-32,33] as fibers embedded in membranes,[34-40] or as free fibers have been reported.[36,38,41,42] Most of the syntheses use self-assembly of oligomeric carbon precursors and block copolymers followed by thermal treatments for template removal (>350 °C) and carbonization (>600 °C). The OMCs synthesized by these methods normally suffer from serious shrinkage during carbonization, which results in reduced pore sizes and volumes. Tubular confinement can have highly beneficial effects[38,39] on the shrinkage behavior and the thermal stability of the embedded fibers. Due to strong adhesion of the carbon to the pore walls of the confinement (e.g. alumina), the mesoporous structure cannot shrink; only the carbon pore walls of the mesostructured carbon can shrink. Therefore this restricted shrinkage effect results not only in much larger pore sizes compared to bulk syntheses from equivalent precursor solutions but also in increasing pore sizes at higher carbonization temperatures. Zheng et al.[38] have realized fibers with pore sizes of up to 15 nm for carbonization at 700 °C

and as a further consequence very high porosity of 1154 m^2/g and 3.44 cm^3/g due to this restricted shrinkage effect. Recently, some of us[39] reported a cubic OMC phase embedded in anodized alumina membranes (AAMs) with a pore size for the spherical pores of 20 nm upon carbonization at 1000 °C, also showing very high porosity of up to 1130 m^2/g and 2.3 cm^3/g. For applications that require larger amounts of free fibers the use of AAMs as template is not reasonable due to the high cost in relation to the OMC yield. Thus other hard templates with tubular pores should also be explored.

A different approach to reduce shrinkage, introduced by Liu et al.[17], uses a co-assembly of resol as carbon precursor and tetraethylorthosilicate (TEOS) as silica precursor for the synthesis of mesoporous carbon/silica nanocomposites. The silica in the walls has two beneficial effects; it reduces the shrinkage and creates additional porosity after removal through etching. Thus several mesoporous carbon bulk materials with varying carbon/silica contents could be synthesized that showed pore sizes around 6 nm and extremely high porosities up to 2470 m^2/g and 2.0 cm^3/g, respectively.

Li-S batteries usually show capacity fading due to dissolution of intermediates – the polysulfides LiS$_n$ – in the electrolyte, which can cause irreversible loss of active sulfur. Thus it is also desirable that the used OMCs should also trap the polysulfides. For these reasons control over the diffusion of both the Li-ions and the polysulfides is necessary. The diffusion is controlled by pore sizes and geometries, but also by the external morphology, which defines the accessibility of the inner pore structure and the length of the diffusion paths. We have recently reported the synthesis of OMC spheres acting as carbon host in highly efficient Li-S batteries.[33] The obtained nanosized morphology was viewed as causing the improved electrochemical capacities and cycling stability at high current rates, especially for high sulfur loadings (70 %), in comparison to the OMC bulk material.[43]

In comparison with those close packed OMC spheres, carbon nanofibers should also provide a suitable morphology for LiS batteries, giving accessible textural porosity for fast diffusion to the mesopores. A great advantage of fiber morphologies is the possibility to produce them in continuous processes. Easy and efficient synthetic routes for carbon fiber synthesis deal with spinning processes, however the resulting fibers do not yet exhibit the desired high specific pore volumes and/or surface areas. Several materials combinations have been reported, as in continuous spinning of a pre-formed aerogel into a 1D carbon nanotube fiber, using chemical vapor deposition.[44] Carbon nanofibers (CNFs) can be also prepared by carbonization of electrospun polymer fibers. By electrospinning and partial decomposition of a polymer blend, porous CNFs were obtained.[45,46] They exhibited micropores and mesopores with broad pore size distributions and BET surface areas above 600 m^2g^{-1}. With this technique, CNFs loaded with cobalt nanoparticles with a lower BET surface area of 417 m^2g^{-1} were also obtained.[47] Additionally, electrospun porous carbon fibers with a BET surface area of only 123 m^2g^{-1} were applied in Li-S batteries and showed a high discharge capacity of about 1400 mAh/g at a very low rate of 0.05 C, where the capacity was found to strongly decrease even at medium charging rates. (900 mAh/g at 0.2 C).[48] Recently, a phenolic resin was used in combination with TEOS and Pluronic F127 to prepare carbon nanofibers using electrospinning. They exhibit disordered micro- and mesopores, and a BET surface area of 1642 m^2/g and a total pore volume of 1.0 cc/g, respectively.[49] As mentioned above, another technique for the generation of hollow carbon tubes implies the replication of AAM (or AAO) membranes as hard template, by successive AAO wall coating and carbonization of carbon precursors. These hollow carbon structures were applied in Li-S batteries, thus showing high specific capacities (730 mAh/g) after 150 cycles at a low rate (C/5).[50] Summarizing, the synthesis of novel highly porous OMCs in the form of nanofibers could

enhance the accessibility of the pores and therefore have beneficial effects for applications dependent on diffusion of guests such as in LiS batteries.

Herein we report the synthesis of mesoporous carbon nanofibers and their application in lithium-sulfur batteries. The fibers were obtained by a two-step casting process. Initially, commercial carbon nanofibers (MF-150, Ø ≈ 150 nm) were cast with a silica precursor solution leading to a silica template with tubular pores after calcination. The silica template was then refilled in a second step with a surfactant-templated precursor solution, carbonized up to 900 °C and finally etched in hydrofluoric acid to release the bimodal mesoporous carbon nanofibers (f-BMC-SIL, fibrous-bimodal mesoporous carbon from silica template). For the sample f-BMC-SIL, a triconstituent solution was used, containing resol as carbon precursor, TEOS as additional silica precursor and the block copolymer Pluronic F127. After carbonization and etching, the OMC nanofibers exhibited pores of ~9 nm from the block copolymer template and additional smaller mesopores from the removal of the silica from the walls of the composite, and showed therefore a large surface area and a very high pore volume of 1928 m^2/g and 2.41 cm^3/g, respectively. The fibers have diameters between 50 to 230 nm and lengths of several micrometers. The process only involves the use of low-cost materials; especially the synthesis of the macroporous silica template is far more cost-effective and scalable than the alternative anodic alumina membranes (AAM). For comparison, the triconstituent co-assembly was also performed using commercial anodic alumina membranes (AAMs) as hard templates, as they are used as model systems for confined mesostructure formation.[51,52] The corresponding fibers f-BMC-AAM (fibrous-bimodal mesoporous carbon from AAMs) show diameters in the range of ca. 90 – 260 nm after template removal, and feature a highly ordered circular hexagonal mesostructure, revealed by 2D small-angle X-ray scattering (2D-SAXS). Nitrogen sorption measurements and transmission electron microscopy studies (TEM, STEM-HAADF) confirm increased pore

sizes for both carbon fiber types compared to the corresponding bulk material due to a restricted shrinkage effect due to the tubular confinement.

The fibers were successfully applied as cathode material in Li-S batteries, they show high initial capacities of up to 1250 mAh/g (50 wt% S) and excellent cycling stability at a high rate of 1C and high sulfur loadings of up to 70 %, accompanied by a very high remaining coulombic efficiency of 99.6 % (100 cycles).

8.2. Experimental Section

Chemicals

Mesoporous Carbon Fibers. Formalin (37 wt% formaldehyde in water) and the triblock copolymers Pluronic P123 ($M_w = 5800$, EO_{20}-PO_{70}-EO_{20}) and Pluronic F127 ($M_w = 12600$, EO_{106}-PO_{70}-EO_{106}) were purchased from BASF AG, phenol from Merck KGaA and TEOS (tetraethyl orthosilicate, $C_8H_{20}O_4Si$) from Sigma Aldrich GmbH. All chemicals were used without further purification. Carbon nanofibers MF-C150 were received from YOUR-TOOL GmbH ($\varnothing = 80 - 150$ nm, length 2-25 µm).

Synthesis

Macroporous Silica. For a silica sol-gel solution, 4 ml of ethanol were mixed with 6 ml TEOS (26.9 mmol), 3 ml water and 1 ml concentrated hydrochloric acid (1.19 g, 12 mmol HCl). The carbon nanofibers MF-C150 were suspended in ethanol and filtered on a Büchner funnel. While applying vacuum to the funnel the silica sol-gel solution was dripped over the

surface to completely wet the nanofibers. The silica/carbon composite was heated to 1000 °C with a ramp of 2 °C/min and calcined for 3 h. The silica yield is normally around 25 wt % of the initial carbon fibers, for example, 4 g of fibers will result in 5 g carbon/silica composite and 1 g of porous silica.

Resol precursor. A low molecular weight precursor for the organic framework was synthesized in a reaction of phenol and formaldehyde in a base-catalyzed process according to Meng et al..[18] For the synthesis, 6.1 g of phenol (64.0 mmol) were molten in a flask with 1.3 g of 20 wt % sodium hydroxide solution (5 mmol). The mixture was heated up to 50 °C, before 10.5 g formalin (37 wt % formaldehyde in water, 129.5 mmol) was added drop wise. The molar ratio of phenol / formaldehyde / NaOH was about 1 : 2 : 0.1. The clear, lightly yellow colored solution was stirred at 75 °C for one hour and then cooled down to room temperature. The precursor solution was neutralized with 1 M hydrochloric acid and the water was removed by vacuum evaporation below 50 °C. The resulting product (10 g) was redissolved in ethanol to a total weight of 50 g (20 wt %).

Synthesis of bimodal mesoporous carbon nanofibers (f-BMC-SIL and f-BMC-AAM)). The preparation of the precursor solution for *f-BMC-SIL and f-BMC-AAM* is based on Liu et al.[17] corresponding to sample MP-C-36*. The mass ratio of Pluronic F127/resol/TEOS/EtOH/HCl/H$_2$O) was 1:0.5:2.08:12:0.0073:1.0. In a typical preparation, 1.0 g of Pluronic F127, 10.0 g of ethanol, and 1.0 g of 0.2 M HCl were mixed well at 40 °C to obtain a clear solution. Then 2.08 g TEOS and 2.5 g of the 20 wt-% resol solution were added, and stirring was continued for 5 h at 40 °C.

The macroporous silica hard template for *f-BMC-SIL* was placed in a glass vial before it was cast with the precursor solution. Here, a mass ratio for the weight ratio precursor solution/porous silica of 40:1 for f-BMC-SIL was chosen, which is equivalent with the weight

ratio for precursor solution to the initial fibers MF-C150 of 10:1 for a silica yield of 25 %. The weight ratio was chosen based of the assumption that the whole volume of the initial dense nanofibers will be converted into pores of the porous silica and finally into OMC fibers. Due to the porosity of the OMC fibers of ca. 80 % (corresponding to 2.0 cm^3/g) their density is only 20 % of the initial dense fibers. Thus 1 g of initial fibers can result in up to 0.2 g of OMC with fiber morphology.

The OMC yield of the precursor solution of MP-C-36* is only 1.5 wt %. Therefore the inverse of the OMC yield, the weight ratio of the precursor solution to OMC is 66:1. Due to the assumed five times higher density of the carbon fibers (MF-C150), the maximum ratio for precursor solutions to the initial fibers MF-C150 should be below 66:5 or 13:1. The chosen ratio of 10:1 was lower.

For comparison, the sample f-BMC-AAM was prepared using commercial anodic alumina membranes (AAM) as anisotropic hard template. Here 1.5 mL of the previously described precursor solution was cast on an anodic alumina membrane (GE Healthcare, Whatman GmbH, Anodisc 47, 0.2 μm pore size), which was placed on a Teflon plate.

In the following the solvent of both samples was evaporated and the composites were thermopolymerized in air for 24 h at 100 °C. Afterwards, the materials were carbonized at 900 °C in nitrogen for 2 h. The heating ramp was 1 °C/min for the first step up to 350 °C. After a dwell time of 3 h, the samples were further heated with 1 °C/min below 600 °C, and 5 °C/min above 600 °C. After carbonization the embedded fibers were immersed in 10 wt % HF solution for 48 h and finally washed several times in water (Millipore Q) and absolute ethanol. The dry powders were then prepared for further characterization.

Electrode preparation.[43] The C/S nanocomposite was prepared following a melt-diffusion strategy. Mesoporous carbon was ground together with sulfur with a mass ratio of 1 : 1 and then heated in a reactor to 155 °C overnight. The C/S cathode materials were slurry-cast from cyclopentanone onto a carbon-coated aluminum current collector. Typically, 82 wt% of C/S composite, 10 wt% Super S carbon and 8 wt% poly(vinylidene fluoride) (PVDF) were mixed with cyclopentanone. The slurries were coated on aluminum current collectors and dried at 60 °C overnight. The electrochemical performance of the prepared cathodes was evaluated using 2325 coin cells cycled at room temperature between 1.5 V and 3.0 V, with lithium metal foil as the anode (Arbin battery cycler). The electrolyte used was 1 M bis-(trifluoromethane)sulfonimide lithium (LiTFSI) in a mixed solvent of dimethoxyethane (DME) and dioxolane (DOL) with a volume ratio of 1 : 1.

Characterization

Transmission electron microscopy (TEM) data were obtained on a JEOL JEM 2011 microscope at an acceleration voltage of 200 kV or a TITAN 80-300 microscope at an acceleration voltage of 300 kV. Bimodal mesoporous carbon fibers (f-BMCs) were dispersed in ethanol and dried on holy or dense carbon grids (Gatan, Inc.). For top views the AAMs were prepared in two steps, dimpling and ion polishing. Scanning electron microscopy (SEM) was performed on a JEOL JSM-6500F scanning electron microscope equipped with a field emission gun, at 3-5 kV. Nitrogen sorption isotherms were obtained at -196 °C using a Quantachrome Nova 4000e. Small-angle X-ray scattering (SAXS) was carried out with a SAXSess system (Anton Paar) equipped with a 2 D CCD detector. The wavelength of the incident beam was $\lambda = 0.154$ nm (Cu-K$_\alpha$), the sample–detector distance was 308 mm. Samples were measured with a tilt angle of 5° with respect to the primary beam.

8.3. Results and Discussion

The synthesis of the sample for f-BMC-SIL starts with the production of the macroporous silica template. After depositing the commercial carbon nanofibers (CNF, MF-C150) from an ethanolic suspension on a filter paper, a mesh of randomly orientated and several micrometer long fibers was obtained. They are bent and mainly exhibit diameters in the range of 50 to 370 nm, while the given average diameter is 150 nm (Figure 8.1 a). The remaining interstitial voids were successfully filled with a hydrolyzed silica precursor, resulting in a dense macroporous silica template after calcination at 1000 °C. During the heating, shrinkage occurred, therefore pores with diameters ranging from 40 to 220 nm were remaining. The surface of the macroporous silica is very rough, which is attributed to a replication of the loosely packed fiber template (Figure 8.1 b). In the following, this template was cast with the resol/TEOS/Pluronic F127 precursor mixture, dried for several hours (triconstituent co-assembly) and thermo-polymerized for 24 h at 100°C.[17,33] The SEM image in Figure 8.1 c represents the top view on the hierarchical bulk composite, composed of the macroporous silica template and the incorporated mesoporous phase after carbonization at 900 °C (f-BMCS-SIL). The image clearly indicates the high degree of filling of the macropores with the mesoporous carbon-silica phase after decomposing the block-copolymer Pluronic F127.
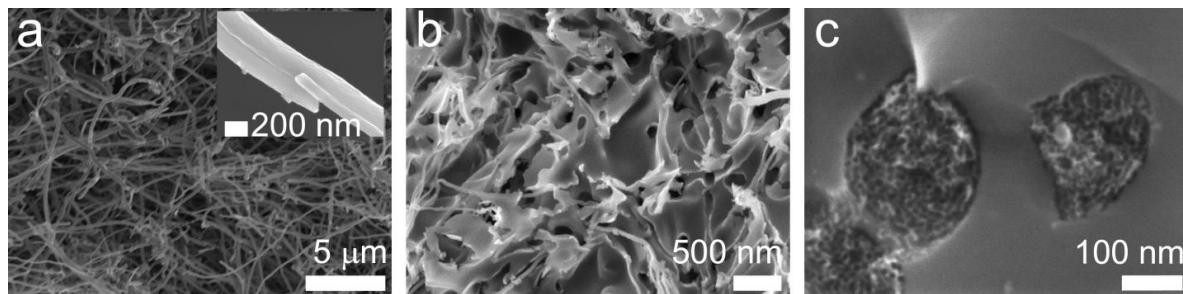
Figure 8.1: SEM images showing different steps during the synthesis of f-BMC-SIL (a) Carbon nanofibers MF-C150 at different magnifications, (b) the macroporous silica after calcination at 1000 °C and (c) the composite, composed of macroporous SiO_2 and embedded mesoporous carbon/silica nanofibers after carbonization at 900°C in nitrogen.

For comparison, we also performed the casting process with the identical precursor solution with anodic alumina membranes with similar pore size and geometry (f-BMC-AAM). The fragile AAM discs are commonly used as template for nanofiber synthesis and can serve as model system for the observation of mesostructure formation.[39,51,53-57] The AAMs exhibit tubular pores oriented perpendicular to surface and are therefore suitable for 2D-SAXS investigation and TEM observations along the fiber axis (in plan view). The membranes also exhibit a certain variation in size and shape of the individual pores, which have an average diameter of around 200 nm. TEM and SAXS (Figure 8.2) reveal a circular hexagonal structure as the major phase for the embedded nanofibers. The TEM images (Figure 8.2 a, b) represent the obtained mesostructure of sample f-BMC-AAM observed along the long axis of the AAM pores, which provide triangular and tubular confined spaces down to about 80 nm (Figure 8.2 b, inset). Here, the circular order of tubular pores is clearly visible, while a minor phase exhibits a columnar hexagonal structure. The strong interaction of the carbon/silica phase with the alumina walls is indicated by the high degree of macropore filling. Usually strong shrinkage is observed for mesoporous structures in AAM pores, for example for pure

silica[55] and carbon.[36] However, for mesoporous carbon samples in AAM also a restricted shrinkage effect was found[38-40] Due to strong adhesion of the carbon to the alumina walls of the membrane, the shrinkage is restricted if no delamination occurs. Therefore, the mesoporous structure cannot shrink, only the walls of the mesoporous carbon can get thinner. As a consequence, the pore size of the mesophase system remains constant or is even increasing.

The complete filling of the pores in the samples discussed here indicates that the shrinkage was restricted. The reason can be two-fold: The resol/TEOS/F127 precursor mixture used here is known to stabilize the mesostructure in bulk material against temperature induced shrinkage.[17] The second reason can be the aforementioned restricted shrinkage effect of the confinement.

2D-SAXS measurements helped to identify the highly ordered 2D-hexagonal mesostructure as averaged structural information of the entire membrane of the sample f-BMC-AAM (Figure 8.2 c). The SAXS pattern is characteristic for a highly ordered circular hexagonal phase as the major phase.[39,55] It can be indexed according to a zone axis parallel to the hexagonal axis of the unit cell (plane group p6mm) with [2-1] parallel to the membrane normal, with lattice plane distances for d_{01} and d_{10} of 12.8 nm and therefore $\mathbf{a} = 14.7$ nm, which is in good agreement with the TEM plan views. The constant $\mathbf{a}$ is 21 % larger as compared to the corresponding bulk material MP-CS-36* ($\mathbf{a} = 12.1$ nm)[17], which clearly shows the restricted shrinkage effect of the confinement. The schematic drawing in Figure 8.2 d illustrates the circular hexagonal order of tubular mesopores, within a confined channel of the macroporous hard template.
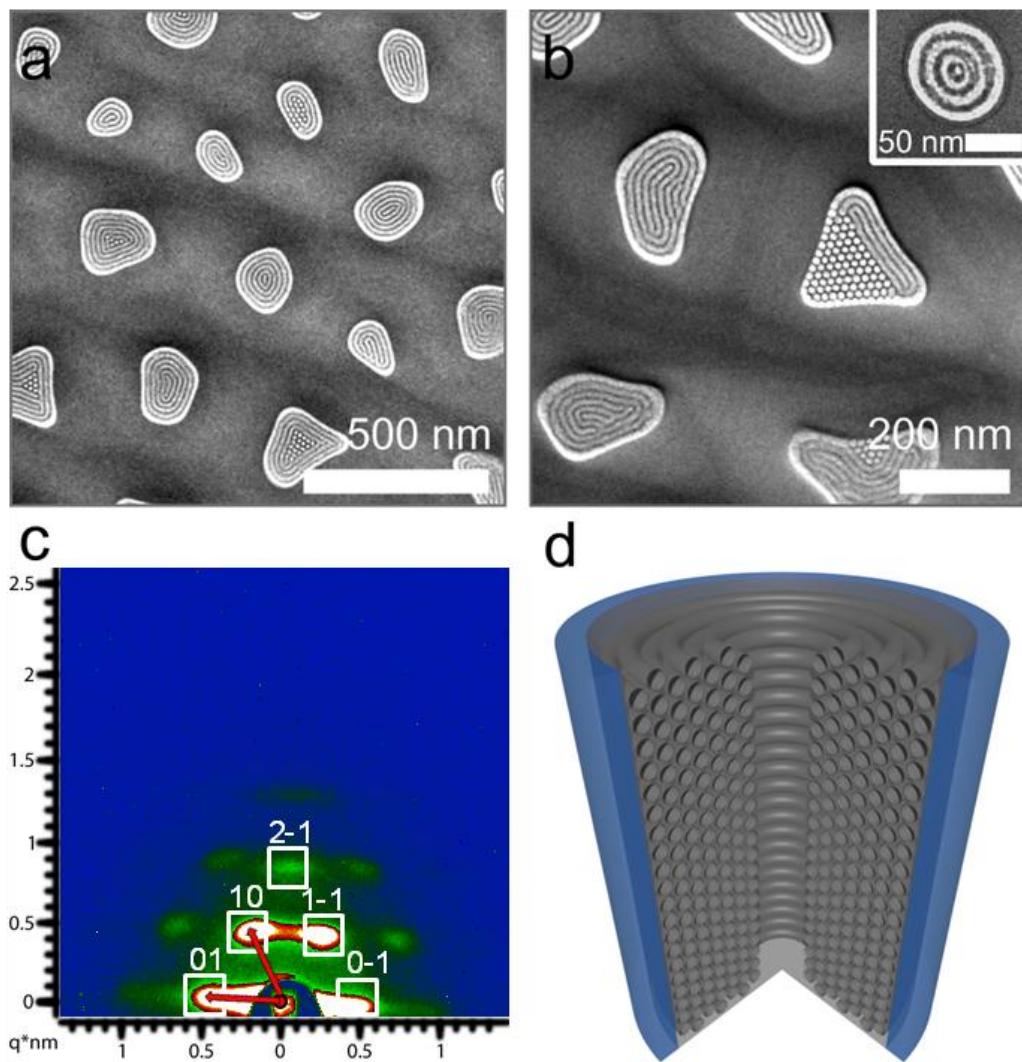
Figure 8.2: (a, b) TEM images of f-BMC-AAM show an ordered carbon/silica mesoporous structure in the pores of AAO membranes (c) SAXS pattern can be indexed in a circular hexagonal unit cell (plane group p6*mm*, a = 14.7 nm). (d) Schematic illustration of the circular hexagonal mesoporous structure in the confined space of a macroporous channel.

Our goal was the final fabrication of free-standing CNFs, which was achieved by removing the macroporous templates for F-BMC-SIL and F-BMC-AAM, respectively. Both the calcined silica and aluminum oxide were completely removed by etching with hydrofluoric acid.

TEM characterization of both freestanding BMC fiber samples is depicted in Figure 8.3. The STEM-HAADF image in Figure 3 a shows a loose bundle of the curved fibers of f-BMC-SIL having diameters of ca, 40 to 200 nm (Figure 8.3 a) and lengths of several micrometers. Therefore they reflect the morphology of the initial dense carbon nanofibers that were used for the synthesis of the macroporous silica template, (MF-C150, Ø = 50 -370 nm, Figure 1 a), but they are thinner. The silica was heated up to 1000 °C during calcination and therefore shrinkage occurred. The fibers in Figure 8.3 a are bent, which is expected to be translated into the silica template and possibly might affect the order of the final mesoporous carbon. With STEM-HAADF and FFT we observed small domains with hexagonal mesostructure (Figures 8.3 b and S1). For sample f-BMC-SIL, these mesoporous carbon nano fibers (CNFs) also depict rough surfaces and partially opened mesopores, which could be beneficial for diffusional access to the pore system. A possible reason might be a preferred condensation of TEOS during the processing at the silica walls, which could affect the dispersion of silica (and thus open space after etching) within the carbon.[58,59]

Figure 8.3 b represents a highly ordered domain within an individual CNF, showing a hexagonal order of uniform pores at the edges, also with [2-1] orientation regarding the long axis of the fiber. A 2D-hexagonal structure was found with this precursor solution for the bulk material[17], therefore a hexagonal structure was also expected in the fiber. In the center of the fiber the structure is tilted out of the columnar projection, we attribute this to the circular arrangement of the pores. These orientations are similar to the highly ordered circular hexagonal structure of f-BMC-AAM in Figure 8.3 c, d (see below). From the FFT, obtained from the entire part of image b, d-spacings of 11.4 nm were obtained for f-BMC-SIL, corresponding to $\mathbf{a} = 13.2$ nm, which is 13 % larger than for the corresponding bulk material MP-C-36* ($\mathbf{a} = 11.7$ nm).[17] However, the restricted shrinkage effect is not as large as compared to f-BMC-AAM. As further consequence of this restricted shrinkage effect, the

pore diameters are also increased to a mean diameter of 8.5 ± 0.5 nm (compared to 5.8 nm[17] for MP-C-36*). The FWHM of the intensity variations in Figure 8.3 b was used to estimate an average pore size from more than 20 pores. In contrast, CNF originating from an AAO hard template (f-BMC-AAM) are very straight and exhibit a highly ordered and oriented mesostructure (Figure 8.3 c, d) with large domains. The fiber edges are also smoother and there are no visible openings of the individual mesopores. Consistent with the SAXS measurements, the FFT (inset) of Figure 8.3 d indicates d-spacings of 12.6 nm (**a** = 14.5 nm) for f-BMC-AAM, that is 10 % larger compared to f-BMC-SIL. Consistently, the pore size is also increased to 9.1 ± 0.5 nm. Here the FWHM of the intensity variations in Figure 8.3 d were used to estimate the average pore size, again from more than 20 pores.
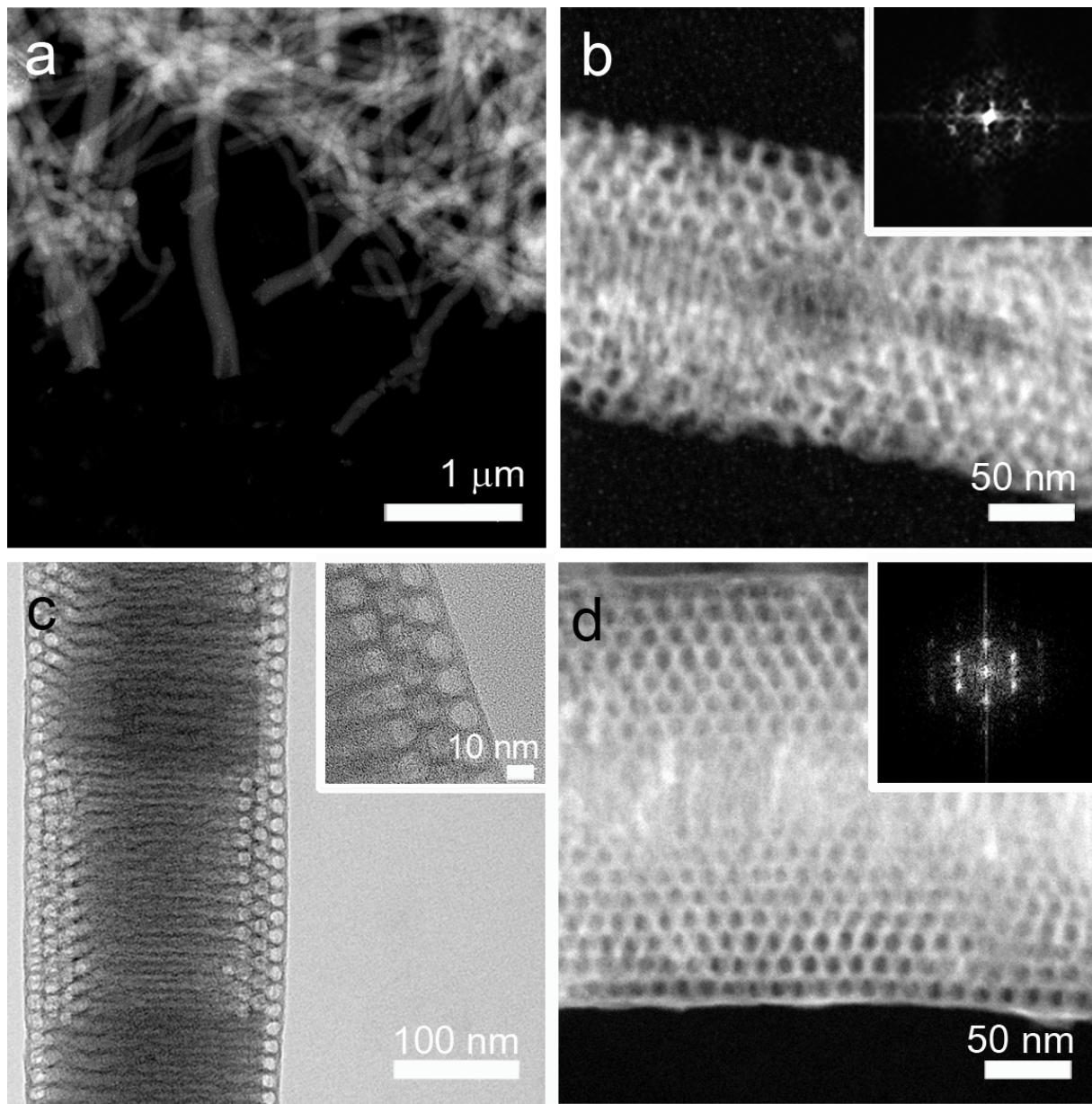
Figure 8.3: STEM-HAADF (a, b, d) and TEM (c) images of the sample f-BMC-SIL (a, b) and f-BMC-AAM (c, d), respectively. Images and Fast Fourier transforms of the entire areas (FFTs, insets) indicate the high order of the mesostructure, obtained after removal of the macroporous templates by HF treatment.

The porosity properties were determined by nitrogen sorption measurements of the free OMC fibers. Figure 8.4 depicts the isotherms of the samples f-BMC-SIL (a) and f-BMC-AAM (c)

with their respective pore size distributions (b, d). The calculation of the pore-size distributions was done with a QSDFT method[60] using a carbon kernel for cylindrical pores for the adsorption branch due to the relatively large hysteresis. The carbon kernel is a good alternative to those that are often used for silica (NLDFT). The calculated values were listed in Table 8.1.

Table 8.1. Porosity properties for mesoporous carbon nanofibers.

Sample Name	BET area (m^2/g)	Pore volume (cc/g)	Pore size (nm)[*]
f-BMC-SIL	1928	2.41	5.5, 8.6
f-BMC-AAM	1822	2.21	5.7, 9.1

[*]QSDFT adsorption branch model for cylindrical pores with carbon as adsorbent.

The sample f-BMC-SIL features a large surface area and a high inner pore volume of 1928 m^2/g and a total pore volume of 2.41 cm^3/g ($p/p_0 = 0.98$), respectively (Figure 8.4 a). Such high values were caused by the co-assembly of the carbon and the silica precursor that reduces shrinkage and gives additional porosity by etching the silica (Figure 8.4 b). Here a first maximum is shown at 1.8 nm, which we tentatively attribute to dissolved silica from the walls of the carbon network, but only 0.17 cm^3/g contribute to the total inner pore volume of 2.1 cm^3/g (pores < 15 nm). The pore size distribution is dominated by pores having maxima at around 5.5 nm (1.0 cm^3/g,) and larger ones between 8-10 nm (0.92 cm^3/g), respectively. We attribute those two pore sizes to parts of the sample where shrinkage occurred (bulk carbon material that did not enter the macropore template, smaller pores) and where

shrinkage was restricted due to the confinement effect (carbon material in the macropore template, larger pores). Therefore the larger pore size is in agreement with the pore sizes estimated from STEM measurements (ca. 8.5 nm, Figure 8.3 b), while the 5.5 nm pores are consistent with the pore size from the bulk sample MP-C-36*.[17] Both pore sizes contribute almost equally to the total pore volume.

For f-BMC-AAM a slight decrease in surface area (1821 m^2/g) and pore volume (2.2 cm^3/g) relative to f-BMC-SIL is observed (2.13 cm^3/g, pores < 15 nm). A volume of ca. 0.2 cm^3/g is attributed to the pores smaller than 3 nm. The pore size distribution shows, similar to f-BMC-SIL, a defined bimodal porosity with peaks at 5.7 (1.0 cm^3/g, 4.5-7.5 nm pores) and 9.2 nm (0.67 cm^3/g, 7.5-15 nm pores), where the 5.7 nm pores relate to the dimensions found for bimodal mesoporous carbon bulk samples.[17] Again the different phases can be related to parts where shrinkage occurred (top-layer on the membrane, Figure S2) and where shrinkage was restricted (fibers in the membrane pores).
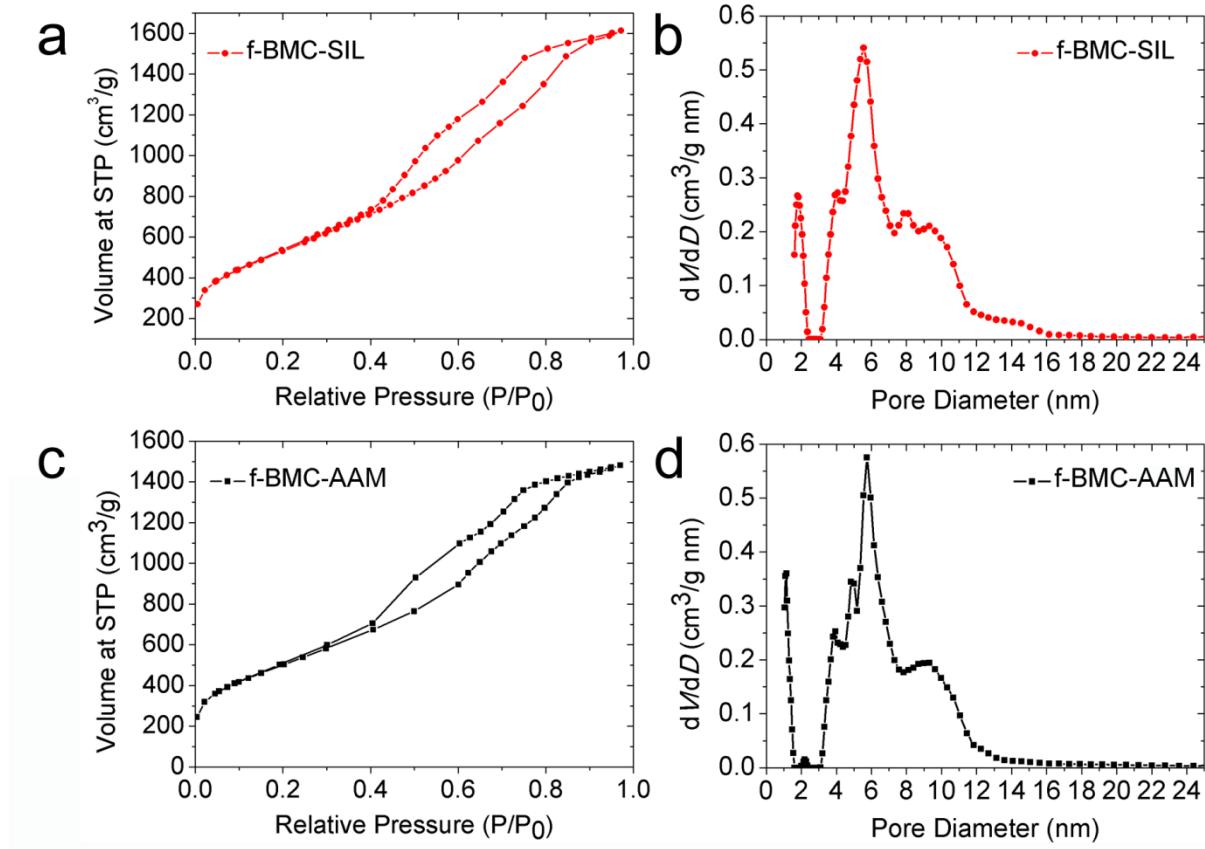
Figure 8.4: Nitrogen-sorption measurements (a, c) and pore size distributions (b, d) for f-BMC-SIL (a, b), and f-BMC-AAM (c, d). The pore size distributions are calculated by a QSDFT method from the adsorption branches.

Lithium-Sulfur Batteries

We showed in chapter 7 that the effect of nanostructuring the conducting sulfur host can positively affect the performance of Li-S-batteries.[33] Here we discuss analogous experiments using the mesoporous carbon fibers as host for the sulfur phase at the cathode. Prior to preparing the final mixture required for cathode fabrication, the OMC fibers need to be loaded with sulfur using a melt diffusion techinque.[43] The SEM images in Figure 8.5 (a-c) demonstrate the loose order of fibers within the bulk, after sulfur loading (f-BMC-SIL-S).

Importantly, individual fibers exhibit no extra sulfur loading on the surface. For a successful application as cathode, a homogenous distribution is required, as demonstrated by EDX mapping (Figure 8.5 d). Here, the rectangular area of the SEM image was scanned, resulting in overlapping intensities for the C-Kα (red) and S-Kα (green).
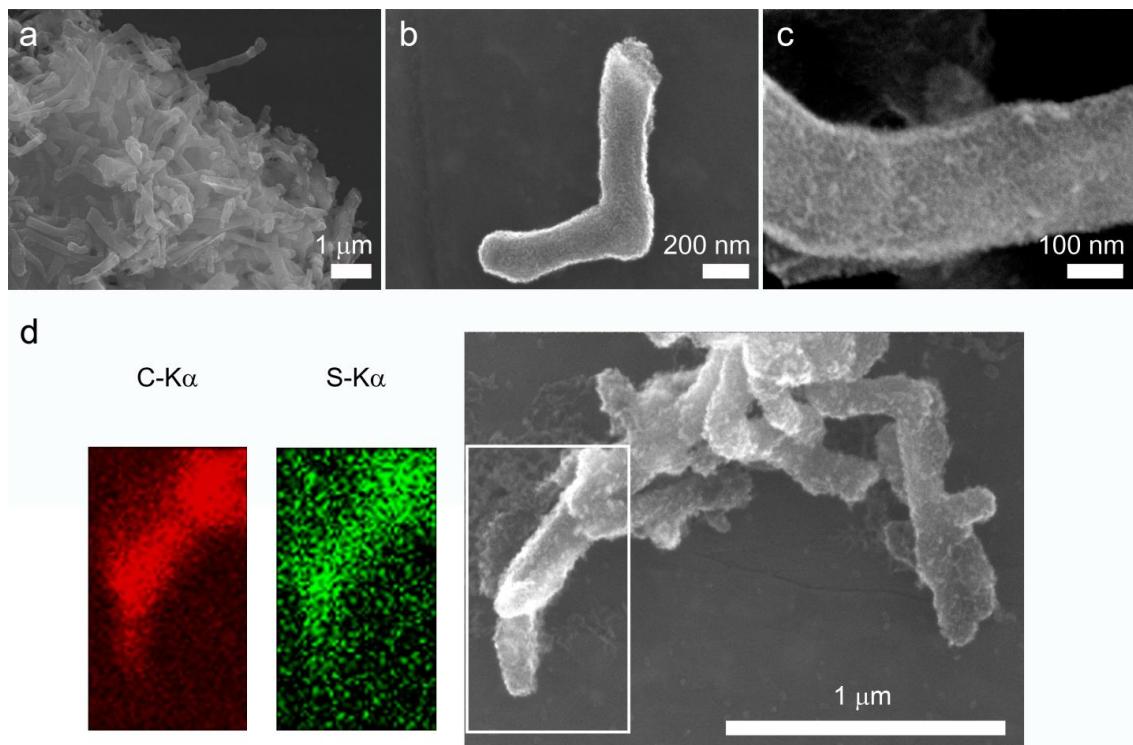
Figure 8.5: (a-c) SEM images of the sample f-BMC-SIL-S showing loosely packed and individual carbon fibers. (d) the EDX mapping experiment, obtained from the rectangular area in the SEM image, demonstrates the homogeneous sulfur distribution (red) within the CNFs (green).

The sample f-BMC-SIL was tested as cathode material and sulfur host in Li-S batteries and investigated concerning reversible capacities and cycling stability at up to 100 cycles, which is depicted in Figure 8.5. The highly porous carbon fibers were loaded with up to 70 % S (f-

BMC-SIL-S70) applied as cathode, and the final batteries were tested at the high rate of 1 C (Figure 8.6).
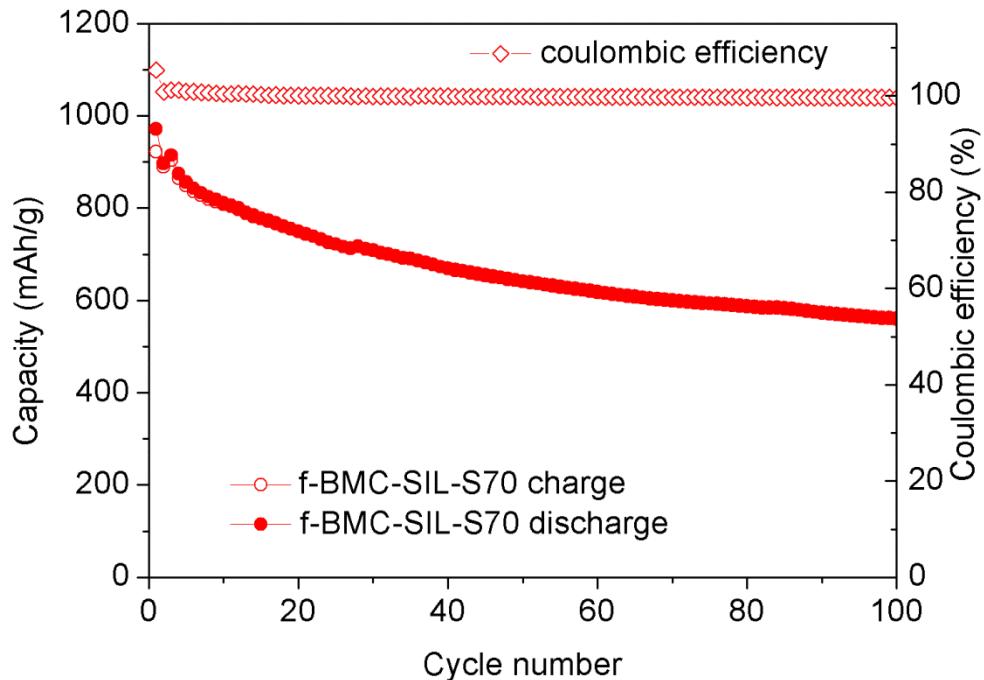
Figure 8.6: Coulombic efficiency and cycling stability of f-BMC-SIL-S70 (1C; 1675 mA/g, full charge in 1 h).

A very high coulombic efficiency – ratio between discharge and charge capacity – of 99.6 % was detected after 100 Cycles. Similar high coulombic efficiencies at lower rates (C/5, C/2) were shown for hollow carbon fibers, which was attributed to a reduced shuttle transport of polysulfides to the Li anode.[50] After the 1st cycle a high discharge capacity of 971 mAh/g was obtained, which decreased to 641 mAh/g (50 cycles) and 559 mAh/g (100 cycles) respectively, and corresponds to a remaining capacity of 66 and 58 %. With a lower sulfur loading of 50 % even higher capacities of up to 1250 mAh/g were measured (Figure S3).

Many approaches regarding additional carbon modification and activation are known to further enhance the performance of Li-S batteries, but here we compare our carbon network with a non-modified bimodal mesoporous carbon bulk, which some of us have reported previously.[43] This carbon bulk was loaded with 60 % sulfur and showed an initial discharge capacity of 618 mAh/g, which is ca. 63 % of f-BMC-SIL and clearly demonstrates the beneficial influence of the fiber morphology on the device performance. After 50 cycles, this reference has a capacity of 453 mAh/g (71 %).[43]

8.4. Conclusions

We have demonstrated the synthesis of mesoporous carbon nanofibers and their application as cathode and sulfur host in high capacity Li-S batteries. Our approach demonstrates the benefits of an alternative macroporous silica hard-template using exclusively low-cost materials. The ordered mesoporous carbon nano fibers exhibited surface areas of up to 1928 m^2/g and an extremely high total pore volume of 2.4 cm^3/g, respectively. The co-assembly approach of a carbon and silica precursor provides additional porosity by etching the silica from the carbon walls together with the tubular silica or AAM template in one step. The resulting fibers f-BMC-SIL and f-BMC-AAM feature a highly ordered hexagonal mesostructure of mainly circular orientation, in addition to residual bulk material with smaller pore size. Due to a restricted shrinkage effect in the tubular confinement the samples exhibit large pores of up to about 9 nm. Due to their high specific pore volume the fibers could host up to 70 wt% sulfur. The lithium-sulfur batteries constructed with these sulfur-loaded carbon fibers show high initial capacities of up to 1250 mAh/g (50 % S) and 970 mAh/g (70 % S), respectively and excellent cycling stability at the high rate of 1C.

8.5. Supporting Information
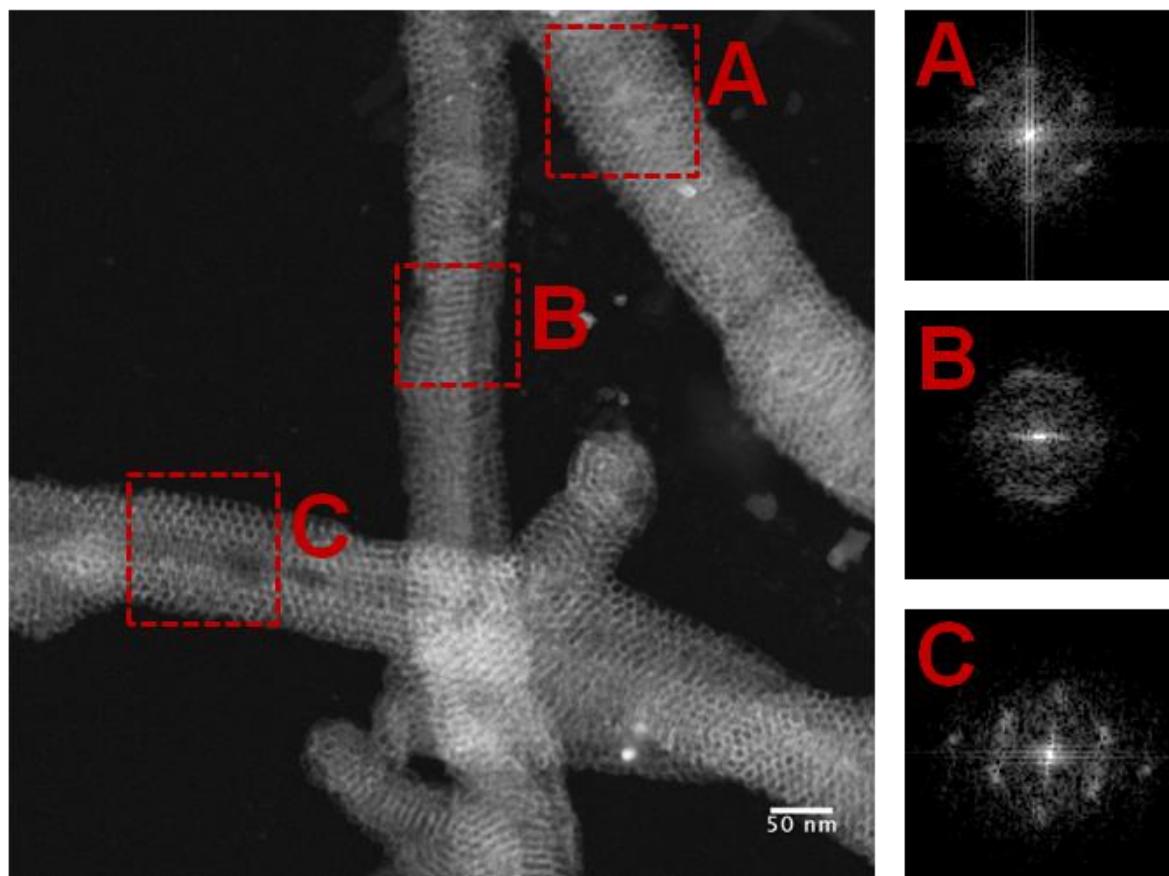
Figure S1: STEM-HAADF image of carbon nanofibers (f-BMC-SIL) after removal of macroporous silica with HF (10 wt%). The FFTs of the highlighted red areas A-C show hexagonally ordered domains within the individual fibers.
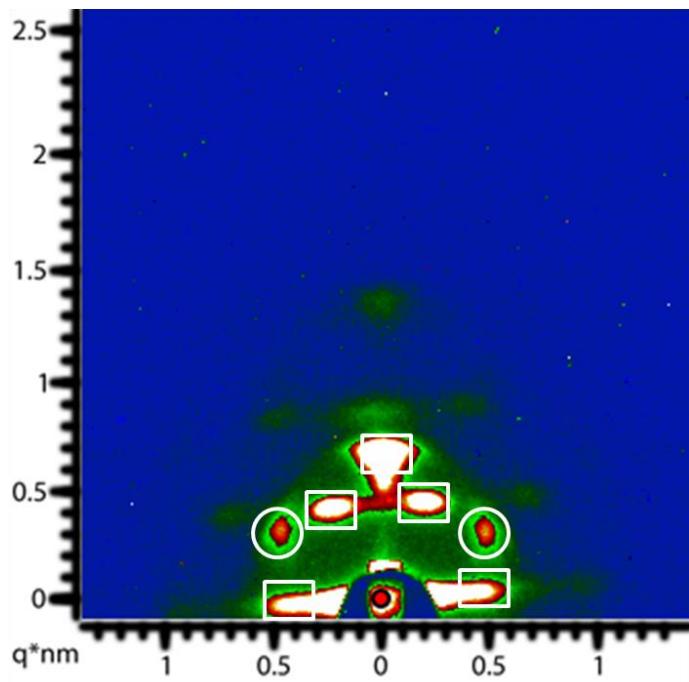
Figure S2: SAXS pattern for the sample f-BMC-AAM indexed in the circular hexagonal (p6mm) unit cell. The squares show the reflections from the mesophases in the AAM pores while the circles show reflections from a top layer on the membrane. This top layer can be indexed in a 2D-hexagonal unit cell (plane group p6mm) with 01 orientation regarding the membrane normal.
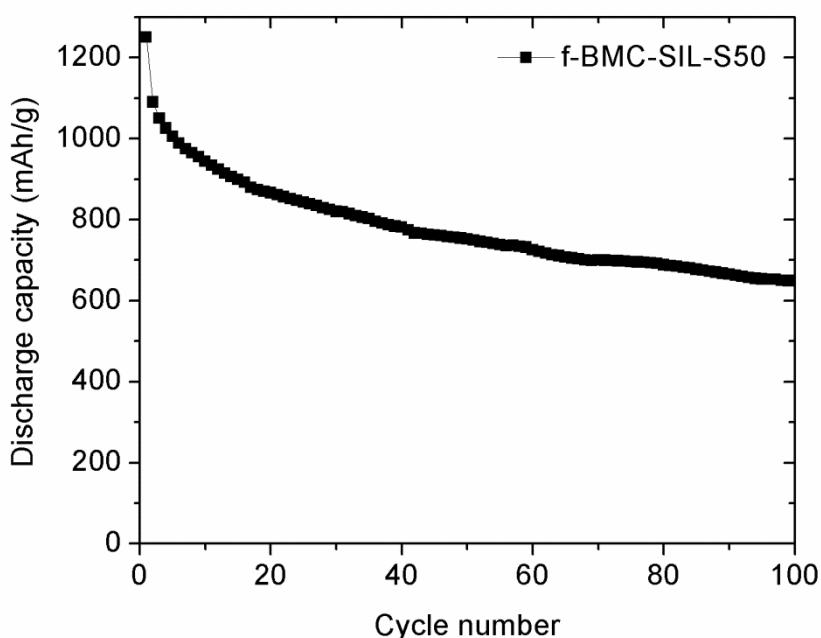
Figure S3: Cycling stability of carbon nanofibers loaded with 50 wt% sulfur (f-BMC-SIL-S50). The discharge capacity drops from initially 1250 mAh/g to 751 mAh/g (50 cycles) and 648 mAh/g (100 cycles), which corresponds to a reduction of ca. 40 and 48 %, respectively. The sample was measured at a rate of 1C.

8.6. Chapter References

(1) Lu, A.-H.; Hao, G.-P.; Sun, Q.; Zhang, X.-Q.; Li, W.-C. *Macrom. Chem. Phys.* **2012**, *213*, 1107.

(2) Ji, X.; Nazar, L. F. *J. Mater. Chem.* **2010**, *20*, 9821.

(3) Liang, C.; Li, Z.; Dai, S. *Angew. Chem., Int. Ed.* **2008**, *47*, 3696.

(4) Wan, Y.; Shi, Y.; Zhao, D. *Chem. Mater.* **2008**, *20*, 932.

(5)   Chang, H.; Joo, S. H.; Pak, C. *J. Mater. Chem.* **2007**, *17*, 3078.

(6)   Evers, S.; Nazar, L. F. *Acc. Chem. Res.* **2012**.

(7)   Wei Seh, Z.; Li, W.; Cha, J. J.; Zheng, G.; Yang, Y.; McDowell, M. T.; Hsu, P.-C.; Cui, Y. *Nature Commun.* **2013**, *4*, 1331.

(8)   Zeigermann, P.; Naumov, S.; Mascotto, S.; Kärger, J.; Smarsly, B. M.; Valiullin, R. *Langmuir* **2012**, *28*, 3621.

(9)   Li, Y.; Fu, Z.-Y.; Su, B.-L. *Adv. Funct. Mater.* **2012**, *22*, 4634.

(10)   Sakamoto, J. S.; Dunn, B. *J. Mater. Chem.* **2002**, *12*, 2859.

(11)   Wu, C.-G.; Bein, T. *Science* **1994**, *266*, 1013.

(12)   Ryoo, R.; Joo, S. H.; Jun, S. *J. Phys. Chem. B* **1999**, *103*, 7743.

(13)   Lee, J.; Yoon, S.; Hyeon, T.; Oh, S. M.; Kim, K. B. *Chem. Commun.* **1999**, 2177.

(14)   Jun, S.; Joo, S. H.; Ryoo, R.; Kruk, M.; Jaroniec, M.; Liu, Z.; Ohsuna, T.; Terasaki, O. *J. Am. Chem. Soc.* **2000**, *122*, 10712.

(15)   Kruk, M.; Jaroniec, M.; Kim, T.-W.; Ryoo, R. *Chem. Mater.* **2003**, *15*, 2815.

(16)   Cychosz, K. A.; Guo, X. F.; Fan, W.; Cimino, R.; Gor, G. Y.; Tsapatsis, M.; Neimark, A. V.; Thommes, M. *Langmuir* **2012**, *28*, 12647.

(17)   Liu, R.; Shi, Y.; Wan, Y.; Meng, Y.; Zhang, F.; Gu, D.; Chen, Z.; Tu, B.; Zhao, D. *J. Am. Chem. Soc.* **2006**, *128*, 11652.

(18)   Meng, Y.; Gu, D.; Zhang, F.; Shi, Y.; Cheng, L.; Feng, D.; Wu, Z.; Chen, Z.; Wan, Y.; Stein, A.; Zhao, D. *Chem. Mater.* **2006**, *18*, 4447.

(19)   Wang, X.; Liang, C.; Dai, S. *Langmuir* **2008**, *24*, 7500.

(20)   Lu, A.-H.; Spliethoff, B.; Schueth, F. *Chem. Mater.* **2008**, *20*, 5314.

(21)   Deng, Y.; Liu, J.; Liu, C.; Gu, D.; Sun, Z.; Wei, J.; Zhang, J.; Zhang, L.; Tu, B.; Zhao, D. *Chem. Mater.* **2008**, *20*, 7281.

(22) Liang, C.; Hong, K.; Guiochon, G. A.; Mays, J. W.; Dai, S. *Angew. Chem, Int. Ed.* **2004**, *43*, 5785.

(23) Tanaka, S.; Katayama, Y.; Tate, M. P.; Hillhouse, H. W.; Miyake, Y. *J. Mater. Chem.* **2007**, *17*, 3639.

(24) Schuster, J.; Koehn, R.; Keilbach, A.; Doeblinger, M.; Amenitsch, H.; Bein, T. *Chem. Mater.* **2009**, *21*, 5754.

(25) Song, L.; Feng, D.; Campbell, C. G.; Gu, D.; Forster, A. M.; Yager, K. G.; Fredin, N.; Lee, H.-J.; Jones, R. L.; Zhao, D.; Vogt, B. D. *J. Mater. Chem.* **2010**, *20*, 1691.

(26) Feng, D.; Lv, Y.; Wu, Z.; Dou, Y.; Han, L.; Sun, Z.; Xia, Y.; Zheng, G.; Zhao, D. *J. Am. Chem. Soc.* **2011**, *133*, 15148.

(27) Labiano, A.; Dai, M.; Young, W.-S.; Stein, G. E.; Cavicchi, K. A.; Epps, T. H.; Vogt, B. D. *J. Phys. Chem. C* **2012**, *116*, 6038.

(28) Labiano, A.; Dai, M.; Taylor, D.; Young, W.-S.; Epps Iii, T. H.; Rege, K.; Vogt, B. D. *Micropor. Mesopor. Mater.* **2012**, *160*, 143.

(29) Wang, Z.; Li, F.; Stein, A. *Nano Lett.* **2007**, *7*, 3223.

(30) Kim, T.-W.; Chung, P.-W.; Slowing, I. I.; Tsunoda, M.; Yeung, E. S.; Lin, V. S. Y. *Nano Lett.* **2008**, *8*, 3724.

(31) Fang, Y.; Gu, D.; Zou, Y.; Wu, Z.; Li, F.; Che, R.; Deng, Y.; Tu, B.; Zhao, D. *Angew. Chemie* **2010**, *122*, 8159.

(32) Zhu, J.; Liao, L.; Bian, X. J.; Kong, J. L.; Yang, P. Y.; Liu, B. H. *Small* **2012**, *8*, 2715.

(33) Schuster, J.; He, G.; Mandlmeier, B.; Yim, T.; Lee, K. T.; Bein, T.; Nazar, L. F. *Angew. Chem.* **2012**, *124*, 3651.

(34) Zheng, M.; Cao, J.; Ke, X.; Ji, G.; Chen, Y.; Shen, K.; Tao, J. *Carbon* **2007**, *45*, 1111.

(35) Steinhart, M.; Liang, C.; Lynn, G. W.; Goesele, U.; Dai, S. *Chem. Mater.* **2007**, *19*, 2383.

(36)   Wang, K.; Zhang, W.; Phelan, R.; Morris, M. A.; Holmes, J. D. *J. Am. Chem. Soc.* **2007**, *129*, 13388.

(37)   Wang, K.; Birjukovs, P.; Erts, D.; Phelan, R.; Morris, M. A.; Zhou, H.; Holmes, J. D. *J. Mater. Chem.* **2009**, *19*, 1331.

(38)   Zheng, M.; Ji, G.; Wang, Y.; Cao, J.; Feng, S.; Liao, L.; Du, Q.; Zhang, L.; Ling, Z.; Liu, J.; Yu, T.; Cao, J.; Tao, J. *Chem. Commun.* **2009**, 5033.

(39)   Schuster, J.; Keilbach, A.; Kohn, R.; Doblinger, M.; Dorfler, T.; Dennenwaldt, T.; Bein, T. *Chem. Eur. J.* **2011**, *17*, 9463.

(40)   Schuster, J.; Köhn, R.; Döblinger, M.; Keilbach, A.; Amenitsch, H.; Bein, T. *J. Am. Chem. Soc.* **2012**, *134*, 11136.

(41)   Liu, H.-J.; Wang, X.-M.; Cui, W.-J.; Dou, Y.-Q.; Zhao, D.-Y.; Xia, Y.-Y. *J. Mater. Chem.* **2010**, *20*, 4223.

(42)   Fang, B.; Kim, M.; Fan, S.-Q.; Kim, J. H.; Wilkinson, D. P.; Ko, J.; Yu, J.-S. *J. Mater. Chem.* **2011**, *21*, 8742.

(43)   He, G.; Ji, X.; Nazar, L. *Energy Environ. Sci.* **2011**, *4*, 2878.

(44)   Motta, M.; Li; Kinloch, I.; Windle, A. *Nano Lett.* **2005**, *5*, 1529.

(45)   Kim, B.-H.; Yang, K. S.; Ferraris, J. P. *Electrochim. Acta* **2012**, *75*, 325.

(46)   Peng, M.; Li, D.; Shen, L.; Chen, Y.; Zheng, Q.; Wang, H. *Langmuir* **2006**, *22*, 9368.

(47)   Aykut, Y. *ACS Appl. Mater. Interfaces* **2012**, *4*, 3405.

(48)   Ji, L.; Rao, M.; Aloni, S.; Wang, L.; Cairns, E. J.; Zhang, Y. *Energy Environ. Sci.* **2011**, *4*, 5053.

(49)   Teng, M. M.; Qiao, J. L.; Li, F. T.; Bera, P. K. *Carbon* **2012**, *50*, 2877.

(50)   Zheng, G.; Yang, Y.; Cha, J. J.; Hong, S. S.; Cui, Y. *Nano Lett.* **2011**, *11*, 4462.

(51)   Platschek, B.; Keilbach, A.; Bein, T. *Adv. Mater.* **2011**, *23*, 2395.

(52)   Cauda, V.; Torre, B.; Falqui, A.; Canavese, G.; Stassi, S.; Bein, T.; Pizzi, M. *Chem. Mater.* **2012**, *24*, 4215.

(53)   Yang, Z.; Niu, Z.; Cao, X.; Yang, Z.; Lu, Y.; Hu, Z.; Han, C. C. *Angew.Chem., Int. Ed.* **2003**, *42*, 4201.

(54)   Platschek, B.; Petkov, N.; Himsl, D.; Zimdars, S.; Li, Z.; Koehn, R.; Bein, T. *J. Am. Chem. Soc.* **2008**, *130*, 17362.

(55)   Platschek, B.; Petkov, N.; Bein, T. *Angew. Chem. Int. Ed.* **2006**, *45*, 1134.

(56)   Platschek, B.; Koehn, R.; Doeblinger, M.; Bein, T. *Langmuir* **2008**, *24*, 5018.

(57)   Keller, A.; Kirmayer, S.; Segal-Peretz, T.; Frey, G. L. *Langmuir* **2011**, *28*, 1506.

(58)   Brinker, C. J. *J. Non-Cryst. Solids* **1988**, *100*, 31.

(59)   Zhuravlev, L. T. *Langmuir* **1987**, *3*, 316.

(60)   Gor, G. Y.; Thommes, M.; Cychosz, K. A.; Neimark, A. V. *Carbon* **2012**, *50*, 1583.

9. Lipid-bilayer Coated Nanosized Bimodal Mesoporous Carbon Spheres for Controlled Release Applications

The last experimental chapter of this thesis is based on a collaboration with Stefan Niedermayer, who functionalized the carbon spheres and performed further studies for controlled release. Alexandra Schmidt was involved to create an efficient lipid-bilayer cap system. Jörg Schuster supported this work by fruitful discussions regarding the carbon chemistry.

9.1. Introduction

Colloidal mesoporous carbon particles feature several properties that make them attractive candidates for applications in controlled release and possibly drug delivery. These properties include high surface areas and pore volumes for high loadings, and good dispersibility. Additionally carbon can be equipped with various chemical functionalities, which are often required to create more complex systems

Up to now, important systems explored in targeted drug delivery are based on mesoporous silica[1], liposomes,[2,3] and polymers.[4-7] Different porous carbon morphologies, such as activated carbon particles,[8,9] carbon nanotubes (CNTs)[9-13] and ordered mesoporous carbon (CMK-3),[14] loaded with certain compounds and exhibiting good biocompatibility[15,16] have been reported in the context of drug delivery. Combining magnetic properties with carbon nanostructures is also being discussed for medical applications.[17] Nevertheless, certain carbon nanomaterials such as multi-walled CNT, carbon fibers and certain types of particles (carbon

black) can lead to cytotoxic effects depending on their size, aspect ratio and surface chemistry.[18] Another study showed that functionalization of CNTs reduced toxic effects to the cytosol.[19]

Several reports describe the formation of mesoporous carbon for drug delivery by replicating silica hard templates. Zhu et al. showed the functionalization of mesoporous carbon with a thermoresponsive polymer.[14] Based on this work, spherical mesoporous carbon in the size range of 500-800 nm was recently prepared, exhibiting a BET surface area of 1069 m^2/g and high pore volume of 1.49 cc/g, with a pore diameter of 6.0 nm.[19] Many approaches for mesoporous carbons are known,[21] and the morphology can be controlled by the dimensions of hard templates. For example, MCM-48 silica particles were used as template for ordered mesoporous carbon (CMK-1).[22] Furthermore mesoporous carbon nanoparticles (MCNs) were applied in drug delivery experiments providing a high BET surface area of 2034 m^2/g and a pore volume of 1.2 cc/g.[23] Also hydrophilic amino-functionalized MCNs in the range of 100 to 150 nm were obtained and their high drug storage capacity was attributed to a BET surface area of 1309 m^2/g and a pore volume of 0.9 cc/g (with small pores below 3 nm).[24] A high biocompatibility was shown for mesoporous carbon nanoparticles hydrothermally derived from resol as carbon source and the block-copolymer Pluronic F127.[16] With this approach particle sizes were obtained from ca. 20 to 140 nm, but the highest BET surface of 1131 m^2/g area was accompanied by a small pore size of 2.6 nm for 90 nm large particles. The influence of the particle size on endocytosis was demonstrated with MCNs having small diameters of around 90 nm.[25] These samples were prepared by a hydrothermal route, using the block co-polymer Pluronic F127 as soft-template, resulting in particles with a BET surface area of 746 m^2/g, a pore volume of 0.76 cc/g, and a pore size of 2.7 nm.

A general route for ordered mesoporous carbon (OMC) with high porosity involves a concerted co-assembly of carbon and silica precursors with Pluronic F127 and successive

template removal after full carbonization, providing a bimodal pore size distribution.[26] Based on this method we recently reported dispersible and porous carbon spheres (sized about 330 nm) using macroporous silica as hard template.[27] Those MCNs provided the highest inner pore volumes for mesoporous carbon nanoparticles of 2.32 cm^3/g and also one of the highest surface areas of 2445 m^2/g with a bimodal pore size distribution of large and small mesopores of 6 nm and 3.1 nm. Those properties make them attractive candidates for drug delivery applications.

In this study we report the synthesis of very small mesoporous carbon nanospheres with extremely high porosity and present the first efficient cap system for colloidal mesoporous carbon nanospheres.

We synthesized very small mesoporous carbon nanospheres with diameters ranging from 45 to 70 nm using a macroporous silica hard template providing appropriate dimensions. Our particles feature a very high BET surface area of 2003 m^2/g and a high pore volume of 1.95 cc/g. To the best of our knowledge this is the highest specific pore volume for mesoporous carbon nanoparticles at a size below 100 nm and also one of the highest surface areas. Additionally a bimodal porosity with maxima at 5.9 and 3.1 nm was achieved by removal of F127 from the pores and silica from the walls. Here we combine an extremely high loading capacity and very suitable particle sizes for an improved cell uptake. The use of supporting lipid bilayers (SLB) as cap systems has been successfully demonstrated for mesoporous silica nanoparticles.[27-33] Being a very simple imitation of a cell membrane, SLBs can enhance circulation times and accumulation in tumor tissue as reported for the delivery of doxorubicin.[34] Compared to liposomes, the solid nanoparticle core offers two major advantages. First, narrow size distributions and second, enhanced stability in comparison with liposomes can be achieved.[30,31,35,36] Therefore we transferred the concept of SLBs to mesoporous carbon and present the first efficient cap system for colloidal mesoporous carbon

nanospheres. Efficient sealing of the mesopores could be obtained by coating each carbon sphere with an SLB. Regarding the lipid formulation, we used a mixture of cationic and neutral lipids (DOTAP and DOPC) and 60 nm NCS. To demonstrate the effectiveness of our cap-system, the controlled release of calcein was studied *in-vitro* by fluorescence spectroscopy.

9.2. Experimental Section

Chemicals.

Sodium dodecyl sulfate, potassium persulfate, ammonium persulfate, methyl methacrylate (99%), tetraethyl orthosilicate (technical grade), concentrated HCl (37% in water), sodium hydroxide, Pluronic F127, Calcein, Triton X-100, sulfuric acid and organic solvents were obtained from Aldrich and used without further purification. Formalin (37 wt% formaldehyde in water) and Phenol was purchased from Merck KGaA and Pluronic F127 from BASF AG. Used Lipids: DOPC (1,2-dioleoyl-sn-glycero-3-phosphocholine, Avanti Polar Lipids), DOTAP (1,2-dioleoyl-3-trimethylammonium-propane, Avanti Polar Lipids).

Synthesis of PMMA spheres.

PMMA spheres of about 70 nm were prepared by a modified route reported elsewhere.[37] The emulsion polymerization was started by adding a solution of 227.2 mg potassium persulfate ($K_2S_2O_8$, 0.84 mmol) in 2 mL water to a mixture of 27.56 g methyl methacrylate (MMA, 275.3 mmol), 196 mg sodiumdodecylsulfate (SDS, 0.68 mmol) in 98 mL water at 70 °C. Previously the water was degassed by streaming nitrogen for 1 h, before SDS and MMA were

added and the mixture was than stirred under refluxing conditions for 1 h at 70 °C. After 2 h of polymerization the reaction was stopped by external cooling and applying air to the three-bottleneck flask (250 mL). The resulting colloidal solution was washed three times with water by centrifugation at 20500 rpm for 30 min. This solution was dried in plastic petri dishes for several days and the resulting flakes of several mm in size were dried at 80 °C for 2 h.

Synthesis of macroporous silica.

For the synthesis of the macroporous silica the obtained PMMA flakes were collected on a filter paper and cast multiple times with a hydrolyzed silica precursor solution. The residual solution was removed by applying vacuum to the Büchner funnel. For the silica solution, 12 mL tetraethyl orthosilicate (TEOS, 53.8 mmol) were added to 8 mL ethanol under stirring. To the clear solution 6 mL water and 1 mL concentrated hydrochloric acid (HCl, 37 %) were dropped and stirred for another 10 min at room temperature.[27] Finally, the PMMA/SiO$_x$ composite was calcined in air at 550 °C for 5 h (ramp; 1 °C/min).

Synthesis of mesoporous carbon spheres

For this purpose a mixture of resol precursor as carbon source, and silica precursor were used for casting the previously prepared macroporous silica template. The resol precursor was prepared according Meng et al.[37] Here, 21 g formalin (37 wt % formaldehyde in water, 0.259 mol) were added dropwise at 50 °C to a solution of 12.2 g Phenol (0.128 mol) and 2.6 g of 20 wt % sodium hydroxide solution (0.013 mol). The final solution was than heated for 1 h at 75 °C and cooled to room temperature. After neutralizing the basic solution using hydrochloric acid (1 M), water was removed by rotary evaporation. The resulting product was diluted in absolute ethanol to achieve a solution of 20 wt % (resol precursor).

For the final casting solution, 2.0 g of Pluronic F127, 20.0 g of ethanol, and 2.0 g of 0.2 M HCl were mixed well at 40 °C. Then 4.16 g TEOS and 5.0 g of the 20 wt % resol solution were added.[26] The resulting yellow solution was stirred for another 5 h at the same temperature. Typically, 10 g of the solution were cast on 100 mg of the macroporous silica template, and the evaporation of the solvents and self-assembly of the F127 occurred at room temperature in an open Petri dish during 2–3 days.

The resulting and filled flakes were collected and thermopolymerized in air at 100 °C for 24 h, followed by carbonization at 900 °C in a stream of nitrogen. Here, the material was heated first to 350 °C (rate: 1 °Cmin^{-1}; dwell time: 3 h), then to 600 °C (rate: 1 °Cmin^{-1}) and finally to 900 °C (rate: 5 °Cmin^{-1}; dwell time: 2 h).

The resulting shiny black bulk material was additionally treated with aqueous hydrofluoric acid (10 wt%) for 2 days, to remove silica from the macroporous template and from walls of the mesoporous carbon phase. This treatment was followed by filtering and threefold washing with water (MilliporeQ) and absolute ethanol.

Oxidation of nanosized mesoporous carbon spheres

To obtain a colloidal suspension of carbon spheres, the bulk material was oxidized in a mixture of ammonium persulfate and sulfuric acid.[42] Specifically, 30 mg NCS were added to a mixture of 2.4 g ammonium persulfate in 4 mL sulfuric acid (1 M). The resulting suspension was stirred for 24 h at room temperature. Subsequently, the particles were washed 5 times by centrifugation (14000 rpm, 16873 rcf, 8 min) and redispersion in 5 mL MilliporeQ water.

Preparation of SLB@NCS loaded with calcein

The amount of 1 mg oxidized colloidal mesoporous carbon was dispersed in 500 µL of an aqueous solution of calcein (1 mM) and stirred (500 rpm) for 2 h at room temperature in the dark. After centrifugation (14000 rpm, 16873 rcf, 8 min), 100 µL of a premixed lipid solution (70 µL DOPC + 30 µL DOTAB, each 2.5 mg/ mL in a mixture of 40 %v EtOH / 60 %v water) were added. Upon addition of 700 µL of MilliporeQ water, the formation of a supported lipid bilayer on the external surface of NCS was induced. The SLB@NCS were then centrifuged and redispersed in 800 µL MilliporeQ water, to eliminate unsupported lipids and ethanol.

In-vitro release experiment

An amount of 200 µL of the aqueous suspension containing SLB@NCS loaded with calcein was transferred into a tube which could be closed with a dialysis membrane (with a molecular-weight cutoff of 16000 g/mol).[39] This custom made cap fits on the opening of a fluorescence cuvette, filled with MilliporeQ water. Only the fluorescent molecules are able to diffuse through the dialysis membrane, whereas the NCS material stays entrapped in the cap and is not able to enter the cuvette, where the dye molecules are detected by fluorescence spectroscopy. For the delivery experiment, a time-based measurement with an excitation wavelength of 495 nm and an emission wavelength of 517 nm was recorded. The dye-loaded sample was monitored in the closed state up to 4 h, showing no significant release of the dye molecules. After the addition of 5 µL Triton X-100 (1:1000 v/v in H_2O) into the tube containing the SLB@NCS, the lysis of the lipids from the NCS nanoparticles allowed the diffusion of calcein out of the pores through the dialysis membrane and their detection in the cuvette. The release in the open state was monitored for additional 3 h.

Characterization

Scanning electron microscopy (SEM) was performed on a JEOL JSM-6500F operating at 3–5 kV (field emission).

Transmission electron microscopy images were obtained with a FEI Titan 80-300 equipped with a field-emission gun (300 kV) using the high-angle annular dark-field mode (STEM-HAADF).

Dynamic light scattering (DLS) of aqueous solutions was recorded on a Malvern Zetasizer-Nano equipped with a 4 mW He-Ne laser (633 nm) and avalanche photodiode detector. Nitrogen sorption measurements were performed on a NOVA 4000e at -196 °C (Quantachrome) after outgassing the sample at 120 °C under vacuum. An NLDFT equilibrium model of N_2 on silica, based on the desorption branch, was used to calculate the pore volume, and the surface area was calculated with the BET model ($p/p_0 = 0.05 - 0.20$).

IR spectra were recorded on a Bruker Equinox 55 FT-IR with KBr pellets.

Fluorescence spectra were recorded on a PTI spectrofluorometer with a photomultiplier detection system (model 810/814). The 1 cm quartz cuvette (QG Hellma) was placed in a cuvette holder with magnetic stirring.

UV-Vis spectra were recorded on a NanoDrop ND-2000 with 1 µL samples.

9.3. Results and Discussion

Three dimensionally ordered macroporous (3DOM) silica, which was further used as hard template, was prepared by replicating an array of close-packed PMMA spheres. PMMA spheres were prepared by emulsion polymerization. The washed particles were dried in petri dishes at room temperature to achieve millimeter sized bulk material. Figure 9.1 a represents an SEM image of an ordered domain of packed PMMA spheres with diameters of around 75 - 80 nm. These PMMA templates were collected, and casted several times with a prehydrolyzed TEOS precursor solution, to achieve a complete filling of the interstitial voids. The resulting PMMA/ SiO_X composite was dried for several hours and calcined at 550 °C to solidify the silica precursor and to remove the PMMA template. The resulting pore diameter is ranging between ca. 60 - 70 nm, which is smaller than the initial PMMA sphere size and can be attributed to heating-induced shrinkage.[39,41] The bulk material shows a good accessibility of the pores through random interpore connections in the range of about 20 nm. A rough silica surface was attributed to the loose initial packing of the PMMA spheres. The random orientation is also presented by a diffuse ring, obtained by the Fast Fourier Transform (inset) of the rectangle area (white). The diffuse ring indicates a d-spacing of around 70 nm, which is slightly smaller than the lattice spacings of the PMMA template (Figure 9.1 b).
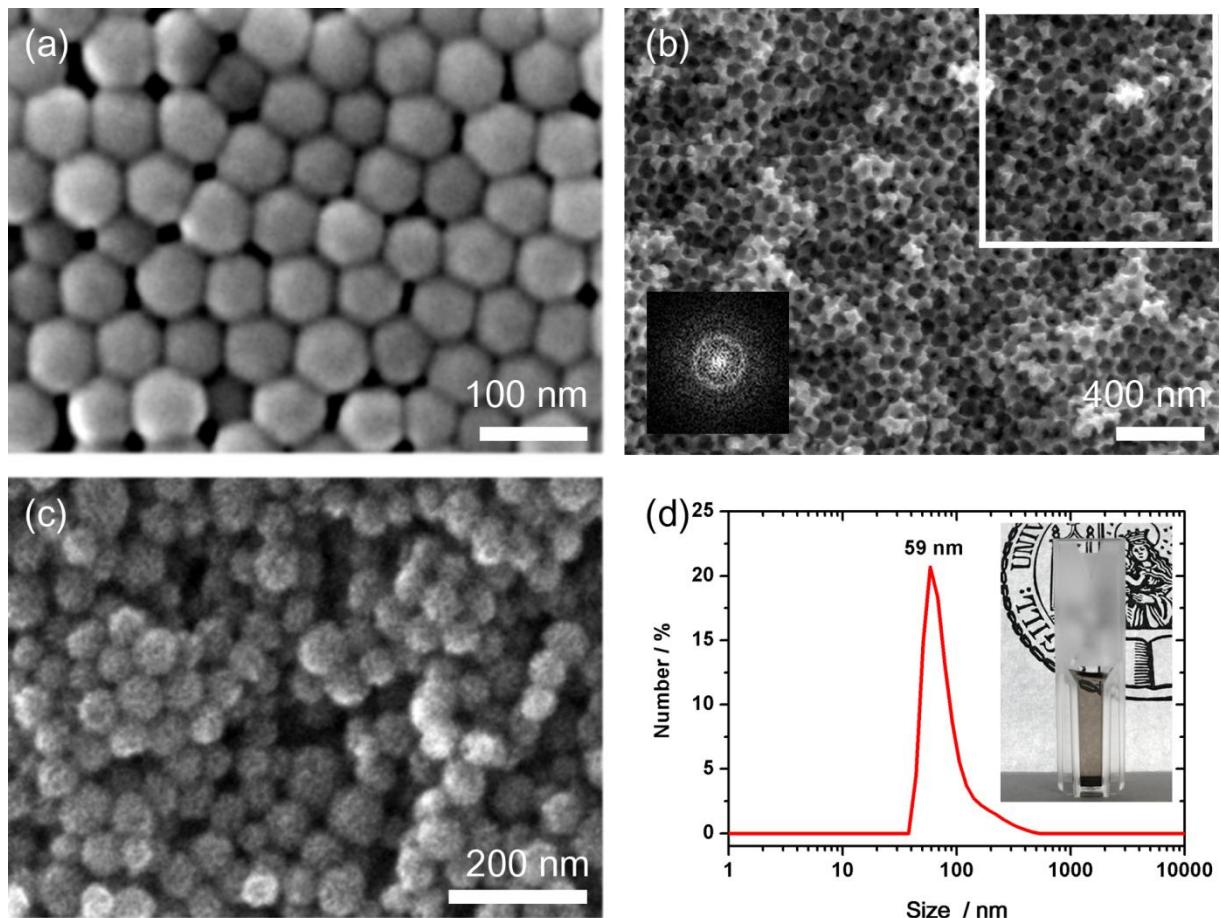
Figure 9.1: SEM images of (a) the PMMA colloidal crystal template before TEOS impregnation, (b) the corresponding randomly ordered (FFT inset) macroporous silica replicate after calcination at 550°C (inset: a 2D fast Fourier transform (FFT) of the white square) and (c) bimodal mesoporous carbon spheres after carbonization at 900°C in nitrogen and final removal of silica residues by HF treatment. (d) DLS and photograph (inset) depicts a homogeneous size distribution of the spheres in solution.

This macroporous silica was further used as hard template for the syntheses of bimodal mesoporous carbon spheres. As carbon source we used resol, which was co-assembled with two porogen compounds, TEOS and Pluronic F127. This precursor mixture enables a homogeneous dispersion of TEOS within the walls of the carbon mesostructure during an

evaporation-induced self-assembly (EISA), occurring during the casting and drying of the precursor within the empty voids of the macroporous silica hard template. Subsequent thermopolymerization at 100 °C for 24 h and carbonization at 900 °C in nitrogen results in full carbonization and conversion of TEOS into silica, dispersed in the walls of the mesoporous network. Simultaneously the total removal of Pluronic F127 is responsible for mesopore formation. All silica residues were successfully etched with hydrofluoric acid (10 wt%), which creates a loose packing of nanosized mesoporous carbon (NCS) particles in the range of 45 to 68 nm (Figure 9.1 c). The particles can be separated either by oxidation with ammonium persulfate or ultrasound treatment, leading to well-dispersed colloidal suspensions (Figure 9.1 d, photograph). The DLS measurement shows a maximum size of 59 nm, which is consistent with the SEM data.

The obtained NCS were also characterized by STEM-HAADF (Figure 9.2 a, b), demonstrating their uniform particle size. The very small carbon spheres feature a rough surface with accessible mesopores and smaller ones that are present in the walls. The pore structure seems to be random, which we attribute to a relatively small confined size within this macroporous template. In contrast, we previously found a pronounced highly ordered hexagonal phase within carbon spheres having diameters of around 330 nm.[27] From nitrogen sorption measurements (Figure 9.2 c) a type IV isotherm was obtained, showing a wide hysteresis and no defined saturation at high relative pressures. We attribute this to a pronounced textural porosity between the particles. A high BET surface area of 2003 m^2/g and a high total pore volume of 1.95 cm^3/g were achieved. The bimodal porosity, resulting from the removal of F127 and silica from the walls, exhibits two maxima at 5.9 and 3.1 nm, respectively. These properties suggest that these small mesoporous particles are attractive

candidates for introducing chemical functionality and for applications as potential drug delivery system.
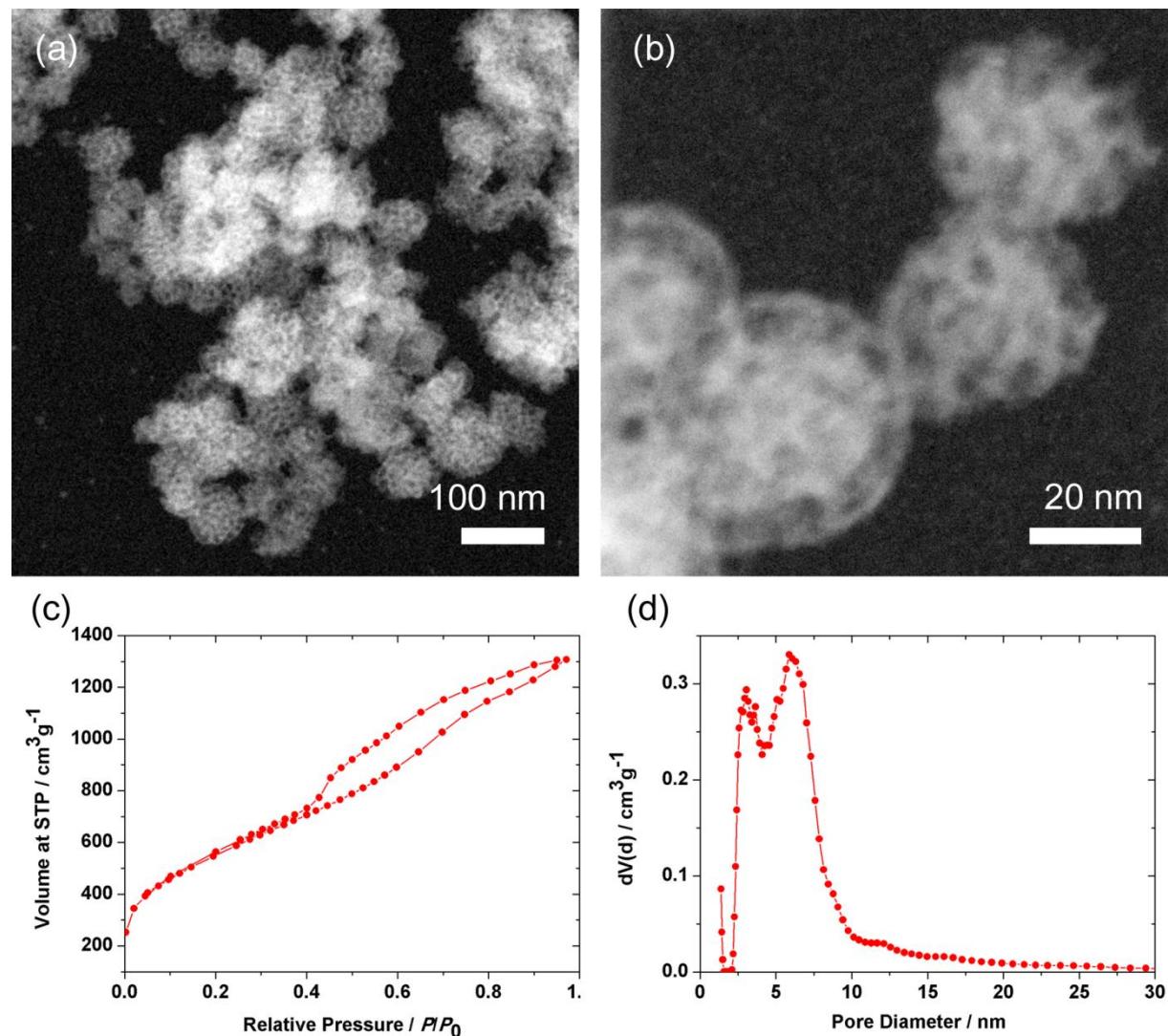
Figure 9.2: (a, b) STEM-HAADF images of mesoporous NCS particles at different magnifications, obtained after HF treatment. Nitrogen sorption measurements reveal a type IV isotherm (c) and a bimodal pore size distribution (d).

For the creation of a SLB@NCS system, the hydrophobic particle surface had to be oxidized. Here we used a procedure already known in the literature.[42] The successful oxidation of NCS

in a solution of ammonium persulfate in sulfuric acid is shown by IR spectroscopy (Figure 9.3). The two peaks arising at 1725 cm^{-1} and 1618 cm^{-1} can be attributed to carbonyl (carboxylic acid and keto-groups) and hydroxyl groups formed during the oxidation process (black curve). This negatively charged surface can now interact with the positively charged head groups of the phospholipids, which facilitates the formation of a SLB around the NCS. To show the potential of SLB@NCS as a release-on-demand system, we demonstrate that the SLB is able to prevent any premature release of dye molecules out of the mesostructure.
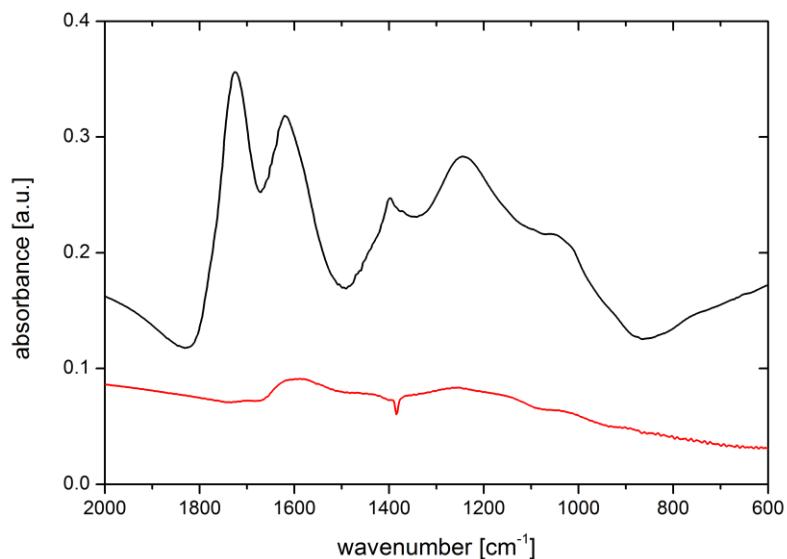
Figure 9.3: Infrared spectroscopy of as synthesized (red) and oxidized NCS (black).

For this purpose, we loaded a fluorescent dye (calcein) as a model for drug molecules into the mesopores of NCS and capped the nanospheres with a lipid bilayer containing DOPC and DOTAP. Afterwards, the calcein-loaded SLB@NCS were transferred into a tube sealed with a dialysis membrane (Figure 9.4 a) and mounted on top of a fluorescence cuvette filled with water. The membrane only allows the dye molecules to diffuse into the cuvette, whereas the

NCS stay entrapped in the tube. As long as the cap system blocks the release of the dye, no fluorescence signal can be detected (Figure 9.4 b).[29,39] In this experiment, even after 4 h, no significant release was observed. Only after rupture of the SLB through the addition of the surfactant Triton X-100, dye molecules were able to diffuse out of the bimodal porous carbon particles across the membrane into the cuvette. The entire amount of calcein was released within 3 h (also see supporting information, Figure S2). Therefore, our results show the ability of SLB@NCS as effective cap system for colloidal mesoporous carbon nanoparticles.
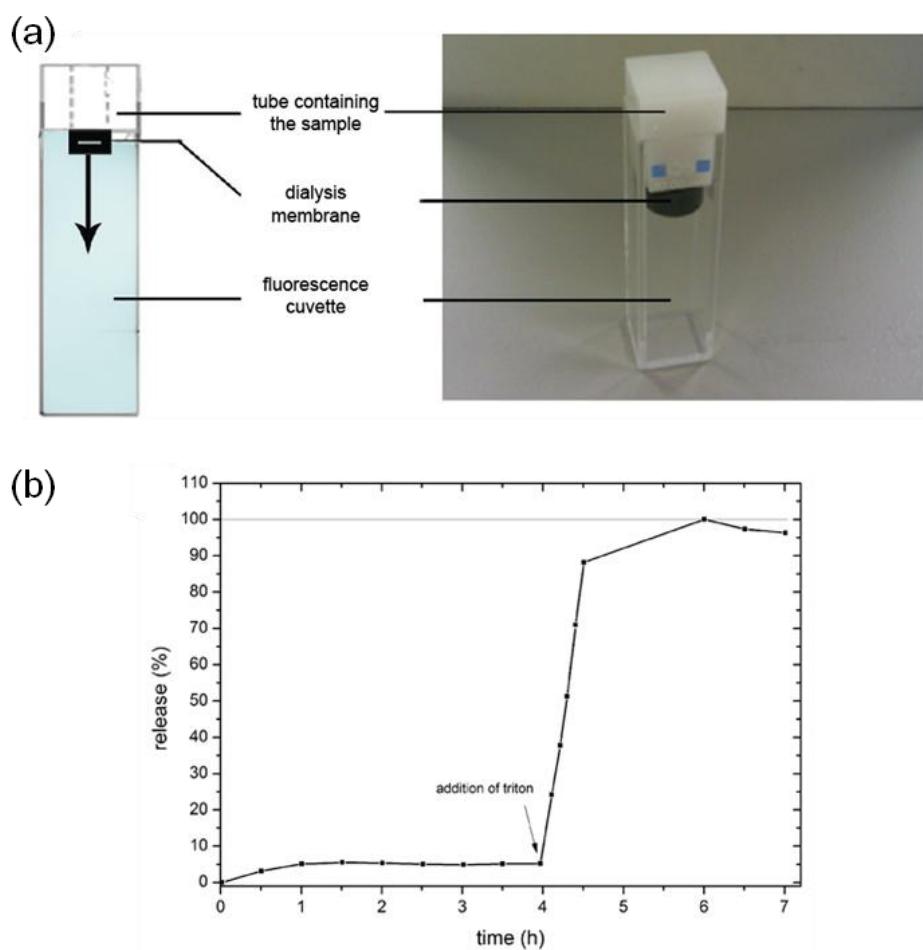
Figure 9.4: (a) Schematic presentation and photo of the release setup. (b) Release profile of calcein in SLB@NCS.

9.4. Conclusions

We present a strategy for the synthesis of 60 nm large and colloidal nanosized carbon spheres (NCS). Their bimodal porosity features a high BET surface area as well as a high pore volume, which makes them attractive candidates for drug delivery agents with high loading capacity.

The synthesis is based on the replication of small macroporous silica hard templates, by concerted co-assembly of a mixture of resol, TEOS and Pluronic F127. After successive thermopolymerization, carbonization and silica removal, the bimodal mesoporous carbon spheres can be separated into colloidal NCS by oxidative treatment. The mesoporous nanoparticles were loaded in a solution with fluorescent calcein as model drug and efficiently sealed with a stable supported lipid bilayer (SLB) cap system. Molecular release experiments demonstrate the effective closure and release of this system, which provides a tight seal until the addition of Triton X-100, which destabilizes the lipid bilayer and initiates a complete and controlled release of the fluorescent dye from the highly porous carbon.

9.5. Supporting Information

Chemical structure of the used phospholipid and lipid:

DOPC (1,2-dioleoyl-sn-glycero-3-phosphocholine, Avanti Polar Lipids)
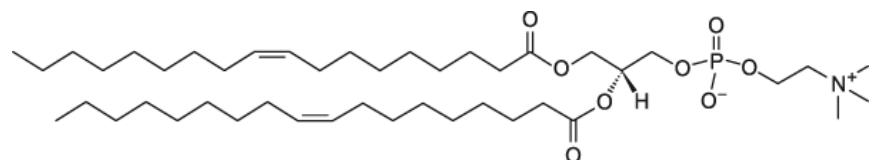
DOTAP (1,2-dioleoyl-3-trimethylammonium-propane, Avanti Polar Lipids)
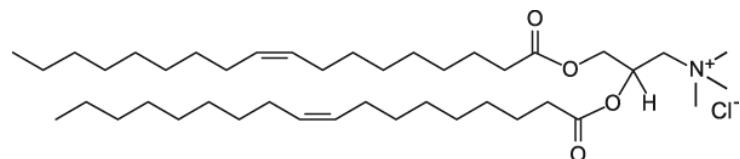
Figure S1: Chemical structures of DOPC and DOTAP.
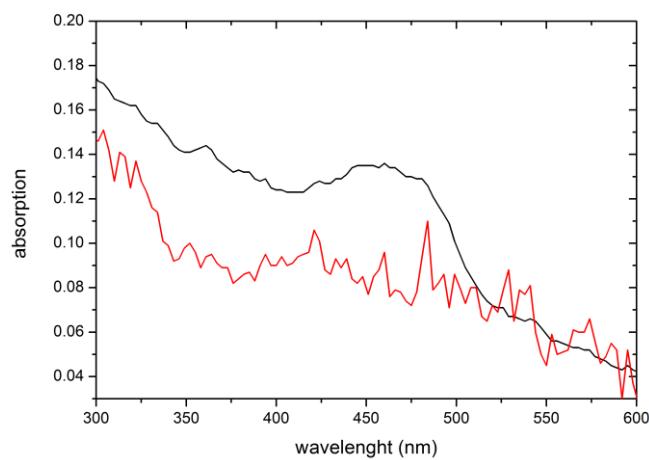
Figure S2: UV-Vis spectrum of SLB@NCS before (black) and after (red) the release experiment.

The black line represents SLB@NCS loaded with calcein. The peak represents the absorption of the loaded calcein. After the release (red line), no peak is visible, indicating complete release of the fluorescent dye out of the mesopores.

9.6. Chapter References

(1)   Yang, P.; Gai, S.; Lin, J. *Chem. Soc. Rev.* **2012**, *41*, 3679.

(2)   Yang, F.; Jin, C.; Jiang, Y. J.; Li, J.; Di, Y.; Ni, Q. X.; Fu, D. L. *Cancer Treat. Rev.* **2011**, *37*, 633.

(3)   Tran, M. A.; Watts, R. J.; Robertson, G. P. *Pigm. Cell Melanoma R.* **2009**, *22*, 388.

(4)   Wagner, E. *Acc. Chem. Res.* **2011**, *45*, 1005.

(5)   Meyer, M.; Dohmen, C.; Philipp, A.; Kiener, D.; Maiwald, G.; Scheu, C.; Ogris, M.; Wagner, E. *Mol. Pharmaceutics* **2009**, *6*, 752.

(6)   Matsumoto, S.; Christie, R. J.; Nishiyama, N.; Miyata, K.; Ishii, A.; Oba, M.; Koyama, H.; Yamasaki, Y.; Kataoka, K. *Biomacromolecules* **2008**, *10*, 119.

(7)   Miyata, K.; Oba, M.; Nakanishi, M.; Fukushima, S.; Yamasaki, Y.; Koyama, H.; Nishiyama, N.; Kataoka, K. *J. Am. Chem. Soc.* **2008**, *130*, 16287.

(8)   Hagiwara, A.; Takahashi, T.; Sawai, K.; Sakakura, C.; Yamaguchi, M.; Osaki, K.; Tsujimoto, H.; Ohyama, T.; Tomoda, H.; Yamamoto, A.; Muranish, S. *Anti-Cancer Drugs* **1994**, *5*, 194.

(9)   Hagiwara, A.; Takahashi, T.; Sawai, K.; Sakakura, C.; Hoshima, M.; Ohyama, T.; Ohgaki, M.; Imanishi, T.; Yamamoto, A.; Muranishi, S. *Cancer* **1996**, *78*, 2199.

(10)   Liu, Z. A.; Sun, X. M.; Nakayama-Ratchford, N.; Dai, H. J. *ACS Nano* **2010**, *4*, 7726.

(11) Ren, J. F.; Shen, S.; Wang, D. G.; Xi, Z. J.; Guo, L. R.; Pang, Z. Q.; Qian, Y.; Sun, X. Y.; Jiang, X. G. *Biomater.* **2012**, *33*, 3324.

(12) Liu, Z.; Chen, K.; Davis, C.; Sherlock, S.; Cao, Q. Z.; Chen, X. Y.; Dai, H. J. *Cancer Res.* **2008**, *68*, 6652.

(13) Liu, Z.; Robinson, J. T.; Tabakman, S. M.; Yang, K.; Dai, H. J. *Mater. Today* **2011**, *14*, 316.

(14) Zhu, S.; Chen, C.; Chen, Z.; Liu, X.; Li, Y.; Shi, Y.; Zhang, D. *Mater. Chem. Phys.* **2011**, *126*, 357.

(15) Carrero-Sánchez, J. C.; Elías, A. L.; Mancilla, R.; Arrellín, G.; Terrones, H.; Laclette, J. P.; Terrones, M. *Nano Lett.* **2006**, *6*, 1609.

(16) Fang, Y.; Gu, D.; Zou, Y.; Wu, Z.; Li, F.; Che, R.; Deng, Y.; Tu, B.; Zhao, D. *Angew.Chem., Int. Ed.* **2010**, *122*, 8159.

(17) Boncel, S.; Herman, A. P.; Walczak, K. Z. *J. Mater. Chem.* **2012**, *22*, 31.

(18) Magrez, A.; Kasas, S.; Salicio, V.; Pasquier, N.; Seo, J. W.; Celio, M.; Catsicas, S.; Schwaller, B.; Forró, L. *Nano Lett.* **2006**, *6*, 1121.

(19) Dumortier, H.; Lacotte, S.; Pastorin, G.; Marega, R.; Wu, W.; Bonifazi, D.; Briand, J.-P.; Prato, M.; Muller, S.; Bianco, A. *Nano Lett.* **2006**, *6*, 1522.

(20) Zhao, P.; Wang, L.; Sun, C.; Jiang, T.; Zhang, J.; Zhang, Q.; Sun, J.; Deng, Y.; Wang, S. *Eur. J. Pharm. Biopharm.* **2012**, *80*, 535.

(21) Ryoo, R.; Joo, S. H.; Kruk, M.; Jaroniec, M. *Adv. Mater.* **2001**, *13*, 677.

(22) Lee, J.; Kim, J.; Hyeon, T. *Adv. Mater.* **2006**, *18*, 2073.

(23) Kim, T.-W.; Chung, P.-W.; Slowing, I. I.; Tsunoda, M.; Yeung, E. S.; Lin, V. S. Y. *Nano Lett.* **2008**, *8*, 3724.

(24) Gu, J. L.; Su, S. S.; Li, Y. S.; He, Q. J.; Shi, J. L. *Chem. Commun.* **2011**, *47*, 2101.

(25) Zhu, J.; Liao, L.; Bian, X.; Kong, J.; Yang, P.; Liu, B. *Small* **2012**, *8*, 2715.

(26)   Liu, R.; Shi, Y.; Wan, Y.; Meng, Y.; Zhang, F.; Gu, D.; Chen, Z.; Tu, B.; Zhao, D. *J. Am. Chem. Soc.* **2006**, *128*, 11652.

(27)   Schuster, J.; He, G.; Mandlmeier, B.; Yim, T.; Lee, K. T.; Bein, T.; Nazar, L. F. *Angew.Chem., Int. Ed.* **2012**, *51*, 3591.

(28)   Ashley, C. E.; Carnes, E. C.; Phillips, G. K.; Padilla, D.; Durfee, P. N.; Brown, P. A.; Hanna, T. N.; Liu, J.; Phillips, B.; Carter, M. B.; Carroll, N. J.; Jiang, X.; Dunphy, D. R.; Willman, C. L.; Petsev, D. N.; Evans, D. G.; Parikh, A. N.; Chackerian, B.; Wharton, W.; Peabody, D. S.; Brinker, C. J. *Nature Mat.* **2011**, *10*, 389.

(29)   Cauda, V.; Engelke, H.; Sauer, A.; Arcizet, D.; Bräuchle, C.; Rädler, J.; Bein, T. *Nano Lett.* **2010**, *10*, 2484.

(30)   Liu, J.; Jiang, X.; Ashley, C.; Brinker, C. J. *J. Am. Chem. Soc.* **2009**, *131*, 7567.

(31)   Liu, J.; Stace-Naughton, A.; Jiang, X.; Brinker, C. J. *J. Am. Chem. Soc.* **2009**, *131*, 1354.

(32)   Nordlund, G.; Sing Ng, J. B.; Bergström, L.; Brzezinski, P. *ACS Nano* **2009**, *3*, 2639.

(33)   Schloßbauer, A.; Sauer, A. M.; Cauda, V.; Schmidt, A.; Engelke, H.; Rothbauer, U.; Zolghadr, K.; Leonhardt, H.; Bräuchle, C.; Bein, T. *Adv. Healthcare Mater.* **2012**, *1*, 316.

(34)   Torchilin, V. P. *Nat. Rev. Drug. Discov.* **2005**, *4*, 145.

(35)   Bayerl, T. M.; Bloom, M. *Biophys. J.* **1990**, *58*, 357.

(36)   Duncanson, W. J.; Figa, M. A.; Hallock, K.; Zalipsky, S.; Hamilton, J. A.; Wong, J. Y. *Biomaterials* **2007**, *28*, 4991.

(37)   Mandlmeier, B.; Szeifert, J. M.; Fattakhova-Rohlfing, D.; Amenitsch, H.; Bein, T. *J. Am. Chem. Soc.* **2011**, *133*, 17274.

(38)   Meng, Y.; Gu, D.; Zhang, F.; Shi, Y.; Cheng, L.; Feng, D.; Wu, Z.; Chen, Z.; Wan, Y.; Stein, A.; Zhao, D. *Chem. Mater.* **2006**, *18*, 4447.

(39)   Schlossbauer, A.; Kecht, J.; Bein, T. *Angew.Chem., Int. Ed.* **2009**, *48*, 3092.

(40)   Holland, B. T.; Blanford, C. F.; Stein, A. *Science* **1998**, *281*, 538.

(41)   Holland, B. T.; Blanford, C. F.; Do, T.; Stein, A. *Chem. Mater.* **1999**, *11*, 795.

(42)   Vinu, A.; Hossian, K. Z.; Srinivasu, P.; Miyahara, M.; Anandan, S.; Gokulakrishnan, N.; Mori, T.; Ariga, K.; Balasubramanian, V. V. *J. Mater. Chem.* **2007**, *17*, 1819.

10. Conclusions and Outlook

This thesis is focused on developing templating strategies for mesoporous and macroporous titania and carbon morphologies in the form of thin films, bulk materials, particles and fibers that can serve in applications where porous structure is essential for optimized functionality.

Macro- or mesoporosity was introduced into 3D architectures by the direct replication of templates, colloidal poly(methylmetacrylate) and block-copolymers, respectively. Macroporous titania films and bulk silica were developed with metal alkoxide precursors and crystalline building blocks using different techniques. The resulting confined macroporous space was the basis for the creation of more complex hierarchical systems. We controlled parameters such as (i) the size of the macropores and size and the ordering of the mesopores; (ii) the composition and crystallinity of the functional scaffold; (iii) the macroscopic shape such as thin films, bulk, particles and fibers. The physical properties of these materials are investigated with a view on diverse applications, i.e., the performance of dye-sensitized solar cells (DSCs), rechargeable lithium-sulfur batteries and controlled drug delivery.

For the development of macroporous oxides PMMA beads were synthesized as sacrificial templates. The uniform colloids were accessible from 40 nm and 320 nm using emulsion polymerization. We combined them in a one-step co-deposition approach or a two-step replication procedure with several molecular titania and silica precursors and/ or different titania nanoparticles. All solid wall components showed individual heating-induced grain growth within the confined space of PMMA beads, and thus texture and structure of the open 3D architectures could be controlled. We also developed ways to optimize the macroscopic quality of particle-derived films, for example by using a post-synthetic humidity treatment.

This synthetic flexibility was employed to create novel homologous hierarchical periodic nanostructures composed of a crystalline macroporous titania scaffold and a mesoporous titania phase. The confined synthesis in these systems showed a strong influence of the 3D scaffold on mesostructure assembly, which had three effects: larger structural parameters after synthesis, limited shrinkage upon heating and enhanced crystallization kinetics of the mesophase. The resulting structure was examined as hierarchical anode in dye sensitized solar cells.

We also used various PMMA beads to produce amorphous macroporous silica, and used the spherical confined space for the synthesis of positive mesoporous replicas of the polymer beads. Thus Pluronic P123 and tetraethyl orthotitanate were used to obtain mesoporosity and crystallinity of titania in the macropores after calcination, while the SiO_2 host was removed with NaOH to obtain spherical anatase particles. This method was also used for the creation of spherical hexagonally ordered mesoporous carbon nanoparticles (> 200 nm) and colloidal nanosized mesoporous carbon (~ 60 nm). Both particles were redispersible in polar solvents and feature very high surface areas and high pore volumes, respectively. To achieve template imbibition, a triconstituent co-assembly of a carbon (resol oligomers) and silica tetraethyl orthosilicate) precursors and Pluronic F127 was used in this synthetic appraoch. After thermopolymerization and carbonization, mesoporous carbon/silica was formed in the confined space. All silica residues were removed with HF to obtain a bimodal porosity in the resulting nano-spheres.

Moreover, this templating approach was transferred to obtain a novel tubular macroporous silica hard template, showing comparable dimensions to anodic alumina membranes. This was achieved by using dense carbon fibers, in contrast to PMMA beads, which were replicated to produce mesoporous carbon fibers. A confinement effect of the macroporous space led to a reduced shrinkage of the mesophase accompanied by larger structural

parameters. Our carbon nanomaterials were further investigated in two widely different applications. Thus spherical ordered mesoporous carbon particles and fibers were implemented as cathodes in Li-S batteries showing high gravimetric discharge capacities (> 1200 mAh/g) and good stability up to 100 cycles of (dis)charging. Both nanostructures performed better than a mesoporous bulk reference carbon material. Finally, we have developed novel colloidal nanosized carbon spheres, loaded with calcein as "model drug" and efficiently sealed with a stable supported lipid bilayer cap system. Controlled molecular release experiments demonstrate the effective sealing and release for this system.

In conclusion, we have developed new strategies for inorganic and organic hierarchical, spherical and fibrous nanostructures, which were based on the replication of various uniform templates, such as PMMA spheres and dense carbon fibers. The obtained morphologies feature diverse properties regarding their structure, crystallinity and porosity. These properties were also affected by the confined macroporous space. The novel morphologies improved the performance of devices for energy conversion and storage and moreover could be used for possible medical applications.

It is envisioned that by extending the nature and size range of the spherical templates one could access an even broader range of confined porous templates. Combining these with various alternative precursor combinations might lead to other new hierarchical architectures, having a macroporous scaffold and mesoporous interior. For example, we are presently investigating the possibility to employ such morphologies in light-induced water splitting reactions.

11. Author Information

11.1.   Curriculum Vitae

Persönliche Daten

Name:	Benjamin Mandlmeier
Geburtsdatum:	05. April 1983
Geburtsort:	Starnberg
Staatsangehörigkeit:	deutsch
Familienstand:	verheiratet

Schulische Ausbildung

09/89 – 08/94	Grundschule Percha
09/94 – 06/02	Landschulheim Kempfenhausen (Berg)
28.06.2002	*Allgemeine Hochschulreife* am LSH Kempfenhausen

Studium und Promotion

10/2002 – 12/2007	Diplomstudiengang Chemie, Ludwig-Maximilians Universität München
28.10.2004	*Diplom-Vorprüfung* an der LMU München
06/2007 – 12/2007	Diplomarbeit bei der BMW AG München, Betreuung durch Prof. Dr. Thomas Bein: *„Beurteilung der Selbstreinigung von multifunktionalen Nanobeschichtungen hinsichtlich einer automobilen Anwendung"*
20.12.2007	*Diplom-Hauptprüfung* an der LMU München
04/2008 – heute	Promotion an der LMU München bei Prof. Dr. Thomas Bein

Sonstige Tätigkeiten

08/2007 – heute	Allgemeine Untersuchungen mittels Rasterelektronenmikroskopie (REM) und Energiedispersiver Röntgenspektroskopie ((EDX), verantwortlicher Mitarbeiter für photoelektrochemische Untersuchungen und Betreuung von Potentiostaten, Sinter- und Syntheseöfen und Plasma-Reiniger.
2008 – heute	Fachliche Anleitung und Ausbildung von Bachelor- und Masterstudenten. Betreuung von Praktika in der Anorganischen und Physikalischen Chemie
2008 – heute	Förderung von hochbegabten Klassen der 8. – 10. Jahrgangsstufe am Münchner Maria-Theresia Gymnasium mit freundlicher Unterstützung durch die Nanosystems Initiative Munich (Mentoring).
08/2009 – heute	Freiberuflicher Mitarbeiter der NanoScape AG (Planegg/ Martinsried)
10/2010 – heute	Mitglied im NIM Graduierten Kolleg

Zusatzqualifikationen

Sprachen	Deutsch (Muttersprache)
	Englisch (fließend)
	Französisch (Grundkenntnisse)
Fachlich	Electrochemical Impedance Spectroscopy (EIS) Summer School (University of Bath, UK)
EDV	Microsoft Office (sehr gut)
	Adobe Illustrator und Photoshop (gut)

11.2.   List of Publications

(1)   B. Mandlmeier, N.K. Minar, J.M. Feckl, D. Fattakhova-Rohlfing, and T. Bein,

Tuning of Crystallinity Parameters in Macroporous Titania Films,

manuscript ready for submission.

(2)   B. Mandlmeier, J. Schuster, G. He, L.F. Nazar and T. Bein,

Bimodal Mesoporous Carbon Nanofibers with High Porosity: Freestanding and

Embedded in Membranes for Lithium-Sulfur Batteries, manuscript ready for

submission.

(3)   B. Mandlmeier, S. Niedermayer, A. Schmidt, J. Schuster, and T. Bein,

Lipid-bilayer coated nanosized bimodal mesoporous carbon spheres for controlled drug

delivery applications, manuscript ready for submission.

(4)   H. Němec, V. Zajac, I. Rychetský, D. Fattakhova-Rohlfing, B. Mandlmeier, T. Bein, Z.

Mics, and P. Kužel, Charge transport in TiO_2 films with complex percolation pathways

investigated by time-resolved terahertz spectroscopy, invited to *IEEE Transactions on*

Terahertz Science and Technology.

(5)   J. Schuster, G. He, B. Mandlmeier, T. Yim, K.T. Lee, T. Bein, and L.F. Nazar,

Spherical Ordered Mesoporous Carbon Nanoparticles with High Porosity for Lithium–

Sulfur Batteries, *Angewandte Chemie International Edition* **2012**, *124*, 3651–3655.

(6)   B. Mandlmeier, J.M. Szeifert, D. Fattakhova-Rohlfing, H. Amenitsch, and T. Bein,

Formation of interpenetrating hierarchical titania structures by confined synthesis in

inverse opal. *Journal of American Chemical Soc*iety **2011**, 133, *43*, 17274-82.

(7)   Y. Liu, J.M. Szeifert, J.M. Feckl, <u>B. Mandlmeier</u>, J. Rathousky, O. Hayden, D.

Fattakhova-Rohlfing, and T. Bein,

Niobium-Doped Titania Nanoparticles: Synthesis and Assembly into Mesoporous Films

and Electrical Conductivity, *ACS Nano* **2010**, *4*, 5373-81.

11.3.   List of Presentations and Posters

2013

(1)   <u>H. Němec1</u>, I. Rychetský, P. Kužel, <u>B. Mandlmeier</u>, D. Fattakhova-Rohlfing, and T.

Bein,

(2)   Transient terahertz conductivity spectra of semiconductor nanostructures with complex

percolation pathways, Optical Terahertz Science and Technologies (OTST 2013), 2013,

Kyoto, Japan, (presentation).

2012

(3)   B. Mandlmeier et al., Ordered Mesoporous Carbon for Lithium-Sulfur Batteries, Center

for NanoSciences (CeNS) Workshop 2012, Venice, Italy (poster).

(4)   I. Kondofersky, B. Mandlmeier, J.Feckl, H.Dunn, et al. Ordered Macroporous Tin

Oxide Nanostructures as an Anode Host Scaffold for Water Splitting Applications,

CeNS Workshop 2012, Venice, Italy (poster).

(5)   <u>B. Mandlmeier</u> et al., Formation of Interpenetrating Hierarchical Titania Structures by

Confined Synthesis in Inverse Opal, Materials Research Society (MRS) Spring Meeting

2012, San Francisco, USA (presentation).

(6) B. Mandlmeier, et al., Confined synthesis of hierarchical titania structures (poster), Deutsche Zeolith-Tagung 2012, Magdeburg, Germany (poster).

2011

(7) B. Mandlmeier et al, Hierarchical periodic titania nanostructures as novel anodes for dye-sensitized solar cells, 4th International Conference on Hybrid and Organic Photovoltaics (HOPV) 2011, Valencia, Spain (poster).

(8) J. Schuster, B. Mandlmeier, A. Keilbach, et al., Morphology-control of ordered mesoporous carbons with extremely high porosity, Deutsche Zeolith-Tagung 2011, Erlangen, Germany (presentation).

(9) B. Mandlmeier, J.M. Szeifert, D. Fattakhova-Rohlfing, T. Bein, Mesopore formation in a 3D macroporous titania host, Deutsche Zeolith-Tagung 2011, Erlangen, Germany.

(10) J.M. Szeifert, J.M. Feckl, B. Mandlmeier, et al. Porous titania nanostructures for hybrid solar cells through fusion of ultrasmall nanocrystals, Deutsche Zeolith-Tagung 2011, Erlangen, Germany (poster).

2010

(11) B. Mandlmeier et al., Synthesis and morphology of ordered hierarchical meso-macroporous titania systems, CeNS Workshop 2010, Venice, Italy (poster).

(12) J.M. Szeifert, J.M. Feckl, B. Mandlmeier, D. Fattakhova-Rohlfing, V. Kalousek, J. Rathousky, D. Kuang, S. Wenger, S. M. Zakeeruddin, M. Grätzel, and T. Bein, Mesoporous Titania for Hybrid Solar Cells through Fusion of Ultrasmall Nanocrystals, QUANTSOL 2010 Winter workshop, Graubünden, Switzerland (presentation)

Autor:

Benjamin Mandlmeier

Arbeitskreisleiter: Prof. Dr. Thomas Bein

Dept. Chemie, LMU München

Gerhard-Ertl-Gebäude, Haus E

Butenandtstr. 11

81377 München - Großhaderm